

University of Memphis

University of Memphis Digital Commons

Electronic Theses and Dissertations

11-29-2022

Improvements in Digital Holographic Microscopy

Raul Andres Castaneda Quintero

Follow this and additional works at: <https://digitalcommons.memphis.edu/etd>

Recommended Citation

Castaneda Quintero, Raul Andres, "Improvements in Digital Holographic Microscopy" (2022). *Electronic Theses and Dissertations*. 3196.

<https://digitalcommons.memphis.edu/etd/3196>

This Dissertation is brought to you for free and open access by University of Memphis Digital Commons. It has been accepted for inclusion in Electronic Theses and Dissertations by an authorized administrator of University of Memphis Digital Commons. For more information, please contact khggerty@memphis.edu.

Improvements in Digital Holographic Microscopy

by

Raul Castaneda

A Dissertation

Submitted in Partial Fulfillment of the

Requirement for the Degree of

Doctor of Philosophy

Major: Electrical and Computer Engineering

Supervisor: Dr. Ana Doblas

The University of Memphis

December 2022

“El límite no es el cielo, es el ataúd”

Métricas Frías.

ACKNOWLEDGEMENT

First of all, I want to thank my advisor Dr. Ana Doblas. Undoubtedly, I would never have been a Ph.D. student at the University of Memphis without all the support that she has given to me. Dr. Doblas, thanks for believing in me, your patience, and each second of your time that you have invested in me explaining Physics, Holography, Maths, Image Processing, and English. But, above all, thank you for teaching me that the most important thing in life is being a better human and a great professional. I really appreciate you.

Also, I want to thank Dr. Carlos Trujillo, professor at EAFIT University (Medellin, Colombia) for his support, willingness to investigate together, and continuous teaching support on the wonderful world of holography and computational science.

Additionally, I am grateful to Drs. Chrysanthé Preza, Madhusudhanan Balasubramanian, and Francisco Muller-Sanchez who have devoted their precious time being in my dissertation committee and providing valuable suggestions. I would also like to thank all the University of Memphis professors who gave me courses during my Ph.D. I have learned a lot from each one of you. Of course, I want to thank my classmates and colleagues at the Optical Imaging Research Lab.

Finally, I want to thank my family, my mom, and my father (R.I.P). Thanks to Michael Salinas, you are my brother; believe me without your help, my stay in America could have been more challenging. Thank you to the Omegarep community, and last, special thanks to Astrid Arias; you were the person that has always encouraged me to keep working during the pandemic time and remain until the end.

ABSTRACT

The Ph.D. dissertation consists of developing a series of innovative computational methods for improving digital holographic microscopy (DHM). DHM systems are widely used in quantitative phase imaging for studying micrometer-size biological and non-biological samples. As any imaging technique, DHM systems have limitations that reduce their applicability. Current limitations in DHM systems are: i) the number of holograms (more than three holograms) required in slightly off-axis DHM systems to reconstruct the object phase information without applying complex computational algorithms; ii) the lack of an automatic and robust computation algorithm to compensate for the interference angle and reconstruct the object phase information without phase distortions in off-axis DHM systems operating in telecentric and image plane conditions; iii) the necessity of an automatic computational algorithm to simultaneously compensate for the interference angle and numerically focus out-of-focus holograms on reconstructing the object phase information without phase distortions in off-axis DHM systems operating in telecentric regime; iv) the deficiency of reconstructing phase images without phase distortions at video-rate speed in off-axis DHM operating in telecentric regime, and image plane conditions; v) the lack of an open-source library for any DHM optical configuration; and, finally, vi) the tradeoff between speckle contrast and spatial resolution existing in current computational strategies to reduce the speckle contrast. This Ph.D. dissertation is motivated to overcome or at least reduce the six limitations mentioned above. Each chapter of this dissertation presents and discusses a novel computational method from the theoretical and experimental point of view to address each of these limitations.

PREFACE

This dissertation document has been written with the intention of summarizing the research work elaborated on during my Ph.D. studies. The Ph.D. was focused on improving the Digital Holographic Microscopy technique, encouraged by the wide range of applications in live and material sciences and its current limitations.

The dissertation is based on five published papers and seven peer-review conference publications. For instance, Chapters 3, 4, 6, and 8 are based on published peer-reviewed papers: 1) R. Castaneda et al., “Fast-iterative blind phase-shifting digital holographic microscopy,” *Appl. Opt.* 59, 7469-7476 (2020); and 2) R. Castaneda and A. Doblas, “Fast-iterative automatic reconstruction method for quantitative phase image with reduced phase perturbations in off-axis digital holographic microscopy,” *Appl. Opt.* 60, 10214-10220 (2021); 3) R. Castaneda et al. “pyDHM: A Python library for applications in Digital Holographic Microscopy,” *Plos ONE* 17: e0275818 (2022); 4) R. Castaneda et al. “Speckle noise reduction in coherent imaging systems via Hybrid Median-Mean Filter,” *Opt. Engineering* 60, 233107 (2021). Chapter 5 presents a joint phase compensation and autofocus method for telecentric off-axis DHM and has been accepted to be presented at 2023 SPIE Photonics West. Finally, Chapter 7 is an extended version of the peer-reviewed paper entitled “Video-Rates Quantitative Phase Imaging Using a Digital Holographic Microscopy and Generative Adversarial Networks” and published in *Sensors*. These results have been presented at the 2021 IEEE Photonics Conference and 2022 OSA Imaging and Applied Optics Congress.

TABLE OF CONTENT

1. INTRODUCTION	1
1.1 Contributions and novelties of the dissertation.....	6
2. PRINCIPLES OF DIGITAL HOLOGRAPHIC MICROSCOPY	11
2.1 Recording stage.....	11
2.2 Numerical reconstruction stage.....	14
3. FAST-ITERATIVE COMPUTATIONAL RECONSTRUCTION ALGORITHM FOR BLIND PHASE-SHIFTING DIGITAL HOLOGRAPHIC MICROSCOPY WITH REDUCED HOLOGRAMS	
3.1 Theoretical framework	27
3.2 Proposed blind PS-DHM using two images	28
3.3 Experimental validation	34
3.4 Conclusion	39
4. FAST-ITERATIVE COMPUTATIONAL RECONSTRUCTION ALGORITHM FOR OFF- AXIS DIGITAL HOLOGRAPHIC MICROSCOPY OPERATING IN TELECENTRIC REGIME AND IMAGE PLANE	41
4.1 Theoretical framework.....	43
4.2 Proposed method	46
4.3 Experimental validation.....	52
4.4 Conclusions.....	56
5. FULL ABERRATION COMPENSATION METHOD FOR NON-IMAGE-PLANE OFF- AXIS DIGITAL HOLOGRAPHIC MICROSCOPY	58

5.1 Theoretical background: out-focus DHM imaging reconstruction	60
5.2 Full aberration compensation proposal: DHM autofocusing and tilting angle phase compensation for telecentric setups	63
5.3 Results for experimental statics samples	70
5.4 Conclusions.....	74
6. OPEN-SOURCE PYTHON LIBRARY FOR DHM	76
6.1 Libraries in DH and DHM	76
6.2 Library framework	80
6.3 Library Structure: available packages in pyDHM	81
6.3.1 Package 1: Utility package.....	82
6.3.2 Package 2: Phase-shifting package	84
6.3.3 Package 3: Fully-compensate phase reconstruction package	88
6.3.4 Package 4: Numerical propagation package	92
6.4 Conclusion	96
7. LEARNING-BASED MODELS FOR VIDEO-RATE QUANTITATIVE PHAS IMAGING USING AN OFF-AXIS DIGITAL HOLOGRAPHIC MICROSCOPE	98
7.1 Introduction.....	99
7.2 ConvA framework and performance in off-axis DHM.....	102
7.2.1 ConvA framework	102
7.2.2 Performance of ConvA model using simulated data	103
7.2.3 Performance of ConvA model using experimental data	106
7.3 cGAN and performance in off-axis DHM	110
7.3.1 cGAN framework.....	110

7.3.2 Experimental results.....	117
7.4 Comparison of the proposed cGAN model against the ConvA and U-Net models.....	123
7.5 Validation of the Proposal's generalization ability to system's diversity.....	127
7.6 Conclusion	129
8. SPECKLE NOISE REDUCTION IN DHM VIA HYBRID MEDIAN-MEAN FILTER.....	132
8.1 Speckle noise	135
8.2 Hybrid Median-Mean Framework	137
8.3 Experimental results.....	138
8.3.1 Laser-Based RGB photography results.....	139
8.3.2 DH and DHM results	141
8.4 Conclusions.....	149
9. CONCLUSIONS.....	151
10. APPENDIX A: COMPARISON OF THE SPECKLE NOISE REDUCTION IN DHM VIA HYBRID MEDIA-MEAN FILTER OR CONVENTIONAL MEDIAN-FILTERED IMAGES	157
11. APPENDIX B: FOURIER SPECTRUM ANALYSIS FOR THE MH2F.....	163
12. REFERENCES	165

LIST OF TABLES

Table 3.1. Performance of the proposed algorithm under Noise Conditions: SNR	34
Table 3.2. Advantages and limitations of the proposed blind phase-shift method for two raw holograms.....	40
Table 4.1. Achievements and limitations of the proposed method.	57
Table 5. 1. Definition of the studied sharpness metrics	64
Table 6. 1. DH and DHM libraries.....	79
Table 6. 2. Summary of the different approaches implemented by the pyDHM library.	81
Table 7.1. Training and prediction times for the compared learning-based approaches	125
Table 7.2. Advantages and limitations of the proposed cGAN model to fully reconstruct quantitative phase images from human red blood cells (RBCs).....	131
Table 8.1. Comparison for the BM3D, NLM, WFT2F, Wiener, and HM2F methods	145

LIST OF FIGURES

Fig. 2.1. Optical Mach-Zehnder DHM system.	11
Fig. 2.2. Representation for the three possible DHM configurations. Panel (a) shows the scheme that allows observing the angle of interference between the object wave and the reference wave. Panel (b) in-line, panel (c) slightly off-axis, and finally, panel (d) off-axis. The ± 1 and DC diffraction orders are marked by blue and red circles, respectively.	15
Fig. 2.3. Demonstration of reconstructed phase images for the different circular masks. The lower the radius of the circular mask, the worse the spatial resolution in the reconstructed amplitude and phase images, providing images not limited by diffraction	20
Fig. 2.4. Spreading of the ± 1 diffraction orders when the DHM system does not operate in telecentric regime.	21
Fig. 2.5. Comparison between non-telecentric and telecentric DHM systems. The first and second rows show the holograms spectrum and the reconstructed phase images, respectively. (a)&(d) and (b)&(e) correspond to two different non-telecentric DHM systems with different radii of curvature C . The last column [(c) and (f)] is the result for a telecentric DHM system.	22
Fig. 3.1. Demonstration of the proposed algorithm based on the estimation of the spectral components D_0 and D_3 using two raw holograms. The panels are: (a) ground truth phase distribution of the simulated object; (b) Fourier transform of the hologram using a reference slightly tilted; (c) Fourier transform of the demodulated components using Eq. (3.4) for different values of the phase steps. The phase steps were 60 deg (True), 80 deg (Wrong), and 60.003 deg (Estimated), respectively. Note that only when the phase step is wrong, it appears and additional order in the D_0 component.	30
Fig. 3.2. Evaluation of the phase distribution estimated by the proposed method. The panels are: (a) estimated D_3 component; (b) Fourier transform of the d_1 demodulated component by spatial filtering of D_3 ; (c) estimated phase image after compensating the interference angle. The mean MSE between the true and the estimated phase images is 1.56×10^{-6}	31
Fig. 3.3. Flowchart of the proposed algorithm.	32
Fig. 3.4. Optical setup of a DHM. The DHM system operates in the telecentric regime. The recorded holograms with the needed phase shift are recorded by rotating a glass slide, which is mounted on a rotational stage.	36
Fig. 3.5. Experimental validation of the proposed method. Panel (a) shows one of the recorded holograms; panel (b) corresponds to the FT of the hologram shows in panel (a). Panels (c)-(d) illustrate the Fourier transforms of the two unknown components, D_0 and D_{-3} . Panel (e) shows the 2D reconstructed phase map and its 3D rendering.	37
Fig. 3.6. Experimental comparison of the proposed method using a Star target. Panels (a) and (b) show the normalized phase image of the star using 2 holograms and 3 holograms, respectively. Panel (c) shows the phase-height profiles of the reconstructed phase maps at two different	

positions, $r_1 = 72 \mu\text{m}$ and $r_2 = 90 \mu\text{m}$, radial positions measured from the center are marked in panel (b). In panel (c), the red and blue profiles correspond to the reconstructed phase profiles using 2 and 3 raw holograms, respectively. The area of the star is $358 \times 358 \mu\text{m}^2$ 39

Fig. 4.1. Representation of the center position of the +1 term, $(u_{\text{max}}, v_{\text{max}})$. (a) The frequential position of the maximum peak coincides with an integer value, and (b) the frequential position of the maximum peak does not coincide with an integer position. The latter case is the most common in experimental DHM systems. The green circle denotes the position of the maximum peak to compute the digital reference wave and reconstruct accurate phase images. 46

Fig. 4.2. Reconstructed phase images of a section of the head of a *Drosophila melanogaster* fly for different values of $(u_{\text{max}}, v_{\text{max}})$. Values are reported in the upper right corner. 47

Fig. 4.3. 3D surface plot for the cost-function J [Eq. (4.4)] vs different values of $(u_{\text{max}}, v_{\text{max}})$. These values were obtained for a *Drosophila melanogaster* fly. 49

Fig. 4.4. Block diagram of the proposed method. 52

Fig. 4.5. Reconstructed phase images of the phase USAF target of Benchmark Technologies (first row), a section of the *Drosophila melanogaster* fly (second row), and glioblastoma cells (third row) for three different algorithms: nested-loops-based algorithm (first column), centroid-based algorithm (second column), and the proposed method (last column). 54

Fig. 4.6. Illustration of the accuracy of the reconstructed phase images based on the precision of the $(u_{\text{max}}, v_{\text{max}})$ values. 56

Fig. 5.1. (a) Performance of different sharpness focusing metrics in terms of the propagation distance (z) of a pure phase USAF target. Panels (b)-(d) correspond to the reconstructed amplitude image at three different propagation distances: $-0.11 \mu\text{m}$, $-0.074 \mu\text{m}$ (e.g., in-focus plane) and $-0.020 \mu\text{m}$. The red rectangle indicates the best in-focus amplitude images. 65

Fig. 5.2. Block diagram of the proposed three-stage method. 67

Fig. 5.3. In panel (a) 3D surface plot for the cost-function J [Eq. (4.4)], using a pure phase USAF target. Panel (b) is the 2D heatmap of J . Panels (c)-(e) are phase images reconstructed for different values of $(u_{\text{max}}, v_{\text{max}})$. Whereas in (c) and (d) illustrate non-optimal compensation, panel (e) corresponds to the optimal compensation for the values of $(u_{\text{max}}, v_{\text{max}})$ reported in panel (b). ... 68

Fig. 5.4. Experimental validation of the proposed method using a phase star target. Panel (a) the out-of-focus hologram. Panel (b) and (c) are the reconstructed phase images at two different propagation distances: 140 mm ($z_{\text{obj}} = 87.5 \mu\text{m}$) and 120.6 mm ($z_{\text{obj}} = 75 \mu\text{m}$), respectively. Panel (d) shows the radial profile of the in-focus reconstructed phase images along the green line marked in panel (c). 71

Fig. 5.5. Experimental validation of the proposed method using biological samples. Panel (a) and (c) are the out-of-focus hologram of RBCs and cheek cells. Panels (b) and (d) are the reconstructed phase images at the in-focus plane. 73

Fig. 5.6. The behavior of the proposed method for different out-focus holograms *for RBC*. For each transverse plane, two different sceneries (FOV-1 and FOV-2) have been recorded. In-focus columns correspond to the in-focus recorded holograms. Columns called Out-focus ($15 \mu\text{m}$), Out-

focus (45 μm), and Out-focus (95 μm), are holograms recorded after displacement the sample 15 μm , 45 μm , and 95 μm , respectively.	74
Fig. 6.1. pyDHM library structure. The library is composed of utility (1), phase-shifting (2), fully-compensated phase reconstruction (3), and numerical propagation (4) packages.	82
Fig. 6.2. Available functions in the utility package.	83
Fig. 6.3. Available functions in the phase-shifting package.....	84
Fig. 6.4. Verification of the in-line PS function: (a) an example code; (b) simulated in-line DHM holograms of a phantom model. Panels (c) - (e) and the reconstructed phase images for the PS5, PS4 and PS3 strategies, respectively.	86
Fig. 6.5. Example of use of the slightly off-axis strategies. (a) a sample code; (b) FT of recorded hologram showing that the DHM system is operating in slightly off-axis configuration. Panel (c) is the reconstructed phase image of a Fresnel lens by the SOSR function using four holograms with a $\pi/2$ phase shifting. Panels (d) and (e) are the reconstructed phase images of a USAF test target using the BPS3 and BPS2 strategies, respectively.	87
Fig. 6.6. Available functions in the fully-compensate phase reconstruction package.....	89
Fig. 6.7. Example of the fully-compensated phase reconstruction package for off-axis DHM holograms recorded in telecentric configuration: (a) a sample code; (b) FT of a recorded hologram to show that the DHM system operates in off-axis and telecentric configuration. Panels (c)-(d) are the fully-compensated reconstructed phase images of a <i>Drosophila melanogaster</i> fly using FRS and ERS functions. Panel (e) shows the fully-compensated reconstructed phase image of a star target using the CFS function.	90
Fig. 6.8. Example of the CNF function for off-axis DHM holograms recorded in a non-telecentric configuration: (a) a sample code; (b) FT of a recorded hologram, notice that the hologram operates in off-axis and non-telecentric configuration. Panel (c) is the binarized image of the FT to select the dimensions of the rectangular filter with parameters (x1, x2, y1, y2). Panel (d) corresponds to the binarized reconstructed phase image after compensating the interfering angle, where X_cent and Y_cent positions are marked. Finally, panel (e) shows the reconstructed phase image of a <i>Drosophila melanogaster</i> fly with minimum phase distortions.	92
Fig. 6.9. Available functions in the numerical propagation package.	93
Fig. 6.10. Example of the angular spectrum approach to numerically focus a hologram using a circular spatial filter tool. Panel (a) is the sample code. Panels (b) show the hologram (c) its spectrum without (c) and with (d) a circular mask. Panels (e) – (g) are the reconstructed intensity images for three propagation distances (z).	94
Fig. 6.11. Examples of the Fresnel and Fresnel-Bluestein propagation approaches to numerically focus holograms using a rectangular mask to filter the object frequencies from the hologram spectrum. Panel (a) is the sample code. Panels (b) show the hologram spectrum (b) and the reconstructed intensity image without (c) and with (d) a rectangular mask of a horse model using the fresnel propagator. Panels (e) – (g) are the hologram spectrum (e), and the reconstructed intensity images after filtering the object frequencies from the hologram spectrum using two	

different magnifications [$2\times$ and $2.5\times$ in panels (f) and (g), respectively] for a 1-cm edge dice using the bluestein propagator. 95

Fig. 7.1. The convolutional autoencoder (ConvA) structure for amplitude and phase imaging in off-axis DHM. 103

Fig. 7.2. Simulated holograms of six different types of cells. (a) Simulated cells' distribution used as phase information; (b) raw off-axis holograms generated by the coherent interference between the simulated cells' distributions in (a) and a tilted uniform plane wave. The interference angles in the holograms are diverse to increase the method's applicability. The size dimension of each sample is 256×256 pixels. 104

Fig. 7.3. Comparison between the reconstructed amplitude (top row) and phase (bottom row) images using unseen dataset. First column: true images. Second column: amplitude and phase images reconstructed using the conventional method. Third column: amplitude and phase images generated by the trained ConvA model. 106

Fig. 7. 4. Illustration of the RBC dataset: (a) Conventional off-axis Mach–Zehnder DHM setup operating in telecentric regime. Input holograms after image orientation; and their respective phase maps reconstruction. The colors squares are used to illustrate the tilt of the interference fringes. 107

Fig. 7.5. Results of the proposed ConvA method applied to RBCs sample in DHM. Panels (a–d) are the DHM holograms. Panels (e–h) are the phase results obtained via the reference method [77]. Panels (i–l) show the phase map obtained by the proposal method. The colored circles in panels (e–l) show differences between the reconstructed phase images; see text for further details. ... 110

Fig. 7.6. Structure of the image-to-image translation conditional generative adversarial network (pix2pix cGAN) for reconstructing quantitative phase images in off-axis DHM. See text for further details. 111

Fig. 7. 7. Structure of the U-net model used for the proposed cGAN. 113

Fig. 7.8. Structure of the discriminator model used for the proposed cGAN. 114

Fig. 7.9. Performance of the cGAN model for the training and validation dataset: (a) The average TSM value of the reconstructed phase maps measured for the complete validation and training dataset; (b) the average STD values for the background regions of the selected 15 phase images per dataset; (c) reconstructed phase maps of the identical hologram of the validation dataset provided by the proposed cGAN model at different epochs. 116

Fig. 7.10. Results of the proposed learning-based method for aberration-free phase reconstruction of RBC samples in DHM. Panels (a)–(d) are the DHM holograms, illustrating different experimental conditions, marked by magenta dashed rectangles. Panels (e)–(h) are the results obtained via the conventional method. Panels (i)–(l) show the phase map obtained by the proposal cGAN model. For the whole set of phase maps presented their \square and TSM values were computed and reported below each phase map image. The colored arrows in panels (e)–(l) show differences between the reconstructed phase images; see text for further details. 119

Fig. 7.11. Quantitative comparison between the highest (a–f) and the lowest (g–l)-quality reconstructed phase images provided by the conventional reference method (first row) to those

obtained by our cGAN model (second row). Panels (a), (d), (g), and (j) are the reconstructed phase images. Panels (b), (e), (h) and (k) display the unwrapped reconstructed phase images. Finally, panels (c), (f), (i) and (l) show the three-dimensional (3D) pseudocolor distribution of the optical thickness. 120

Fig. 7.12. Evaluation of the traditional reference and GAN models to reconstruct aberration-free phase images in time-lapse DHM imaging. The blue arrow marks the flow direction. The yellow star marks the identical RBC across the time-lapse sequence. The red and green arrows show differences between the reconstructed phase images. 122

Fig. 7.13. Phase reconstructions by the tested learning-based models. The performance is quantitatively performed in terms of the thresholding-and-summation metric and the normalized standard deviation. 124

Fig. 7.14. Comparison between the U-Net model and our cGAN model. The first column displays the selected DHM holograms from the validation dataset. The reconstructed phase images obtained by the conventional method are illustrated in the second column. Columns 3 and 4 show the reconstructed phase images achieved by the U-Net and our cGAN model. The colored circles and arrows indicate differences between the reconstructed phase images. 126

Fig. 7.15. Evaluation of the generalization of the cGAN model to a common-path DHM system. The first column shows selected DHM holograms recorded using a Fresnel-based DHM system. Columns 2, 3, and 4 display the reconstructed phase images obtained by the conventional method, the U-Net model, and the proposed cGAN model, respectively. The dark blue circles mark the region where we estimated the \square value. 129

Fig. 8.1. (a) Pseudocode of the *hybrid median-mean filter* (HM2F). (b) Illustration of the hybrid median-mean filter for a maximum kernel size of $k = 5$. The input image correspondst to the noisy image. Each median filter creates a reduced speckle-noise image (e.g., denoising speckle image). The final denoised image is obtained as the average between the median filtered image and the mean result of the previous iteration. 137

Fig. 8.2. Illustration of the optical configurations. (a) Color laser-based photography, (b) DH, and (c) DHM systems following a Mach – Zehnder arrangement. BE, beam expander; BS, beam-splitter; DM, dichroic mirror; L, lens; M, mirror; MO, microscope objective; O, object beam; R, reference beam; SF, spatial filter; TL, tube lens. 139

Fig. 8.3. Validation of the proposed HM2F method in laser-based photography. Denoised RGB images of the four-color cube after applying different denoising approaches. (a) Original noisy image; denoised image using (b) BM3D, (c) Wiener filter, (d) NLM filter, (e) proposed HM2F, and (f) CMF. Panel (g) compares the response of these methods to blur by plotting the first-order derivate of a step function defined by the mean profile along the vertical direction of the region marked by the green rectangle in Panel (a). 141

Fig. 8.4. Denoising images obtained after applying two different approaches (CMF and HM2F) and two different kernel sizes. Panels (a) – (d) correspond to the denoised amplitude images using the CMF and HM2F approaches. Panel (e) corresponds to the quantitative comparison of the speckle contrast and the FWHM value of the first-order derivate of a step function defined by the

profile along the transverse direction marked by the green line in Panel (a) versus numbers of iterations (i.e., kernel size) for the CMF and HM2F methods. 143

Fig. 8.5. DH results for dice (a – f), and horse (g – l). The methods used are BM3D, NLM, WFT2F, Wiener, and HM2F. Panels (m) and (n) show the histograms of the dice and horse, respectively. The average mean and standard deviation values in 10 different zones for the dice and horse model are reported below each panel. 144

Fig. 8.6. Experimental results for the star target. The reconstructed phase image corresponds to (a) original noisy phase image, (b) denoised CMF phase image, (c) denoised BM3D phase image, (d) denoised NLM phase image, (e) denoised WFT2F phase image, (f) denoised Wiener phase image, and (g) denoised HM2F phase image. The kernel size for panels (b) and (g) is 5×5 147

Fig. 8.7. Experimental results for a transverse section of the head of a *Drosophila melanogaster* fly. The reconstructed phase image corresponds to (a) original noisy image, (b) BM3D, and (c) NLM. 148

Fig. A.1. (a) Pseudocode of the median filter average (MFA) and its working principle for a maximum kernel size of $k = 5$ 158

Fig. A.2. Denoising images obtained after applying three different approaches and two different kernel sizes. (a)-(b) Reconstructed images using the conventional median filter; (c)-(d) Reconstructed images using the median-filter average (MFA); (e)-(f) Reconstructed images using the HM2F. Panel (g) corresponds to the quantitative comparison of the speckle contrast versus numbers of iterations (i.e., kernel size) for the different methods. Panel (h) compares the response of the three methods by estimating the first-order derivate of a step function defined by the profile along the transverse direction marked by the green line in Fig. A2(a). 160

Fig. A.3. Experimental results for the star target. Panel (a) is the noisy reconstructed phase image. Panel (b) is the reconstructed phase images using the WFT2F method. Panels (c)-(d) reconstructed images using the conventional median filter; panels (e)-(f) correspond to the reconstructed images using the MFA. Finally, panels (g)-(h) are the reconstructed images using the HM2F. 162

Fig. B.1. (a) Simulated star target (e.g., original/noiseless image). (b)-(e) Noisy images with speckle noise of different variance. (f)-(m) Denoising images after applying the HM2F for two different kernel size. 163

Fig. B.2. Power intensity spectrum vs the number of pixels. See the text for details. 165

LIST OF ABBREVIATIONS

Abbreviation	Definition
AMP	Integrated Amplitude Modulus
BFM	Bright-Field Microscopy
BM3D	3D Block Matching
BPS	Blind Phase Shifting
ConvA	Convolutional Autoencoder
CFS	Cost Function Search function
cGAN	Convolutional Generative Adversarial Network
CGH	Computer Generated Hologram
CMF	Conventional Median Filter
CNN	Convolutional Neural Network
CNT	Compensation Non-Telecentric function
CSM	Confocal Scanning Microscopy
DIC	Differential Interference Contrast Microscopy
DH	Digital Holographic
DHM	Digital Holographic Microscopy
DL	Deep Learning
DLHM	Digital Lensless Holographic Microscopy
EL	Energy of Laplacian
FPS	Frames Per Second
ERS	Efficient ROI Search function
FPS	Frames Per Second
FRS	Full ROI Search function

FT	Fourier Transform
FWHM	Full Width at Half Maximum
GPU	Graphical Processing Unit
HM2F	Hybrid Median – Mean Filter
IFT	Inverse Fourier Transform
IP	Image Plane
MO	Microscope Objective
MSE	Mean Square Error
NLM	Nonlocal Means
NV	Normalized Variance
OCT	Optical Coherence Tomography
OS	Optical sectioning
PCM	Phase-Contrast Microscopy
PS-DHM	Phase-Shifting Digital Holographic Microscopy
QPI	Quantitative Phase Imaging
RBC	Red Blood Cell
RI	Refractive Index
RL	Resolution Limit
RMSE	Root-Mean-Square Error
ROI	Region Of Interest
SC	Speckle Contrast
SNR	Signal-To-Noise Ratio
SOSR	Quadrature phase-shifting method

TC	Tamura Coefficient
TL	Tube Lens
TPEM	Two-Photon Excitation Microscopy
TSM	Thresholding-and-Summation Metric
TV	Tenengrad Variance
WFT2F	2D Windowed Fourier Transform Filter

LIST OF MATHEMATICAL SYMBOLS

\otimes_2 : 2D convolution operator

$*$: complex conjugate operator

$|\cdot|^2$: square module operator

$\theta = (\theta_x, \theta_y)$: vector representation of the interference angle between the object and reference waves

$\Delta\phi_i$: phase shift in the i th- hologram

$\Delta\phi'_i = \Delta\phi_i - \Delta\phi_1$: normalized phase shift in the i th- hologram

Δ_{xy} = square pixel size of the camera

(Δ_x, Δ_y) : pixel size of the camera along the x - and y -direction, respectively

A_r : amplitude of the reference wave

C : curvature of the spherical wavefront introduced by the non-telecentric optical configuration

d : distance between the BFP of the MO lens and the FFP of the TL lens

$d_0 = 1 + |u_{IP}|^2$: spatial distribution of the reference and object intensities

D_0 : 2D Fourier Transform of the spatial distribution of the reference and object intensities

$d_{+1} = u_{IP}(\mathbf{x}) \cdot \exp[i k \sin\theta \mathbf{x}]$: complex spatial distribution of the real image

D_{+1} = 2D Fourier Transform of the complex real spatial distribution

$d_{-1} = u_{IP}(\mathbf{x}) \cdot \exp[-i k \sin\theta \mathbf{x}]$: complex spatial distribution of the virtual image

D_{-1} = 2D Fourier Transform of the complex virtual spatial distribution

$d_3 = d_{+1} + \exp(-i2\Delta\phi)d_{-1}$: combined complex spatial distribution using the real and virtual image

D_3 = 2D Fourier Transform of the combined complex spatial distribution using the real and virtual image

f_{MO} : focal length of the MO lens

f_{TL} : focal length of the TL lens

$\mathbf{x} = (x, y)$: lateral/transverse spatial coordinates

$\mathbf{u} = (u, v)$: lateral/transverse spatial frequencies

$u_m = \sin\theta / \lambda$: spatial modulation frequency of the interference pattern

$u_c = NA/(\lambda M_L)$: cutoff frequency of the DHM system defined by the diffraction limit.

$h(x,y)$: hologram

$H(u,v)$: 2D Fourier Transform of the hologram

$h_F(x,y)$: 2D inverse Fourier Transform of the filtered hologram spectrum

$H_F(u,v)$: Filtered hologram spectrum

$\hat{a}_z = |h_F|$: reconstructed amplitude image given by the modulus square of the inverse Fourier transform of the filtered hologram.

k : wavenumber

λ : wavelength

J : cost function

M_L : lateral magnification of the $4f$ system

M_A : axial magnification of the $4f$ system

$M \times N$: pixels of the camera's sensor

(m,n) : discrete lateral coordinates of the sensors

$o(x,y)$: complex amplitude distribution of the object wave

$p(x,y)$: amplitude transmittance of the pupil distribution

$P(u,v)$: 2D Fourier Transform of the amplitude transmittance of the pupil distribution

$r(x,y)$: reference plane wave

$r_D(x,y)$: digital reference plane wave

(u_0, v_0) : lateral pixel positions of the center of the DC term

(u_{\max}, v_{\max}) : lateral pixel positions of the +1 term

(u_{\max}^0, v_{\max}^0) : integer pixel positions of the +1 term given by finding the maximum peak/value

$u(x,y,z)$: complex object wavefield at a distance z from the image plane of the $4f$ system

$\hat{u}(x, y; z)$: reconstructed complex distribution of the object wavefront after filtering the +1 term from the off-axis hologram and compensating for the tilted reference wavefront.

$u_{IP}(x,y)$: complex object wavefield at the image plane of the $4f$ system

$\hat{u}_{IP}(x, y)$: reconstructed complex object wavefield at the image plane of the $4f$ system

$\hat{a}_{IP}(x, y) = |\hat{u}_{IP}(x, y)|$: reconstructed 2D amplitude map computed as the absolute square module of $\hat{u}_{IP}(x, y)$

\bar{a}_{IP} : mean of the reconstructed amplitude image

$\sigma(\hat{a}_{IP})$: standard deviation of the reconstructed amplitude image

$\hat{\phi}(x, y)$: reconstructed 2D phase map computed as the angle of $\hat{u}_{IP}(x, y)$

n : refractive index of the sample

t : thickness of the sample

z : propagation distance between the out-of-focus hologram plane and the in-focus plane

z_{obj} : axial distance between the front focal plane of the MO lens and the actual object position

S_x, S_y, L : filter's parameter

$Thres[\bullet]$: thresholding operator

SC: speckle contrast

σ : standard deviation

\bar{I} : mean intensity

g : noisy input image

\hat{g} : denoising image

(δ_x, δ_y) : lateral size of the speckle grain in DH along the x- and y-direction, respectively

D : dispersion parameter

1. INTRODUCTION

Biological research relies heavily on cell imaging to evaluate cellular physiological status and behavior. Cells provide structure and function for all living things, containing whole biological machinery responsible for what happens inside bodies, from microorganisms to humans. Since cells' dimensions vary approximately from 1- 100 μm , advances in microscopic imaging systems with high magnification are essential to enhance our understanding of cellular mechanisms such as cell division, motility, proliferation, and interaction. Such fundamental knowledge can result in transformative advances in new diagnostic methods and disease treatment. Different microscopy techniques have been developed by the need to study cells and understand the micro-size world. The simplest microscopic imaging modality to analyze biological samples is bright-field microscopy (BFM) [1,2]. Since most unstained biological specimens are colorless and translucent, BFM images of them have poor contrast. Another disadvantage of BFM is that it is not suitable for thick samples since they do not present optical sectioning (OS) capability, restricting its use for cells grown in monolayers. Therefore, BFM cannot accurately image the three-dimensional (3D) shape of live cells in complex, 3D spatial environments. This limitation results in a significant gap in our understanding of dynamic changes occurring in the 3D cell shape and behavior of thick unstained specimens. Nonetheless, these unstained (i.e., transparent) biological specimens induce phase shifts in the transmitted light beam, making them suitable for imaging using phase imaging modalities such as phase-contrast microscopy (PCM) [3,4], differential interference contrast microscopy (DIC) [5,6] and Hoffman contrast modulation [7]. Although the optical principle is different in PCM and DIC, both techniques are traditionally qualitative phase methods, aiming to convert optical path changes into intensity variations. Because they are traditionally qualitative, there is no information on the actual phase value, not being able to convert these phase changes

into thickness and refractive index values. Also, ideal phase contrast samples in PCM and DIC should generally have features with an optical path difference of less than one-tenth wavelength [8], limiting its use for thick samples. Single- and multi-photon fluorescence microscopic modalities such as confocal scanning microscopy (CSM) [9,10] and two-photon excitation microscopy (TPEM) [11,12] allow imaging of thick samples with a spatial resolution power up to 115 nm. Nonetheless, all fluorescent-based microscopic imaging modalities suffer from chemical phototoxicity. The presence of any chemical toxicity could lead to misleading information due to the cellular damage caused by long-term light exposure. Cell toxicity induced by the chemical toxicity induced by the fluorophores may result in severe organ dysfunction and disease, making fluorescent-based imaging modalities unsuitable for studies that investigate the response to therapy in the variations of the images.

This chemical toxicity problem can be reduced by using label-free (i.e., unstained) imaging modalities such as optical coherence tomography (OCT) [13,14] and digital holographic microscopy (DHM) [15–17], among many others [18–20]. While the hallmark of OCT is the understanding of the dynamics in 3D processes thanks to its high imaging depth (up to a couple of millimeters) and fine axial resolution, its poor lateral resolution limit ($>1\ \mu\text{m}$) prohibits its feasibility evaluating sub-domain cell differentiation. In contrast, DHM technology offers 3D real-time imaging capability of dynamic processes with nanoscale temporal sensitivity and a lateral (xy) resolution as low as 200 nm. Although the reconstructed amplitude and phase images in each transverse plane provided by DHM systems may contain out-of-focus information, the axial position of sample' organelles and cells within the sample's volume is well determined in DHM systems from a single image after applying computational autofocus approaches thanks to the optical recording of the complex amplitude distribution scattered by the sample. This feature is a

main difference between DHM and other imaging techniques, including BFM, widefield fluorescent microscopy, PCM, and DIC. Another advantage of DHM is that any phototoxicity problem is significantly avoided since this imaging modality requires low-power radiation. Nonetheless, there is no DHM system able to image thick samples, restricting the thickness of the microscopic samples to be less than 30 μm (e.g., samples are considered optically thin). Over the last decade, DHM systems have become one of the most innovative and relevant label-free imaging techniques for quantitative phase imaging (QPI) [21,22]. The hallmark of QPI-DHM is the reconstruction of 3D topographic profiles of biological and non-biological samples using a single-shot technique. Such topographic reconstruction is possible since the complex (e.g., both amplitude and phase information) wavefield scattered by the microscopic object can be recorded using DHM systems. Therefore, one can accurately reconstruct the amplitude and phase distributions of the microscopic object under research after applying a computational method. DHM systems have been applied to a broad range of biomedical studies, including cells proliferation [23–26], analysis of cellular volume [27], and detection of carcinomas tissues [28–30]. Moreover, DHM systems have been used for detecting and diagnosing diseases such as malaria [31,32], diabetes [33], anemia [34], among others [35–37].

Although the potential of DHM is clear, current DHM systems present some limitations (i.e., hardware and software), which are related to the operation principle of DHM. Among the hardware limitations, reconstructed amplitude and phase images in DHM are limited by diffraction [38], and affected by speckle noise [39], since the illumination source in DHM must be coherent. The software limitations are related to the computational efficiency and accuracy of DHM. High-performance DHM computational algorithms, which provide accurate amplitude and phase images, should be robust, automatic, and fast (i.e., they should take a reduced processing time).

We understand automatic computational algorithms as such computational methods that require minimum user input, being suitable for beginning graduate students and researchers without knowledge of computational reconstruction approaches (i.e., biologists). Ideally, DHM computational algorithms should be video-time algorithms enabling live cell imaging.

Despite the success of DHM as a measuring, classifying, and diagnostic tool in life and material sciences, DHM systems have not achieved their full potential yet due to their current limitations. For instance, because DHM systems can be utilized for quantitative analysis of biological systems and disease diagnostics, their performance in reconstructing phase information with high accuracy is a factor to be followed closely. This Ph.D. work is devoted to improving the performance of DHM systems, and investigating new computational strategies and approaches. In particular, the Ph.D. work focuses on six limitations. Firstly, we investigate the current limitation on the number of holograms required in phase-shifting methods applied to slightly off-axis DHM systems. Conventional phase-shifting methods require more than three holograms and accurate knowledge of the phase shifts between the registered holograms to reconstruct the object phase information. In this dissertation, we introduce a computational method to reconstruct object phase information in slightly off-axis DHM by applying a computational method that only requires two holograms with an arbitrary phase shift. The second limitation is the lack of an automatic and robust computational algorithm to compensate for the interference angle and reconstruct the object phase information without phase distortions in off-axis DHM systems operating in telecentric and image plane conditions. Here we present a fast and automatic algorithm to reconstruct the quantitative phase distribution of unstained biological samples with a minimum or no phase perturbation for holograms recorded in off-axis architecture. The third limitation is the necessity of an automatic computational algorithm to simultaneously compensate for the interference angle and numerically

focus out-of-focus holograms on reconstructing the object phase information without phase distortions in off-axis DHM systems operating in telecentric regime. We present a fast and automatic algorithm to reconstruct the in-focus information to solve this limitation. Another limitation is the deficiency of reconstructing phase images without phase distortions at video-rate speed in off-axis DHM operating in telecentric regime, and image plane conditions, easing applications in particle tracking. We have investigated deep-learning approaches to reconstruct quantitative phase images from holograms recorded in off-axis DHM systems for this limitation. The lack of an open-source library for any DHM optical configuration is also addressed in this Ph.D. work by creating a Python library for DHM applications. Python is an open-source high-level programming language used by hundreds of researchers worldwide. The proposed library, called pyDHM, allows the numerical processing of digital holograms registered by many DHM systems. Finally, the last limitation addressed in this Ph.D. thesis is the tradeoff between speckle contrast and spatial resolution existing in current computational strategies to reduce the speckle contrast. To mitigate this tradeoff, we have proposed a single-shot denoising technique that reduces speckle noise with minimum penalization of the spatial resolution. The proposed single-shot denoising method is based on the synergetic combination of two well-known approaches in image processing: the median filter and the mean approach [40].

This Ph.D. thesis is organized as follows: Chapter 2 describes the principles of DHM. Chapter 3 discusses a fast-iterative computational reconstruction algorithm for blind phase-shifting DHM. Chapter 4 is related to investigating and validating a fast-iterative computational reconstruction algorithm for off-axis DHM systems operating in telecentric regime and image plane. Chapter 5 extends the application of the fast-iterative computational reconstruction for out-of-focus off-axis holograms. In Chapter 6, we present our open-source Python library for DHM applications. Three

different deep learning models have been described and discussed to reconstruct off-axis raw holograms in Chapter 7. Finally, Chapter 8 demonstrates the applicability of the hybrid median-mean filter to reduce speckle noise without severe resolution penalization.

1.1 Contributions and novelties of the dissertation

The main objective of this Ph.D. dissertation is the reduction or mitigation of some of the main drawbacks that cramp the DHM applications. We have investigated and developed new strategies to overcome such DHM limitations and increase its scope during this work. In particular, we have focused on addressing the following DHM disadvantages: i) the absence of robust, fast, simple, and automatic computational methods to reconstruct free-of-aberration phase images in DHM applied to static and dynamic samples; ii) the lack of a simple computational approach to reduce the speckle noise with minimum penalization of the resolution in the denoised images; and finally, iii) the lack of a robust and complete open-source library for DHM. The more remarkable contributions and novelties of this dissertation are:

i) **Fast-iterative blind phase-shifting digital holographic microscopy using two images** -we have implemented a new computational strategy to obtain phase images for slightly off-axis DHM using two raw holograms with unknown and arbitrary phase shifts. The proposed computational method provides reconstructed phase images 4 times faster in the processing time than the previous blind phase-shifting method also based on demodulation of the hologram's terms [41], without reducing the accuracy of the reconstructed phase maps. The main novelties for this contribution are:

- Development of a cost function whose minimum corresponds to reconstructed phase images free of aberrations.

- A minimum number of raw holograms with unknown and arbitrary phase shifts recorded in a slightly off-axis DHM.
- Reduced processing time (e.g., $8.6\times$ and $4\times$ in simulation and experimental data, respectively) without reducing the accuracy of the reconstructed information.

ii) **Fast-iterative automatic reconstruction method for quantitative phase image with reduced phase perturbations in off-axis digital holographic microscopy** - We have developed a novel automatic and fast algorithm to reconstruct quantitative phase images of unstained biological and non-biological samples with minimal or no phase perturbation. The proposed method is available for image-plane holograms recorded by off-axis DHM systems operating in telecentric regime. One of the main contributions of this work is a ready-to-use MATLAB GUI plugin. The source code, example datasets and short user manual can be found on GitHub. The main novelties for this contribution are:

- Development of a cost function that quantified the number of phase jumps present in the reconstructed phase image.
- Minimizing the proposed cost function enables the automatic reconstruction of quantitative phase images without or minimum phase aberrations.
- The proposed method requires minimum input parameters (e.g., the raw off-axis hologram, the wavelength of the illumination source, and the pixel size of the sensor).
- The proposed method is $40\times$ faster than the nested-loops algorithm and $2.3\times$ faster than the centroid-based algorithm.

iii) **Fast-iterative automatic reconstruction method for off-axis digital holographic microscopy operating in non-image-plane (e.g., reconstruction of out-of-focus holograms)** - We have presented a novel approach for automatic focusing and compensation of the interference

angle in QPI-DHM using out-of-focus holograms. The proposed method automatically finds the best-focused plane of an out-of-focus hologram and reconstructs its free-of-aberration phase image. The main novelties for this contribution are:

- Development of the protocol to synergically find the best-focused axial plane and reconstruct phase images with reduced phase distortions.
- The proposed computational approach has reduced processing time; it is 20× faster than the nested-loops autofocusing strategies.
- The proposed method provides the 3D reconstruction of in-focus and out-of-focus holograms, being suitable for particle tracking DHM applications.

iv) **Open-source Python Library for DHM** - We have introduced the *pyDHM* library, an open-source library to reconstruct holograms recorded by a broad range of optical DHM configurations. The library enables the focusing of out-of-focus holograms. The *pyDHM* library is posted publicly on GitHub [42]. The main novelties for this contribution are:

- An open-source python library for DHM. The library contains different computational implementations for: (1) reading and showing the complex distribution of a sample (e.g., utility package); (2) performing numerical propagations of complex wavefields to provide in-focus DH and DHM images (e.g., numerical propagation package); (3) reconstructing the phase distribution of samples in in-line and slightly off-axis DH and DHM systems using PS techniques (e.g., phase-shifting package); and (4) reconstructing phase images in single-shot off-axis DHM systems operating in telecentric and non-telecentric configuration using automatic methods to estimate the best digital reference wavefront (e.g., fully-compensated phase reconstruction package).
- Instructional videos for using the proposed library.

v) **Deep learning model to computationally reconstruct off-axis holograms** - We have investigated a convolutional autoencoder, U-Net, and conditional adversarial network (cGAN) to fully reconstruct quantitative phase images recorded in off-axis DHM systems operating in telecentric regime. The proposed cGAN model was trained using two customized metrics, which were specifically designed for tracking the imaging characteristics in DHM: (1) the number of phase discontinuities using a thresholding-and-summation metric (TSM) and (2) the noise level measured in homogenous regions of the reconstructed phase maps using the standard deviation (σ). The main novelties for this contribution are:

- Investigation of the best learning-based method to reconstruct off-axis DHM holograms of biological samples with minimum phase distortions from raw holograms without the need for robust pre- or post-numerical procedures.
- The proposed cGAN model allows the retrieval of inner structures of experimental RBCs' information, whereas convolutional autoencoders and U-Net models do not.
- The proposed cGAN model is suitable for video-rate quantitative phase imaging of dynamic samples.

vi) **Speckle noise reduction in DHM via Hybrid median-mean** - We have proposed a new single-shot image processing method, named hybrid median-mean filter (HM2F), to reduce speckle noise in digital holography (DH) and DHM. The proposed HM2F is based on the average of conventional median-filtered images with different kernel sizes. Our experimental results demonstrate that the HM2F is an effective denoising tool for reducing the speckle noise in color laser-based photography, DH, and DHM systems with minimum addition of blurring effects. The synergic combination of the median filter and mean approach provides a denoised image without significant spatial resolution reduction. The performance of the HM2F approach has been

compared with the state-of-the-art methods in speckle denoising (e.g., BM3D, NLM, WFT2F, and Wiener). The HM2F has been implemented as a Python and MATLAB script and is available on GitHub. The main novelties for this contribution are:

- A single-shot denoising method for reducing speckle noise by the synergic combination of two well-known image processing methods: the median and mean filters.
- The performance of the HM2F is more constant across the different types of images
- The HM2F is a simple but efficient method, requiring only a single parameter (e.g., the maximum kernel size of the median filter).
- The HM2F has the lowest processing time compared to the state-of-the-art speckle denoising methods (BM3D, NLM, and WFT2F).
- The HM2F is suitable for any image distorted by speckle noise.

2. PRINCIPLES OF DIGITAL HOLOGRAPHIC MICROSCOPY

DHM can be understood as a hybrid imaging technique based on two stages: i) the optical recording of a hologram and ii) the numerical reconstruction of the hologram recorded. The first stage consists of recording the interference pattern produced by the coherent superposition of two wavefields, named reference and object waves, using a digital sensor (e.g., CMOS or CCD cameras). This interference pattern is commonly known as a hologram. Figure 2.1 shows the optical configuration of a Mach-Zehnder DHM system, one of the most common configurations for studying transmissive samples (e.g., biological samples). On the contrary, Michelson interferometers are the most common DHM optical systems for studying reflective samples (e.g., material inspection). The second stage refers to the computational reconstruction process, which depends highly on the optical configuration of the DHM.

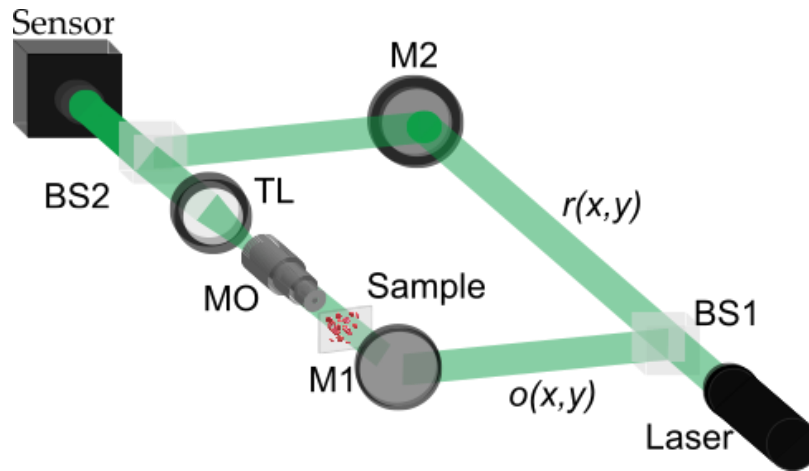


Fig. 2.1. Optical Mach-Zehnder DHM system.

2.1 Recording stage

An optical interferometer is required to record a hologram in a DHM system. For instance, one can use a Mach-Zehnder interferometer for investigating transmissive samples, Fig. 2.1. In this

optical configuration, the collimated light emitted by a coherent source such as a laser of wavelength λ is split into two beams by a first beamsplitter (BS1). The reflected beam (e.g., the object beam) illuminates a sample with a 2D complex amplitude distribution $o(x,y)$. A microscopic imaging system, comprised of an infinity-corrected microscope objective (MO) lens and a tube lens (TL), is inserted within the optical path of the object arm. This imaging system collects the light scattered by the sample and generates the image of the wavefront scattered by the microscopic sample at the back focal plane (BFP) of the TL, named the image plane (IP) of the DHM system. If the object is set at the front-focal plane (FFP) of the MO lens, the image of the sample whose amplitude distribution is $u_{IP}(x,y)$ is then obtained at the back-focal plane (BFP) of the TL. This plane is known as the microscope's image plane (IP). The complex amplitude distribution $u_{IP}(x,y)$ produced by the microscope at the IP is given by

$$u_{IP}(x,y) = \frac{1}{M^2} e^{ik(2f_{MO}+d+f_{TL})} \exp\left(i \frac{k}{2C}(x^2+y^2)\right) \times \left[o\left(\frac{x}{M}, \frac{y}{M}\right) \otimes_2 P\left(\frac{x}{\lambda f_{TL}}, \frac{y}{\lambda f_{TL}}\right) \right], \quad (2.1)$$

where $k = 2\pi/\lambda$ is the illumination wavenumber, \otimes_2 denotes the 2D convolution operator, f_{MO} is the focal length of the MO lens, f_{TL} is the focal length of the TL, d is the distance between the BFP of the MO and TL lenses, and $M = -f_{TL}/f_{MO}$ stands for the lateral magnification of the imaging system which does not depend on the distance d . $P(u,v)$ is the 2D Fourier transform of the amplitude transmittance of the pupil distribution, $p(x,y)$. The quadratic phase factor $\exp\left(i \frac{k}{2C}(x^2+y^2)\right)$ with a radius of curvature $C = f_{TL}^2/f_{TL} - d$ is associated with a non-telecentric geometry ($d \neq f_{TL}$) for the optical microscope [38]. When the microscope operates in the telecentric regime ($d = f_{TL}$), no quadratic phase factor appears in Eq. (2.1).

The transmitted beam passing the BS1 (e.g., the reference beam) is a plane wave with 2D complex amplitude distribution $r(x,y)$. The reference beam propagates with no perturbation

through a second mirror (M2). The reference wave is reflected by a second beamsplitter BS2 that recombines both object and reference waves, generating an interference pattern (e.g., hologram) at any transverse plane after the BS2. The BS2 transmits the object beam without any perturbation.

A digital sensor records the intensity distribution of the interference between the complex wavefield produced by the microscope at a distance z from the IP interference pattern. The hologram, captured at any plane from the IP, is the result of,

$$u(x, y; z) = \frac{i}{\lambda z} e^{ikz} \left\{ u_{IP}(x, y) \otimes_2 \exp\left(i \frac{k}{2z} (x^2 + y^2)\right) \right\}, \quad (2.2)$$

and a tilted plane wavefront,

$$r(x, y) = \sqrt{I_R} \exp\left[i \frac{2\pi}{\lambda} (\sin \theta_x \cdot x + \sin \theta_y \cdot y)\right] \quad (2.3)$$

where I_R is the irradiance of the reference wavefront, and $\boldsymbol{\theta}=(\theta_x, \theta_y)$ is the vector representation of the titled reference angle to the optical axis, which coincides with the center of the object wavefront. In Mach-Zehnder-based DHM systems, this angle can be changed by tilting the optical elements that reflect the reference wavefront R (e.g., the BS2 and/or M2 in Fig. 2.1). The irradiance distribution of the hologram $h(\mathbf{x}; z)$ is

$$h(\mathbf{x}; z) = |u(\mathbf{x}; z)|^2 + |r(\mathbf{x})|^2 + u(\mathbf{x}; z) \cdot r^*(\mathbf{x}) + u^*(\mathbf{x}; z) \cdot r(\mathbf{x}), \quad (2.4)$$

where $\mathbf{x} = (x, y)$ are the lateral spatial coordinates, z is the propagation distance between the IP (e.g., the BFP for the TL) and the sensor's plane, $|\cdot|^2$ represents the square modulus, and $*$ is the complex conjugate operator. Note that $z < 0$ refers to planes in front of the IP. In Equation (2.4), the first two terms are related to the irradiance of both object and reference wavefronts. On the other hand, the third and fourth terms in Eq. (2.4) encode the complex amplitude information of the object wavefront scattered by the sample. These terms represent the object's real and twin

images. From Eq. (2.4), it is clear that the object information $o(x,y)$, encoded in $u(x,y;z)$ is mixed with other undesired terms.

2.2 Numerical reconstruction stage

The reconstruction algorithms aim to separate the object information from these undesired terms in Eq. (2.4) to provide well-contrast amplitude and phase images from the complex in-focus amplitude distribution $u_{\text{IP}}(x,y) = u(x,y;z = 0)$ with minimum distortions. Considering that the 2D Fourier transform of a tilted plane wave is a shifted Dirac function, $\delta(\bullet)$ and that the convolution property of the Delta function [43], the 2D Fourier transform of the hologram, $H(\mathbf{u};z)$ is

$$H(\mathbf{u};z) = DC(\mathbf{u};z) + U\left(u - \frac{\sin \theta_x}{\lambda}, v - \frac{\sin \theta_y}{\lambda}; z\right) + U^*\left(u + \frac{\sin \theta_x}{\lambda}, v + \frac{\sin \theta_y}{\lambda}; z\right), \quad (2.5)$$

where $\mathbf{u} = (u,v)$ are the transverse spatial frequencies. The first term in Eq. (2.5) corresponds to the DC diffraction term, $DC(\mathbf{u};z) = \text{FT}\left\{\left|u(\mathbf{x};z)\right|^2 + \left|r(\mathbf{x};z)\right|^2\right\} = U *_2 U^* + R *_2 R^*$ where $*_2$ is the 2D cross-correlation operator. The capital letters and $\text{FT}[\cdot]$ refer to the 2D Fourier transform distributions to simplify our notation. The spatial frequencies of the DC term are always placed at the center of the hologram spectrum. The second and third terms in Eq. (2.5) are the +1 and -1 diffraction order, respectively. Those terms encode the complex amplitude information of the object wavefront scattered by the sample. The spatial frequencies of the ± 1 terms, respectively the $U(\cdot)$ and $U^*(\cdot)$ terms, are located symmetrically around the DC term at locations that depend on the interference angle $\boldsymbol{\theta} = (\theta_x, \theta_y)$, see [Fig. 2.2(a)]. In other words, the different components of the hologram spectrum may overlap based on the interference angle between the two wavefronts of the DHM system. Knowledge of the hologram's spectral composition is critical to selecting the reconstruction method. For example, off-axis DHM systems are those in which the angle between

the object and reference wavefronts is such that the terms in Eq. (2.5) are not superimposed [Fig. 2.2(d)]. The reconstruction method for off-axis DHM systems involves a spatial filtering approach using a single hologram [44,45]. The other extreme case occurs when no interference fringes are observed in the hologram since the interference angle between wavefronts is zero. Therefore, the three terms in Eq. (2.5) entirely overlap [Fig. 2.5(b)]. These DHM systems operate in an in-line (or on-axis) regime. The third DHM configuration, slightly off-axis DHM systems, lies between these two extremes; the interference angle between both wavefronts is not null but small enough to produce some overlapping between the different components of the hologram spectrum [Fig. 2.2(c)].

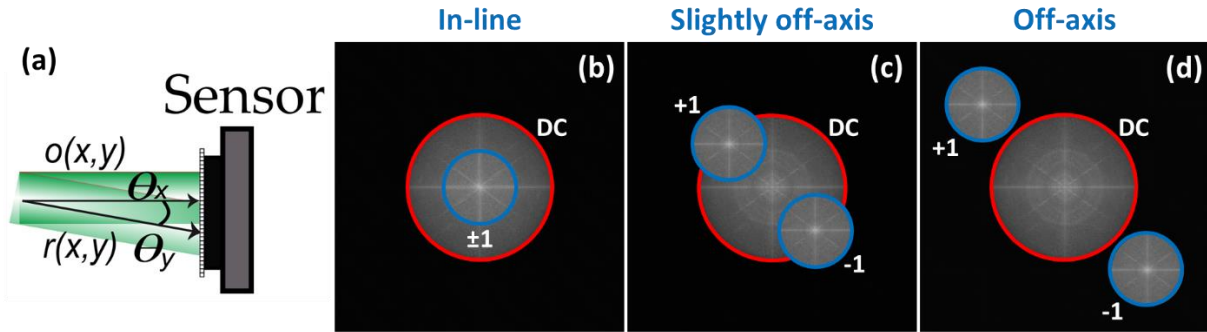


Fig. 2.2. Representation of the three possible DHM configurations. Panel (a) shows the interference angle between the object and reference waves. Panels (b)-(d): in-line, slightly off-axis, and off-axis. Blue and red circles mark the ± 1 and DC diffraction orders, respectively.

For in-line and slight off-axis DHM systems, the reconstruction algorithms involve phase-shifting (PS) techniques, requiring the recording of multiple holograms in which the phase of the reference wavefront is shifted (e.g., phase-shifted holograms) [46,47]. The main advantage of PS algorithms is that the reconstructed phase images are obtained via point-wise subtractions and division operations between the recorded phase-shifted holograms. Traditionally, PS algorithms are aimed exclusively at strictly in-line DHM systems. We highlight the traditional PS algorithms

requiring five, four, and three phase-shifted holograms among the different PS algorithms. In the five- and four-step algorithms, the phase shift between the holograms is $\pi/2$. Consequently, the point-wise phase images are reconstructed by

$$\varphi(x, y) = \tan^{-1} \left(\frac{2[h(x, y; 3\pi/2) - h(x, y; \pi/2)]}{2h(x, y; \pi) - h(x, y; 0) - h(x, y; 2\pi)} \right), \quad (2.6)$$

and

$$\varphi(x, y) = \tan^{-1} \left(\frac{h(x, y; 3\pi/2) - h(x, y; \pi/2)}{h(x, y; \pi) - h(x, y; 0)} \right), \quad (2.7)$$

for the five- and four-step algorithms, respectively. The third variable of the hologram distribution in these equations refers to the phase shift of the reference wavefront. For example, $h(x, y; 3\pi/2)$ is a recorded hologram in which there is a phase shift of $3\pi/2$ to the first hologram. One can reconstruct the phase distribution using a three-step PS algorithm with a phase shift of $2\pi/3$ between holograms as

$$\varphi(x, y) = \tan^{-1} \left(\sqrt{3} \frac{h(x, y; \pi/3) - h(x, y; 5\pi/3)}{h(x, y; 5\pi/3) + h(x, y; \pi/3) - 2h(x, y; \pi)} \right). \quad (2.8)$$

Although the three-step PS algorithm requires fewer holograms, being more suitable for real-time DHM imaging, this implementation is more sensitive to noise than the four- and five-step PS algorithms in experimental conditions. For this reason, four- and five-step algorithms are still used in many phase-shifting DHM configurations.

Due to the experimental difficulty in perfectly aligning the object and reference wavefronts, thus achieving a strictly in-line setup, slightly off-axis DHM systems are commonly preferred. For slightly off-axis DHM systems, traditional PS algorithms must be modified to compensate for the interference angle between both interfering wavefronts. De Nicola *et al.* proposed a four-step PS strategy with a phase shift of $\pi/2$ between consecutive holograms [48]. In this quadrature method,

the complex amplitude distribution of the object can be reconstructed by summing the individual products between the recorded holograms and their corresponding digital reference wavefronts

$$\begin{aligned}\hat{u}(x, y) = & h(x, y; 0)\hat{r}(x, y; 0) + h(x, y; \pi/2)\hat{r}(x, y; \pi/2) \\ & + h(x, y; \pi)\hat{r}(x, y; \pi) + h(x, y; 3\pi/2)\hat{r}(x, y; 3\pi/2).\end{aligned}\quad (2.9)$$

Equation (2.9) provides the complex amplitude distribution of the specimen without the DC term and the conjugate image, enabling the computing of amplitude and phase images via $|\hat{u}(x, y)|$ or $\text{atan}(\text{imag}[\hat{u}(x, y)] / \text{real}[\hat{u}(x, y)])$, respectively.

The main disadvantage of traditional in-line and slightly off-axis PS approaches is that most of these methods require i) accurate knowledge of the phase shift between the recorded holograms, and ii) this phase shift must be equal within the acquisition sequence [46,47]. These two requirements can be experimentally challenging due to inaccuracies prevalent in most phase-shifting devices, particularly those based on mechanical movements. In addition, the reconstruction algorithms in in-line and slightly off-axis DHM systems using PS strategies require multiple recorded holograms, restricting the use of those systems for live-cell imaging and dynamic analysis. Therefore, DHM systems operating in an off-axis regime are the most used DHM system for real-time imaging [49]. These systems allow the reconstruction of an object's amplitude and phase information from a single recorded hologram. The reconstruction algorithms for reconstructing a phase image in off-axis DHM systems involve two steps. The first step is the spatial filtering of the frequencies related to the object from the hologram spectrum. Due to the off-axis configuration, the ± 1 diffraction orders are arranged symmetrically around the DC term in the Fourier space [Fig. 2.2(c)]. From the hologram spectrum [Eq. (2.5)], the spectral object information (i.e., the $+1$ term) can be filtered [44,45].

$$H_F(\mathbf{u}) = U \left(u - \frac{\sin \theta_x}{\lambda}, v - \frac{\sin \theta_y}{\lambda}; z \right). \quad (2.10)$$

Equation (2.10) represents the filtered hologram spectrum, which is the spectrum of the sample displaced at the spatial frequencies $(\sin \theta_x / \lambda, \sin \theta_y / \lambda)$. Now, suppose the hologram is recorded under IP conditions. In that case, (e.g., $z = 0$), the amplitude distribution scattered by the sample can be obtained as the absolute value of the inverse Fourier transform of Eq. (2.10). In contrast, the spatial filtering step is enough for amplitude imaging, quantitative phase image requires the phase compensation of the tilting angle between the object and reference wavefronts (the second step of the reconstruction procedure. The compensation can be performed by multiplying the inverse Fourier Transform of Eq. (2.10), $h_F(\mathbf{x})$, by a replica of the reference wavefront, called digital reference wavefront, $r_D(\mathbf{x})$. The generation of the digital reference wavefront requires the knowledge of the interference angle $\boldsymbol{\theta} = (\theta_x, \theta_y)$, which depends on the wavelength λ of the light sources used to record the hologram, the features of the sensor (i.e., $M \times N$ square pixels of Δ_{xy}), and the subtraction between the pixel locations of the DC and the +1 terms in the hologram spectrum [50]. Once the digital reference wavefront is generated, the quantitative phase image is estimated as the angle of

$$\hat{u}(\mathbf{x}) = r_D(\mathbf{x}) \cdot h_F(\mathbf{x}) \quad (2.11)$$

where $\hat{u}(\mathbf{x})$ is the reconstructed complex distribution of the object wavefront after filtering the +1 term from the off-axis hologram and compensating for the tilted reference wavefront.

The relevant parameters to properly filter the object frequencies from the hologram's spectrum, $H_F(\mathbf{u})$, are the radius and center of the circular mask. A circular mask with the appropriate radius and center enables the reconstruction of accurate amplitude and phase images limited by diffraction (e.g., diffraction-limited images). The radius of the circular mask depends on the lateral

magnification M_L and numerical aperture NA of the DHM system [38]. Both requirements are satisfied if the radius ρ of the circular mask is equal to $1/3\sqrt{|u_0 - u_{\max}|^2 + |v_0 - v_{\max}|^2}$, where (u_0, v_0) are the DC coordinates, being equal to $u_0 = M/2+1$ and $v_0 = N/2+1$. Note that the size of the DC term is always $2u_c$ being $u_c = \text{NA}/(\lambda M_L)$. If the DHM system works in the diffraction limit and telecentric regime ($C = \infty$), the size of the ± 1 terms is u_c (e.g., half size of the DC term) [38]. Figure 2.3 shows the reconstructed phase image in an off-axis DHM system operating in the telecentric regime for different radius of the circular mask. Figure 2.3(a) is the original phase object (i.e., ground truth), and its Fourier transform is shown in Fig. 2.3(b). The colored circles in the $+1$ diffraction order mark the different circular masks. Note that the dashed red circle corresponds to the diffraction limit condition (e.g., the diameter of the circular mask is equal to the maximum spatial frequency passing through the imaging system, u_c). Figures 2.3(c)-(e) are the reconstructed phase images for the different circular masks. Panel (c) corresponds to the reconstructed phase image filtering the object spectrum using the yellow circle in Fig. 2.3(b). The diameter of the yellow mask is $u_c/2$. Panel (d) corresponds to the reconstructed phase image filtering the object spectrum using the purple circle in Fig. 2.3(b). The diameter of the purple mask is $0.8u_c$. Finally, panel (e) is the reconstructed phase image when the size of circular mask corresponds to the diffraction limit condition, dashed red circle in Fig. 2.3 (b). The smallest resolvable detail distinguished on the reconstructed star target has been marked by a solid red circle. In this pattern, the high spatial frequencies are found towards the center of the pattern. The higher the spatial frequencies, the highest the spatial resolution, being able to distinguish finer details. As one can realize, we can observe the same details on the star target if the circular mask in the spatial filter is equal or larger than u_c . Otherwise, the reconstructed star target shows reduced spatial resolution.

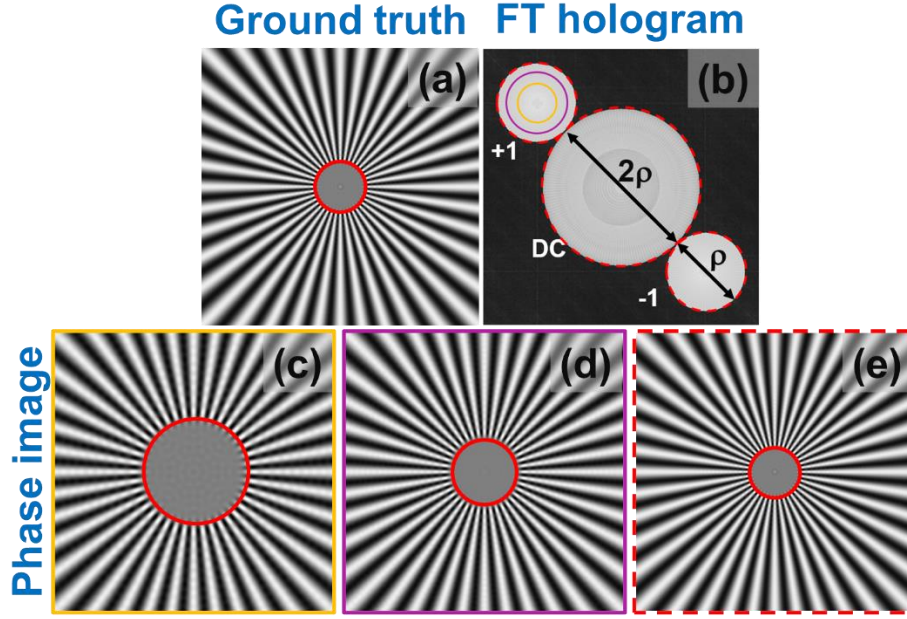


Fig. 2.3. Demonstration of reconstructed phase images for the different circular masks. The lower the radius of the circular mask, the worse the spatial resolution in the reconstructed amplitude and phase images, providing images not limited by diffraction.

In addition to accurately determining the interfering angle between the object and reference wavefronts, the reconstruction algorithms depend on the microscope's optical configuration. The shape of the ± 1 diffraction orders change between DHM systems operating in telecentric and non-telecentric configurations [38], depending on the radius of the curvature of the spherical wavefront in Eq. (2.1), C^{-1} . The smaller the radius of curvature C , the wider the ± 1 orders, being the area of the ± 1 diffraction orders inversely proportional to C [38]. Figure 2.4 illustrates the changes in the size of the ± 1 diffraction orders based on the radius of curvature C . The ± 1 diffraction orders are rectangular-based compact support functions in non-telecentric DHM systems. However, these terms are circular compact support functions in telecentric-based DHM systems whose diameter is related to the resolution (u_c) of the microscopic imaging system [38]. The reconstructed phase image from a non-telecentric DHM system is distorted by the quadratic phase factor that appears in Eq. (2.1). Figure 2.5 illustrates the relevance of difference in the hologram's spectrum and the

reconstructed phase images for non-telecentric and telecentric DHM systems. The first row in Fig. 2.5 shows the Fourier transform of holograms for two non-telecentric systems [panels (a)-(b)] and the telecentric-based DHM system [panel (c)]. It is clear that the reconstructed phase image from a non-telecentric DHM system is distorted by the quadratic phase factor. Therefore, this quadratic phase factor should be suppressed to reconstruct accurate quantitative phase images in non-telecentric DHM systems. This quadratic phase factor can be suppressed computationally by a point-wise subtraction of the reconstructed phase with and without a sample, e.g., performing a double-exposure technique where two holograms should be recorded [51]. Single-shot computational approaches have also been proposed to eliminate the quadratic phase factor by multiplying the inverse Fourier transform of Eq. (2.11), $h_F(x)$, with the conjugated replica of the distorted phase term, $\exp\left[-i\frac{2\pi}{\lambda C}\left[(x-x_C)^2+(y-y_C)^2\right]\right]$ knowing its center (x_C, y_C) and radius of curvature (C) . These parameters can be estimated by analyzing the hologram's spectrum [52].

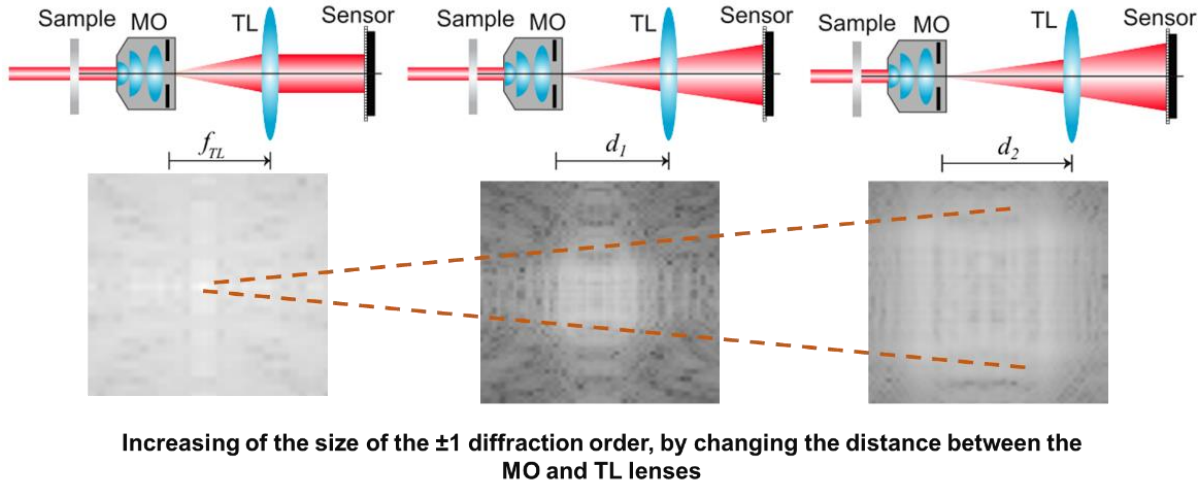


Fig. 2.4. Spreading of the ± 1 diffraction orders when the DHM system does not operate in telecentric regime.

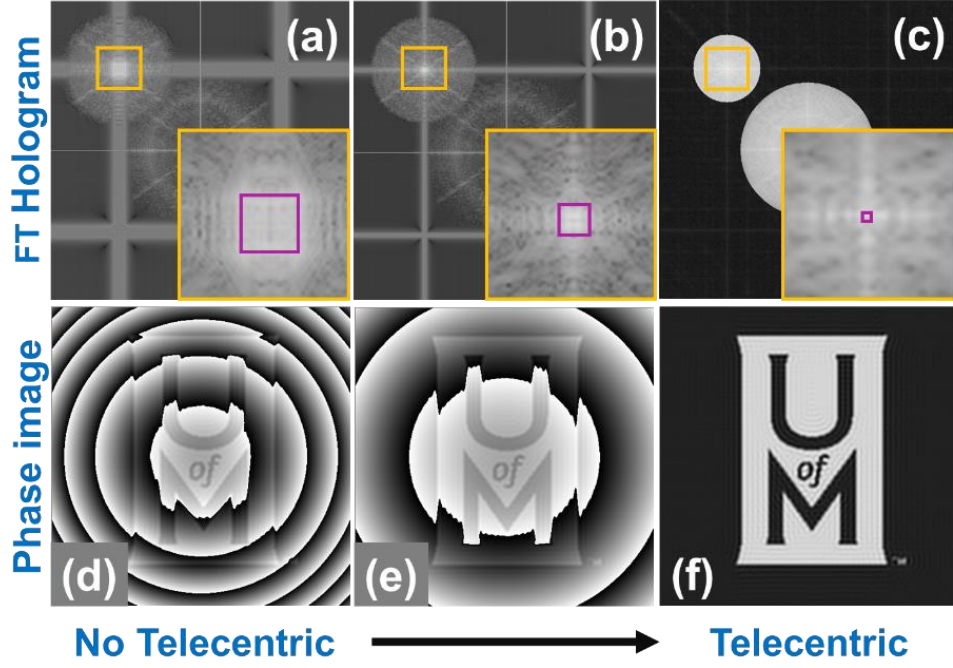


Fig. 2.5. Comparison between non-telecentric and telecentric DHM systems. The first and second rows show the holograms spectrum and the reconstructed phase images. (a)&(d) and (b)&(e) correspond to two different non-telecentric DHM systems with different radii of curvature C . The last column [(c) and (f)] is the result of a telecentric DHM system

Finally, numerical propagators of complex wavefields are required in DHM if digital holograms are not recorded at the IP since the object's reconstructed information must be numerically focused considering the axial distance z between the sensor/hologram plane and the in-focus plane [53]. Conventional numerical propagators are based on the angular spectrum or Fresnel Transform approaches [54]. The angular spectrum approach represents a complex amplitude wavefront as a combination of infinite plane wavefronts following Huygens' principle. Therefore, the in-focus complex amplitude distribution can be estimated as

$$\hat{u}_{IP}(x, y) = \text{FT}^{-1} \left[\hat{U}(u, v; z) \cdot \exp \left(-i \frac{2\pi}{\lambda} z \sqrt{1 - \lambda^2 (u^2 + v^2)} \right) \right], \quad (2.12)$$

where $\text{FT}^{-1}[\cdot]$ denotes the inverse 2D Fourier transform operator, and $\hat{U}(x, y; z)$ is the 2D Fourier transform of the reconstructed complex amplitude distribution $[\hat{u}(x, y; z)]$ after applying PS

algorithms or spatial filtering and phase compensation to the interfering angle. The phase map of the $\hat{u}(x, y; z)$ distribution should have been compensated for any quadratic phase factor. The Fresnel Transform approach is another method to solve the Fresnel-Kirchhoff diffraction equation using the paraxial approximation [54]. The paraxial approximation involves the sensor/hologram plane dimensions are smaller than the propagation distance, i.e., large propagation distances. Based on the Fresnel Transform, the relationship between the out-of-focus distribution, $\hat{u}(x, y; z)$, and the in-focus complex amplitude distribution, $\hat{u}_{ip}(x, y)$, is expressed as

$$\hat{u}_{ip}(x, y) = \frac{-i}{2\lambda} \iint \hat{u}(x_0, y_0; z) \exp\left(-i \frac{\pi}{\lambda z} (x^2 + y^2)\right) \exp\left(i \frac{2\pi}{z} (xx_0 + yy_0)\right) dx_0 dy_0. \quad (2.13)$$

Some constant phase factors have been neglected in Eq. (2.13). The third term within the integral in Eq. (2.13) is related to the kernel of a 2D Fourier transform with frequencies $u = x/z$ and $v = y/z$. Although the low-computational complexity of the Fresnel transform enables fast numerical processing, this traditional approach imposes a fixed magnification of the propagated wavefield according to the illumination wavelength and the system's geometry. A third numerical propagator can be employed to overcome this limitation. In a modified version of the Fresnel approach, the kernel of the Fourier transform in Eq. (2.13) is modified by inserting the Bluestein substitution [55] to convert this expression into a convolution operation in which the magnification of the propagated wavefield can be chosen at will at the expense of higher computational complexity.

3. FAST-ITERATIVE COMPUTATIONAL RECONSTRUCTION ALGORITHM FOR BLIND PHASE-SHIFTING DIGITAL HOLOGRAPHIC MICROSCOPY WITH REDUCED HOLOGRAMS

In-line DHM systems are the most efficient ones based on the spatial bandwidth of the camera since the angle between the reference and object waves is zero. Conventionally, the main drawback of in-line DHM systems is its applicability to the study of dynamic samples, since it requires recording at least three phase-shifted holograms and the subsequent application of phase-shifting methods optimized for DHM (PS-DHM) to reconstruct the complex object information. To increase the applicability of PS-DHM, the phase-shifting technique should be fast in both recording time and processing time. Over the years, different approaches have been developed to address these requirements. It has been proven that accurate results can be obtained with a minimum of two recorded holograms in in-line DHM systems with or without prior knowledge of the phase shifts [56–59]. Most of those approaches need precise knowledge of the phase step between both recorded holograms. However, such knowledge can be experimentally arduous without achieving accurate enough values. A rigorous study of two-frame algorithms in in-line DHM systems has been recently presented by Flores *et al.* [60], showing the potential of these approaches. Alternatively, two-frame algorithms have been successfully demonstrated in slightly off-axis DHM systems. It is important to mention that slightly off-axis systems refer to those in which the DC term and the ± 1 diffracted terms partially overlap. Several reconstruction methods have been proposed to reconstruct the phase map in slightly off-axis DHM systems in which there is no overlap between the ± 1 terms. In 2011, Han *et al.* proposed a multicolor, slightly off-axis DHM system in which a color sensor simultaneously recorded a hologram within the red channel and the intensity of the object beam using the blue channel [61]. The complex object distribution was then reconstructed after subtracting these two images, compensating the reference wave and

the spatial filtering of the object frequencies. Another widely used algorithm is the subtraction of two recorded phase-shifted holograms, which removes the DC term in the spectrum. Then, as in the previous approach, the complex object distribution is reconstructed after compensating the reference wave and filtering the object frequencies [62,63]. In those approaches, the intensity of the reference wave needs to be measured in advance, and its intensity should not be less than 2 times the maximum intensity of the object wave. The major limitation of those approaches is their application to live imaging due to the additional recording of the reference wave. Also note that the reference intensity depends on the object intensity, which depends on the imaged sample, meaning that a recording protocol is needed to change the reference intensity for each sample automatically. An alternative approach has also been demonstrated using a Hilbert transform [64]. It is important to mention that this approach requires the compensation of the global phase shift introduced between both holograms. If the interference fringes are horizontal or vertical, one can estimate the phase step by subtracting the phase value of each hologram. From each hologram, the phase is estimated by summing the fringe pattern columns or rows, depending on the direction of the fringes, and fitting the resulting vector to a sine wave [64]. Otherwise, this phase shift, which introduces a constant phase value, can be determined as the residual phase in the absence of sample and subtracting from the measured phase. In other words, the recorded holograms should exhibit an area free of the specimen such that the constant phase can be measured. This condition may reduce the usable field of view to provide accurate phase measurements. In Refs. [65–68] authors describe alternative two-frame reconstruction algorithms applied to slightly off-axis DHM systems that reconstruct the complex information of the object without prior knowledge of the hologram phase shift, namely blind PS methods. However, some of these works require the object and/or reference intensities, demanding a total of four images [65], or cannot retrieve aberration-free

phase images [66,67]. In 2014, Guo *et al.*, proposed a method based on a phase derivative approach [69]. The main limitation of that method is that it requires a hologram and the recording of the object and reference beams, namely three shots. However, an advantage of that phase derivative method is that it is a purely local method, not requiring any integral operation such as the Fourier transform or the Hilbert transform, which could significantly reduce the computing complexity and memory demands of the data processing system. In 2019, a π -shifted spatially multiplexed interference microscope was proposed [70,71]. In that work, the authors simultaneously recorded two holograms mutually phase-shifted by π radians in a single shot. Reconstructed phase images of high quality were obtained by employing the Hilbert spiral transform on the π hologram. To finish this brief review, in 2019, Doblas *et al.* presented an iterative-blind phase shift (PS) extraction method based on the demodulation (i.e., Fourier spectrum) of the different components of the recorded holograms [41]. Although the blind PS method yields an accurate estimation of the phase shifts and the phase distribution, it requires three phase-shifted recorded holograms, reducing the applicability of PS-DHM in live imaging.

This chapter presents an alternative fast-iterative blind PS method that provides accurate phase reconstruction using two recorded holograms with arbitrary phase-shift. The algorithm has the features of recovering complex object information without having any knowledge of the phase shift in each recorded hologram. This algorithm is also based on the demodulation of the terms composing the Fourier transform of the hologram, as recently published [41]. The advantages of the proposed two-frame approach are: a minimum number of images needing only two recorded holograms, a minimum phase error of the order of 0.005% independently of the phase step ranging from 0 to 180 deg., a maximum correlation coefficient between the phase and the retrieved phase image equal to 1, and, finally, a reduced processing time compared with the previous three-frame

approach [41]. This chapter is organized as follows: Section 3.1 describes the theoretical framework. In Section 3.2, presents the proposed method. The experimental validation of the proposed method is shown in Section 3.3. This chapter finishes with the conclusions of the proposed method in Section 3.4. This work has been published in Applied Optics [72] and presented at the 2020 OSA Imaging and Applied Optics Congress [73].

3.1 Theoretical framework

In PS-DHM systems, the complex wavefield distribution (e.g., amplitude and phase) of a microscopic sample is reconstructed after the optical recording of multiple holograms and their corresponding processing. The hologram can be written as a linear combination between three unknown components $\{d_0, d_{+1}$ and $d_{-1}\}$, where the weighting of each component depends on the phase shift $\Delta\varphi_n$ introduced by the reference wave. Assuming that the reference wave is a plane wave with an arbitrary phase shift, the hologram can be rewritten as

$$h(\mathbf{x}) = d_0(\mathbf{x}) + e^{-i\Delta\varphi} d_{+1}(\mathbf{x}) + e^{i\Delta\varphi} d_{-1}(\mathbf{x}), \quad (3.1)$$

where $d_0(\mathbf{x}) = 1 + |u_{IP}(\mathbf{x})|^2$ is the two first terms of Eq. (3.1) assuming that the irradiance of the reference plane wave is 1, and $d_{\pm 1} = \exp(\mp ik_0 \sin \theta \cdot \mathbf{x}) \cdot u_{IP}(\mathbf{x})$ are the real and virtual images of the complex object distribution $u_{IP}(\mathbf{x})$. Note that $\mathbf{x} = (x, y)$ is the vector representation of the lateral spatial coordinates, and $\boldsymbol{\theta} = (\theta_x, \theta_y)$ is the vector representation of the interference angle of the tilted reference angle to the optical axis, representing the center of the object wave. Based on the composition of the hologram distribution in terms of $\{d_0, d_{+1}$, and $d_{-1}\}$, the object information (u_{IP}) can be reconstructed from either the d_{+1} or d_{-1} components using three recorded holograms $\{h_1, h_2$, and $h_3\}$, with their respective phase shift $\{\Delta\varphi_1, \Delta\varphi_2$, and $\Delta\varphi_3\}$, to determine the unknow

components. Conversely, without lack of generality, the hologram can also be written as the sum of two components as

$$h(\mathbf{x}) = d_0(\mathbf{x}) + e^{i\Delta\varphi_n} d_3(\mathbf{x}), \quad (3.2)$$

where,

$$d_3(\mathbf{x}) = d_{+1}(\mathbf{x}) + e^{-i2\Delta\varphi} d_{-1}(\mathbf{x}). \quad (3.3)$$

From Eq. 3.2, one realizes that only two recorded holograms, $\{h_1, h_2\}$ with the corresponding phase shifts $\{\Delta\varphi_1, \Delta\varphi_2\}$, are needed to estimate the two unknown components. Without a lack of generality, it is assumed that the first phase shift is zero, and therefore one must only introduce one phase step $\Delta\varphi'_2 = \Delta\varphi_2 - \Delta\varphi_1$. Using matrix notation, the estimated unknown components are computed by solving

$$\begin{pmatrix} d_0 \\ d_3 \end{pmatrix} = \begin{pmatrix} 1 & 1 \\ 1 & e^{i\Delta\varphi'_2} \end{pmatrix}^{-1} \begin{pmatrix} h_1 \\ h_2 \end{pmatrix}. \quad (3.4)$$

This equation shows that the estimated values of the unknown components $\{d_0, d_3\}$ depend on the value of the phase step $\Delta\varphi'_2$ involved in recording the holograms. Equation (3.4) is applicable if the phase step is not an integer multiple of 2π , $\Delta\varphi'_2 \neq 2m\pi$ being m an integer number.

3.2 Proposed blind PS-DHM using two images

Figure 3.1 illustrates the impact of the correct phase step in the reconstruction of the unknown components simulating a numerical pure phase object (i.e., amplitude distribution is equal to 1). The Fourier spectrum of the simulated hologram of the amplitude distribution of this object with a slightly tilted reference plane wave is shown in Fig. 3.1(b). In this simulation, the phase step of the reference wave was $\Delta\varphi'_2 = 60^\circ$. Panels in Fig. 3.1(c) show the Fourier transforms of the

estimated two unknown components [Fourier Transform of Eq. (3.4)] for two different values of the $\Delta\phi'_2$. Figure 3.1 shows that only when the phase step $\Delta\phi'_2$ coincides with the real one of the reference waves [column named as True in [Fig. 3.1(c)], the spectrum of the d_0 component is composed by two orders: the DC term, set at the center of the spectrum (D_0), and the other order is located at the frequency $\mathbf{u}_m = \sin(\boldsymbol{\theta})/\lambda_0$ (i.e., spatial frequency proportional to the interference angle $\boldsymbol{\theta} = (\theta_x, \theta_y)$). When the phase step used in Eq. (3.4) is different from the real one, three orders can be observed in the D_0 component. The second column in Fig. 3.1(c) shows the spectrum of the unknown components when the value of $\Delta\phi'_2$ is wrong. The position of the additional order, which is a residual order, is located at $-\mathbf{u}_m$. Based on this observation, the cost-function to be minimized is defined as

$$J = \frac{2|D_0(-\mathbf{u}_m)|}{|D_0(\mathbf{0})| + |D_0(-\mathbf{u}_m)|}. \quad (3.5)$$

The cost-function J quantifies the ratio difference between the expected central and the residual order in the estimated D_0 component. The value of the cost-function Eq. (3.5) is reported in the first row of Fig. 3.1(c). If the phase step used in Eq. (3.5) is the correct one, then $D_0(-\mathbf{u}_m) = 0$, and the value of the cost-function is equal to zero, $J = 0$. Note that for the particular case shown in Fig. 3.1(a), the cost-function is almost zero, $J = 2.9 \times 10^{-5}$, whereas for $\Delta\phi'_2 = 80$ deg, the cost function is $J=0.12$. Therefore, the utilization of a phase-step value different from the correct one produces a higher cost-function value. Note that there is a difference of four orders of magnitude between both reported J values. This approach is based on the simultaneous estimation of the phase step and the unknown components by minimizing the cost-function Eq. (3.5) using the Matlab built-in function *fminunc*, which finds a local minimum of an unconstrained multivariable function using

a quasi-Newton algorithm. The input parameters of the *fminunc* function are the cost-function [Eq. (3.5)], an initial phase step, which is a random value between 0–360 deg generated using the Matlab built-in function *randi*, and a set of optimization options. In this algorithm, the input parameters of the cost-function are the two recorded holograms and the positions of the expected and residual orders in the Fourier spectrum. The optimization options are the maximum number of iterations allowed and a termination tolerance on the cost function. The tolerance has been set up to 10^{-6} , which is the default value, since a lower tolerance value does not lead to improved results. Although up to 30 iterations were allowed, it did not take more than eight iterations in the simulated data. Experimentally, the maximum number of iterations was four. It is important to mention that this work does not provide a rigorous study of these optimization options, and the selection of a different algorithm and/or optimization options may yield better results. The last image in the estimated column, Fig. 3.1(c) shows the estimated unknown components provided by our method. The estimated phase step was $\Delta\phi'_2 = 60.003^\circ$, which means a difference error of $5 \times 10^{-3} \%$ compared with the real value and the value of the cost-function was almost zero, $J=1.6 \times 10^{-5}$.

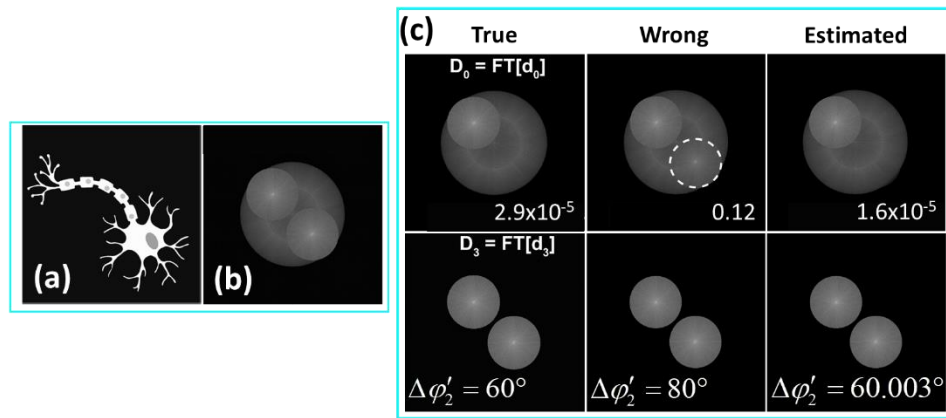


Fig. 3.1. Demonstration of the proposed algorithm based on the estimation of the spectral components D_0 and D_3 using two raw holograms. The panels are: (a) ground truth phase

distribution of the simulated object; (b) Fourier transform of the hologram using a reference slightly tilted; (c) Fourier transform of the demodulated components using Eq. (3.4) for different values of the phase steps. The phase steps were 60 deg (True), 80 deg (Wrong), and 60.003 deg (Estimated), respectively. Note that only when the phase step is wrong, it appears an additional order in the D_0 component.

Once the unknown components have been estimated, one dismisses the d_0 component since the complex object information is only encoded on the d_3 component. In fact, the d_3 component contains both the real (d_{+1}) and virtual (d_{-1}) information of the object, as seen in Eq. (3.4). Figure 3.2 shows the steps to reconstruct the phase distribution of the object. These steps consist of the spatial filtering of the d_{+1} component, the compensation of the tilt angle introduced by the reference wave, and, finally, the computation of the angle of the resultant image. It is important to mention that this approach is suitable for slightly off-axis DHM systems in which the interference angle is such that there is no overlap between the $d_{\pm 1}$ components. The quality of the estimated phase is quantified by the mean-square error (MSE) between the true phase map and the estimated phase map. This error is reported in Fig. 3.2(c). Note that the value of the MSE is 1.56×10^{-6} .

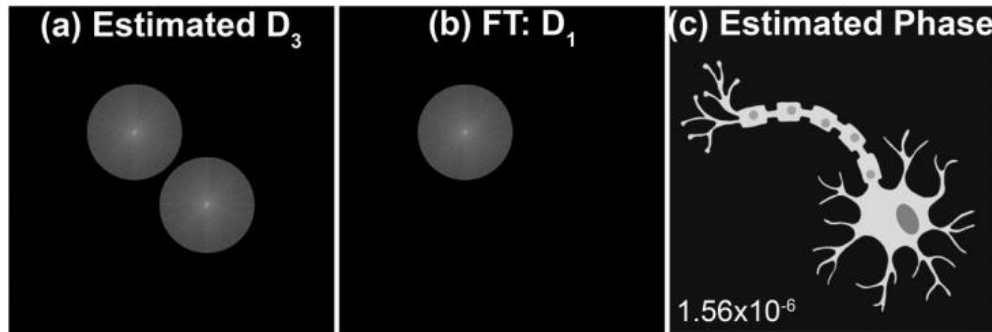


Fig. 3.2. Evaluation of the phase distribution estimated by the proposed method. The panels are: (a) estimated D_3 component; (b) Fourier transform of the d_1 demodulated component by spatial

filtering of D_3 ; (c) estimated phase image after compensating the interference angle. The mean MSE between the true and the estimated phase images is 1.56×10^{-6} .

The flowchart of the proposed method is illustrated in Fig. 3.3. The input parameters for the proposed method are: two recorded holograms with an arbitrary phase-shift, the wavelength λ used to record the hologram, and the pixel size of the camera Δ_{xy} .

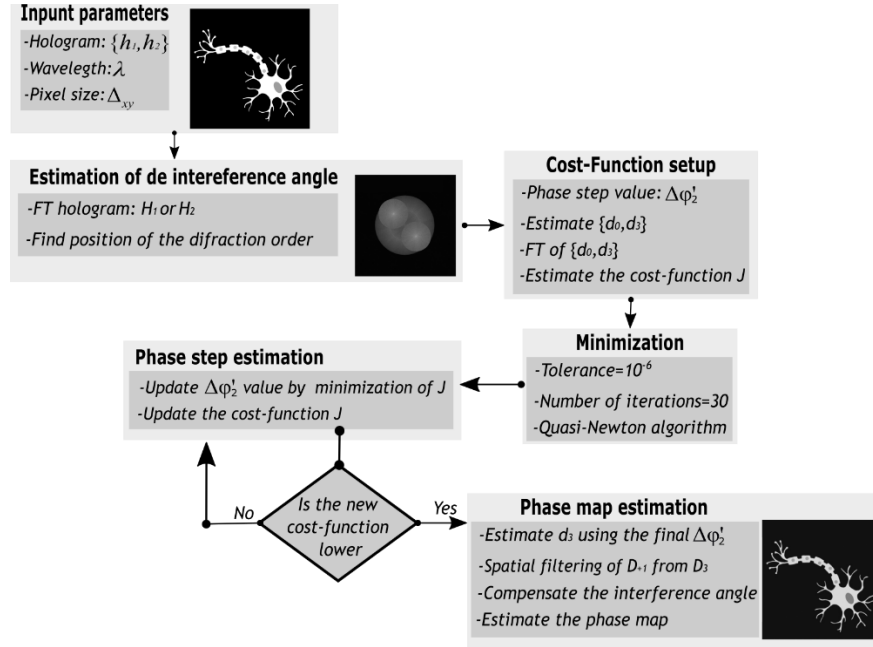


Fig. 3.3. Flowchart of the proposed algorithm.

Testing the validity of the proposed method using two holograms was completed by estimating the MSE value between the true and estimated phase maps after running the proposed method 20 times. The only difference between the realizations is the initialization of the phase steps, which is a random value between 0–360 deg. While the true phase step was 60 deg, the estimated phase-step (mean \pm standard deviation) value obtained by minimizing the proposed cost function was (60.0028 ± 0.0004) deg, showing high accuracy of the calculated phase step. There is an error difference of $4.7 \times 10^{-3} \%$ between the estimated phase step and the ground truth. This accurate estimation of the phase-step results on well-estimated phase images, as quantified by the maximum

value of the correlation coefficient (a value of 1 computed using the Matlab built-in function *corr2* between the true and estimated phase maps) and the small values of the MSE error (mean = 1.6×10^{-6} ; and standard deviation = 2×10^{-22}). Note that the small value of the standard deviation in the MSE value is correlated with the repeatability of the proposed method. Regarding the processing time, the computing time was 9.3 ± 1.4 s (mean \pm standard deviation) for a phase image of 1024×1024 pixels and a Windows-based i7-6700 CPU (3.40 GHz) 16.0 GBytes RAM desktop computer. Compared with the previous three-hologram-based blind PS-DHM algorithm, the proposed method is $8.6\times$ faster in processing time. The average computing time has been reduced from 80 s [41] to 9.3 s. Although the MSE error of the simulated-reconstructed phase image is smaller when one uses the algorithm of Ref. [41] (i.e., three instead of two recorded holograms), which is 3.87×10^{-12} compared to 1.6×10^{-6} , the experimental results of the following section show that this difference is not observable. In addition, a simulation study was conducted to investigate the influence of the phase step in the proposed two-frame blind PS algorithm. For this study, the true phase step was changed from 5 deg to 180 deg, in steps of 5 deg. The error difference between the calculated phase step and the true value was (0.0015 ± 0.0012) %, showing the high accuracy of the proposed approach to estimate the true phase step independently of its value. Again, this accurate estimation leads to well-estimated phase images with a reduced MSE value (mean = 4.9×10^{-7}). The proposed approach was verified to work for a minimum phase step equal to 1 deg. The phase steps higher than 180 deg were not considered since they behave the same.

Table 3.1. Performance of the proposed algorithm under Noise Conditions: SNR

SNR(dB)	$\Delta\varphi'_2$ (deg)	MSE $\times 10^{-5}$ (a. u.)
5	$60.001 \pm 4.0 \times 10^{-3}$	2 ± 0.60
10	$60.002 \pm 1.7 \times 10^{-3}$	1.1 ± 0.30
15	$60.002 \pm 1.9 \times 10^{-3}$	0.61 ± 0.18
20	$60.003 \pm 6.0 \times 10^{-4}$	0.30 ± 0.09
25	$60.003 \pm 3.0 \times 10^{-4}$	0.24 ± 0.11
30	$60.003 \pm 1.8 \times 10^{-4}$	0.18 ± 0.02
35	$60.003 \pm 1.3 \times 10^{-4}$	0.16 ± 0.01
40	$60.003 \pm 7.0 \times 10^{-3}$	0.16 ± 0.01
45	$60.003 \pm 5.0 \times 10^{-3}$	0.16 ± 0.01

Notation (mean \pm standard deviation).

Finally, the sensitivity of the proposed PS algorithm is evaluated for noisy conditions. For this study, it has been considered that the ground truth phase map [Fig. 3.1(a)] is distorted by noise that follows a white Gaussian distribution. The resultant noisy phase image is generated by adding the noise map to the truth phase image. For a particular signal-to-noise ratio (SNR), 15 noisy phase images were generated. Table 3.1 shows the estimated phase step provided by the proposed approach and the MSE value between the estimated phase image and the noisy truth map. The true phase step was again 60 deg. With the proposed approach, the lowest and highest error difference between the true and estimated phase shift was 0.0017% and 0.005%, respectively. The root-mean-square error (RMSE) between the estimated phase shift and the ground truth one is 0.0026. Based on these two values, one concludes that the proposed method is quite robust under noisy conditions. Note that the similarity between the true noisy phase map and the estimated phase map is still high, with an MSE value smaller than 2×10^{-5} .

3.3 Experimental validation

The validation of the proposed method has been performed by reconstructing two QPI targets by Benchmark Technologies. Figure 3.4 illustrates the optical setup of the experimental DHM setup. The employed PS-DHM system was a Mach–Zehnder interferometer using a rotating glass in the

reference wave to generate the phase shifting of the interferential fringes. As an illumination source, a laser diode emitting at a wavelength of 535 nm (CPS532, Thorlabs) was used. In the object arm, a telecentric imaging system was inserted composed of an infinity-corrected 4×/0.1 MO (Olympus) and a TL of a focal length of 300 mm. The utilization of a telecentric imaging system in DHM ensures that the DHM is shift-invariant without the need to compensate any spherical phase factor on the reconstructed phase image [74,75]. This imaging system generates a magnified 6.67× image of the sample under research; this lateral magnification is estimated by the ratio between the focal lengths of the TL and the MO, $M = -f_{TL} / f_{MO} = 6.67 \times$. To ease the reconstruction stage, in-focus holograms were recorded by setting a CMOS camera (acA1920-25um, Basler) with 1920×1080 square pixels of a 2.4 μm pixel size at the IP of the imaging system. The optical setup was fixed to ensure that the real and virtual images of the hologram do not overlap in the Fourier domain. Still, these terms overlap with the D_0 component (i.e., our system operated in slightly off-axis mode). The condition that the phase-shifting must differ from a multiple of 2π is experimentally satisfied by plotting a profile of the interference pattern and rotating the glass slide until the positions of the maximum intensity values have been laterally displaced. Note that one can implement different approaches to provide the required phase shifting of the holograms, such as beam splitters [71,75,76] or polarization elements [62,63].

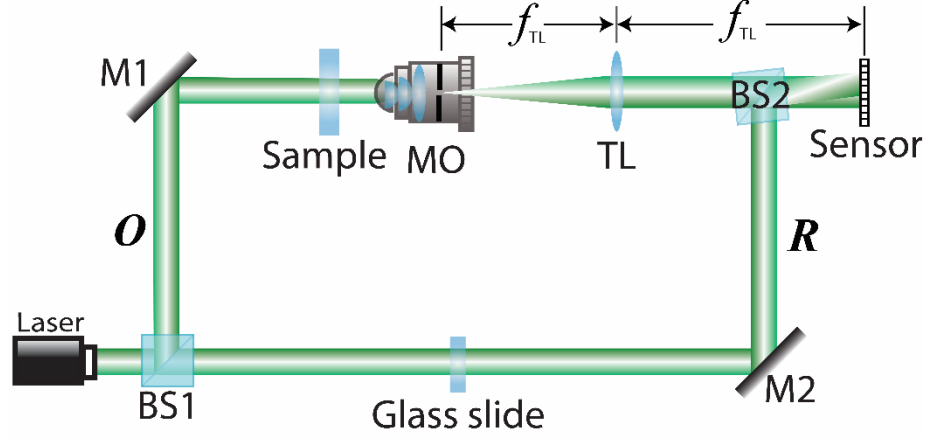


Fig. 3.4. Optical setup of a DHM. The DHM system operates in the telecentric regime. The recorded holograms with the needed phase shift are recorded by rotating a glass slide, which is mounted on a rotational stage.

In the first experiment, a USAF 1951 target was used. Figures 3.5(a) and 3.5(b) show one of the two holograms (h_1) needed in the algorithm and its Fourier spectrum (H_1), respectively. As shown in Fig. 3.5(b), the holograms were recorded in slightly off-axis architecture. It was guaranteed that no overlapping occurred between the spectrum of d_{+1} and d_{-1} , so one can spatially filter the d_{+1} from the d_3 term without losing high spatial frequencies (i.e., high-resolution images should be reconstructed). Figures 3.5(c)-(d) show the Fourier transforms of the estimated unknown components, D_0 , and D_3 , respectively. The algorithm only required a maximum of four iterations for successfully determining both D_0 , and D_3 . From the results of the method is found that the phase shift between both recorded holograms is 146.78 deg. Once one has estimated the D_3 component, one can filter the D_{+1} term and compensate for the interference angle introduced by the tilted reference wave. After these two processes, the reconstructed 2D phase image and its 3D rendering are shown in Fig. 3.5(e). Clearly, Fig. 3.5(e) shows the good quality of the reconstructed information being able to distinguish up to the three vertical bars in element 5 of group 7, which corresponds to a separation of 2.461 μm , thus being the experimental resolution limit. Note that

there is a high agreement between the experimental value and the sparrow resolution limit of the experimental imaging system, defined by $0.47\lambda/\text{NA} = 2.50\text{ }\mu\text{m}$ being NA, the numerical aperture of the MO lens [77]. The resolution limit could be improved by using a MO lens with a higher NA. The goodness of the proposed blind two-frame PS algorithm is not affected by the choice of the MO lens.

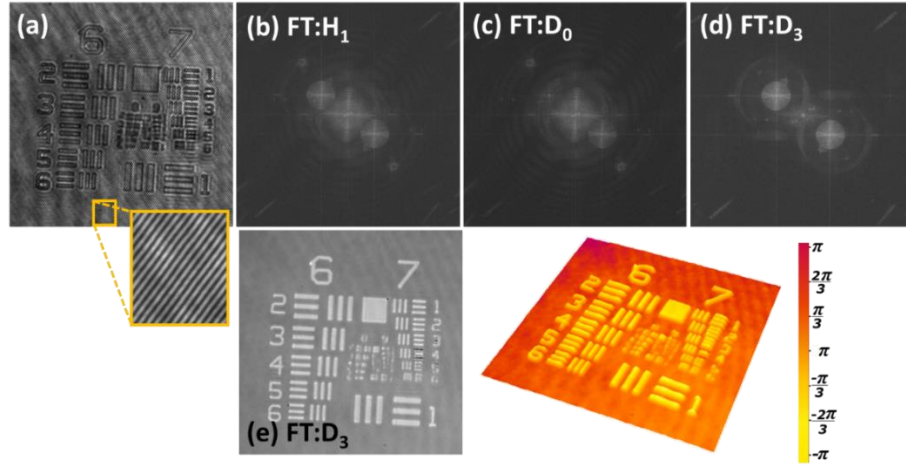


Fig. 3.5. Experimental validation of the proposed method. Panel (a) shows one of the recorded holograms; panel (b) corresponds to the FT of the hologram shows in panel (a). Panels (c)-(d) illustrate the Fourier transforms of the two unknown components, D_0 and D_{-3} . Panel (e) shows the 2D reconstructed phase map and its 3D rendering.

Finally, a second experiment is aimed at validating the accuracy of the proposed blind two-frame PS-DHM approach by comparing its quantitative results to the blind PS-DHM method that uses three phase-shifted holograms [41]. For this comparison, the QPI star target from Benchmark Technologies was selected. After applying the corresponding algorithms, the phase steps were estimated as: $\Delta\phi'_2 = 274.52^\circ$, and $\Delta\phi'_2 = 273.89^\circ$ for the proposed method and the method reported in Ref. [41], respectively. Note that the MSE value between both $\Delta\phi'_2$ estimated is 0.4, corresponding to an error difference of 0.23%. Panels (a) and (b) in Fig. 3.6 show the normalized phase images reconstructed by both approaches. Note that each phase map has been normalized

by each map's maximum and minimum values. Clearly, there is a high similarity between both retrieved phase maps. This high similarity is verified by the high correlation coefficient (correlation coefficient = 0.97) and the low value of the MSE (MSE value = 4.3×10^{-2}) between both images. The high agreement of both methods is also verified by comparing the measured phase heights at different spatial distances of the object (marked by dashed black lines). The profiles for two different radial distances from the star's center (radio equal to 70 μm and 90 μm) are shown in Fig. 3.6(c). From an observation of these profiles, one can conclude that there is a nearly perfect overlap between both estimated phase-height profiles regardless of the object's frequency. Therefore, the accuracy of the proposed algorithm is demonstrated against the previous one which requires three phase-shifted holograms [41]. In addition, it is important to mention that the processing time has been reduced from 52 s to 13 s, resulting in an experimental reduction of the processing time by a factor of 4. Thereby, the proposed method requires a smaller number of phase-shifted holograms and less processing time, making a PS-DHM approach more suitable for live imaging and video-rate QPI visualization. Finally, the phase map of the star target was estimated using the approach described in Ref. [62] and the estimated phase step from this method as the global phase value. The correlation coefficient between the estimated phase map presented here [Fig. 3.6(a)] and the one obtained by Ref. [62] is 0.99, verifying the high similarity of the phase step.

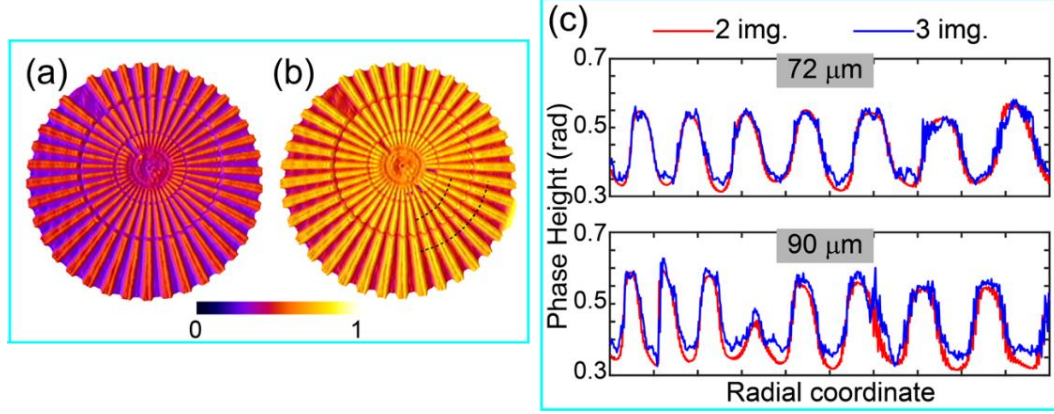


Fig. 3.6. Experimental comparison of the proposed method using a Star target. Panels (a) and (b) show the normalized phase image of the star using 2 holograms and 3 holograms, respectively. Panel (c) shows the phase-height profiles of the reconstructed phase maps at two different positions, $r_1 = 72 \mu\text{m}$ and $r_2 = 90 \mu\text{m}$, radial positions measured from the center are marked in panel (b). In panel (c), the red and blue profiles correspond to the reconstructed phase profiles using 2 and 3 raw holograms, respectively. The area of the star is $358 \times 358 \mu\text{m}^2$.

3.4 Conclusion

In this chapter, a fast-iterative PS-DHM method based on the demodulation of the different components of phase-shifted holograms was presented. The proposed blind method only uses two-frame holograms with an arbitrary phase shift. The main advantage of the proposed method is the reduction in both the acquisition and computation time; the final phase image is restored using 33% fewer data since only two phase-shifted holograms are needed, as opposed to the standard three-frame PS algorithms. The processing time of the proposed approach was compared to the previous three-frame approach reported in [41]. The simulated and experimental results show that the processing time has been improved by a factor of 8.6 and 4 times, respectively, without reducing the phase reconstruction accuracy. The only requirement of this approach is that the PS-DHM system must operate in slightly off-axis regime without overlapping between the spectrum of the $d_{\pm 1}$ terms. Regarding the limitation of the proposed algorithm in terms of the intensity between the object and reference beams, it is predicted that the proposed algorithm will always

work as far as the maximum peaks of the $D_{\pm 1}$ terms in the hologram spectrum are distinguishable. Some preliminary simulated results (not shown here) confirm that the proposed blind PS approach is suitable for an amplitude difference of $20\times$ between the object and reference beams, which provides a hologram with fringes' contrast as low as 0.1. A more detailed investigation of this difference will be reported in future work. The simulated and experimental results show that the proposed approach provides accurate quantitative phase images paving the route for video-rate PS-DHM in live and material sciences. Table 3.2 provides a summary of the advantages and limitations of the proposed method. More information about the implementation for Python and MATLAB can be found online in the public repository, <https://oirl.github.io/Blind-PS-DHM-methods/>.

Table 3.2. Advantages and limitations of the proposed blind phase-shift method for two raw holograms.

Advantages	Limitations
<ul style="list-style-type: none"> ✓ Two holograms are required with an arbitrary and unknown phase-shift. ✓ The processing time is reduced 8.6 times in simulation data. ✓ The processing time is reduced 4 times in experimental data without reducing the accuracy of the phase and amplitude reconstruction maps. 	<ul style="list-style-type: none"> ➤ Just operate for slightly off-axis without overlapping between the $D_{\pm 1}$. ➤ The optical configuration of the DHM system should be telecentric ➤ The phase-shift between the two holograms cannot be a multiple of 2π.

4. FAST-ITERATIVE COMPUTATIONAL RECONSTRUCTION ALGORITHM FOR OFF-AXIS DIGITAL HOLOGRAPHIC MICROSCOPY OPERATING IN TELECENTRIC REGIME AND IMAGE PLANE

This chapter presents a reconstruction algorithm to reconstruct the complex object information for an off-axis DHM operating in the telecentric regimen and IP. Because DHM systems can be utilized for quantitative analysis of biological systems and diagnostics of diseases, its accuracy for retrieving the phase information is without doubt a factor to be followed closely. The DHM technology relies on computational approaches for retrieving the amplitude and phase sample distribution. The mandatory numerical steps used in off-axis DHM technique are spatial frequency filtering [44,78] of the hologram spectrum and the compensation of the tilt between the reference and object waves, see Chapter 2 for more details. Depending on the optical configuration of the DHM system, numerical propagation and/or aberration correction may be required. The DHM computational processing should be performed automatically and adaptable to different sample and imaging conditions to increase its applicability in biomedicine. An inaccurate compensation of the tilt between the reference and object waves could introduce errors in the quantitative phase measurements. One straightforward compensation method for precise extraction of the phase is manually selecting the tilt of the reference wave. This approach requires the manual generation of several reference waves until obtaining a phase reconstruction without sawtooth fringes. Selecting the best-reconstructed phase image can be a challenging task for the end-user in DHM since it depends significantly on the user's expertise. Several research works have focused on developing computational approaches to automatically reconstruct phase images without any phase perturbations automatically. In 2004, Carl et al. proposed an automatic method for reconstructed phase images in an off-axis DHM system [79]. In their method, the parameters to compensate the tilt and the spherical wave introduced by the non-telecentric configuration of the DHM system

were estimated from a recorded hologram in which no sample was used (e.g., blank hologram). This method was implemented following an iterative process in which the optimized parameters were obtained by minimizing the standard deviation of the unwrapped reconstructed phase image in the blank hologram. The major inconveniences of this method are the computational time, the need for a blank hologram, the user's input of the size of the object spectrum, and the need for an unwrapping method. The drawbacks of a blank hologram, and the use of an unwrapping method were overcome in an upgraded version of this method [52], and the estimation of the size of object spectrum can be overcome by thresholding the spectrum of the hologram [78,80]. The main difference between these two approaches is the estimation of the tilt parameters. Whereas the authors in Ref. [78] used a centroid-based algorithm to determine the tilt parameters, Trujillo et al. generated multiple tilted plane waves with different parameters and searched for the reconstructed phase image without sawtooth fringes [22]. Whereas these algorithms aim to correct phase aberrations due to the interference tilt and the spherical wave introduced by the DHM system operating in non-telecentric configuration, automatic reconstruction phase methods based on polynomial curve fitting can correct high-order aberrations. In 2006, Colomb et al. proposed an automatic method in which the coefficients of the phase aberrations were estimated by fitting selected line profiles into polynomial curves [81]. Originally, these line profiles were extracted from regions in the unwrapped reconstructed phase image where the sample information was constant. To avoid the user's input in selecting these flat regions, Nguyen et al. proposed the use of a convolutional neural network (CNN) to perform automatic background region detection [82]. The performance of those fitting-based automatic methods are significantly dependent on the size of the flat regions as well as the performance of the unwrapping algorithm. In 2014, Liu et al. avoided these issues by proposing a nonlinear optimization procedure to estimate the Zernike

coefficients of the phase aberrations [83]. These coefficients were estimated by maximizing the spectral energy metric of a single recorded hologram. The method described in Ref. [83]. works for DHM systems operating in a non-telecentric regime. In this Chapter, we present a different type of nonlinear optimization procedure to provide fast, accurate, and automatic compensation of the interference tilt in QPI-DHM operating in telecentric mode. The proposed approach is based on minimizing a cost function to provide precise phase measurements in off-axis DHM systems operating in telecentric regime. The proposed method has been implemented in a user-friendly tool, and it is available at <https://oirl.github.io/tuDHM/>. We intend to offer a more accessible reconstruction tool, which could increase the applicability of DHM systems. The developed software tool will allow researchers in life and material sciences, even those without computational reconstruction knowledge, to analyze their results accurately, leading to new discoveries. This Chapter follows the next structure. Section 4.1 presents the theoretical framework of the proposed automatic algorithm to reconstruct quantitative phase images with minimum phase distortions. In Section 4.2, describes the proposed method. Section 4.3 is devoted to validating the method experimentally. Finally, Section 4.4 summarizes the main achievement of this procedure. This work has been published in Applied Optics [84] and presented at the 2021 OSA Imaging and Applied Optics Congress [85].

4.1 Theoretical framework

In DHM systems, the compensation process is a key step in reconstructing aberration-free quantitative phase images. The mandatory numerical steps used in off-axis DHM technique operating in telecentric regime are the spatial frequency filtering [44,78] of the hologram spectrum and the compensation of the tilt between the reference and object waves. Equation (2.10) represents the filtered hologram spectrum, which is the spectrum of the sample displaced at the spatial

frequencies, $(\sin\theta_x/\lambda, \sin\theta_y/\lambda)$ being $\theta = (\theta_x, \theta_y)$ the angle of the reference beam to the optical axis, assuming that the center of the object beam coincides with the optical axis. The amplitude distribution scattered by the sample can be obtained as the absolute value of the inverse Fourier transform of Eq. (2.10). However, the phase distribution requires the compensation of the lateral displacement introduced by the tilted reference beam. Thus, for QPI-DHM measurements, one should compensate the reference tilt. This compensation can be performed in both real and Fourier space. To compensate the reference angle using the Fourier space, the filtered hologram spectrum [Eq. (2.10)] should be centered on a new matrix. In the real space, the reference angle is compensated by multiplying the inverse Fourier transform of Eq. (2.10), $h_F(\mathbf{x})$, and a digital replica of the reference wave, $r_D(\mathbf{x})$, commonly called the digital reference wave. If the sensor plane coincides with the IP of the microscope, the reconstructed phase image $\varphi_o(\mathbf{x})$ is given by the angle of

$$o(\mathbf{x}) = r_D(\mathbf{x}) \cdot h_F(\mathbf{x}) \quad (4.1)$$

Otherwise, when the hologram is not recorded under IP conditions, one must numerically refocus the complex information of the object reconstructed by [Eq. (2.12)] via angular spectrum or Fresnel transform [54]. If the hologram is recorded onto the surface of a discrete sensor with $M \times N$ square pixels of Δ_{xy} side, the discrete digital reference waver $r_D(m, n)$ is expressed as

$$r_D(m, n) = \sum_{m, n} \exp \left[i \frac{2\pi}{\lambda} (mM \sin \theta_x + nN \sin \theta_y) \Delta_{xy} \right], \quad (4.2)$$

where (m, n) are the discrete lateral coordinates of the sensor. As Eq. (4.2) shows, the computation of the numerical digital reference wave requires information about the optical setup, and precise

knowledge of the interference angle $\theta = (\theta_x, \theta_y)$. For the case of a titled uniform plane wave, this interference angle is estimated as

$$\theta_x = \sin^{-1} \left(\frac{|u_0 - u_{\max}| \lambda}{M \Delta_{xy}} \right), \quad (4.2)$$

and

$$\theta_y = \sin^{-1} \left(\frac{|v_0 - v_{\max}| \lambda}{N \Delta_{xy}} \right), \quad (4.3)$$

where (u_0, v_0) , and (u_{\max}, v_{\max}) are the lateral pixel positions of the center of the DC and +1 terms in the Fourier domain, respectively. The angle of the reference wave is determined by the wavelength of the light source, the features of the digital sensor, and the subtraction between the pixel positions of the DC and the +1 terms. The DC term is always placed at the center of the Fourier spectrum, being equal to $u_0 = (M/2) + 1$, and $v_0 = (N/2) + 1$. Therefore, the only parameter to be known is the position of the maximum peaks in the +1 term, (u_{\max}, v_{\max}) , for estimating Eq. (4.2) and Eq. (4.3). If the frequency of the plane reference wave coincides with an integer pixel position [Fig. 4.1(a)], the values of (u_{\max}, v_{\max}) can be determined directly by estimating the maximum peak in the +1 term. However, experimentally, this condition may not always be satisfied due to the discretization of the continuous complex distribution provided by the sensor. Figure 4.1(b) shows the most common experimental scenario where the maximum peak of the +1 term does not accurately represent in an integer position, leading to an imprecise compensation of the reference wave. In this case, one should find the optimal non-integer discrete position of the maximum peak.

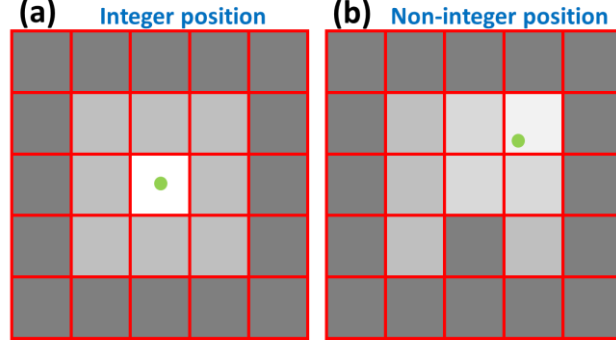


Fig. 4.1. Representation of the center position of the +1 term, (u_{\max}, v_{\max}) . (a) The frequential position of the maximum peak coincides with an integer value, and (b) the frequential position of the maximum peak does not coincide with an integer position. The latter case is the most common in experimental DHM systems. The green circle denotes the position of the maximum peak to compute the digital reference wave and reconstruct accurate phase images.

4.2 Proposed method

This section is devoted to describing our approach to finding the optimized non-integer values of (u_{\max}, v_{\max}) . Different approaches have been proposed to solve this problem. For instance, in 2017, Trujillo *et. al.*, estimated the optimized values of (u_{\max}, v_{\max}) using an iterative approach based on double nested loops [80]. In particular, Trujillo's method was based on a mean-thresholding-and-intensity-summation metric. For each value of (u_{\max}, v_{\max}) , including non-integer values, the authors compute the digital reference wave $r_D(x)$, reconstruct the phase image, generate the binary phase image using a fixed threshold and sum all pixels in each binary image. For the optimal values of (u_{\max}, v_{\max}) , no phase perturbations (i.e., aberration-free) should appear in the reconstructed phase image (or minima phase perturbations in the presence of high-order aberrations such as astigmatism and coma). Therefore, its binary image should be white (i.e., all pixels in the binary phase image should be 1). Nonetheless, if the values of (u_{\max}, v_{\max}) are not the optimal ones, the reconstructed phase image is distorted by a residual plane tilt and, therefore, its binary image is a

combination of black and white pixels. The higher the number of black pixels in the binary phase image, the higher the residual plane tilt.

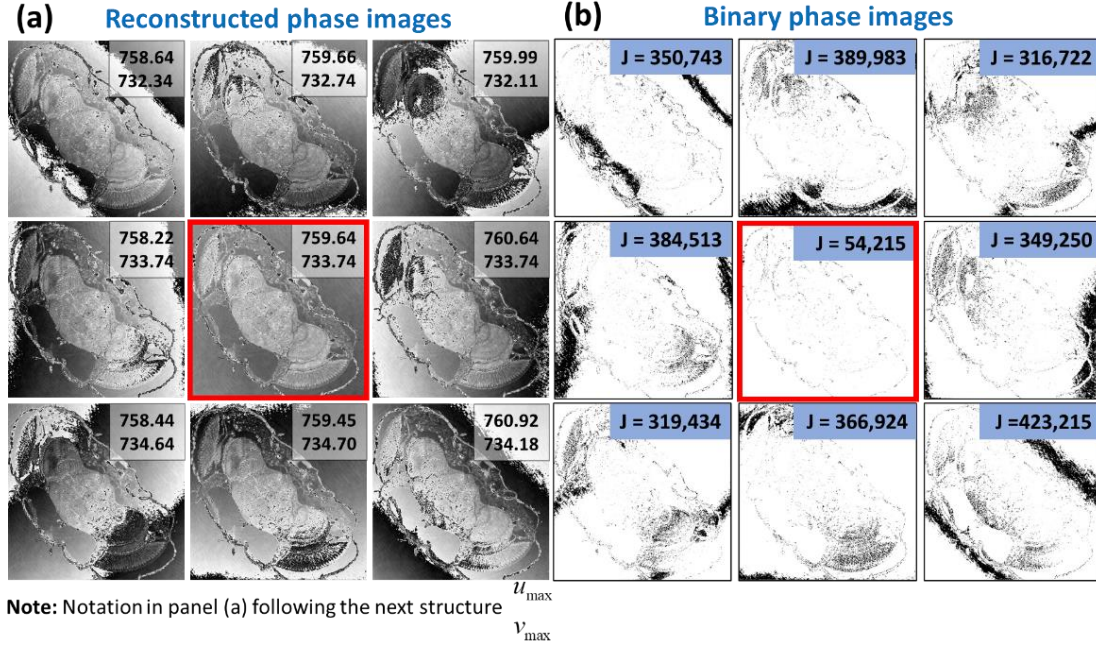


Fig. 4.2. Reconstructed phase images of a section of the head of a *Drosophila melanogaster* fly for different values of (u_{\max}, v_{\max}) . Values are reported in the upper right corner.

Figure 4.2(a) shows the reconstructed phase images of a section of the head of a *Drosophila melanogaster* fly using different values of the position of the maximum peak, (u_{\max}, v_{\max}) , to generate the digital reference wave. All figures illustrate non-optimal compensations, corresponding to erroneous positions of (u_{\max}, v_{\max}) . However, at the center on Fig. 4.2(a), the optimal compensation of the reference wave is shown. The values of (u_{\max}, v_{\max}) are reported in the upper right corner of the reconstructed phase images. As expected, the best-reconstructed phase image should provide a free-aberration phase. In other cases, reconstructed phase images with

perturbations (i.e., non-optimal phase reconstructions) have a higher number of dark pixels. These dark pixels are related to the off-center in the spectrum of the non-optimal phase reconstructions.

The difference between Ref. [80] and the proposed method is the implementation of the search for the optimal values of (u_{\max}, v_{\max}) . Trujillo *et al.* implemented their approach using nested loops to find the values of (u_{\max}, v_{\max}) by searching the maximum number of pixels equal to 1 in the binary image [80], Fig. 4.2(b). Conversely, in this work, the implementation is based on unconstrained nonlinear optimization algorithms, based on the minimization of a cost-function which is intrinsically faster than nested loops. The values of (u_{\max}, v_{\max}) are found by searching the minimum number of pixels equal to 0 (e.g., black pixels) in the binary image. Therefore, the proposed cost function tracks the number of black pixels,

$$J = M \cdot N - \sum_{m,n} \text{binarization}(\varphi_o). \quad (4.4)$$

The first term in Eq. (4.4) is the maximum possible number if the reconstructed binary phase image has no perturbation. The second term corresponds to the summation over all the pixels of the reconstructed binary phase image, providing the highest value when the reconstructed phase image is optimal, it entails the lowest value of the cost-function J . The binary phase images for the *Drosophila melanogaster* and their resulting cost-function is illustrated in Fig. 4.2(b), the value of the cost-function is reported in the top right corner for each binarized phase images. The plot for the cost-function value with respect to the values of (u_{\max}, v_{\max}) is shown in Fig.4.3. The reader can notice that the cost-function J contains a well-defined global minimum (blue rectangle in Fig. (4.3)). For non-optimal reconstructed phase images, the value of the second term in Eq. (4.4) starts to decrease due to the presence of dark values, resulting in a cost function with a value higher than

its minimum. Whereas the binary images for non-optimal reconstructions show a higher number of dark pixels, the binary image for the optimal compensation is almost white, demonstrating that the best phase reconstruction provides the minimum cost function value [Eq. (4.4)].

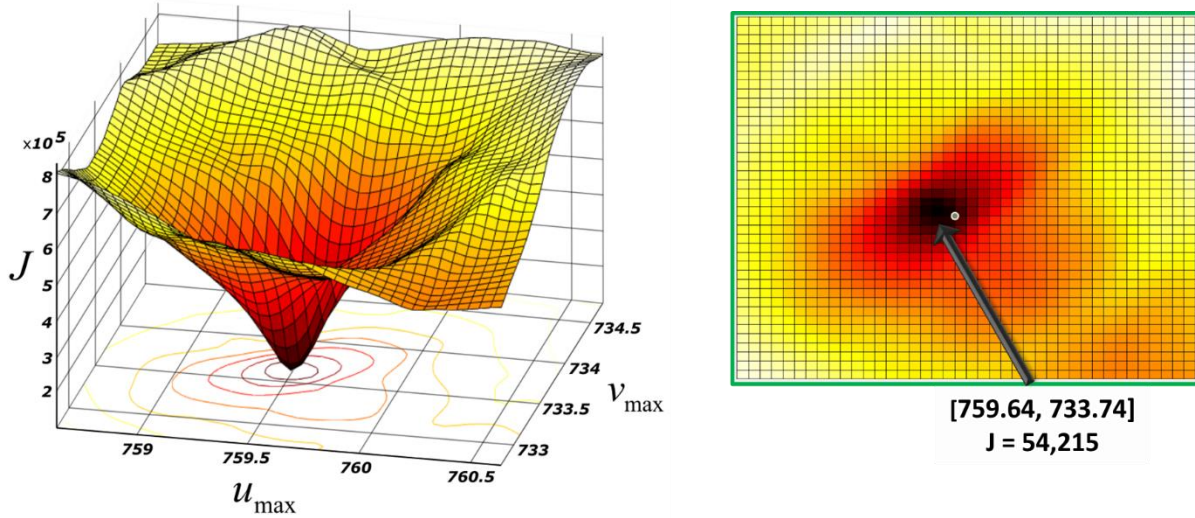


Fig. 4.3. 3D surface plot for the cost-function J [Eq. (4.4)] vs different values of (u_{\max}, v_{\max}) . These values were obtained for a *Drosophila melanogaster* fly.

The block diagram of the proposed method is shown in Fig. 4.4. The block diagram comprises four main stages: input parameters, spatial filtering, compensation, and output. The input parameters of the proposed algorithm are an image-plane hologram (h) recorded in a telecentric architecture and IP, the source's wavelength (λ), and the pixel size Δ_{xy} . The second stage is the spatial filtering of the +1 order. This filtering is performed by applying a circular mask filter and multiplying for the Fourier transform hologram. The center for the circular mask is estimated by the integer position of the maximum peak of the +1 term in the hologram spectrum. The radius of the circular mask filter depends on the magnification and numerical aperture of the DHM system [38]. Nonetheless, without knowing this information, the radius of the circular mask can be assumed to be equal to $1/3\sqrt{|u_0 - u_{\max}^0|^2 + |v_0 - v_{\max}^0|^2}$. The next step is the compensation of the

tilt of the plane reference wave. This stage is split into two parts: the setting of the cost function and its minimization. In MATLAB we have used the built-in function *fminunc*. This function finds a local minimum of an unconstrained multivariable function using the quasi-Newton or trust-region algorithms. The scope of this research work is the investigation and validation of an automatic reconstruction approach for DHM that requires the minimum number of user inputs (e.g., hologram, wavelength, and pixel size). Because the trust-region algorithm requires a gradient function as the input of the minimization process, we have implemented the quasi-Newton algorithm. This work does not thoroughly study the minimization solver and algorithm. Note that the selection of a different solver and algorithm, and the use of parallel computing may yield reduced response time; however, that investigation is beyond the scope of this research.

The input parameters of the *fminunc* function are the cost-function [Eq. (4.4)], the integer position of the maximum peak in the filtered hologram spectrum, (u_{\max}, v_{\max}) , and a set of optimizations options. The optimization options are the maximum number of iterations allowed and a termination tolerance on the cost function. The tolerance has been set to 10^{-3} since a lower tolerance value does not improve results. Regarding the number of iterations, the steps of the proposed method are repeated until convergence. Convergence is defined when the norm of the gradient of the cost-function is smaller than the tolerance. For the tested holograms, convergence is achieved within the first five iterations. The number of iterations is highlighted dependent on the initial value in the minimization approach. Since the hologram has been recorded in a telecentric-based DHM system and the reference wave is a tilted plane wave, the center integer position of the +1 term, (u_{\max}^0, v_{\max}^0) , is the best candidate to start the search of the optimal non-integer spatial frequency (u_{\max}, v_{\max}) since the optimal values should be close to the integer position of the +1

term. Nonetheless, in the event of not achieving convergence, we have set 30 iterations as the maximum number of iterations allowed before the algorithm breaks the execution.

The estimation of the cost function [Eq. (4.4)] requires the binarization of the reconstructed phase image that depends significantly on the digital reference wave via the position (u_{\max}, v_{\max}) . The binary image is obtained by applying the MATLAB built-in function *imbinarize* to the reconstructed phase image. The *imbinarize* function uses Otsu's method, and its input parameter is the reconstructed phase image. In this study, the default threshold value of Otsu's method is used since it provides the best-reconstructed phase image with minimum phase perturbations. For each iteration of the minimization process, the algorithm finds a pair of possible values (u_{\max}, v_{\max}) , generates the corresponding digital reference wave, and computes the reconstructed phase image reconstruction. This resulting phase image is binarized, and the cost function J is computed. The proposed algorithm is an iterative method, starting with the integer position of the maximum peak in the +1 term, (u_{\max}^0, v_{\max}^0) until finding the optimal non-integer position. Once the optimal values of (u_{\max}, v_{\max}) are estimated, the final phase image can be reconstructed without phase aberrations due to the interference tilt. It is important to remember that the amplitude image can be estimated after the spatial-filtering step.

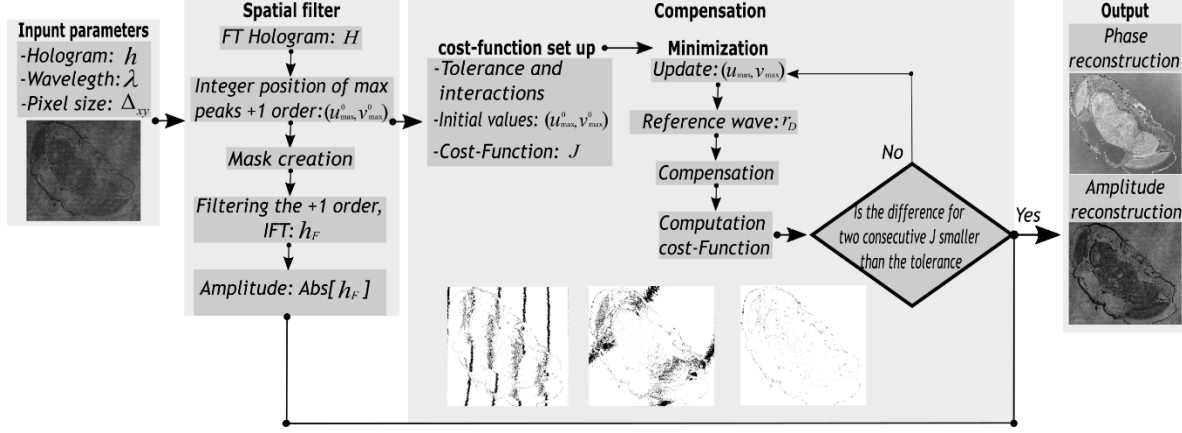


Fig. 4.4. Block diagram of the proposed method.

4.3 Experimental validation

To evaluate the proposed method's performance, we have compared the performance of our method to the one from nested loops [80] and centroid-based [78] algorithms. For this comparison, we have used three different optically-thin samples, a USAF target of Benchmark Technologies, a transverse section of the head of a *Drosophila melanogaster* fly, and glioblastoma cells. Figure 4.5. shows the respective reconstructed phase images. For the phase USAF target, we have measured the average phase and its standard deviation of the elements in Group 6 to be equal to (2.00 ± 1.90) rad for the nested loops algorithm, (1.32 ± 0.17) rad for the centroid-based algorithm, and (1.83 ± 0.16) rad for the proposed method. Regarding manufacturer specification, the nominal phase value of these elements is 1.84 rad, considering $(= 2\pi(n-1)t/\lambda)$ for a wavelength of $\lambda = 532$ nm, thickness of $t = 300$ nm, and refractive index of $n = 1.52$. The error difference between the experimental and nominal phase values is 0.54%, verifying the high accuracy of the proposed method to quantify phase measurements. The error difference for the nested loops and centroid-based algorithms is 8.7% and 28.3%, respectively, being higher due to the wrapped phase values. It is important to remember that, in biological imaging, phase measurements enable the

estimation of biological parameters such as the integral intracellular refractive index [86]. Therefore, accurate phase measurements are imperative since variations in phase values are used as a diagnostic and measuring tool in biological research.

The accuracy of the performance of each compensation method is estimated by binarizing its reconstructed phase image and counting the ratio between the total number of white pixels versus the total number of pixels in the reconstructed phase image. Considering that the best reconstructed phase image's binarized phase image has a very minimal or no dark pixels at all. For example, in the USAF target, the image has $1024 \times 1024 = 1.408 \times 10^6$, and the binarized phase image has 9.96×10^5 white pixels, resulting in 95% of the total image (i.e., the performance of the method is 0.95). These values are reported in the left bottom corner of each phase image in Fig. 4.5. Based on these values, the reconstructed phase images estimated by our proposed method provide the best reconstructed phase images without residual phases. This high performance is achieved because our proposed method achieves high precision in calculating the position of (u_{\max}, v_{\max}) . The values for (u_{\max}, v_{\max}) are reported under each phase image. The phase measurements are strongly dependent on ambient fluctuations and the experimental implementation. The maximum number of the decimal digits in the (u_{\max}, v_{\max}) values should be the one that generates a trustable reference wave and provides accurate phase measurements.

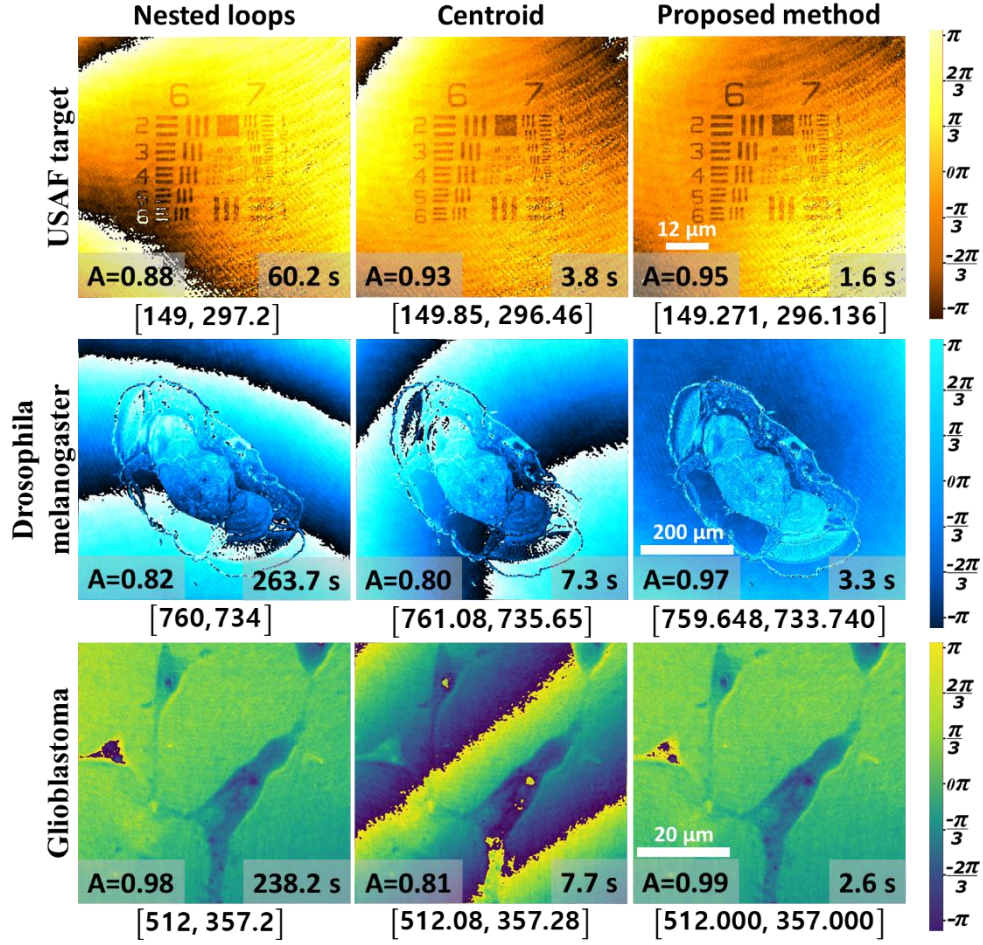


Fig. 4.5. Reconstructed phase images of the phase USAF target of Benchmark Technologies (first row), a section of the *Drosophila melanogaster* fly (second row), and glioblastoma cells (third row) for three different algorithms: nested-loops-based algorithm (first column), centroid-based algorithm (second column), and the proposed method (last column).

Regarding the processing time, the proposed method was evaluated using a Windows-based i7-8700 K CPU (3.70 GHz) 16.0 Gbyte RAM desktop computer. The average processing time of our method is 1.55 s for holograms of 1024×1024 pixels, and 2.95 s for a hologram of 2048×2048 pixels. Note that the processing time has been reduced by a factor of $2.3\times$ compared with the centroid-based algorithm [78]. Regarding the nested-loops-based algorithm [80], which is the slowest algorithm in this comparison, our method is around $40 \times -90\times$ faster than the nested-loops-based method. The processing time is reported in the upper right corner for each phase image.

Based on this analysis, the proposed method provides precise values of u_{\max} and v_{\max} , and precise phase measurements without phase perturbations.

To finalize the discussion of the proposed method, Fig. 4.6 shows the behavior of the reconstructed phase regarding the number of decimal digits (e.g., 1, 2, 4, and 6 decimal digits) to report the (u_{\max}, v_{\max}) values. By default, the output values of the MATLAB *fminunc* function have six decimal digitals. The values (u_{\max}, v_{\max}) are reported in the top right corner of the reconstructed phase images in Fig. 4.6. Testing the accuracy of the reconstructed phase images based on the precision of the values of (u_{\max}, v_{\max}) has been performed by comparing the reconstructed phase images and measuring the mean square error (MSE) between the reconstructed phase image using 6 decimal digits and the corresponding one using less digits. The MSE values are reported in the bottom left corner of the reconstructed phase images in Fig. (4.6). As expected, the highest the precision of the values (u_{\max}, v_{\max}) , the minimum the error in the reconstructed phase image. However, this statement does not address the question of how many decimal digits are sufficient. Because phase measurements are strongly dependent on ambient fluctuations and the experimental system, we have defined a trustable digital reference wave (e.g., precise reference wave) as the one that provides phase measurements with an error smaller than the phase divergence of the experimental system. Among the different DHM systems, common-path DHM systems provide a phase error in the order of 0.0003 rad [87]. Based on these phase errors and the reported MSE values in Fig. 4.6, we conclude that we need at least three decimal digits in the values of (u_{\max}, v_{\max}) to generate a trustable reference wave and provide accurate phase measurements across any DHM implementation.

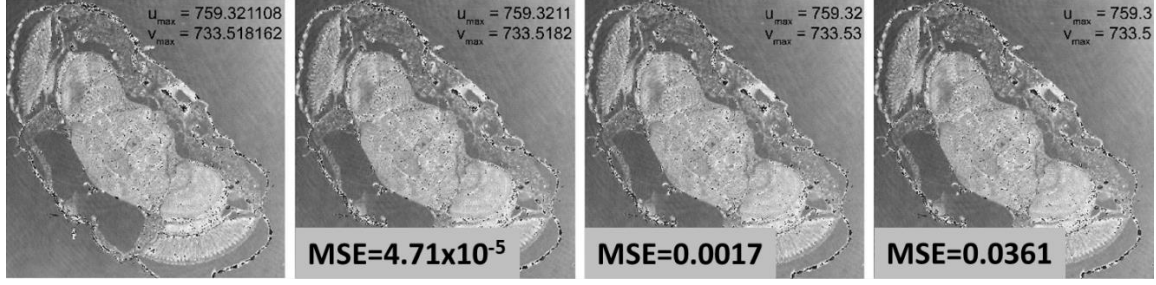


Fig. 4.6. Illustration of the accuracy of the reconstructed phase images based on the precision of the (u_{\max} , v_{\max}) values.

4.5 Conclusions

This work presents an automatic and fast method to reconstruct the quantitative phase distribution of unstained biological samples with a minimum or no phase perturbation. The proposed method compensates for the tilt between the reference and object waves in off-axis DHM systems operating in telecentric configuration. The input parameters in our method are an in-focus hologram, the wavelength of the source, and the pixel size. The limitations of the proposed technique are: (1) one cannot reconstruct phase images of defocused holograms; (2) the approach only works for off-axis DHM systems operating in the telecentric regime; and (3) there is no compensation of high-order aberrations. Compensation for high-order aberrations, such as astigmatism, and coma, is required to ensure accurate quantitative phase analysis. Future work will address these limitations to provide a more general reconstruction approach to ensure accurate quantitative phase analysis applicable to any off-axis DHM system. In addition, future work will also investigate the applicability of the technique for optically thick samples by integrating our method with phase unwrapping methods. Among the hallmarks of the proposed approach is the high accuracy in estimating the parameters of the digital reference wave. The interference angle is calculated precisely, within three decimal places, without compromising the computation time. The proposed method performs $40\times$ faster than a previously reported automatic approach based

on nested-loops and $2.3\times$ faster than the centroid-based algorithm. The experimental results show that the proposed approach provides quantitative phase images without phase perturbations. Although the proposed method has been validated for transparent biological samples, it can also be applied for reflective-based DHM systems. A ready-to-use version of the MATLAB GUI plugin (Appendix A provides short user manual), the source code, example data sets, and a short user manual can be found online. All resources will be posted publicly on GitHub [88].

Table 4.1. Achievements and limitations of the proposed method.

Achievements	Limitations
<ul style="list-style-type: none"> ➤ Automatic method ➤ Quantitative aberration-free quantitative phase images for off-axis telecentric-based DHM systems operating in IP. ➤ Accuracy of three decimals for the interference angle ➤ $40\times$ faster than the nested-loop algorithm ➤ $2.3\times$ faster than the centroid-based algorithm 	<ul style="list-style-type: none"> ➤ Not operational for defocused holograms (e.g., DHM operating outside the IP). ➤ Not operational for non-telecentric-based DHM systems. ➤ Samples must be optically thin.

5. FULL ABERRATION COMPENSATION METHOD FOR NON-IMAGE-PLANE OFF-AXIS DIGITAL HOLOGRAPHIC MICROSCOPY

One of the main attributes of DHM is its capability to focus computationally at different transverse planes within the sample's volume from a single off-axis hologram. This advantage of DHM is possible because of the ability to record the complex amplitude information of inspected objects within an intensity-like hologram image. This advantage makes DHM systems suitable to live cell imaging applications, such as particle tracking to determine the three-dimensional location of specimens such as cells and bacteria [89–91]. Other application examples of such property are the study of the motility of biological samples [92–94], the tracking of gold nanoparticles [95], and polystyrene [35] or particle tracking to allow the characterization of fluids [96].

Regardless of the DHM systems, the applicability of DHM technology can be hampered by the inaccurate reconstruction of the phase images due to the presence of phase aberrations, such as tilting, defocus, spherical and high-order aberrations. These aberrations distort the phase images, generating unreal phase information that misleads the measurement of the thicknesses and refractive index. In DHM, first-order (e.g., defocus) aberrations appear when the out-focus holograms are reconstructed. Out-of-focus holograms are those holograms in which the sensor plane is different than the image plane of the DHM imaging system or the transverse section of the sample is different than the object plane of the MO lens (e.g., the sample is not placed at the working distance from the MO lens). In other words, the sample and the sensor planes are not located in conjugated planes (e.g., no direct imaging processing between both planes). Under this experimental condition, one reconstructs out-focus amplitude and phase images, disallowing the direct observation and analysis of samples. Several computational autofocusing methods have been proposed in DHM to correct the defocus aberration, reconstructing in-focus amplitude and

phase images. Most of those approaches use sharpness quantification criteria for determining the correct propagation distance (e.g., the axial separation between the recorded out-of-focus plane and the image plane) [97–100]. Generally, those approaches produce a stack of images amplitude/phase images with different propagation distances. A sharpness quantification metric is evaluated for each reconstructed amplitude/phase image [101] to select the optimal propagation distance within the stack of reconstructed images.

The integrated amplitude modulus (AMP) [97], the Tamura coefficient [102], energy of Laplacian [103], normalized variance [104], and Tenengrad variance [105], are counted among the state-of-the-art sharpness quantification metrics. The main limitation of these strategies is they require the generation of multiple reconstructed amplitude/phase images with different propagation distances using nested loops to search for the sharpest reconstructed amplitude/phase images. The selection of the sharpest reconstructed amplitude/phase images is highly dependent on the range (e.g., maximum and minimum value) and step of the propagation distances, leading to methods with high computational effort and processing times due to the fine search of the propagation distance parameter. Note that the correct selection of the minimum, maximum, and step values for the propagation distances are fundamental to ensure that in-focus amplitude/phase images are properly reconstructed.

Other approaches based on the learning-based models have been presented to avoid the user's input in selecting the range and step for the propagation distance. For instance, in 2017, Pitkäaho *et al*, presented one of the first applications of deep learning for DHM, demonstrating the use of convolutional neural networks for autofocusing strategies [106]. One year after, Lam *et al*, implemented a machine learning approach based on a convolutional neural network to predict the

best/focus plane for amplitude and phase objects in DH [107] (e.g., DHM systems without the imaging system – no MO and TL lenses in the object arm).

This chapter presents an accurate and automatic reconstruction method for out-focus pure phase objects. The proposed autofocusing DHM method is based on the minimization of two cost functions. The minimization of the first cost function is responsible for estimating the best focal plane (e.g., propagation distance), reducing the computational effort of conventional nested loop approaches. The second cost function compensates for the tilt interference angle, providing quantitative phase images with reduced phase aberrations. This second cost function is the same one as implemented in Chapter 4. The synergetic minimization of both cost functions allows us to reconstruct in-focus quantitative amplitude and phase distributions in off-axis DHM systems operating in telecentric regime. To the best of our knowledge, this is the first work in which the autofocusing and accurate compensation of the interference angle introduced in off-axis DHM systems are tackled simultaneously. The Chapter is organized as follows. Section 5.1 presents a brief framework for out-focus DHM imaging reconstruction. In Section 5.2, the proposed method is described and compared with a nested-loop autofocusing approach. Experimental results and Conclusions are reported in Sections 5.3 and 5.4, respectively.

5.1 Theoretical background: out-focus DHM imaging reconstruction

In DHM, the reconstruction procedure consists of recovering the complex object information from the recorded hologram [Eq. (2.4)]. In off-axis DHM, the complex amplitude distribution of the object is given by Eq. (2.11). Note that, in this chapter, the hologram is not recorded under IP conditions (e.g., camera not placed at the back focal plane of TL or the sample not placed at the front focal plane of the MO lens), needing to numerically refocus its complex information via angular spectrum [108] and the Fresnel transform [109]. The selection between the angular

spectrum algorithm and the Fresnel transform method depends on the propagation distance and the optical parameters of the DHM system, including the source's wavelength (λ), the dimension of the camera's sensor (e.g., $M \times N$ pixels) and the pixel size (e.g., Δ_{xy}) [110]. As the authors shown in Ref. [110], the propagation distances commonly used in most DHM systems required the angular spectrum approach. Following the Huygens' principle, the angular spectrum approach represents a complex amplitude of a wavefront as a combination of infinite plane wavefronts. Therefore, the in-focus complex amplitude distribution, $\hat{u}_{ip}(x, y)$, can be estimated as

$$\Gamma(\xi, \eta, z) = \text{IFT} \left\{ \text{FT}\{h(x, y; 0)\} \exp \left[i \frac{2\pi z}{\lambda} \sqrt{1 - \lambda^2(u^2 + v^2)} \right] \right\}, \quad (5.1)$$

where z is the propagation distance in the image space, (u, v) are lateral spatial frequencies, and $\text{IFT}[\cdot]$ and $\text{FT}[\cdot]$ are the 2D inverse Fourier transform and the Fourier transform, respectively. In Eq. (5.1), the $\hat{u}(x, y; z)$ complex distribution is the reconstructed object wavefront after filtering the +1 term from the off-axis hologram and compensating for the tilted reference wavefront [Eq. (4.3)]. The phase map of $\hat{u}(x, y; z)$ distribution, $\hat{\phi}(x, y; z)$, should have been compensated for any quadratic phase factor. Whereas the in-focus amplitude object distribution is estimated by the absolute square modules of Eq. (5.1), the in-focus phase object information is given by the angle of Eq. (5.1). It is important to mention that Eq. (5.1) only compensates the first-order aberration (e.g., defocus) introduced by recorded out-of-focus hologram. Note that the object phase distributions may be distorted by additional aberrations, such as the well-known spherical aberration introduced by non-telecentric imaging configurations and high-order aberrations (e.g., coma, astigmatism).

To finish this section, let us emphasize more the propagation distance (z). Technically, out-of-focus holograms refer to such holograms in which the object plane and the image plane are not

conjugated. Based on this definition, there are two possibilities. The first one is related to the optical configuration in which the sample is placed at the working distance of the MO lens (e.g., the object plane is the front focal plane of the MO lens), but the sensor's plane is different than the image plane (e.g., the back focal plane of the TL lens). In this case, the propagation distance z is the axial separation between the image and sensor planes. The second scenario is where the sensor plane coincides with the image plane, setting the object outside the front focal plane of the MO lens. This configuration is more suitable for commercial DHM prototypes, and particle tracking applications since the 3D object is moving within the imaging volume. In this scenario, the propagation distance z used in Eq. (5.1) is related to the axial separation between the front focal plane of the MO lens and the actual object position and the axial magnification of the DHM system. The optical imaging configuration of a telecentric-based DHM system follows a $4f$ system between the MO and TL lenses. In other words, the axial separation between the MO and TL lenses is equal to the sum of their focal length, meaning that the back focal plane of the MO lens coincides with the front focal plane of the TL lens (Fig. 2.4). In this configuration, one finds a plane wave in both object and image spaces. One of the main features of this afocal configuration is that the lateral magnification M_L is the same for any transverse plane within the image space. Also, in this configuration, the axial magnification is given by the square of the lateral magnification, $M_A = M_L^2$. This axial magnification must be considered when inserting the z value. The z value used in Eq. (5.1) should be equal to $z = M_L^2 \times z_{obj}$ being z_{obj} the axial distance between the front focal plane of the MO lens and the actual object position (e.g., how far the sample is from the front focal plane of the MO lens). For instance, if an object is located at a distance equal to $15 \mu\text{m}$ from the front focal plane of the MO lens, and the lateral magnification of the $4f$ DHM system is $40\times$, one

reconstructs the in-focus information using Eq. (5.1) and a propagation distance equal to $z = 15 \times 40^2 = 24,000 \mu\text{m}$.

5.2 Full aberration compensation proposal: DHM autofocusing and tilting angle phase compensation for telecentric setups

This section presents a two-stage computational approach for reconstructing phase images from raw out-of-focus holograms. In the first stage of the proposed method, we have implemented a minimization algorithm to determine the best in-focus plane of any specimen automatically (e.g., find the z value in Eq. (5.1)). The second stage focuses on the reconstruction of phase images with reduced phase distortions by compensating the interference angle of the off-axis configuration. This second stage is a replica of the proposed cost function discussed in Chapter 4 that tracks the minimum number of phase discontinuities in the reconstructed phase image.

The cost function in the first minimization algorithm uses a sharpness metric (e.g., a function that quantifies the grade of focusing in an image [103]) to determine the best in-focus plane. The common principle of these sharpness functions is that in-focus images are those images in which their object's edges are well-defined. Therefore, one can estimate the optimal value of the propagation distance by analyzing the sharpness function on the amplitude distribution provided by Eq (5.1) for different values of the propagation distance and searching for the propagation distance that provides a maximum or minimum value in the sharpness metric. A singularity of DHM is that the in-focus amplitude image of pure phase objects is uniform (e.g., equal to 1), making only the edges of the objects on the amplitude images visible when the objects are out of focus. The most common five sharpness metrics for pure phase objects are: (1) AMP; (2) the Tamura coefficient (TC) [102], the energy of Laplacian (EL) [103]; (4) the normalized variance (NV) [104]; and (5) Tenengrad variance (TV) [105]. Table 5.1 shows the definition of these

sharpness functions. Note that in this table, $\hat{a}_{IP} = |\hat{u}_{IP}|$ refers to the reconstructed amplitude image for a given z value, and $\bar{\hat{a}}_{IP}$ and $\sigma(\hat{a}_{IP})$ are the mean and standard deviation values of the reconstructed amplitude image. Also, in Table 5.1, (m,n) are the discrete pixel coordinates, and S_x, S_y and L are filters.

Table 5. 1. Definition of the studied sharpness metrics

Sharpness curve function	Definition
AMP	$\text{AMP} = \sum_{m,n} \hat{a}_{IP}(m,n) $
TC	$\text{TC} = \text{sqrt} \left[\sigma(\hat{a}_{IP}) / \bar{\hat{a}}_{IP} \right]$
TV	$\text{EL} = \sum_{m,n} \left[\sqrt{[\hat{a}_{IP}(m,n) \times S_x]^2 + [\hat{a}_{IP}(m,n) \times S_y]^2} \right]^2$ $S_x = \begin{bmatrix} -1 & 0 & 1 \\ -2 & 0 & 2 \\ -1 & 0 & 1 \end{bmatrix} \text{ and } S_y = \begin{bmatrix} 1 & 2 & 1 \\ 0 & 0 & 0 \\ -1 & -2 & -1 \end{bmatrix}$
NV	$\text{NV} = \frac{1}{\bar{\hat{a}}_{IP}} \sum_{m,n} [\hat{a}_{IP}(m,n) - \bar{\hat{a}}_{IP}]^2$
EL	$\text{EL} = \sum_{m,n} [\hat{a}_{IP}(m,n) \times L]$ $L = \begin{bmatrix} -1 & -4 & -1 \\ -4 & 20 & -4 \\ -1 & 4 & 1 \end{bmatrix}$ <p style="text-align: right;">where</p>

We have evaluated the behavior of these sharpness metrics by reconstructing an out-focus hologram of a pure phase USAF target for 100 different propagation distances. The propagation distance used in Eq. (5.1) ranges from $-0.125 \mu\text{m}$ to $0 \mu\text{m}$, with steps of $0.002 \mu\text{m}$. Figure 5.1(a) plots the normalized sharpness metrics versus the propagation distance (z). Figures 5.1(b)-(d) show the reconstructed amplitude images ($\hat{a}_{IP} = |\hat{u}_{IP}|$) at different propagation distances.

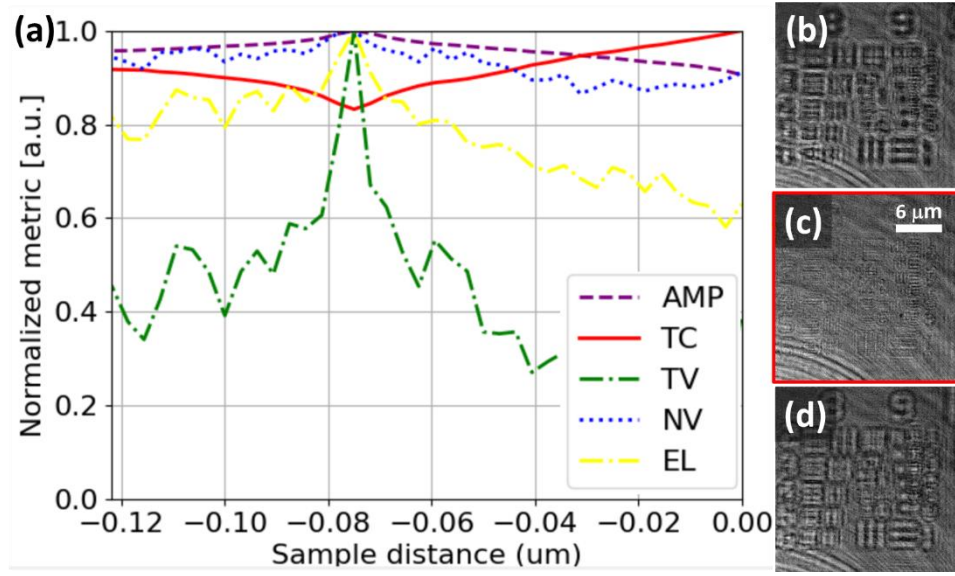


Fig. 5.1. (a) Performance of different sharpness focusing metrics in terms of the propagation distance (z) of a pure phase USAF target. Panels (b)-(d) correspond to the reconstructed amplitude image at three different propagation distances: $-0.11 \mu\text{m}$, $-0.074 \mu\text{m}$ (e.g., in-focus plane) and $-0.020 \mu\text{m}$. The red rectangle indicates the best in-focus amplitude images.

The block diagram of the proposed autofocusing phase method for off-axis telecentric-based DHM hologram is shown in Fig. 5.2. The proposed method contains three steps. The first step involves the definition of the input parameters: the out-of-focus hologram (h), the wavelength of the illumination source (λ), and the pixel dimensions of the camera (e.g., Δ_{xy}). The second step is focused on the minimization algorithm using the TC sharpness metric as the cost function to determine the in-focus propagation distance. Remember that the TC metric is estimated from the reconstructed amplitude image, $\hat{a}_{IP} = |\hat{u}_{IP}|$. The reconstructed amplitude image is independent of the phase compensation of the interference angle. Therefore, to alleviate the computation effort in this step, the reconstructed amplitude image is equal to the modulus square of the inverse Fourier transform of the filtered hologram, $\hat{a}_z = |h_F(x, y; z)|$. The minimization of the TC metric is provided by the MATLAB built-in *fminunc* function, which finds a local minimum of an

unconstrained multivariable function using the quasi-Newton algorithm [111]. The *fminunc* function requires four parameters: (i) the function to be minimized (e.g., the TC metric defined in Table 5.1); (ii) the reconstructed amplitude image after filtering the +1 term from the off-axis hologram, $\hat{a}_z = |h_F(x, y; z)|$; (iii) the initial value (e.g., seed) of the propagation distance; and (iv) a set of optimization options. Because the TC metric only contains a global minimum, we have set the initial propagation distance equal to zero to reduce the user's input. Regarding the optimization options, these parameters are the maximum number of iterations allowed and a termination tolerance on the cost function. Whereas we have set the maximum number of iterations equal to 100, the tolerance has been set up to the default value (10^{-6}) since a lower tolerance value does not lead to different propagation distances. It is important to mention that, in this work, we have not provided a rigorous study of the minimization solver, algorithm, and optimization options. The selection of different solver, algorithm, and optimization options may give a different result. Nonetheless, this fine-tuning investigation is beyond the scope of this chapter and may be investigated in the future.

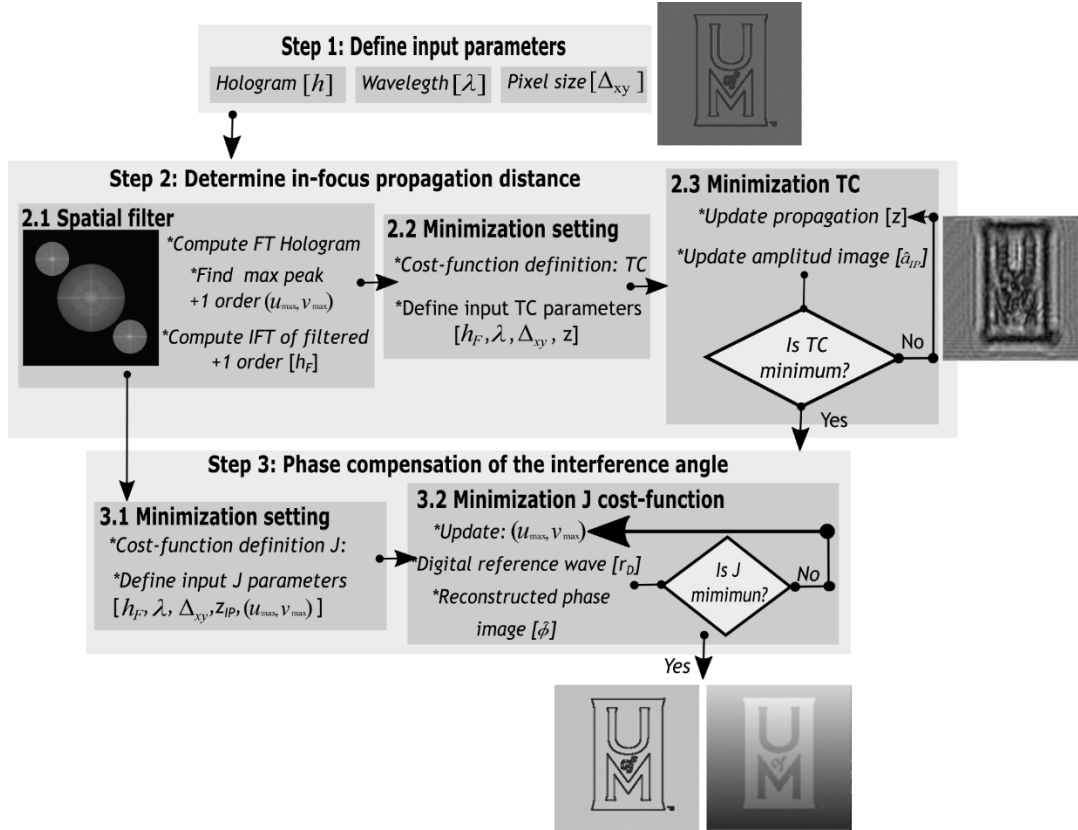


Fig. 5.2. Block diagram of the proposed three-stage method.

After estimating the propagation distance for the best in-focus plane based on the reconstructed amplitude image, the third step compensates for the interference angle introduced by the off-axis configuration. In this step, we have also implemented a minimization algorithm using the MATLAB built-in *fminunc* function. The cost function to be minimized is given by Eq. (4.4) and Fig. 5.3 shows the behavior of the cost-function. The input parameters required in this second minimization algorithm are the inverse Fourier Transform of the filtered hologram spectrum, h_F , the pixel position of the maximum peak of the +1 term, the pixel sizes, and the propagation distance found in the previous step. The detailed procedure of this minimization is explained in Chapter 4.

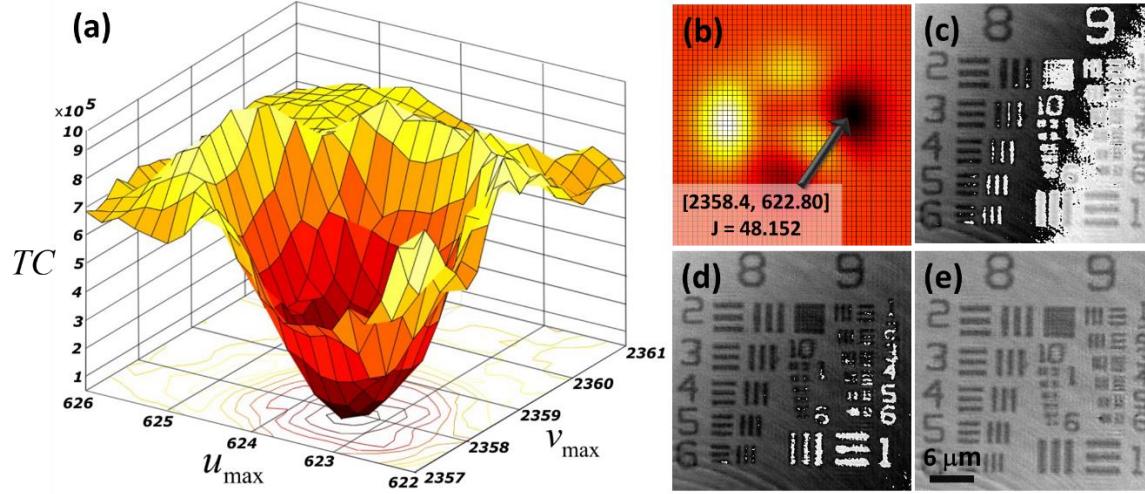


Fig. 5.3. In panel (a) 3D surface plot for the cost-function J [Eq. (4.4)], using a pure phase USAF target. Panel (b) is the 2D heatmap of J . Panels (c)-(e) are phase images reconstructed for different values of (u_{\max}, v_{\max}) . Whereas in (c) and (d) illustrate non-optimal compensation, panel (e) corresponds to the optimal compensation for the values of (u_{\max}, v_{\max}) reported in panel (b).

To finalize this section, we have compared the performance of the proposed method and the same procedure (e.g., first searching for the propagation distance based on the amplitude image and second compensation of the interference angle) using for-nested loops. The TC sharpness metric was also used for the for-nest-loop approach, selecting the propagation distance of the in-focus plane as the minimum value [101]. Note that one constraint of the nested loops is that the range of the propagation distance must be large, while the search step must be as minimum as possible. In the phase-compensation stage, we also have nested loops to find the optimal non-integer pixel center of the +1 term [80]. More details of this implementation are reported in Chapter 4. Table 5.2 compares the performance of these two algorithms reconstructing two experimental out-of-focus holograms: a phase USAF and star target. The quantitative comparison is evaluated based on five parameters: (1) the minimum TC value; (2) the in-focus propagation distance; (3) the optimal values of (u_{\max}, v_{\max}) that generate a reconstructed phase image with

minimum phase aberrations; (4) the accuracy of the reconstructed phase image based on the number of pixels that are wrapped; and (5) the processing times for each stage and the total method. From Table 5.2, it is possible to observe that both methods find the in-focus propagation distance since the TC value is the same. Although the proposed method estimates the propagation distance with a higher precision (e.g., two decimal digits), we have not observed major differences in the reconstructed amplitude images. Nonetheless, it is important to mention that the nested-loop implementation could lead to a very different result if the search step is not adequate. Regarding the compensation of the interference angle, the difference in the estimation of the u_{\max} and v_{\max} values is up to a pixel. Remember that Chapter 4 shows that a difference of a pixel in the estimation of these parameters can be detrimental for quantitative phase imaging. In fact, the reconstructed phase images estimated by the proposed method have the highest accuracy, being equal to 0.98 in both experimental reconstructions. Finally, the most noticeable difference between these strategies is the processing times. The average processing time for the nested-loop approach is 282.19 and 50.5 seconds for holograms of 2048×2048 and 1024×1024 pixels, respectively. The processing time in our method has been reduced by a factor $20\times$ compared to the nested-loop implementation. This processing time is reported based on a Windows-based AMD Ryzen 5 3500U CPU (2.10 GHz) 8.00 Gbyte RAM desktop computer.

Table 5.2. Comparison of Nested-Loop (NL) and Proposed method.

Sample		Phase USAF target		Star target	
Method		NL	Proposed method	NL	Proposed method
Image size		2048×2028		1024×1024	
TC value		0.6817	0.6816	0.7494	0.7494
In-focus plane (mm)		-121	-121.11	-39	-39.18
U_{\max}		1611.11	1610.02	805	806
V_{\max}		425.20	425	214	214
Accuracy phase		0.83	0.98	0.92	0.98
Processing times (s)	Auto focusing	182.93	10.43	31.56	3.09
	Full compensation	94.29	2.53	15.50	0.25
	Total	282.19	14	50.5	5.46

5.3 Results for experimental statics samples

We have evaluated the performance of the proposed method using three different specimens: a star target by Benchmark Technologies, red blood cells (RBCs), and human cheek cells. Figure 5.4 shows the results from the star target. The out-of-focus hologram of this sample has been recorded using a DHM setup using a Fresnel biprism. A CCD digital sensor acquiring images of $5,472 \times 3,648$ square pixels of 2.4- μm pitch is employed. A monochromatic low-power 532 nm laser diode module (CPS532, Thorlabs) is used as a light source. The DHM imaging system comprises a 200-mm TL lens and an infinity-corrected 40 \times /0.75 NA Nikon MO lens. The imaging system operates at the telecentric regimen to compensate for the optical spherical aberrations introduced by the MO lens. More information on this DHM system can be found in [112].

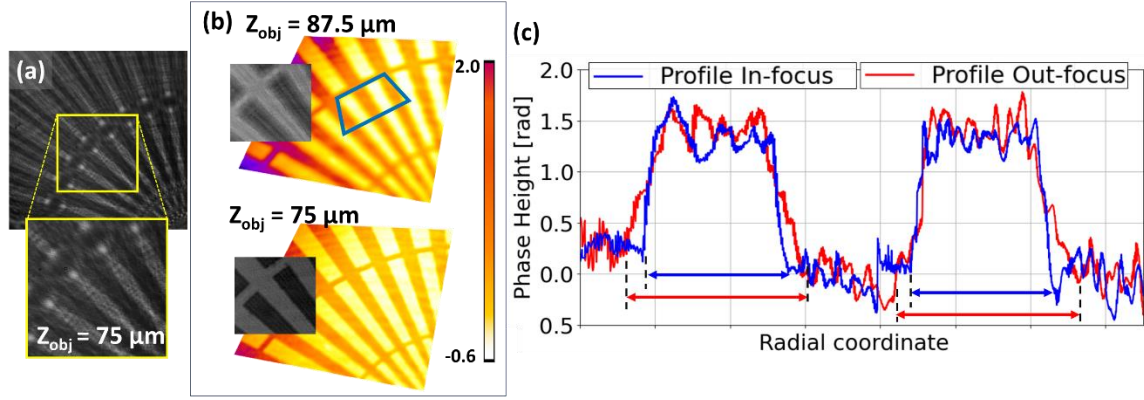


Fig. 5.4. Experimental validation of the proposed method using a phase star target. Panel (a) the out-of-focus hologram. Panel (b) and (c) are the reconstructed phase images at two different propagation distances: 140 mm ($z_{obj} = 87.5 \mu\text{m}$) and 120.6 mm ($z_{obj} = 75 \mu\text{m}$), respectively. Panel (d) shows the radial profile of the in-focus reconstructed phase images along the green line marked in panel (c).

The star target has been located approximately at $75 \mu\text{m}$ from the front focal plane of the MO lens to record a defocused hologram, Fig. 5.4(a). Assuming the system's magnification equal to $40\times$, the propagation distance in Eq. (5.1) is approximately 120 mm. Figures 5.4(b) are the reconstructed phase images at two different axial planes: an out-of-focus plane located at $z = 140$ mm ($z_{obj} = 87.5 \mu\text{m}$) and the image plane located at $z_{IP} = 120.6$ mm ($z_{obj} = 75 \mu\text{m}$). The zoom-in areas in panels (b) highlight the differences between both reconstructed phase images. Although the off-axis compensation methods yield aberrations-free phase reconstructions, only our proposal provides in-focused information on the sample. The profile for a radial distance marked in panel (b) for each phase reconstruction is shown in Fig. 5.4(c). The red and blue profiles correspond to the reconstructed phase for out-of-focus and in-focus reconstruction, respectively. From these profiles, we quantified the distance on the base (blue and red narrows in Fig. 5.4(c)), the distance of the base for the out-focus profile increases by a factor of $1.3\times$ respect to the in-focus profile. This behavior shows that blurry effects on the edge image are presented for the out-focus phase reconstruction.

This proposed method has been further evaluated using two biological samples: RBCs and check cells. For the RBC sample, the optical setup to record the RBC hologram is the same as the one from the star target. However, in this experiment, the sample was located at $15\text{ }\mu\text{m}$ from the front focal plane of the MO lens, being approximately $z = 24\text{ mm}$ the image plane. Figure 5.5(a) corresponds to the experimental out-of-focus RBC hologram. The yellow rectangle in Fig. 5.5(a) encloses a zoom-in region to ease the observation of the out-of-focus RBCs. Figure 5.5(b) is the best-reconstructed phase image found by the proposed method at a distance $z = 23.32\text{ mm}$ (e.g., $z_{\text{obj}} = 15\text{ }\mu\text{m}$). Since the shape of the RBCs is well-defined in the reconstructed phase image, one can conclude that the proposal yields phase information without or with minimum phase distortions. The red rectangle in Fig. 5.5 (b) encloses a zoom-in region of the studied sample to display its three-dimensional (3D) pseudocolor phase distribution. The processing time to find the best focal plane and compensate for the interference angle from the out-of-focus RBCs hologram is 8.52 s.

Figures 5.5(c) and (d) show the hologram and reconstructed unwrapped phase images of out-of-focus check cells. The unwrapping algorithm is based on the proposed method by Herraiz *et al.*, [113]. This experimental hologram was recorded in a Mach-Zehnder interferometer with a 632-nm diode laser as the illumination source and a monochromatic 23U445 camera from Imaging Source built with a sensor of 1280×960 square pixels of $3.75\text{-}\mu\text{m}$ pitch. The telecentric-based DHM imaging system has a $40\times/0.65$ NA Olympus, MO lens and a 200-mm TL lens. We do not have any prior information on the axial location of the sample, mimicking a more realistic scenario in 3D particle tracking. Nonetheless, the proposed method found that the sample plane was located at a distance $z_{\text{obj}} = 0.037\text{ }\mu\text{m}$ (e.g., $z = 14.80\text{ mm}$) from the front focal plane of the MO lens. In this case, the processing time is 5.09 s.

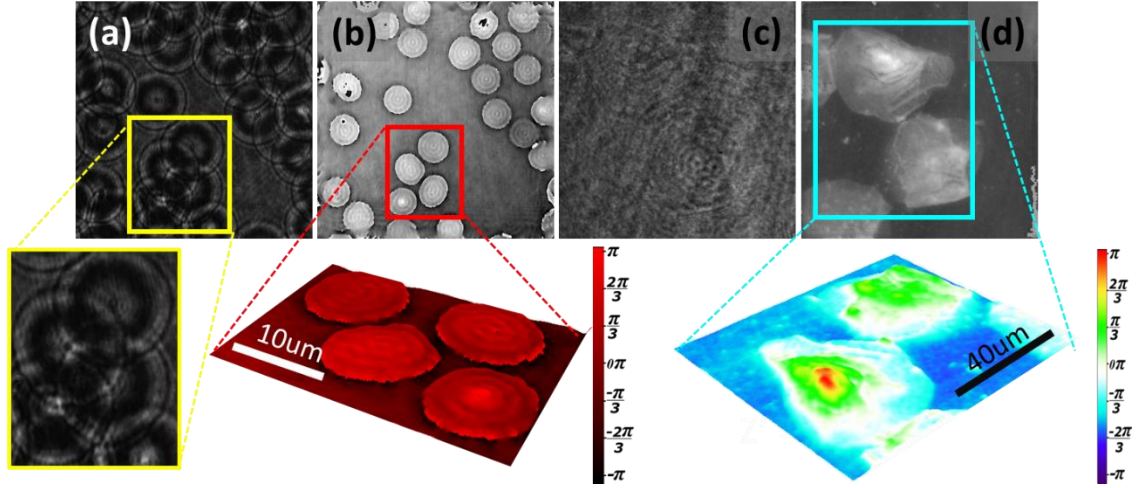


Fig. 5.5. Experimental validation of the proposed method using biological samples. Panel (a) and (c) are the out-of-focus hologram of RBCs and cheek cells. Panels (b) and (d) are the reconstructed phase images at the in-focus plane.

We have tested the performance and robustness of the proposed method with different defocused holograms from RBCs, which are not completely pure phase samples. The propagation distance has been changed from of the in-focus plane (e.g., front focal plane of the MO lens) to an axial plane that is located $95\text{ }\mu\text{m}$ from the front focal plane of the MO lens. For a complete study, we have recorded two different fields of views in each transverse plane. We have reconstructed the phase image for each FOV 100 times to find that the estimated propagation distance was almost identical (e.g., the STD of the 100 estimated propagation distances is approximately 10^{-14}). Regarding the accuracy of the reconstructed phase images, the values of the u_{max} and v_{max} were always the same, demonstrating that the proposed method always converge to the global minimum. Figure 5.6 shows that the reconstructed phase images for the highest propagation present low quality since the angular spectrum is not valid anymore. However, Fig. 5.6 shows that the algorithm's performance is sample dependent. We do not always obtain the reconstructed phase images with the smaller number of phase jumps. This result is due to the assumption that the system

operates in telecentric regime, which is not entirely true due to ambient fluctuations. Future work should increase the kernel function of the phase compensation, allowing high-order phase terms to complete phase compensation.

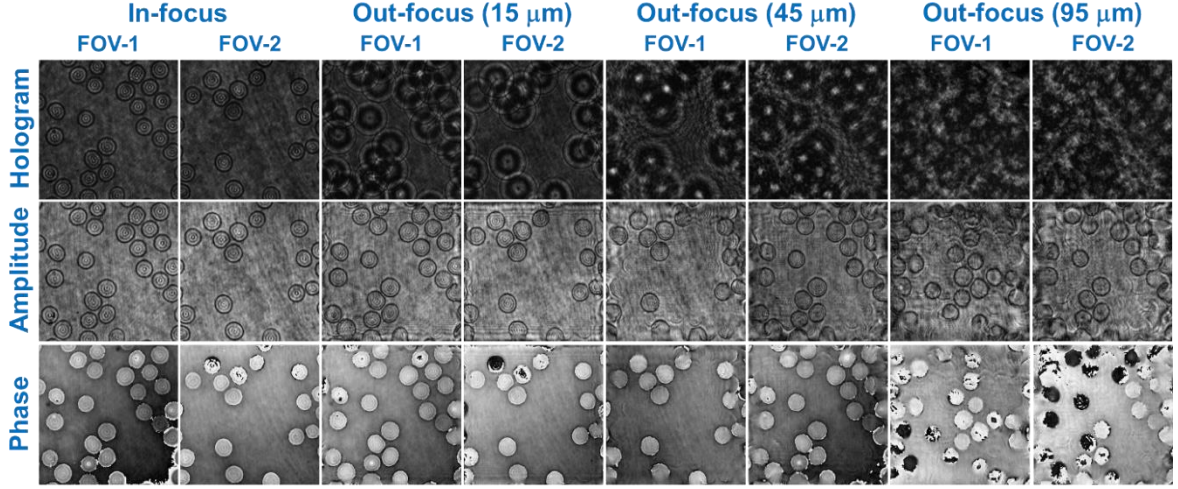


Fig. 5.6. The behavior of the proposed method for different out-of-focus RBCs holograms. For each transverse plane, two different sceneries (FOV-1 and FOV-2) have been recorded. In-focus columns correspond to the in-focus recorded holograms. Columns called Out-focus (15 μm), Out-focus (45 μm), and Out-focus (95 μm), are holograms recorded after displacement the sample 15 μm , 45 μm , and 95 μm , respectively.

5.4 Conclusions

This work presents a new strategy for autofocusing defocused phase images in off-axis telecentric-based DHM. The proposed method finds the best in-focus plane of pure phase objects by minimizing the TC sharpness function using the reconstructed amplitude images. This propagation distance is inserted as an input parameter on a second minimization stage to reconstruct phase images with minimum phase aberrations. This proposed method addressed one of the limitations of DHM computational methods, enabling the simultaneous and automatic reconstruction of phase images from out-of-focus holograms. Our experimental results demonstrate the capability of the proposed method for high-quality quantitative phase imaging of biological samples. The

synergetic implementation of two minimization algorithms reduces the processing time, being 11 seconds for a hologram of 2048×2048 pixels. This processing time has been reduced by a factor $20\times$ compared with the conventional nested-loop method (11 seconds versus 282.19 seconds). The advantages of our method are its reduced number of inputs and processing time, without penalizing the accuracy.

6. OPEN-SOURCE PYTHON LIBRARY FOR DHM

The reconstruction algorithms in DHM are significantly dependent on the optical architecture: in-line, slightly off-axis, and off-axis DHM architectures. At present, individual DHM research groups have developed and implemented their own numerical reconstruction algorithms to obtain amplitude and phase images [17]. In this Chapter, we implemented a DHM Python library, named as *pyDHM*, for reconstructing amplitude and phase images for a broad range of optical DHM configurations. The *pyDHM* is a user-friendly library written in the robust programming language of Python. The *pyDHM* implements phase-shifting approaches for in-line and slightly off-axis systems and enables phase compensation for telecentric and non-telecentric systems. In addition, *pyDHM* includes three propagation algorithms for numerical focusing complex amplitude distributions in DHM and digital holography. This chapter follows the following structure. Section 6.1 provides a literature overview of existing libraries in DH and DHM to motivate the need for an additional library suitable for any optical configuration. In Section 6.2, the *pyDHM* library framework is introduced. Section 6.3 shows the library structure and examples. Finally, in Section 6.4, the conclusions, and limitations of the *pyDHM* are presented. This work has been published in PLOS ONE [114] and was presented at the 2022 OSA Imaging and Applied Optics Congress [115].

6.1 Libraries in DH and DHM

The performance of DHM technologies relies heavily on computational reconstruction processing to provide trustworthy sample information. The required computational reconstruction algorithms are uniquely dependent on the optical configuration of the DHM system. An incorrect selection of the reconstruction algorithms leads to distorted and inaccurate amplitude and phase measurements.

DHM systems record the interference pattern (e.g., hologram) generated between the scattered light from the sample, named object wavefront, and a known reference wavefront. DHM systems operate in off-axis, slightly off-axis or in-line (also known as on-axis) configurations based on the interference angle. Therefore, the selection of the DHM reconstruction algorithms depends on this interference angle. For example, off-axis DHM systems enable the reconstruction of the complex amplitude distribution of an object wavefront from a single hologram since the three components of the hologram are entirely separable in the Fourier domain [44,45]. Therefore, the reconstruction algorithm in off-axis DHM systems requires spatial filtering of the sample frequency components in the Fourier domain of the recorded hologram. In contrast, the spectral components of a hologram in the Fourier domain overlap totally or partially in in-line and slightly off-axis DHM systems, respectively, requiring the acquisition of multiple phase-shifted holograms and the application of phase-shifting (PS) techniques [116,117] to reconstruct the desired object information. In addition, the selection of the DHM reconstruction algorithms also depends on whether the DHM imaging system operates in telecentric or non-telecentric regimes. As previously explained in Chapter 2, DHM systems operating in the telecentric regime only require the interference angle compensation in the off-axis and slightly off-axis configuration. Oppositely, non-telecentric DHM systems should compensate for the spherical phase factor recognized in DHM and associated with a non-telecentric imaging system [74,75,118,119]. Finally, the DHM configuration can operate in an IP configuration, meaning that in-focus DHM holograms are recorded, so there is no need to apply numerical propagations to focus the amplitude and phase images. However, if out-of-focus holograms are recorded, the user should numerically propagate the complex amplitude distribution to provide in-focus images. Among the different numerical

propagation algorithms to reconstruct DHM images, the most used computational approaches in DHM are the angular spectrum [54,120] and the Fresnel transform [121].

Considering the wide range of DHM configurations, each research group within the DHM community develops and implements its own computational reconstruction algorithms based on its experimental digital holography (DH) and DHM systems [17]. Nonetheless, some research groups have developed and implemented libraries and plugins to address the need for an open-source reconstruction toolbox in DHM and DH. Maybe, GWO is the first library for numerical propagation, and was presented in 2010 by Shimobaba *et al.* GWO library enables diffraction calculations of complex amplitude distributions using the angular spectrum and Fresnel approaches using a Graphics Processing Unit (GPU) [122]. Since the GWO library was based on the C language and, consequently, was not user-friendly, in 2012, the same authors developed a new C++ class library for diffraction and calculations using computer-generated holograms (CGHs) [123]. In 2015, Piedrahita-Quintero *et al.* developed a JAVA plugin for numerical wavefields propagation [124]. This plugin enabled the propagation of complex amplitude distributions using angular spectrum, Fresnel, and Fresnel–Bluestein approaches. This plugin's most important feature is embedded within the well-known open-source software for image processing called ImageJ [125]. In 2017, the same authors upgraded their previously-developed JAVA-based plugin to a GPU-accelerated library, JDiffraction [126]. In 2020, Trujillo *et al.* developed an ImageJ-based open-source plugin for in-line digital lensless holographic microscopy (DLHM) [127]. This plugin contains two modules to simulate holograms using the discrete version of the Rayleigh–Somerfield diffraction formula and to reconstruct holograms using the Kirchhoff–Helmholtz diffraction integral. That same year, Hong *et al.* introduced the OpenHolo library, a library capable of generating holograms using the most popular CGH algorithms [128].

This library also includes standard tools for holography, like phase unwrapping algorithms, and reconstruction algorithms for simulated holograms recorded in off-axis and in-line architecture using the Rayleigh-Sommerfeld diffraction integral. From 2014 to date, the Manoharan Lab at Harvard University has implemented the HoloPy library, a Python-based library, to perform scattering and optical propagation theories focusing on in-line DLHM systems [129]. Table 6.1 summarizes the existing DH and DHM libraries with their respective applications.

Table 6. 1. DH and DHM libraries.

Library	Propagation algorithms/focusing	In-line	Slightly off-axis	Off axis	DHM or DLHM?
GWO	Yes	No	No	No	DHM
Numerical Wave propagation	Yes	No	No	Yes	DHM
JDiffracton	Yes	No	No	Yes	DHM
ImageJ DLHM	Yes	Yes	No	No	DLHM
OpenHolo	Yes	No	No	Yes	DHM
HoloPy	Yes	Yes	No	No	DLHM
pyDHM	Yes	Yes	Yes	Yes	DHM

Despite all these efforts, a library containing the needed computational reconstruction approaches to reconstruct DHM images, regardless of the optical configuration of the system, does not still exist. This Chapter presents a Python library focused on DHM applications, named *pyDHM*, for reconstructing DHM images for various experimental DHM implementations. We aim to provide the DH and DHM community with a complete set of tools for holographic processing in a widely supported and easy-to-use programming language. Note that any DH/DHM

user has access to our codes so that they can modify them for their own application. The library consists of four packages. The first package contains a set of useful functions, such as calculating the hologram spectrum and displaying the amplitude and phase images. The second package is related to reconstructing in-line and slightly off-axis DHM systems using phase-shifting techniques. The third package reconstructs phase images from off-axis DHM holograms using telecentric and non-telecentric configurations. Finally, the last package includes algorithms for propagating the complex amplitude distribution using the angular spectrum and the Fresnel and Fresnel-Bluestein transform approaches. Our proposed library has been validated with experimental and simulated holograms recorded using different setups.

6.2 Library framework

DH and DHM systems are based on optical interferometry, which involves the digital recording of the interference pattern (e.g., digital hologram) between the complex amplitude distribution scattered by a microscopic object (e.g., the object wavefront) and a uniform reference wavefront. This section briefly describes different DHM configurations and their corresponding numerical reconstruction algorithms. The reconstruction approach depends on the interference angle between the reference and object waves in the recorded hologram (e.g., in-line, slightly off-axis or off-axis configuration), the regime of the microscopic imaging system (e.g., telecentric versus non-telecentric configuration), and the position of the hologram plane to the image plane of the microscopic imaging system (e.g., in-focus versus out-of-focus). The *pyDHM* library contains three algorithms for in-line DHM systems (5 Frames, 4 Frames, and 3 Frames). We also have included here algorithms for slightly off-axis DHM systems (quadrature method, 3-blind-raw and 2-blind-raw) in the library. Regarding the approaches for compensating off-axis holograms, *pyDHM* implements three different automatic approaches for holograms recorded in telecentric

architecture, and one strategy for holograms recorded in non-telecentric configuration. Finally, we have included three algorithms for propagating optical fields, such as the angular spectrum and the Fresnel and Fresnel-Bluestein transform approaches. Table 6.2 summarizes some approaches implemented in the *pyDHM* library.

Table 6. 2. Summary of the different approaches implemented by the *pyDHM* library.

DHM system	Approach	Equation
In-line	5 Frames [46,47]	$\varphi(x, y) = \tan^{-1} \left(\frac{2[h(x, y; 3\pi/2) - h(x, y; \pi/2)]}{2h(x, y; \pi) - h(x, y; 0) - h(x, y; 2\pi)} \right)$
In-line	4 Frames [46,47]	$\varphi(x, y) = \tan^{-1} \left(\frac{h(x, y; 3\pi/2) - h(x, y; \pi/2)}{h(x, y; \pi) - h(x, y; 0)} \right)$
In-line	3 Frames [46,47]	$\varphi(x, y) = \tan^{-1} \left(\sqrt{3} \frac{h(x, y; \pi/3) - h(x, y; 5\pi/3)}{h(x, y; 5\pi/3) + h(x, y; \pi/3) - 2h(x, y; \pi)} \right)$
Slightly off-axis	Quadrature method [48]	$\hat{u}(x, y) = h(x, y; 0)\hat{r}(x, y; 0) + h(x, y; \pi/2)\hat{r}(x, y; \pi/2) \\ + h(x, y; \pi)\hat{r}(x, y; \pi) + h(x, y; 3\pi/2)\hat{r}(x, y; 3\pi/2)$
Out-of-focus holograms	Angular spectrum [54]	$\hat{u}_{IP}(x, y) = \text{FT}^{-1} \left[\hat{U}(u, v; z) \exp \left(-i \frac{2\pi}{\lambda} z \sqrt{1 - \lambda^2 (u^2 + v^2)} \right) \right]$
Out-of-focus hologram	Fresnel transform [54]	$\hat{u}_{IP}(x, y) = \frac{-i}{2\lambda} \iint \hat{u}(x_0, y_0; z) \exp \left(-i \frac{\pi}{\lambda z} (x^2 + y^2) \right) \exp \left(i \frac{2\pi}{z} (xx_0 + yy_0) \right) dx_0 dy_0$

6.3 Library Structure: available packages in *pyDHM*

The *pyDHM* library consists of four packages. The first utility package includes essential functions such as reading, displaying images, and filtering Fourier spectrums of holograms. The second

package is related to reconstructing in-line and slightly off-axis DHM systems using phase-shifting techniques. The third package reconstructs phase images from off-axis telecentric-based DHM holograms. Finally, the last package includes algorithms for propagating complex amplitude distributions using the angular spectrum, the Fresnel and Fresnel-Bluestein transform approaches. This section explains each package in detail, including the functions and required parameters. We also present sample codes and results for illustrating the performance of the *pyDHM* library. Figure 6.2 illustrates the utility packages included in *pyDHM* library and the implemented functions.

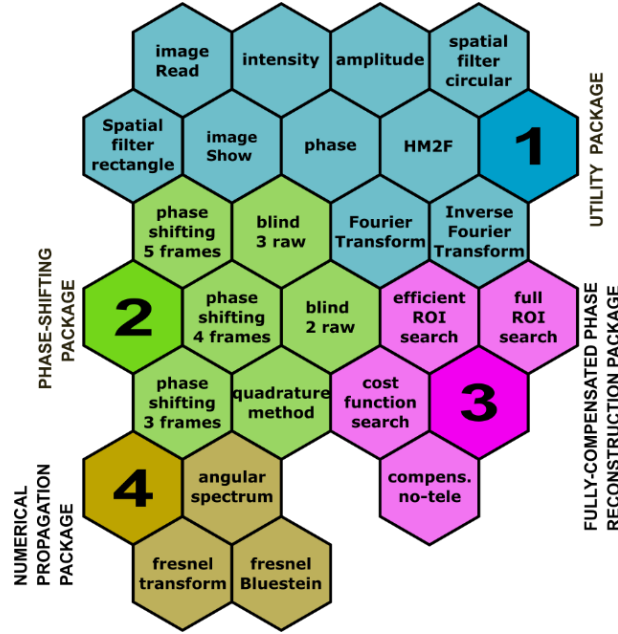


Fig. 6.1. *pyDHM* library structure. The library is composed of utility (1), phase-shifting (2), fully-compensated phase reconstruction (3), and numerical propagation (4) packages.

6.3.1 Package 1: Utility package

The first package in the *pyDHM* library contains functions for reading and displaying images, computing the Fourier transform (FT), and applying filters to reduce speckle noise [130]. Since the library focuses on DHM applications dealing with complex amplitude distributions, one can display any complex wavefield's amplitude, intensity, or phase map. Although these operations can be straightforwardly implemented in Python for experienced users, this package is aimed to

provide compact and user-friendly codes. This package is imported by typing the following code lines, *from pyDHM import utilities*. Figure 6.3 shows the information for each package function, including the declaration statement and the parameters needed. Examples of the use of this package are shown in the upcoming figures.

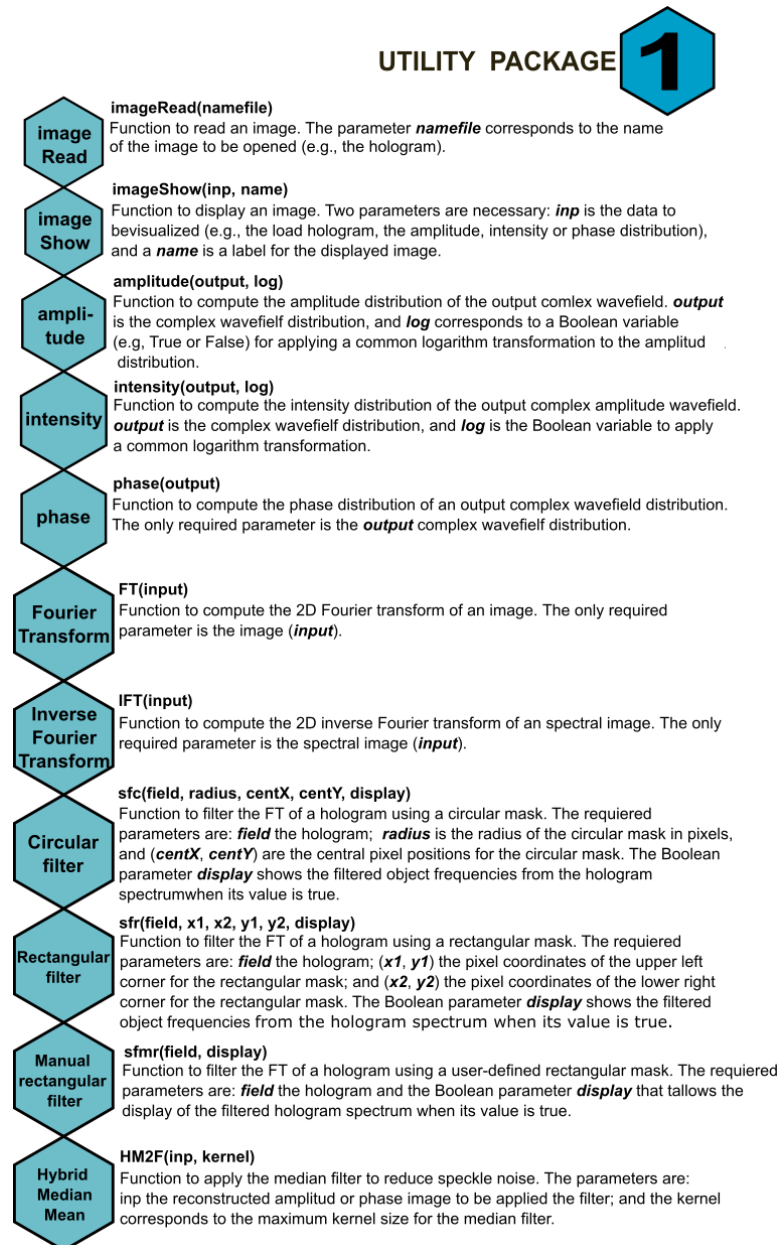


Fig. 6.2. Available functions in the utility package.

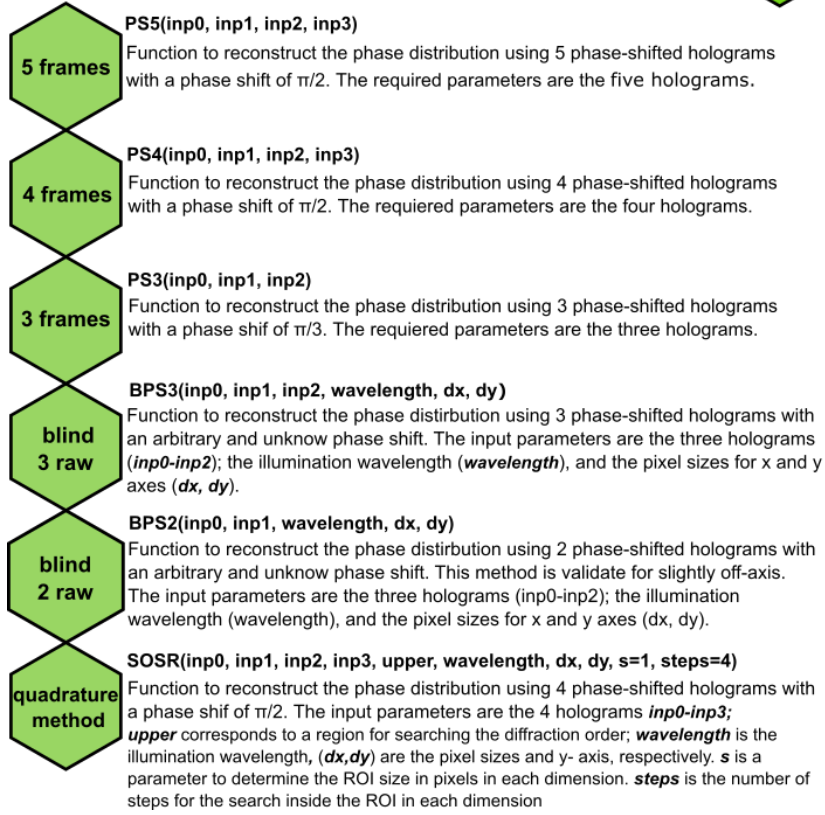


Fig. 6.3. Available functions in the phase-shifting package.

6.3.2 Package 2: Phase-shifting package

The second package in the *pyDHM* library contains the phase-shifting strategies for reconstructing the complex amplitude distribution in in-line and slightly off-axis systems: the following code line, *from pyDHM import phaseShifting*, calls this package. The package is composed of six different phase-shifting approaches: the traditional phase-shifting techniques in which the phase shifts are known using 5 (PS5), 4 (PS4), and 3 (PS3) phase-shifted images, which corresponds to 5 Frames, 4 Frames, and 3 Frames, whose mathematical equations are shown in Table 6.2. Besides, this package contains the quadrature PS method (SOSR), this method is based on the SOSR approach proposed by De Nicola *et al* [48], and two blind PS approaches using 3 (BPS3) and 2 (BPS2)

frames [41,73] for slightly off-axis DHM systems. The two blind PS approaches require a DHM operating in a telecentric regime. Figure 6.4 illustrates the different PS strategies implemented in the phase-shifting package, their definition line statement, and respective parameters. These {PS5, PS4, PS3} functions require the input (inp) of multiple phase-shifted holograms. The number of holograms and the phase shift value depend on the phase-shifting strategy used. For example, 5 holograms (e.g., inp0, inp1, inp2, inp3, inp4) are required with phase shift of $\pi/2$ (e.g., 0, $\pi/2$, π , $3\pi/2$, 2π) for the PS5 function. The phase shift in the PS4 algorithm is the same as the one from PS5. However, for the PS3 function, the phase shift is equal to $2\pi/3$. The SOSR strategy is based on the quadrature phase-shifting method proposed by De Nicola et. al [48]. The main difference between the original SOSR strategy and our implementation is that we have upgraded the method to automatically calculate the best digital reference wavefront to reconstruct fully compensated phase maps. The best digital reference wavefront is found using the ROI search [80]. The SOSR function requires 10 input parameters: 4 phase-shifted holograms with a phase shift of $\pi/2$; a True/False Boolean variable, *upper*, which is related to the position of the spectrum of the real image in the Fourier domain; *wavelength* is the wavelength of the illumination source used to record the hologram; *dx* and *dy* are the pixel sizes for both the input and output planes along the x- and y- directions; and *s* and *step* are two parameters for determining the ROI in the spatial frequencies domain for the compensation step. This ROI (centered at its brightest pixel) is gridded into a regular rectangular grid, whose size in pixels is given by $1+2s$ in each dimension. The number of points inside this grid in each dimension is given by *step*; these points are placed apart equidistantly. Therefore, $step^2$ is the total number of points to be used inside the ROI. For instance, if using $s=1$ and $step=4$, a 3x3 pixels ROI size with 16 points inside is selected. If using $s=2$ and $step=4$, a 5x5 pixels ROI size with 16 points is selected, implying that a larger ROI with a lesser

density of points will be used for the search. The user can adjust these parameters at will, considering that although a more accurate search can be performed by increasing their values, the procedure's computational complexity also increases. Finally, the parameters of the BPS3 and the BPS2 algorithms are the input phase-shifted holograms with arbitrary phase shift, and the wavelength of the illumination source and the pixel size along the x- and y-direction (e.g., dx and dy , respectively) to generate the digital reference wavefront and reconstruct fully-compensated phase maps. The variables (e.g., wavelength, dx , dy) in the functions should be inserted in the same units.

(a) Example code for the in-line PS strategies

```

1- # import packages
2- from pyDHM import utilities
3- from pyDHM import phaseShifting

4- #Load the holograms

5- inp0 = utilities.imageRead('holo1.jpg')
6- inp1 = utilities.imageRead('holo2.jpg')
7- inp2 = utilities.imageRead('holo3.jpg')
8- inp3 = utilities.imageRead('holo4.jpg')
9- inp4 = utilities.imageRead('holo5.jpg')

10- #Phase shifting using the PS strategies
11- output = phaseShifting.PS5(inp0,inp1,inp2,inp3,inp4)
output = phaseShifting.PS4(inp0,inp1,inp2,inp3)
output = phaseShifting.PS3(inp0,inp1,inp2)
12- #Display the phase reconstruction
13- phase = utilities.phase(output)
14- utilities.imageShow(phase, 'Phase reconstruction')

```

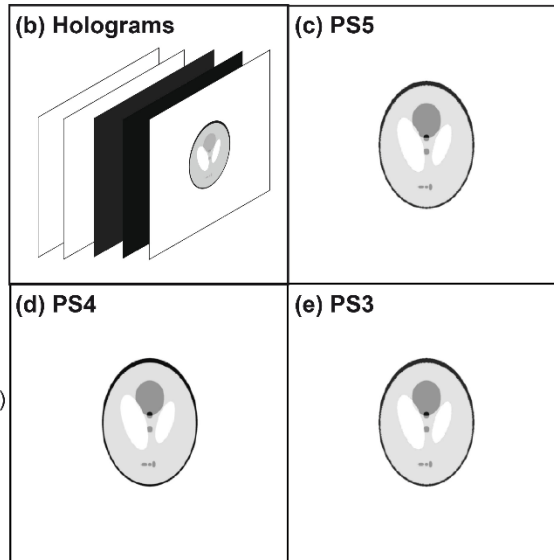


Fig. 6.4. Verification of the in-line PS function: (a) an example code; (b) simulated in-line DHM holograms of a phantom model. Panels (c) - (e) and the reconstructed phase images for the PS5, PS4 and PS3 strategies, respectively.

These six PS algorithms have been validated using simulated and experimental holograms. Figure 6.4 shows the code and an example for the PS5, PS4, and PS3 algorithms. The code starts importing the utility package and the PS package, lines 2-3 in Fig. 6.4(a). Lines 5-9 are the commands to read the phase-shifted holograms. For simplicity, we do not display any of these

input holograms. Line 11 calls functions to display the PS5, PS4 or PS3 implementation. Finally, line 13 is the command to display the phase distribution reconstructed by the selected algorithm. Figure 6.4(c) illustrates the reconstructed phase distribution from the simulated phase-shifted phantom hologram [Fig. 6.4(b)] recorded in an in-line DHM system with a phase shift of $\pi/2$. Figures 6.4(d) and (e) show the reconstructed phase images of the simulated phantom hologram using PS4 and PS3 functions, respectively.

The performance of the slightly off-axis PS strategies is evaluated using two different experimental samples. The SORS function is validated by reconstructing the phase image of a Fresnel lens with a phase shift of $\pi/2$ between holograms introduced by a liquid lens [131]. The sample used for validating the blind strategies (i.e., the BPS3 and BPS2 algorithms) is a phase USAF test target. Figure 6.5(a) shows the sample code to use the slightly off-axis strategy algorithms, see the Fourier spectrum of one hologram from the Fresnel lens in Fig. 6.5(b). Again, line 10 corresponds to the command for the slightly off-axis strategies (e.g., SOSR, BPS3, and BPS2) with their corresponding parameters. Figures 6.5(c) to (e) show the reconstructed phase images of the Fresnel lens and the USAF target with minimum phase distortions.

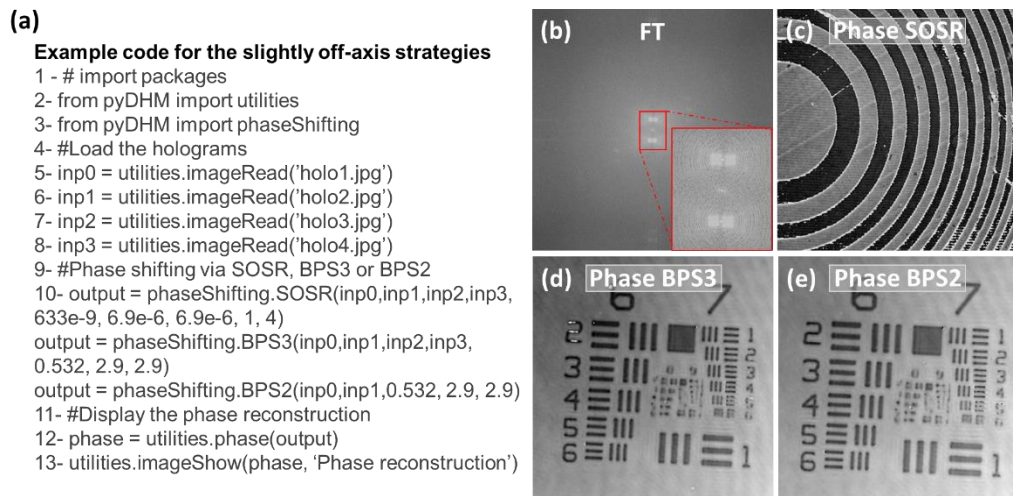


Fig. 6.5. Example of use of the slightly off-axis strategies. (a) a sample code; (b) FT of recorded hologram showing that the DHM system is operating in slightly off-axis configuration. Panel (c)

is the reconstructed phase image of a Fresnel lens by the SOSR function using four holograms with a $\pi/2$ phase shifting. Panels (d) and (e) are the reconstructed phase images of a USAF test target using the BPS3 and BPS2 strategies, respectively.

6.3.3 Package 3: Fully-compensate phase reconstruction package

The third package of the *pyDHM* library is devoted to the phase reconstruction of DHM holograms without or with minimal perturbations (e.g., fully-compensated reconstructed phase images without distorting sawtooth fringes) using an off-axis system. One includes the library *from pyDHM import phaseCompensation* line to call this package. This package implements four functions, three functions for holograms recorded in telecentric regime: the full-ROI-search (FRS) function, the efficient-ROI -search (ERS) function, and the cost-function-search (CFS) function. And one function for holograms recorded in non-telecentric regime, the compensation non-telecentric (CNT) function. Figure 6.6 shows the definition statement and a brief description of each package function. For example, the FRS function has seven input parameters: the off-axis hologram (*inp*), a True/False Boolean variable (*upper*) for choosing the region where the algorithm would find the maximum peak value of the +1 or -1 order for the filtering step. *Wavelength* corresponds to the wavelength used to record the hologram; *dx* and *dy* are the pixel size of the camera sensor for the acquisition of the hologram along the x- and y- direction, respectively, and *s* and *step* are parameters for selecting the search region to find the best phase reconstructed image. These parameters determine the ROI size and the number of points inside this search region. For example, if using *s* = 2 and *step* = 10, a 2×2 pixels ROI size with 100 spatial frequency locations is selected to search for the best phase reconstructed image [80]. For using the efficient ROI search, the EFR function must be executed. This function has the same parameters as the FRS function. To run the cost-function search, the CFS function must be called. The parameters for this function are *inp*, *wavelength*, *dx*, and *dy*. By the other hand, the CNT function contains 8

parameters. Whereas the first ones are *inp*, *wavelength*, *dx*, *dy*, already defined parameters, (x_1, x_2, y_1, y_2) are the pixels position to create a rectangular mask for filtering the +1 diffraction order, where (x_1, y_1) and (x_2, y_2) are the pixel position of the upper-left and bottom-right corner, respectively.

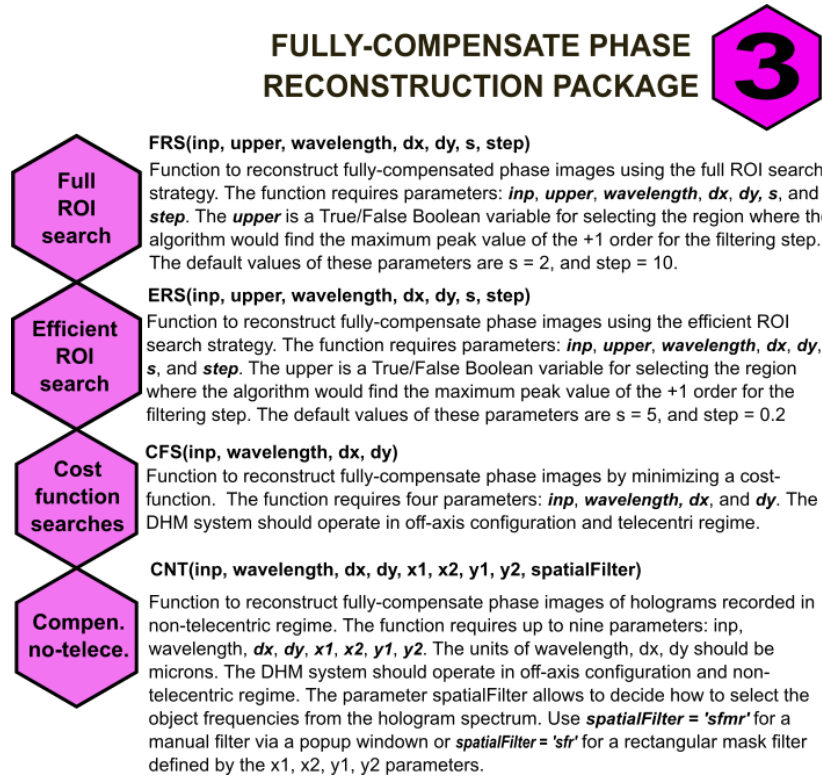


Fig. 6.6. Available functions in the fully-compensate phase reconstruction package.

Two examples are shown as examples for evaluating the performance of the fully-compensate phase reconstruction package using an off-axis DHM system operating in the telecentric regime. The *full* and *efficient ROI search* strategies have been validated using the hologram of a transverse section of the head of a *Drosophila melanogaster* fly [75]. The parameters of the DHM system to record this sample are wavelength $\lambda = 633$ nm and a camera with a pixel size $dx = dy = 6.9$ μm . The hologram of a phase star target has been used to validate the cost-function search strategy using $\lambda = 532$ nm, and $dx = dy = 2.6$ μm . These two holograms were recorded at the IP of the

microscope. Therefore, no refocusing step is necessary for the reconstruction stage. The sample code is shown in Fig. 6.7(a). The code starts with the import of the utility and the fully-compensated phase reconstruction packages; lines 2-3 in [Fig. 6.7(a)]. In line 5, the hologram is loaded. Line 7 calls the functions for reconstructing off-axis holograms in telecentric regimen: FRS, ERS, or CFS function. In Fig. 6.7(b), the common logarithm of the power spectrum of the hologram of a transverse section of the head of a *Drosophila melanogaster* fly is shown to demonstrate that an off-axis setup in telecentric regime is used. After applying the three different approaches in this package, the reconstructed phase images are illustrated in Fig. 5(c) – (e).

(a) Example code for the compensation strategies in telecentric regime

```

1- # import packages
2- from pyDHM import utilities
3- from pyDHM import phaseCompensation

4- #Load the hologram
5- inp = utilities.imageRead('hologram.jpg')

6- #Phase compensation using FRS, ERS, CFS
7- output = phaseCompensation.FRS(inp, True,
    0.633, 6.9, 6.9, 2, 10)
output = phaseCompensation.ERS(inp, True,
    0.633, 6.9, 6.9, 5, 0.2)
output = phaseCompensation.CFS(inp, 0.532, 2.6, 2.6)

8- #Display the phase reconstruction
9- phase = utilities.phase(output)
10- utilities.imageShow(phase, 'Phase reconstruction')

```

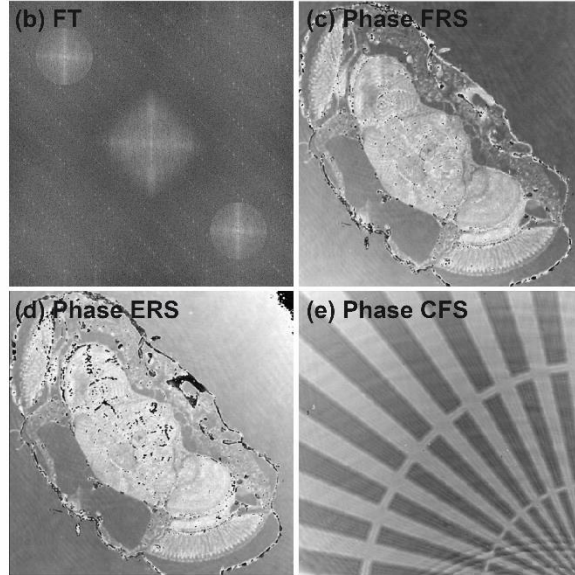


Fig. 6.7. Example of the fully-compensated phase reconstruction package for off-axis DHM holograms recorded in telecentric configuration: (a) a sample code; (b) FT of a recorded hologram to show that the DHM system operates in off-axis and telecentric configuration. Panels (c)-(d) are the fully-compensated reconstructed phase images of a *Drosophila melanogaster* fly using FRS and ERS functions. Panel (e) shows the fully-compensated reconstructed phase image of a star target using the CFS function.

Regarding the CNT function, a hologram of a *Drosophila melanogaster* fly recorded in non-telecentric regime has been used [75]. The parameters of the DHM system to record this sample

are wavelength $\lambda = 633$ nm and a camera with a pixel size $dx = dy = 6.9$ μm . The sample code is shown in Fig. 6.8(a). The CNT function allows the spatial filtering of the object frequencies from the hologram spectrum using a rectangular mask defined by their pixel corners (e.g., $x1$, $x2$, $y1$, and $y2$) or manually drawn using a popup window. Before running the CNT function with the spatial filter option *sfr*, the user may need to select the pixels position ($x1$, $y1$) and ($x2$, $y2$) of the rectangular mask to filter the +1 term. For this task, one should compute the Fourier transform of the hologram (line 7). Figures 6.8(b) and (c) show the Fourier transform and the binarized Fourier transform of the hologram. The latter display is recommended to select the positions of the rectangular mask, the red rectangle inside Fig. 6.8(c). Line 11 runs the CNT function using the two possible filter options (e.g., *sfr* and *sfrm*). When running this function, the binarized phase image is shown after compensating the interfering angle but without compensation of the quadratic phase factor [Fig. 6.8(d)]. Using this image, the user selects the central pixel position (X_cent , Y_cent) of the quadratic phase mask. After closing this image, the CNT function asks the user the values for this position: “Enter the pixel position X_cent for the center of circular phase map on x-axis,” and “Enter the pixel position Y_cent for the center of circular phase map on y-axis” for X_cent and Y_cent , respectively. The curvature of the quadratic phase factor is estimated by the size of the rectangular mask since the spreading of the +1 term and the curvature value are inversely related [38]. When these values are introduced, the search for the reconstructed phase image starts, providing the optimal reconstructed phase image with minimum phase distortions [Fig. 6.8(e)].

(a) Example code for the compensation strategy in non-telecentric regime

```

1- # import packages
2- from pyDHM import utilities
3- from pyDHM import phaseCompensation

4- #Load the hologram
5- inp = utilities.imageRead('hologram.tif')

6- #FT of the hologram
7- ft_holo = utilities.FT(inp)
8- ft_holo = utilities.intensity(ft_holo, True)
9- utilities.imshow(ft_holo, 'FT hologram')

10- #Phase compensation using CNT approach
11- output = phaseCompensation.CNT(inp, 0.633, 6.9,
    6.9, 200, 287, 180, 267, spatialFilter = 'sfr')
output = phaseCompensation.CNT(inp, 0.633, 6.9,
    6.9, spatialFilter = 'sfmr')

12- #Display the phase reconstruction
13- phase = utilities.phase(output)
14- utilities.imshow(phase, 'Phase reconstruction')

```

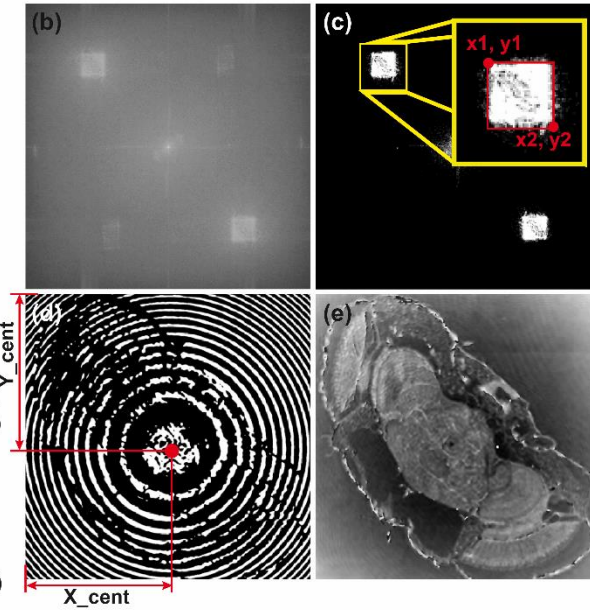


Fig. 6.8. Example of the CNT function for off-axis DHM holograms recorded in a non-telecentric configuration: (a) a sample code; (b) FT of a recorded hologram, notice that the hologram operates in off-axis and non-telecentric configuration. Panel (c) is the binarized image of the FT to select the dimensions of the rectangular filter with parameters (x1, x2, y1, y2). Panel (d) corresponds to the binarized reconstructed phase image after compensating the interfering angle, where X_cent and Y_cent positions are marked. Finally, panel (e) shows the reconstructed phase image of a *Drosophila melanogaster* fly with minimum phase distortions.

6.3.4 Package 4: Numerical propagation package

The final package in *pyDHM* is the numerical propagation package. This package allows the numerical propagation of the scalar complex diffractive wavefield at different propagation distances. The package is called by the following code line *from pyDHM import numerical Propagation*. The package implements three different propagators: angular spectrum (angularSpectrum), the Fresnel transform (fresnel), and the Fresnel-Bluestein transform (bluestein). Figure 6.9 shows the declaration statement and the parameters needed for each propagator. For example, the *angularSpectrum* and *fresnel* propagator functions have five parameters. *field* is the input complex wavefield to be propagated. The distance to propagate the input wavefield is represented by *z*. *Wavelength* is the wavelength of the illumination source used

to record the hologram. Finally, dx and dy are the pixel size for the input and output planes along the x- and y- directions. The *bluestein* propagator function has two additional parameters (e.g., $dxout$ and $dyout$) related to the pixel size at the output plane.

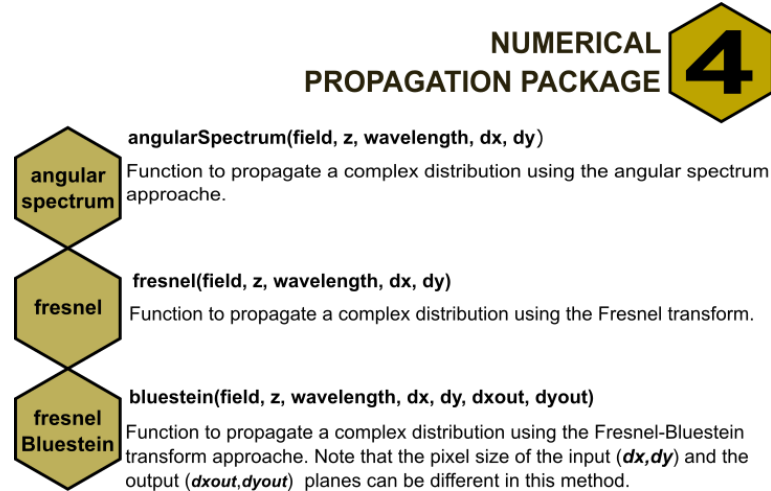


Fig. 6.9. Available functions in the numerical propagation package.

The evaluation of the numerical propagation package is shown in Fig 6.10. The focusing for a out-of-focus hologram of a USAF test target recorded in off-axis configuration is done using the *angularSpectrum propagator*. The hologram was recorded using a wavelength of 633 nm. The camera with a pixel size $dx=dy=6.9 \mu\text{m}$ was located approximately 3 cm from the back focal plane of the TL. Figure 6.10(a) shows a sample code. The code starts with the import of the utility, and the numerical propagation packages; see lines 2-3 in Fig. 6.10(a). In lines 5-6, the hologram is loaded and displayed [Fig. 6.10(b)]. The Fourier Transform of the hologram is computed (line 8) and displayed (lines 9-10) in Fig. 6.19(c). We have applied a circular mask (line 12) to filter the spatial frequencies of the object from the hologram spectrum [Fig. 6.10(d)]. Line 14 calls the angular spectrum function. Finally, lines 16-17 are used to show the reconstructed intensity image. Figs. 6.10(e)-(g) show the numerical intensity reconstruction for three different propagation

distance ($z = 0, 1$, and 3.3 cm). Inside each panel, the zoom-in rectangle areas highlight the effect of the propagation distance to focus the USAF target.

(a) Example code for propagation with angular spectrum

```
1- # import packages
2- from pyDHM import utilities
3- from pyDHM import numericalPropagation

4- #Load the hologram
5- input= utilities.imageRead('hologram.tif')
6- utilities.imageShow(input, 'Out-of-focus Hologram')

7- #FT of the hologram
8- ft_holo = utilities.FT(input)
9- ft_holo = utilities.intensity(ft_holo, True)
10- utilities.imageShow(ft_holo, 'FT hologram')

11- #Circular spatial filter
12- filter = utilities.sfc(input, 160, 303, 276, True)

13- #Propagation using the angular spectrum
14- output = numericalPropagation.angularSpectrum(filter, z,
        0.633, 6.9, 6.9)

15- #Display the output field
16- intensity = utilities.intensity(output, False)
17- utilities.imageShow(intensity, 'Output field')
```

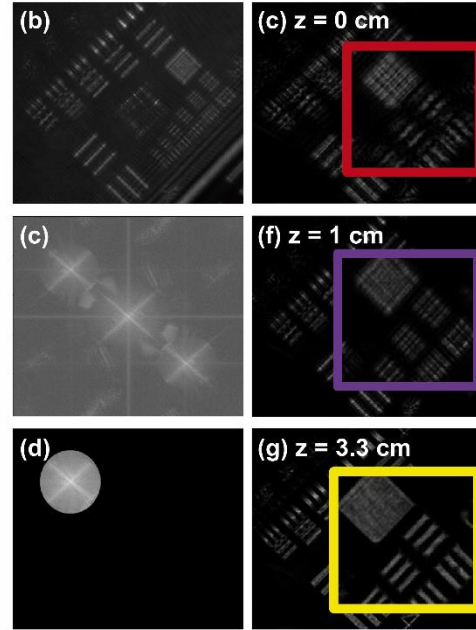


Fig. 6.10. Example of the angular spectrum approach to numerically focus a hologram using a circular spatial filter tool. Panel (a) is the sample code. Panels (b) show the hologram (c) its spectrum without (c) and with (d) a circular mask. Panels (e) – (g) are the reconstructed intensity images for three propagation distances (z).

Finally, the performance of the Fresnel and Fresnel-Bluestein transform propagators has been validated by propagating an experimental hologram recorded using a Mach-Zehnder interferometer [132]. A hologram of a horse model is used for the Fresnel propagator, whereas a 1cm edge dice is used for the Fresnel-Bluestein propagator. The sample code for the Fresnel and Bluestein propagators is shown in Fig. 6.11(a). Lines 2-3 are used to import the utility and numerical propagation packages. In lines 8-10, the computing and display of the Fourier transform of the hologram is implemented. In these examples, we have used a rectangle mask (line 12) to filter the hologram spectrum's object frequencies [Figs. 6.11(b) and (e)]. Lines 14 and 15 calls the Fresnel and the Bluestein propagators, respectively. The parameters for the horse model hologram

are $z = 45$ cm, wavelength = 633 nm, and $dx = dy = 5$ μ m. Figures 6.11(c)-(d) are the reconstructed amplitude images without [Fig. 6.11(c)] and with [Fig. 6.11(d)] spatial filtering of the object frequencies in the hologram spectrum. The reconstruction parameters for the dice hologram are $z = 30$ cm, $\lambda = 633$ nm, and $dx = dy = 7.4$ μ m. The most important feature of the bluestein function (line 15) is that the output pixel sizes (dx_{out} and dy_{out}) are required as input parameters. Therefore, one can control the magnification of the reconstructed image using the Fresnel-Bluestein approach by modifying the value of these parameters. For this example, the output pixel sizes have been adjusted to 14.8 μ m [Fig. 6.11(f)], and 18.5 μ m [Fig. 6.11(g)]. These values provide an effective lateral magnification of $2\times$ and $2.5\times$ to the output size of the original hologram.

(a) Example code for propagation with Fresnel and Fresnel-Bluestein transform

```

1- # import packages
2- from pyDHM import utilities
3- from pyDHM import numericalPropagation

4- #Load the hologram
5- input= utilities.imageRead('hologram.bmp')
6- utilities.imageShow(input, 'Out-of-focus hologram')

7- #FT of the hologram
8- ft_holo = utilities.FT(input)
9- ft_holo = utilities.intensity(ft_holo, True)
10- utilities.imageShow(ft_holo, 'FT hologram')

11- #Rectangular spatial filter
12- filter = utilities.sfr(input, 280, 500, 150, 340, True)

13- #Propagation using Fresnel transforms
14- output = numericalPropagation.fresnel(input, -450,
    0.000633, 0.005, 0.005)
    output = numericalPropagation.bluestein(filter, 0.03, 633e-9,
    7.4e-6, 6.4e-6, 1.48e-5, 1.48e-5)

15- #Display the output field
16- intensity = utilities.intensity(output, False)
17- utilities.imageShow(intensity, 'Output field')

```

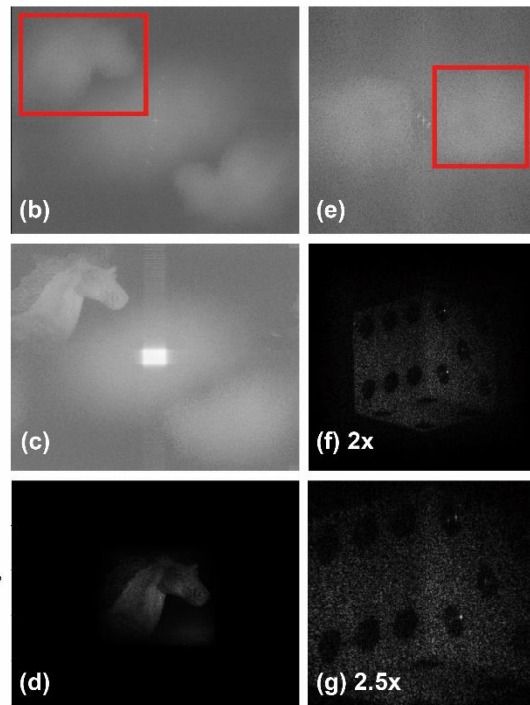


Fig. 6.11. Examples of the Fresnel and Fresnel-Bluestein propagation approaches to numerically focus holograms using a rectangular mask to filter the object frequencies from the hologram spectrum. Panel (a) is the sample code. Panels (b) show the hologram spectrum (b) and the reconstructed intensity image without (c) and with (d) a rectangular mask of a horse model using the fresnel propagator. Panels (e) – (g) are the hologram spectrum (e), and the reconstructed intensity images after filtering the object frequencies from the hologram spectrum using two

different magnifications [$2\times$ and $2.5\times$ in panels (f) and (g), respectively] for a 1-cm edge dice using the bluestein propagator.

6.4 Conclusion

This work presents the *pyDHM* library, a Python library for the numerical processing of digital holograms registered in DHM systems. The library contains different computational implementations for: (1) reading and showing the complex distribution of a sample (e.g., utility package); (2) performing numerical propagations of complex wavefields to provide in-focus DH and DHM images (e.g., numerical propagation package); (3) reconstructing the phase distribution of samples in in-line and slightly off-axis DH and DHM systems using PS techniques (e.g., phase-shifting package); and (4) reconstructing phase images in single-shot off-axis DHM systems operating in telecentric and non-telecentric configuration using automatic methods to estimate the best digital reference wavefront (e.g., fully-compensated phase reconstruction package). We have presented a sample code for each function implemented in the *pyDHM* library and validated its performance using simulated or experimental images. To increase the applicability of this library in our community, we have also included simulated and experimental holograms and some instructional videos on using the library. The *pyDHM* library is posted publicly on GitHub [42,133]. The GitHub repository includes complete documentation of the functions implemented, sample codes, and troubleshooting guidelines for correctly using the library. To increase the applicability of this library in our community, the GitHub repository also includes simulated and experimental holograms and some instructional videos on how to install and use the library [134–137]. In future works, we will expand the codes within our library and reduce its processing time using GPU implementations. Current implementations within the *pyDHM* library require that the users select the adequate reconstruction method based on the optical configuration

of the DHM systems. Future work will focus on an automatic algorithm to reconstruct DHM holograms without prior knowledge of the DHM configuration (e.g., only hologram, source's wavelength, and sensor's pixel size). Because of the broad applicability of DHM systems in biology and medicine, we will create a graphical user interface (GUI) for the pyDHM library, aiming that users who lack coding skills and background in Optics and DHM could adopt this library. Such an app will allow the users to input a single hologram or a sequence/video of holograms, enabling the processing of the whole hologram series. Some reprocessing steps will be avoided, such as selecting the spatial filter mask to optimize such video processing. Our final goal is to expand such app further so that pyDHM can be used to analyze biological systems, including motility analysis for microorganism tracking and cell counting.

7. LEARNING-BASED MODELS FOR VIDEO-RATE QUANTITATIVE PHASE IMAGING USING AN OFF-AXIS DIGITAL HOLOGRAPHIC MICROSCOPE

The conventional quantitative phase reconstruction methods in off-axis image-plane DHM rely on computational processing that involves the spatial filtering of the sample spectrum and the tilt compensation between the interfering waves to reconstruct the phase of biological samples accurately. An incorrect selection of the frequency components may lead to phase measurements that are not limited by diffraction (e.g., low-resolution images), and inaccurate tilting angle compensation could introduce errors in the quantitative phase measurements. Any DHM reconstruction algorithm should be automatic and adaptable to any sample and imaging conditions to increase its applicability in life and materials studies. One of the biggest challenges in DHM is the recovery of phase maps free of aberration at video rates, providing quasi-real-time data processing [138]. Regardless of the implementation, current DHM reconstruction methods present a long processing time of 2.95 seconds for an image with 2048x2048 pixels, hampering the use of DHM for video-rate renderings of dynamic biological processes. This chapter investigates deep learning (DL) approaches to reconstructing phase images in off-axis DHM. In particular, firstly, we have investigated a convolutional autoencoder (ConvA) using simulated and experimental data. Next, we implemented a conditional generative adversarial network (cGAN) for robust and fast quantitative phase reconstruction imaging in DHM.

This Chapter is organized as follows. In Section 7.1, there is a review of the state-of-art of DL approaches used in DH and DHM. Section 7.2 shows the implementation of a ConvA for obtaining amplitude and phase images using simulated and experimental data. In section 7.3, a cGAN model is presented and validate using experimental holograms of statics and dynamics RBCs. Section 7.4

is devoted to comparing the performance of the proposed cGAN model against the U-Net and autoencoder Models. In Section 7.5, we validate the generalization ability of the trained cGAN method regarding system diversity using DHM holograms were recorded in a common-path DHM system. Finally, in Section 7.6, we summarize the main achievements of the Chapter. This work has been published in Sensors [139], and presented in the 2021 IEEE Photonics Conference (IPC) [140]; the 2022 Optica Imaging and Applied Optics Congress [141].

7.1 Introduction

Despite the successful performance of DHM systems, its applicability to in situ clinical research has been partially hampered by the need for a standard phase reconstruction algorithm that provides quantitative phase distributions without any phase distortion [17]. Accurate phase measurements are imperative since variations in phase measurements are used as a diagnostic and measuring tool in life sciences [17,69,142]. As was explained in previous chapters, the DHM technology retrieves this phase distribution after applying a computational reconstruction approach. At present, individual DHM research groups have developed and implemented their numerical algorithms to reconstruct their phase images [17]. The DHM reconstruction algorithm should be automatic and adaptable to any sample and imaging conditions to increase its applicability in life and material sciences. Although several automated DHM reconstruction approaches have been proposed, see Chapters 4 and 6, often these proposals yield reconstructed phase images with phase nuisances, preventing any quantitative analysis. In addition, the computational complexity of all these methods still restricts the proper recovery of phase maps free of aberration at video rates, providing quasi-real-time data processing. In biological imaging, phase measurements enable estimating biological parameters such as the integral intracellular refractive index (RI) [27,86,143]. The phase value (ϕ) is proportional to the sample thickness (t)

and RI. Accurate phase and RI measurements are imperative since variations in RI values are used as a diagnostic and measuring tool in biological research [17,33]. RI can be used to determine cell biophysical parameters (such as dry mass and protein concentration) and to study certain cell metabolic activities (such as cell division and infection). For example, optical diagnosis of malignant tissues can be distinguished from healthy tissues by comparing their RI values. Since RI values could be used for cell morphology and growth in cell biology, disease diagnosis in hematology, and cancer cell and circulating tumor cell detection in pathology, accurate RI values are mandatory. Dr. Kedar Khare stated in [17] the need for standardization of phase estimation algorithms in digital holographic microscopy.

As in many areas of science and engineering, deep learning strategies have been used to improve the potential of DHM technology. Deep learning and neural networks have enhanced the performance of traditional reconstruction algorithms. For example, deep learning has been utilized to automatically determine the in-focus reconstruction plane in DHM [106,144] and obtain color holographic microscope reconstructions [145]. Yin *et al.* proposed a deep learning framework for a reflection digital holographic setup without a microscopic imaging system (e.g., lensless configuration) in which the sample information was loaded on a phase-only spatial light modulator (e.g., non-biological samples) [146]. In 2019, Rivenson *et al.* presented a neural network model to retrieve the amplitude and phase reconstruction for lens-free DHM systems [147]. The same year, Wang *et al.* proposed a different approach for retrieving the complex information (e.g., amplitude and phase) of holograms using a neural network based on the Y-Net model [148] in common-path microscopy. In 2020, Vijayanagaram implemented a neural network model based on a U-Net architecture for numerical reconstruction of artificially generated in-line holograms [149]. Recently, Di *et al.* proposed a powerful strategy for quantitative phase image by

implementing the PhaseNet convolutional neural network for reconstructing phase maps of size 128×128 recorded from a common-path digital holographic microscope in times of ~ 0.014 s (~ 71.43 fps) [150]. In a recent paper, Moon *et al.* experimentally validated a conditional generative adversarial network (cGAN) for removing superimposed noise in the Gabor (in-line) holograms of red blood cells and elliptical cancer cells; the proposed cGAN model required the processing of off-axis DHM holograms before training the learning-based model [151]. The cGAN reported in [151] was applied to noise removal, not phase reconstruction. The inputs to that cGAN were reconstructed phase images obtained using a Fresnel propagator. The aim of that work was not quantitative phase imaging in off-axis DHM. Ma *et al.*, proposed a two-stage generative adversarial network (GAN) to provide accurate phase maps in DHM [152]. The two-stage GAN required a preprocessing stage to remove the interference fringes of the sample that were in the DHM hologram by background segmentation. Then, the vacancy sample area was in painted with fringes generated by a deep learning algorithm prior to recovering the compensated phase maps. Since the implementation of the two-stage GAN was focused on a reflection (e.g., Michelson-based) DHM system, the model was not validated with biological samples. Although many studies have been reported involving deep learning models for holographic reconstruction, to the best of our knowledge, no learning-based method has been reported in the literature for full phase compensation (e.g., no phase aberrations) in transmission off-axis DHM using biological samples. In this study, a conditional generative adversarial network (cGAN) is presented. The cGAN is trained to reconstruct quantitative phase images free of aberration without the need for any pre- or post-numerical procedures, reducing the computational complexity of traditional reconstruction methods. Our cGAN reconstructs and compensates phase images from DHM holograms as inputs. The main differences (not the only ones) between our cGAN and the one

reported in Ref. [152] are: (1) the number of layers of the generator is different, since the size of the input images and the task to be performed are different; (2) The activation function of the symmetrical layers is different; (3) The authors used the structural similarity index to evaluate the performance of the trained network while we use two customized metrics focused on phase images with minimum phase aberrations and noise; and (4) the discriminator is difference (Markovian [146] vs. our CNN pathGAN discriminator).

7.2 ConvA framework and performance in off-axis DHM

7.2.1 ConvA framework

The first learning-based model investigated to reconstruct amplitude and phase images from raw holograms recorded in off-axis DHM systems is the convolutional autoencoder (ConvA). This DL approach (e.g., ConvA) is an unsupervised neural network (NN) that encodes features and structures from unlabeled data. Generally, the ConvA compresses the input data into lower-dimensional, retrieving the data from this representation. The ConvA model consists of two main parts: the encoder and decoder. Whereas the NN in the encoder learns to represent information using lower-dimensional representation to recreate the original input, the decoder recreates the high-dimensional data from the lower-dimensional representation [153]. Previous research studies have shown the application of ConvA to reduce noise [154,155]. However, in this contribution, we investigate the performance of a ConvA model to fully reconstruct amplitude and phase images from raw DHM holograms without the need for any spatial filtering process, thus reducing the computational complexity of the DHM reconstruction method once the ConvA model is properly trained. The structure of the proposed ConvA model is depicted in Fig. 7.1. The encoder part of this model is composed of three convolutional layers, with 256, 128, and 64 filters, each having a stride of 2 pixels. Finally, a flattened layer is added to transform the bi-dimensional information

obtained by the stack into a one-dimensional vector, which is further summarized by a latent layer of 512 neurons. As expected, the decoder part of the model is a mirrored version of the autoencoder resulting in an output grayscale image of 256×256 pixels. The training of this model was performed via a logarithmic loss function with a batch size of 16 images, a gradient descent optimizer. The epochs differed from amplitude and phase imaging, being 20 for amplitude reconstructions and 30 for phase reconstructions. These epochs were estimated by calculating the MSE between the true and predicted image during the validation. The ConvA model was implemented in Python 3.7.6, and the libraries of Keras and TensorFlow were used.

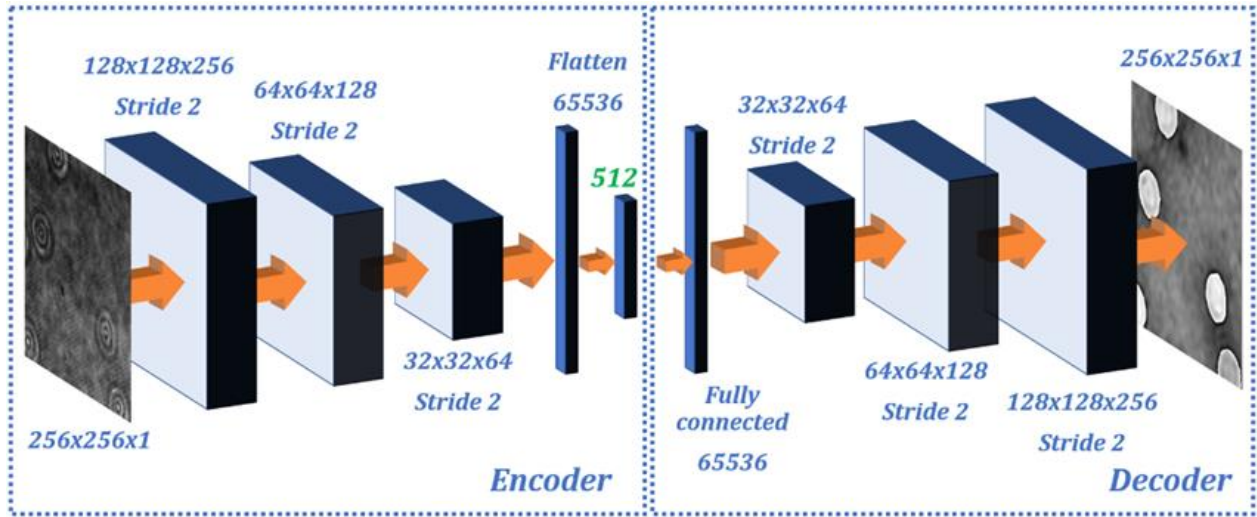


Fig. 7.1. The convolutional autoencoder (ConvA) structure for amplitude and phase imaging in off-axis DHM.

7.2.2 Performance of ConvA model using simulated data

Initially, due to the lack of an accessible database of biological off-axis holograms, we tested the performance of the ConvA model for reconstructing amplitude and phase information using simulated data. We created a simulated database mimicking the recording of in-focus holograms using an off-axis DHM system. The simulated biological samples consist of six different cells [A,

B, C, D, E, and F in Fig. 7.2(a)], located at random spatial positions within an imaged field of view of 256×256 pixels. To simulate a realistic distribution of the cells, the density of cells ranges from 3 to 8 cells within the field of view, see raw cell distributions in Fig. 7.2(b). Finally, simulated off-axis holograms were generated by interfering with a uniform plane wave and the object beam in which its phase information is the distribution of the cells. Considering that the change of the interfering angle (e.g., the tilt of the uniform plane wave) yields a different set of reconstruction parameters, the simulated holograms were generated using different interfering angles between the object and reference beams, see Fig. 7.2(b). Note that we always guarantee the off-axis architecture (e.g., not overlapping between the diffraction orders in the hologram's spectrum). A total of 4,338 simulated off-axis holograms were created. Each hologram was reconstructed to generate the corresponding amplitude and phase images using the automatic method proposed by Trujillo *et al.* [80]. 80% of this dataset was used to train the ConvA network, and the remaining 20% was used to test its performance.

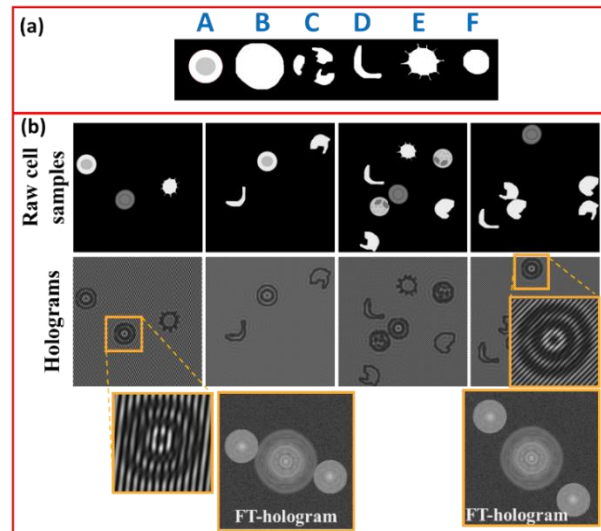


Fig. 7.2. Simulated holograms of six different types of cells. (a) Simulated cells' distribution used as phase information; (b) raw off-axis holograms generated by the coherent interference between the simulated cells' distributions in (a) and a tilted uniform plane wave. The interference angles in

the holograms are diverse to increase the method's applicability. The size dimension of each sample is 256×256 pixels.

Figure 7.3 shows the reconstructed amplitude and phase images of the three cells' distribution from the testing dataset (e.g., unseen data during the training) after training the ConvA model. The reconstructed amplitude images are shown in the top row of Fig. 7.3 (green rectangle), and the bottom images in Fig. 7.3 are the reconstructed phase images (red rectangle). Figures 7.3(a) and (d) are the true amplitude and phase images. Figures 7.3(b) – 7.3(e) are the reconstructed amplitude and phase images using the conventional method [80]. Finally, Figs. 7.3(c) – 7.3(f) are the reconstructed amplitude and phase using the trained ConvA model. Clearly, both amplitude and phase images look alike. We have compared the accuracy of the ConvA model to reconstruct amplitude and phase images using raw holograms by measuring the minimum square error (MSE) between the conventional reconstructed images and the predicted. The MSE value was below 0.0005 (e.g., 2.3591×10^{-4} for reconstructing amplitude images and 1.1584×10^{-4} for phase imaging), validating the performance of the ConvA model to reconstruct simulated noiseless holograms.

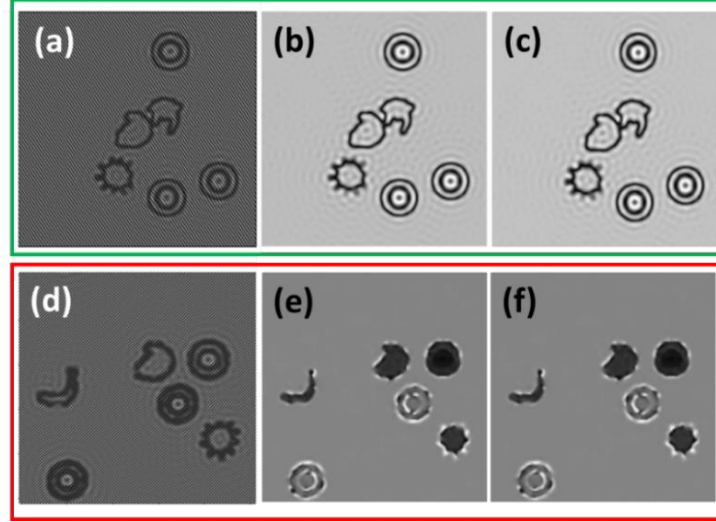


Fig. 7.3. Comparison between the reconstructed amplitude (top row) and phase (bottom row) images using unseen dataset. First column: true images. Second column: amplitude and phase images reconstructed using the conventional method. Third column: amplitude and phase images generated by the trained ConvA model.

7.2.3 Performance of ConvA model using experimental data

Next, we validated the performance of the ConvA model using experimental data. For this reason, we have set up a traditional Mach-Zehnder off-axis DHM system, Fig. 7.4(a), to record experimental holograms. In this setup, the light source is a 532-nm diode laser, which is expanded and collimated by a beam expander and then divided into two waves by a first beam splitter. The object wave illuminates the sample after being reflected by a plane mirror. The light scattered by the specimen is collected by an imaging system 40 \times /0.65NA infinity-corrected MO lens and a tube lens TL of focal distance $f_{TL} = 200$ mm. The MO and TL lenses operate in the telecentric regime to avoid spherical aberrations introduced by the optical configuration. On the other hand, the reference wave propagates with no perturbations to the second beam splitter after being reflected by a plane mirror, where this wave is recombined with the object wave to create the off-axis DHM hologram finally. In this configuration, the off-axis angle between the interfering waves is adjusted by tilting the mirror in the reference arm or the second beam splitter. The hologram is recorded by

a CMOS sensor of 1920×1200 square pixels with a $5.86 \mu\text{m}$ side. The CMOS sensor is located precisely at the back focal plane of the tube lens (e.g., IP of the microscope), recording in-focus holograms.

A microscopic slide containing normal (healthy) human red blood cells (RBCs) from Carolina Biological Supply Company (item #C25222) is used to create our experimental dataset to train and validate the proposed learning-based methods. Although these RBCs present some absorption, they can be considered phase objects when no staining is applied. Unstained RBCs have been widely imaged in DHM, enabling the detection of malaria [31,32] and screening of diabetes [33], and sickle cell anemia [24], as well as other inherited anemias [34].

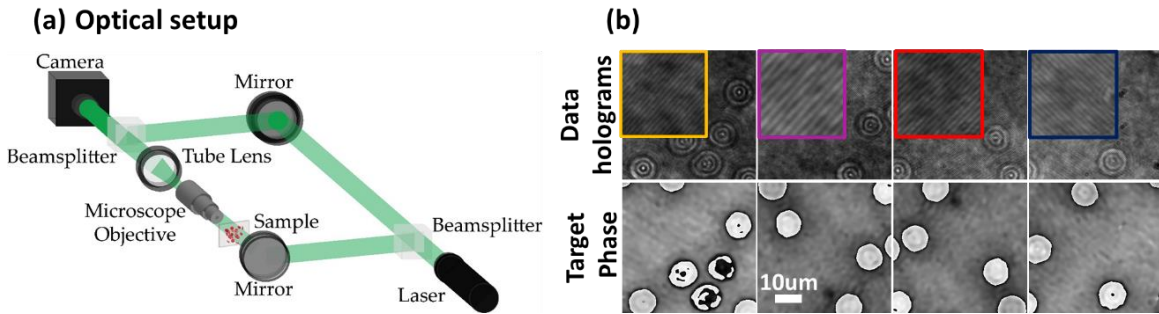


Fig. 7. 4. Illustration of the RBC dataset: (a) Conventional off-axis Mach–Zehnder DHM setup operating in telecentric regime. Input holograms after image orientation; and their respective phase maps reconstruction. The colors squares are used to illustrate the tilt of the interference fringes.

To create a dataset of DHM holograms and their corresponding fully compensated phase reconstructions, the following procedure is executed: i) a sample of unstained red blood cells is placed at the sample plane of the DHM setup and a total of 120 records are done, Fig. 7.4(b). The recorded holograms were augmented via image orientation by rotating the holograms randomly in 90 or 180 degrees and applying data augmentation a total of 858 holograms were obtained. ii) For the DHM hologram obtained in i), a fully compensation and phase reconstruction process is

performed using a computationally faster version of [80] (reference method). iii) Finally, sections of 256×256 pixels are cropped from every obtained hologram and their respective phase map, Fig. 7.4(b). to make up the database.

Our dataset is composed of raw DHM holograms and their corresponding reconstructed phase images. The procedure to create this dataset is the following. A microscopic slide containing unstained red blood cells is placed at the sample plane of the DHM system. We have recorded a total of 120 different in-focus DHM holograms, Fig. 7.4(b). The recorded holograms were augmented via image orientation by rotating the holograms randomly in 90 or 180 degrees. After this data augmentation, a total of 858 in-focus RBCs holograms were obtained. We have reconstructed the quantitative phase images of these holograms [second row in Fig. 7.4(b)] using an optimized version of [80]. After reconstructing the holograms, each pair of holograms and reconstructed phase images are cropped into patches of 256×256 pixels. Based on the camera specifications, each pair of holograms and reconstructed phase images is divided into 28 pairs of images (i.e., holograms and reconstructed phase images) to generate an experimental dataset of 1,820 instances.

The results of the learning-based ConvA model after its proper training are illustrated in Fig. 7.5. Figures 7.5(a)-(d) show four different holograms of the validation dataset. These holograms [Figures 7.5(a)-(d)] present different experimental conditions, such as the presence of dust in the sample, some defocusing effects, and changes in the background intensity. The latter may be related to temporal fluctuations in the experimental conditions from the illumination source and/or the implementation of the system. Whereas panels (e-h) in Figure 7.5 [second row] show the reconstructed phase images for the conventional method [80], panels (i-l) are the reconstructed

phases for the ConvA model [third row]. Apart from the presence of some noise in the RBCs' edges, the ConvA model can recover the phase information of the RBCs. Even note that some detailed features inside the RBCs, highlighted by the green circles, are retrieved by the ConvA model. The ConvA method also reduces the background noise in the phase reconstructions, as it can be visually validated within the regions encircled by the red lines. Moreover, the blue circles show that the proposed ConvA learning-based model properly reconstructs the information of some cells that are incorrectly imaged by the conventional method. This failure of the traditional approach is due to the illumination inhomogeneities for different regions of the acquired DHM holograms. After training the model, the convolutional autoencoder requires 5 ms to compute a phase map of 256×256 pixels running on a personal computer powered by an Intel Core i7-8700 @ 3.20GHz. The conventional method requires 35 ms to reconstruct the same image using the same laptop, leading to a 7-fold reduction in time achieved by the ConvA model. In summary, the ConvA method recovers the phase information of biological samples accurately from a single DHM hologram with reduced computational complexity.

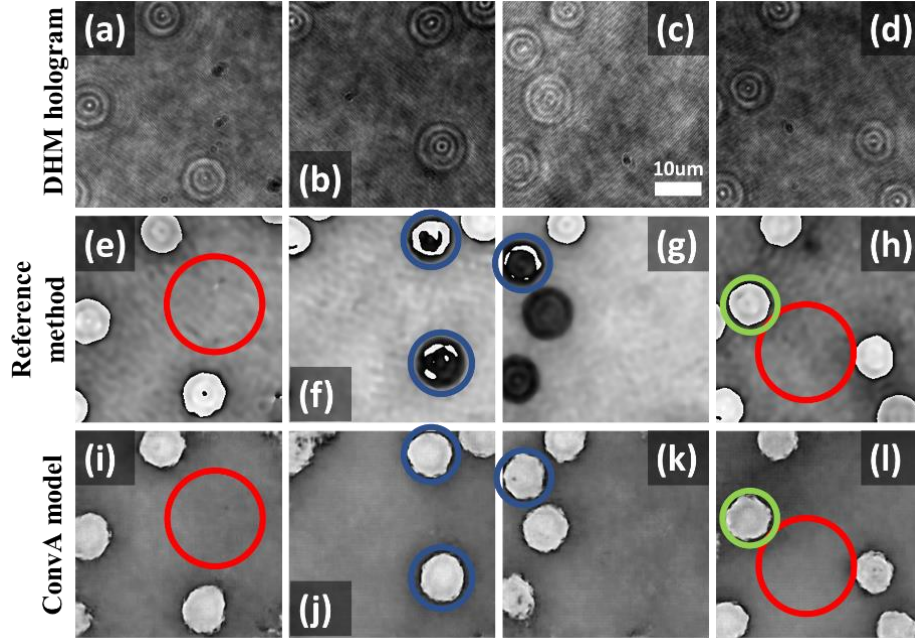


Fig. 7.5. Results of the proposed ConvA method applied to RBCs sample in DHM. Panels (a–d) are the DHM holograms. Panels (e–h) are the phase results obtained via the reference method [80]. Panels (i–l) show the phase map obtained by the proposal method. The colored circles in panels (e–l) show differences between the reconstructed phase images; see text for further details.

7.3 cGAN and performance in off-axis DHM

Despite the success of the ConvA model in reconstructing phase images, the convolutional encoder introduces some noise in the cells' edges, reconstructing RBCs with irregular shapes. For this reason, we have investigated the performance of a conditional generative adversarial network (cGAN) to reconstruct quantitative phase images free of aberration without needing any pre- or post-numerical procedures.

7.3.1 cGAN framework

The structure of the cGAN model for image-to-image translation (pix2pix cGAN [156]) is depicted in Fig. 7.6. This cGAN model comprises two submodules: a generative model and a discriminator model. The pix2pix cGAN refers to a type of cGAN neural network that learns to

map from an input image, generating an image that is conditional on the discriminator. The discriminator must establish if the output image from the generator is a believable alteration of the input image.

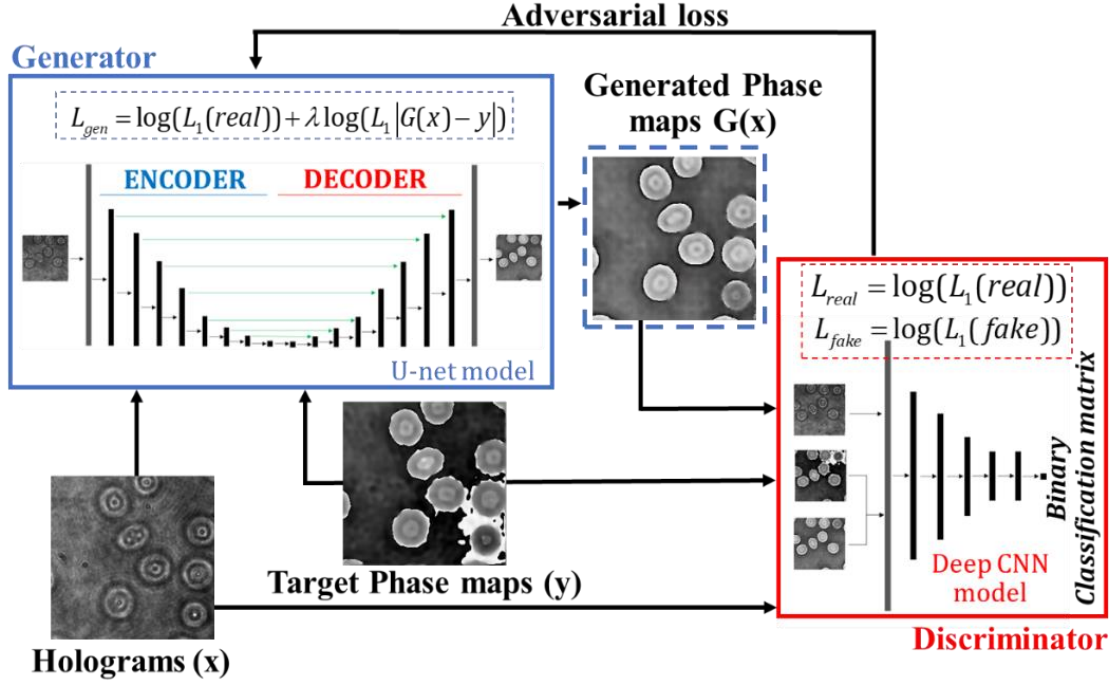


Fig. 7.6. Structure of the image-to-image translation conditional generative adversarial network (pix2pix cGAN) for reconstructing quantitative phase images in off-axis DHM. See text for further details.

The generative model produces free-of-aberration phase maps given DHM holograms as inputs. The supervised training of this submodule is defined by a weighted sum of two loss functions. The first function is an L1 loss which penalizes the difference between the model's generated reconstructed phase maps, $G(x)$, and the traditional method's target reconstructed phase maps, y . The second function is the adversarial loss from the discriminator model. The discriminator model is trained to determine whether the generator has built an input phase map (i.e., yielding to a fake/artificial signal) or a target phase map (i.e., an actual signal). The factor λ is fixed as 100 to

favor the L1 loss $|G(x) - y|$ during training [156]. This parameter encourages the generator to produce plausible translations of the DHM holograms, not just plausible phase maps in the target domain. The models were trained with the Adam version of the stochastic gradient descent [157] with a small learning rate of 0.002 during 100 epochs.

A U-Net architecture [158] was used as the generative model because it accurately reconstructs high spatial frequencies features [159]. The hallmark of the U-Net model is an accurate reconstruction of the phase values in those regions where the sample presents sharp jumps, such as the edges of the RBCs. The U-Net structure is based on a traditional bidimensional convolutional autoencoder for image-to-image translation with skip connections, Fig. 7.8. The additional skip connections between asymmetrical layers in the U-Net structure guarantee that the bottleneck of the autoencoder structure can be circumvented. In other words, the skip connections shuttle the low-level information of the input DHM holograms directly across the network [159]. The model's encoder part comprises eight convolutional layers with a 2-pixel stride in each dimension to downsample their feature size from 256×256 to 1×1 . The number of filters in these convolutional layers was increased from 64 to 512 to account for the information from the datasets. The decoder part of the model is almost a mirrored version of the encoder. The differences between the encoder and decoder parts are the transpose bidimensional convolutional layers and the implemented dropout layers after its first four layers. The output in the generator model is a $256 \times 256 \times 3$ entries array produced with a final hyperbolic tangent activation function which presents better results for different GAN architectures.

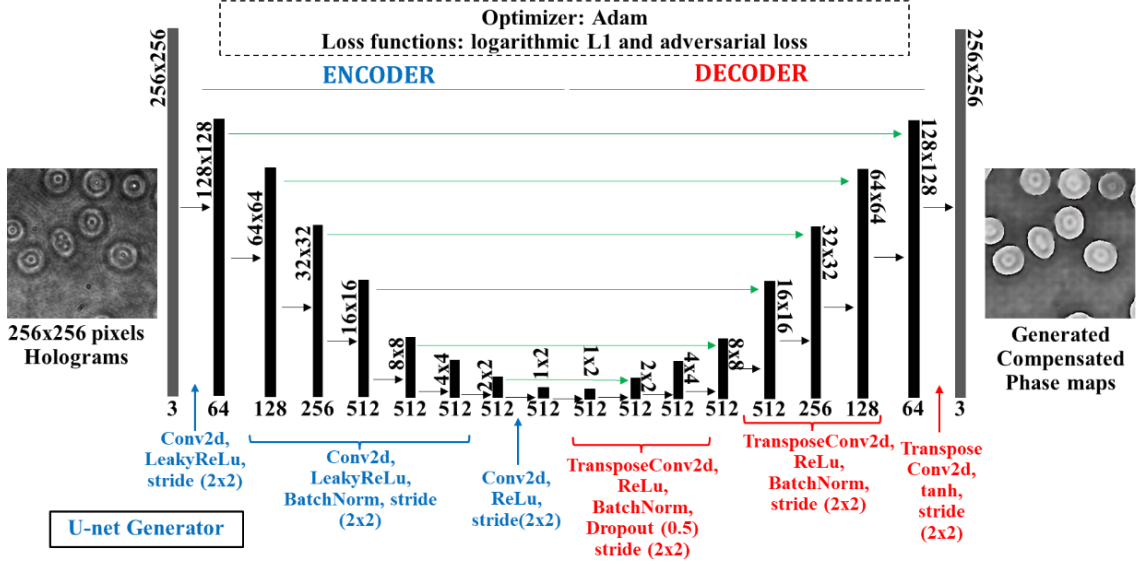


Fig. 7. 7. Structure of the U-net model used for the proposed cGAN.

In the proposed cGAN architecture, the discriminator model is a deep convolutional neural network for binary classification. Each input to this model is a pair of an off-axis in-focus DHM hologram and its corresponding phase image concatenated horizontally in a $256 \times 256 \times 6$ entries array. This patchGAN discriminator [51] processes 70×70 pixel regions of the input images, and the results of all patches are averaged to obtain an overall classification outcome for the input image. The model consists of six bidimensional convolutional layers in which the stride is fixed at 2 in each dimension to down sample the feature maps size after each convolution, Fig.7.7. The activation function of the first five layers is the LeakyReLU [160] to avoid blockage during training due to negative values in the input signals. In layers 2 to 5, batch normalization is also applied over every instance. The number of feature maps increases in each of these convolutional layers up to 512 to adjust the complexity of the model according to the data.

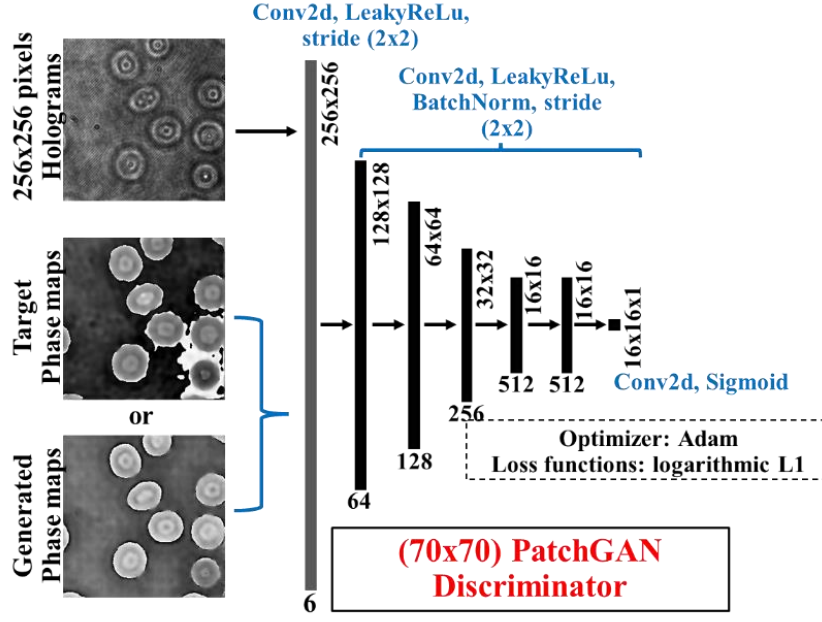


Fig. 7.8. Structure of the discriminator model used for the proposed cGAN.

Since the composite loss functions of the GAN models do not converge, due to the adversarial fitting of the two involved sub-models, customized metrics must be used to guide the proper training of this learning-based proposal. Two metrics were selected in every epoch of the training stage to quantify the method's performance at reconstructing phase maps without phase perturbations from raw DHM holograms. The first metric was a thresholding-and-summation metric (TSM) which accounted for phase discontinuities in every generated phase map. Whereas distorted phase images in DHM generate threshold phase images with a mix of black and white pixels [80], the reconstructed phase image without phase aberrations is the one whose threshold phase image is white (i.e., all pixels in the threshold phase image should be one). Therefore, the customized metric (TSM) counted the number of black pixels in the binary phase image is

$$\text{TSM}[\hat{h}_{nor}(m,n)] = 1 - \frac{1}{M \times N} \sum_{m=0}^M \sum_{n=0}^N \text{Thres}[\hat{h}_{nor}(m,n); 0.2]. \quad (7.1)$$

In Eq. (7.1), \hat{h}_{nor} stands for the normalized reconstructed phase map generated by the method in every training step; m and n are integer numbers running from 0 to M and N , respectively; M , and N are the number of pixels in each dimension of the output phase image, which coincides with the dimensions of the input hologram; $Thres[\bullet]$ represents a thresholding operator that converts each image pixel value larger than 0.2 into one, otherwise zero [80]. Figure 7.9(a) shows the plot of the average TSM values measured from reconstructed phase maps generated by the model for the full training (orange curve) and validation (blue curve) DHM holograms. Fig. 7.9(a) shows that the normalized TSM for the validation dataset does not change considerably after the 10th epoch. Therefore, the network has converged in terms of the number of reconstructed phase discontinuities after the 10th epoch. Figure 7.9(c) shows a set of generated phase maps at different epochs for the same hologram of the validation dataset. The proposed model reconstructed the phase discontinuities correctly after reaching the convergence.

The second customized metric Involved measurement of the standard deviation (σ) inside one background region of the phase maps (i.e., an area in which the phase measurement is constant). For simplicity, the region must be selected where no RBCs is present in the reconstructed phase images. An example of the region chosen to calculate the σ value is shown in Fig. 7.9c; see the area enclosed by the blue square. This metric was calculated only for 15 generated phase maps per dataset, which provided a good representation of the σ metric for the whole dataset. Fig. 7.9c plots the average σ values for the selected 15 phase maps per dataset. The σ metric allows quantifying the noise of the generated phase images, which must converge (i.e., the σ value is as low as possible) after the proposed method is adjusted correctly. According to this metric, the generated phase maps for the validation dataset present the minor noise level at the 12th epoch. After this

point, the σ value starts increasing again. The average metric converges at the 12th epoch for the training dataset. Nonetheless, after this epoch, the model appears to start overfitting. Overfitting in supervised learning occurs when the tendency of the model's performance on the training data diverges from the performance of the model on the validation data. The latter implies that the model is being fine-tuned to predict the training samples while at the same time it is failing to adequately predict the validation samples, which are the actual targets of the learning procedure. Therefore, considering that the model presented the least noise level at the 12th epoch, and the normalized TSM had already converged, we concluded that the best-fitted model coefficients for our learning-based method were found at this epoch (i.e., the 12th epoch).

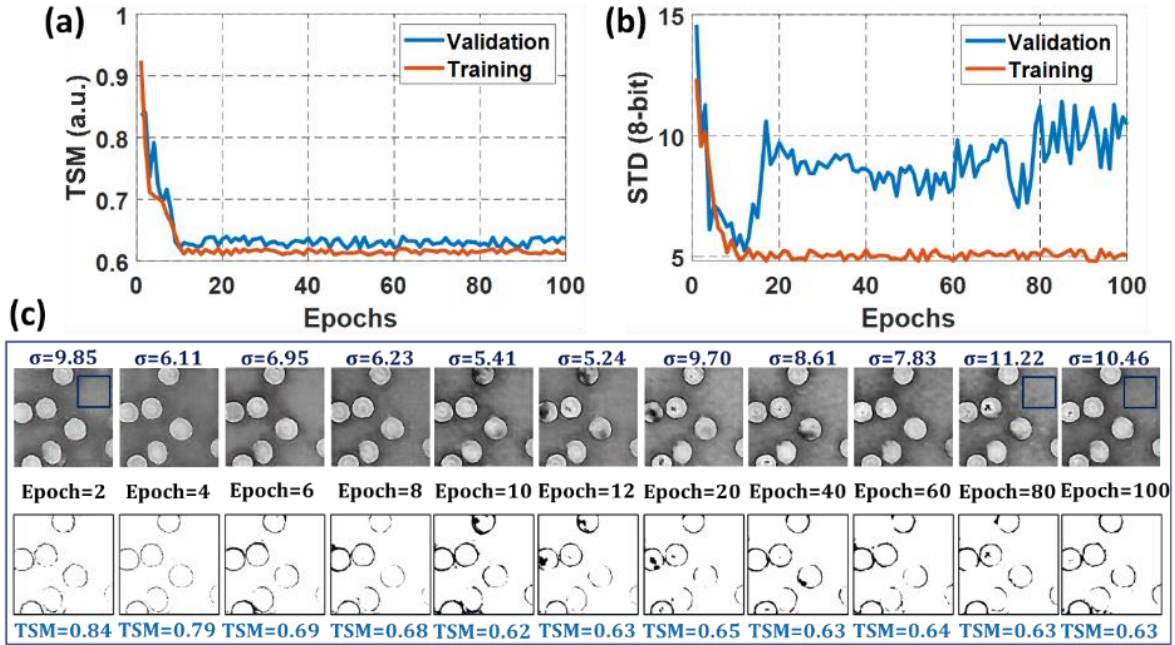


Fig. 7.9. Performance of the cGAN model for the training and validation dataset: (a) The average TSM value of the reconstructed phase maps measured for the complete validation and training dataset; (b) the average STD values for the background regions of the selected 15 phase images per dataset; (c) reconstructed phase maps of the identical hologram of the validation dataset provided by the proposed cGAN model at different epochs.

7.3.2 Experimental results

Once the generator was adjusted correctly within the GAN training, the learning-based model is used to reconstruct free-of-aberration phase images of static and dynamic human RBCs from experimental holograms recorded in an off-axis telecentric DHM system. To use the proposed learning-based method, a sample code to reconstruct quantitative free-of-aberration phase images from RBC holograms recorded in an off-axis telecentric-based DHM is freely available in Ref. [161]. The model in this repository contained the weights yielded during the training stage described in Section 7.3.1 and used in this section to retrieve the reported results. Therefore, any user can use this implementation to process off-axis diffraction-limited DHM recordings without needing further fitting stages or robust pre- or post-processing procedures. Note that it is only required to match the field of view between the input hologram and the one used to train the network.

In our first experiment, we have compared the performance of our learning-based cGAN model, after proper training, to that of the traditional reconstruction method [80] to analyze human RBCs in static conditions, see Fig. 7.10. For the comparison, four different holograms were randomly selected from the validation dataset, see Figs. 7.10(a)–(d). Again, these holograms present different experimental conditions, marked by magenta dashed rectangles, such as the presence of dust in the sample, some defocusing effects, and changes in the background intensity. The latter may be related to temporal fluctuations in the experimental conditions from the illumination source and/or the implementation of the system. Whereas panels (e-h) in Fig. 7.10 (second row) show the reconstructed phase images for the conventional method, panels (i-l) are the reconstructed phases for the proposed learning-based method (third row). Based on these results, our proposed cGAN model achieves similar performance as the traditional reference method [Figs. 7.10(e) –(h)]. However, the conventional method introduces some random phase distortions in some holograms,

reconstructing low-quality phase images [Figs 7.10(f) – (g)]. Contrarily, the cGAN model reconstructs these quantitative phase maps successfully without undesired phase distortions [Figs 7.10(j) – (k)]. The colored arrows in these panels show other differences between the reconstructed phase images. For example, the green arrows indicate background regions in the reconstructed phase images with different phase values. Whereas the conventional method fails to quantify the background phase level correctly, the proposed method successfully provides a homogeneous background level for most testing DHM holograms. The blue arrows highlight RBCs whose phase distribution presents some distortions in the traditional method. The poor reconstruction performance of the conventional approach is related to the reliance on the estimated parameters of the digital reference wavefront to the temporal fluctuations in the experimental recording conditions. Although the performance of the cGAN method seems superior, the cGAN model introduces some blurring effects when reconstructing the contour of some RBCs, as the red arrows show.

For a better comparison of the differences between the reconstructed phase maps produced by the traditional reference method [Fig. 7.10(e)–(h)] and the cGAN model [Fig. 7.10(i)–(l)], we have measured the two customized metrics described in Section 7.3.1 (i.e., the TSM and σ). The values of these two metrics are reported below each phase map image, Figs 7.10(e)–(l). Based on the reported TSM values, the cGAN model reconstructs phase images with lower TSM values than those obtained by the conventional method. Equation (7.1) shows that the best-reconstructed phase image (i.e., phase image with minimum phase aberration) provides the lowest TSM value. Regarding the σ value, the metric was measured in the region highlighted by the yellow rectangle in panels (e)–(h) of Fig. 7.10. Based on the reported σ values, the cGAN model reconstructs phase images with lower σ values than those obtained by the conventional method. These results allow

us to conclude that the performance of the proposed learning-based method is better in terms of the quality of the reconstruction (i.e., minimum phase aberration and reduced background noise).

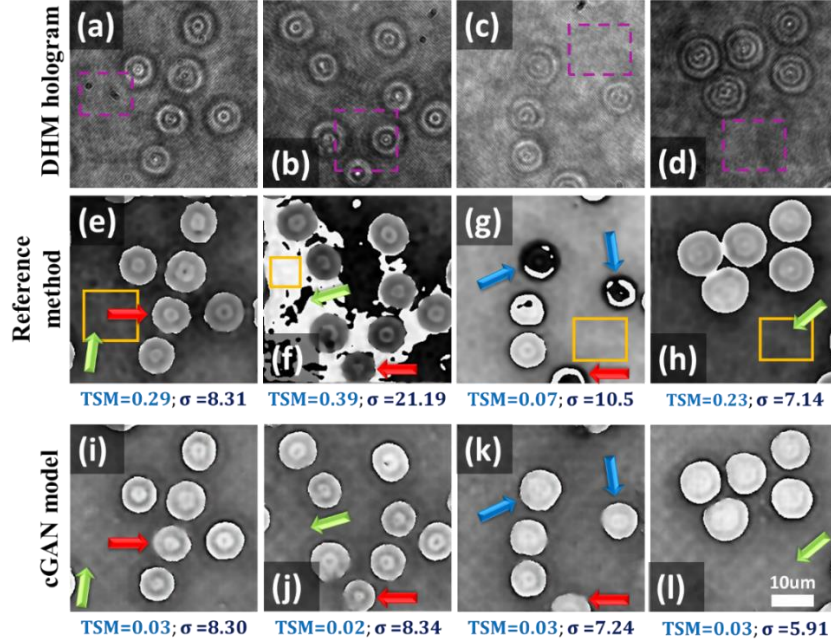


Fig. 7.10. Results of the proposed learning-based method for aberration-free phase reconstruction of RBC samples in DHM. Panels (a–d) are the DHM holograms, illustrating different experimental conditions, marked by magenta dashed rectangles. Panels (e–h) are the results obtained via the conventional method. Panels (i–l) show the phase map obtained by the proposal cGAN model. For the whole set of phase maps presented their σ and TSM values were computed and reported below each phase map image. The colored arrows in panels (e–l) show differences between the reconstructed phase images; see text for further details.

We have compared the highest- and the lowest-quality reconstructed phase images provided by the conventional reference method to those obtained by the cGAN model to further validate of method performance for the static holograms. Figure 7.11 shows the unwrapped reconstructed phase images and their corresponding 3D topographical view. We have used the Goldstein algorithm to unwrap the reconstructed phase images is used [162]. The unwrapped phase values (φ) have been converted in RBC's thickness (t) via $\varphi = 2\pi t / [\lambda_0(n_s - n_m)]$ where $\lambda_0 = 532$ nm is

the illumination wavelength, $n_s = 1.406$ is the RBC refractive index [163], and $n_s = 1$ is the surroundings' refractive index. As Fig. 7.11 shows, both methods provide similar results for the highest-quality reconstructed phase image reconstructed by the reference method [Figs. 7.11(a)–(f)]. However, the cGAN model achieves improved results for the lowest-quality phase map reconstructed by the conventional method, comparing Fig. 7.11(g)–(i) versus Fig. 7.11(j)–(l). Note that the presence of phase aberrations in Fig. 7.11(g) leads to reconstructing an RBC with negative optical thickness with respect to the background phase level. Quantitatively, the optical thickness of an RBC is around $0.8 \mu\text{m}$, as was previously reported via a phase-shifting DHM [131]. Whereas the cGAN method provides RBCs with an optical thickness of around $0.8 \mu\text{m}$ in Figures 7.11(f) and 7(l), the optical thickness of the RBCs in Figure 7.11(i) is around $1.5 \mu\text{m}$. Apparent morphological changes are introduced by the erroneous reconstruction of the phase image provided by the reference method. This inaccurate result could lead to misleading sample identification, illness screening, or other diagnostics based on quantitative phase imaging.

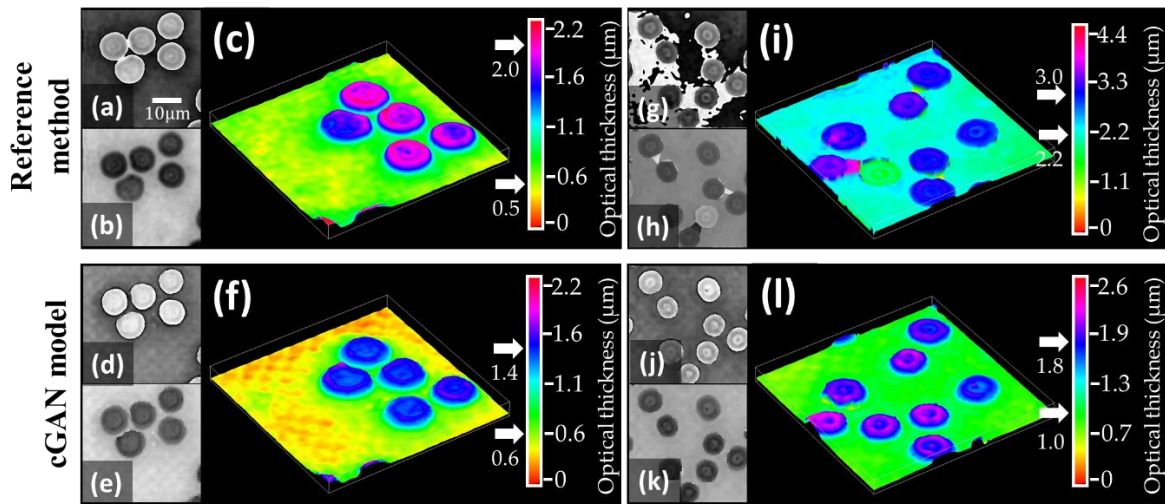


Fig. 7.11. Quantitative comparison between the highest (a–f) and the lowest (g–l)-quality reconstructed phase images provided by the conventional reference method (first row) to those obtained by our cGAN model (second row). Panels (a), (d), (g), and (j) are the reconstructed phase images. Panels (b), (e), (h), and (k) display the unwrapped reconstructed phase images. Finally,

panels (c), (f), (i) and (l) show the three-dimensional (3D) pseudocolor distribution of the optical thickness.

In our next experiment, we investigate the performance and the robustness of the cGAN model for reconstructing aberration-free phase images in time-lapse DHM imaging. For this study, we mimicked the flow of red blood cells in a capillary by mounting a static microscopic sample of RBCs in a motorized translational stage. The velocity of the motor was such that the RBCs' flow was $2.75 \mu\text{m/s}$. We have recorded a sequence of 300 holograms that tracks the flow of RBCs within blood plasma. It is important to highlight that all the recorded cells were in focus (e.g., the image plane condition was met for all cells). This experiment would be completely equivalent to the one in which the capillary depth is smaller than the depth of field of the objective lens, which is approximately $0.69 \mu\text{m}$ based on the manufacturer's specifications. These recorded holograms were used as input images of our trained cGAN model. Figure 7.12 summarizes the performance of the traditional reference method [80] and the proposed learning-based model. This figure displays five randomly selected phase images. The n value stands for the i -th frame in the time-lapse recording sequence. Whereas the RBC flow is marked by the blue arrow in Fig. 7.12(b), the yellow star is a visual aid to track the identical RBC across the time-lapse sequence. One realizes that the traditional reference method reconstructs phase images with phase aberrations and varying background levels across the time-lapse sequences, see the red arrows in Fig. 7.12(a). In addition, the poor performance of the traditional method inhibits the proper visualization of inner structures in the dynamic imaged sample. In contrast, the performance of the cGAN model is superior, providing reconstructed RBCs images with fewer phase aberrations, a homogeneous background marked by the green arrows in Fig. 7.12(b), and reduced noise. However, the proposed cGAN model does not exploit one of the major advantages of DHM, which is the reconstruction of quantitative phase images of defocused samples (e.g., cells, bacteria, and organisms located at

different depths). In future work, we will investigate the performance of the cGAN model to reconstruct defocused holograms at different depths for several biological samples by implementing a microscopic slide with a flow path, enabling the recording of out-of-focus holograms.

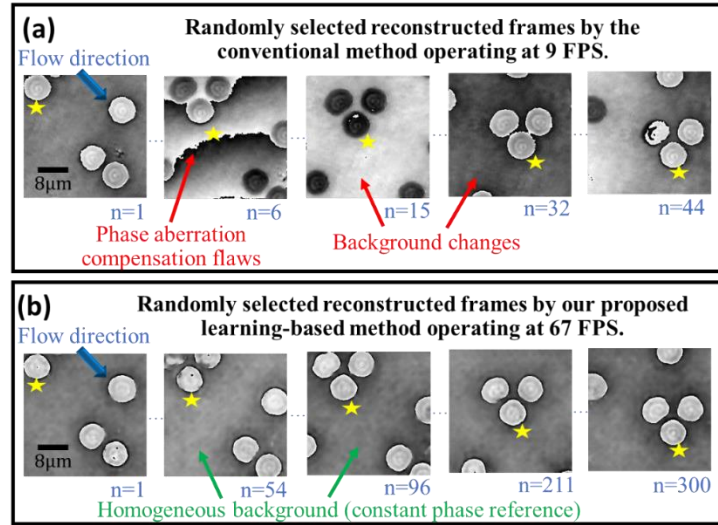


Fig. 7.12. Evaluation of the traditional reference and GAN models to reconstruct aberration-free phase images in time-lapse DHM imaging. The blue arrow marks the flow direction. The yellow star marks the identical RBC across the time-lapse sequence. The red and green arrows show differences between the reconstructed phase images.

Video S1 [164] displays the rendering of the time-lapse reconstructed phase images for both the conventional method and the cGAN model. This video demonstrates the superior performance of our proposed method. Note that all the reconstructed phase images generated by the cGAN model present a homogenous background, resulting from the accurate compensation of the digital reference wavefront. In addition, the majority of inner structures in the imaged RBCs are retrieved without any phase distortion. Contrarily, the conventional method fails to reconstruct several frames in the time-lapse sequence, resulting in an unstable reconstruction technique. To finalize, we have estimated the number of frames per second (FPS) required for each method to reconstruct these phase images from the raw DHM holograms. For simplicity, we have excluded the

acquisition time in the estimation of the FPS. The processing time for each DHM reconstruction method is reported based on a laptop powered by an Intel Core I7 6700HQ CPU running at 2.60 GHz with 8 GB of RAM and hosting an NVIDIA Geforce GTX 960M GPU with 2 GB of RAM running at 1 GHz. Whereas the conventional method requires approximately 115 ms to reconstruct each raw hologram, the proposed fitted generator reconstructs each quantitative phase image in 14.8 ms on average, being $7.7\times$ faster. According to these processing times, the video reconstruction is equal to 9 and 67 FPS for the conventional and the proposed method, respectively. The values of the FPS are also reported in Fig. 7.12 and Video S1.

7.4 Comparison of the Proposed cGAN Model against the ConvA and U-Net Models

In this section, we compare the performance of the cGAN model with respect to the one of the equivalent U-Net and ConvA models. For a fair comparison, the U-Net and the ConvA models have the same architecture as the cGAN generator, omitting the skip connections in the ConvA model. The three models have been trained using an experimental dataset of 1,820 pairs of DHM holograms, and their corresponding reconstructed phase images: 1,512 and 308 pairs for training and validating, respectively. Whereas the parameter adjusting during the cGAN fitting has been dictated by two adversarial L1 loss functions and its convergence by customized metrics, a logarithmic loss function has been used to tune the parameters of both the ConvA and U-Net models. The number of epochs required for each model to be correctly fitted has been determined following different convergence criteria: minimizing a thresholding-and-summation metric (TSM) and the standard deviation (σ) for the cGAN (Section 7.3), and the root-mean-square error (RMSE) for the U-Net and ConvA models.

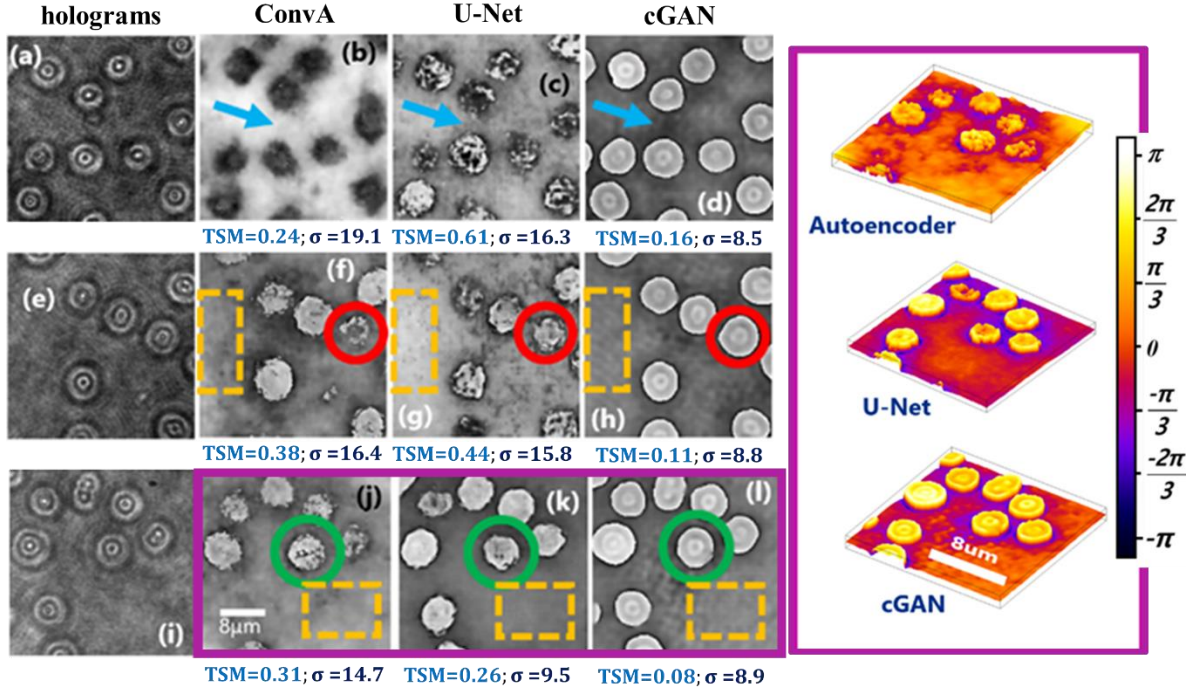


Fig. 7.13. Phase reconstructions by the tested learning-based models. The performance is quantitatively performed in terms of the thresholding-and-summation metric and the normalized standard deviation.

Once the models have been appropriately trained, they have been used to reconstruct unseen DHM holograms that were not included during the training stage. Figure 7.13 shows three different holograms and their reconstructed phase images for each model. The TSM, which accounts for the number of phase discontinuities in the reconstructed phase maps, is smaller on average for the cGAN (0.12) than the ConvA (0.31) and the U-Net (0.43) models. The cGAN model also provides the lowest noise level (e.g., an average σ of 8.73). The average σ is 16.7 and 13.8 for the ConvA and the U-Net, respectively. These quantitative results suggest the superior performance of the cGAN model for reconstructing high-quality phase images with minimum phase nuisances in DHM. We have also measured each model's training and prediction times to complete the performance comparison. The training time has been calculated by considering all the required epochs during the training stage. The prediction time is computed on a batch reconstruction of 100

holograms. The results are reported in Table 1. The systems' hardware specifications of the models training and prediction are detailed in [165] and [139], respectively. According to the results in Table 1, although the cGAN model requires around five times the training time of the other models, once they are correctly fitted, their prediction time is in the same order. Based on all these metrics (e.g., TSM, noise level, training, and prediction time), the cGAN model is the most promising strategy for fully-compensated phase images without phase aberrations in image-plane off-axis DHM.

Table 7.1. Training and prediction times for the compared learning-based approaches

Model	Training time (min)	Prediction time (ms)
CA	21	1211
U-Net	24	1456
cGAN	108	1492

Figure 7.14 provides a more detailed comparison between the performance of the cGAN method against that of the U-Net model. Again, the implemented U-net model has the same parameters as the generator model in the proposal cGAN model. Overall, the training hyperparameters of this U-Net model are the same employed by the cGAN model generator. The main difference is using a logarithmic loss function to adjust the U-Net model weights. The U-Net model converged after 50 epochs. For each image in the validation dataset, this convergence was estimated by measuring the root-mean-square error (RMSE) between the reconstructed phase images of the conventional method and the one of the U-Net model at every epoch. Considering the training dataset for the cGAN model (1,508 pairs of images), the measured RMSE on the validation data was 0.25. Since the input reconstructed phase images were normalized before training and prediction, this RMSE value means that there is an error of 25% between the target phase images and the reconstructed U-Net images. To minimize the RMSE error, increasing the training dataset to 24,491 pairs of images was mandatory. In this case, the convergence of the U-

Net model was reached with an RMSE value of 0.04 at epoch 28. Figure 7.14 compares the reconstructed phase images obtained by the traditional method, the U-Net model (trained with 24,491 pairs of images), and the proposal cGAN model (trained with 1,512 pairs of images).

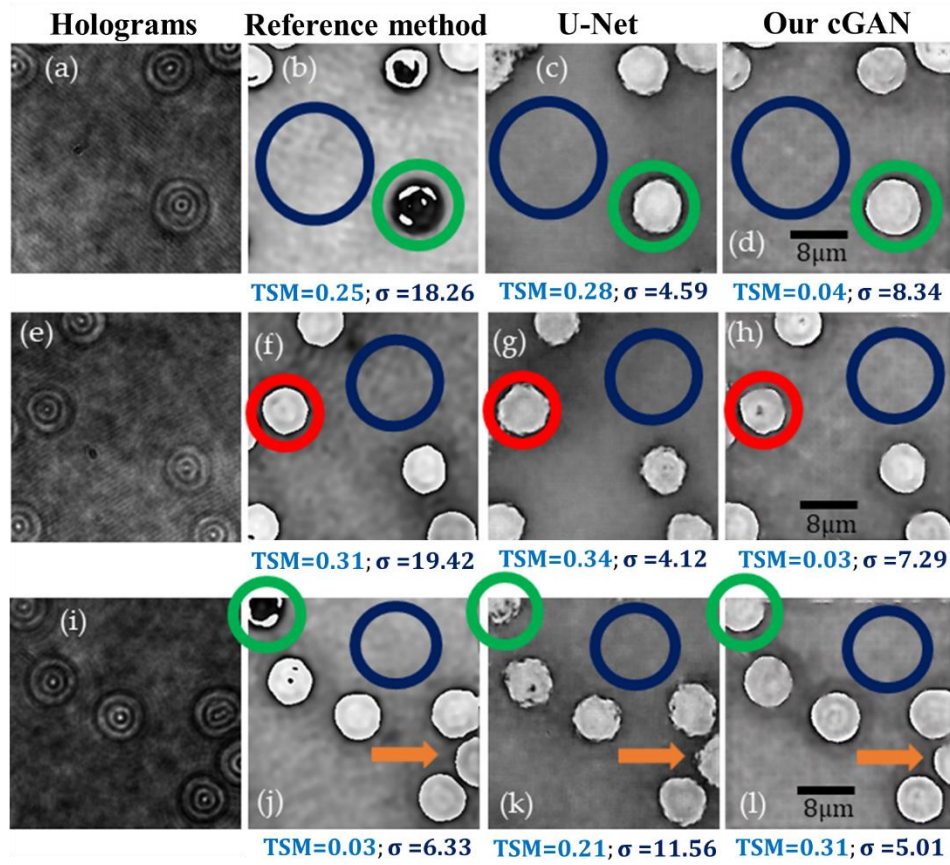


Fig. 7.14. Comparison between the U-Net model and our cGAN model. The first column displays the selected DHM holograms from the testing dataset. The reconstructed phase images obtained by the conventional method are illustrated in the second column. Columns 3 and 4 show the reconstructed phase images achieved by the U-Net and our cGAN model. The colored circles and arrows indicate differences between the reconstructed phase images.

Note that Figure 7.14 also shows the performance of the U-Net and proposed cGAN models using the new validation dataset to assess the goodness of these models for different experimental conditions and show that no overfitting occurs. This second testing dataset consists of 7,005 pairs of images recorded to avoid similarities between the training and testing datasets due to the identical experimental conditions of the one-time acquisition process. This dataset has been used

to assess the effectiveness of the proposed model for different experimental conditions and to show that no overfitting occurs during the training of our proposed cGAN model. The proposed cGAN model outperforms the U-Net model based on the reported TSM values even though the training dataset of the cGAN model is $16.2\times$ smaller than the one used in the U-Net model. The cGAN model reconstructs phase images with lower TSM values than those obtained by the U-Net model. In addition, the cGAN model retrieves the edges of the RBCs with greater accuracy than the U-Net model, as pointed out by the green circles and the orange arrows. We have measured the σ values were measured in the regions encircled by the dark blue lines in Fig. 7.14 to quantify the difference in the noise level. Based on these σ values, the U-Net model reconstructs phase images less sensitive to noise than the reconstructed cGAN phase images (e.g., lower σ values). Nonetheless, the σ values are approximately $2.24\times$ lower than those provided by the conventional method. Although the cGAN model may introduce some remaining nuisances in the reconstructed phase images, as indicated by the red circles in Fig. 7.14, overall, the proposed cGAN method achieves better results than the traditional method and the U-Net model.

7.5 Validation of the Proposal's Generalization Ability to System's Diversity

To validate the generalization ability of the proposed method in regard to system diversity, DHM holograms were recorded in a common-path DHM system using a Fresnel biprism. This DHM system was comprised of a $40\times/0.7$ Nikon MO lens, and the camera used had 5471×3648 square pixels of $2.4\text{-}\mu\text{m}$ side. The Fresnel-biprism-based DHM system still operated in the telecentric regime, and the camera was located at the microscope's image plane. More details on this DHM system can be found in [166]. Note that a minimum preprocessing of the DHM holograms recorded by the Fresnel-based DHM system is required. The preprocessing step consisted of resizing the raw holograms to reduce their size by 40% and matching the field of view to those

provided in the Mach–Zehnder-based holograms. After this step, we have evaluated the traditional method and the U-Net and cGAN models to reconstruct these Fresnel-based DHM holograms. Figure 7.15 shows selected holograms from the Fresnel-based DHM system and their corresponding reconstructed phase images to test the generalization ability of the proposed cGAN model. As shown in Fig. 7.15, the reconstructed phase images obtained by the traditional method present RBCs with a different phase value even though all cells are expected to yield the same phase values within experimental error margins. This phase difference in the RBCs is due to a phase difference of π introduced by the Fresnel biprism between each interfering wave. Nonetheless, both learning-based methods reconstruct all cells with the same phase values. The green arrow and the region enclosed by the red circle in Fig. 7.15(g)-(k) illustrate that the U-Net model provides distorted details of RBCs. In contrast, the cGAN model reconstructs the specimen's details accurately, as shown in the region inside the green circles and pointed out by the orange arrows. The measured σ values, computed for the region encircled by the dark blue circle, are similar for the three methods. In summary, the cGAN model can reconstruct quantitative phase images from off-axis DHM holograms with minima distortions, highlighted by the red circles in Fig. 7.15, regardless of the optical configuration of the transmission DHM system.

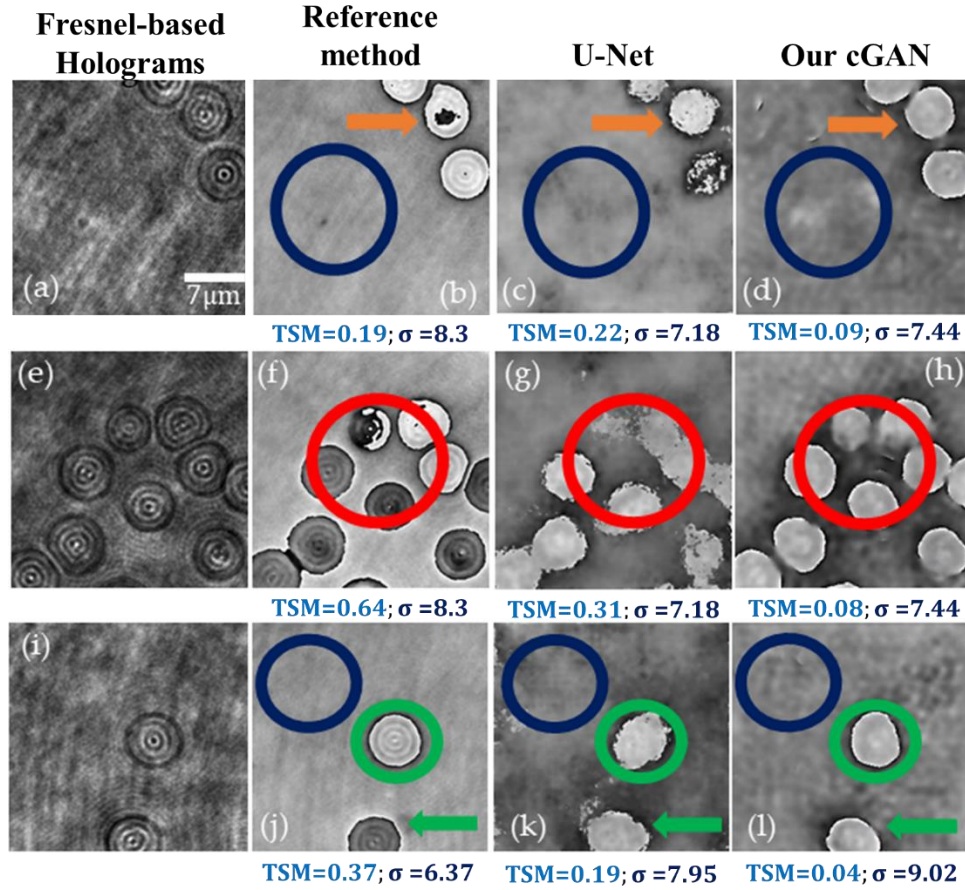


Fig. 7.15. Evaluation of the generalization of the cGAN model to a common-path DHM system. The first column shows selected DHM holograms recorded using a Fresnel-based DHM system. Columns 2, 3, and 4 display the reconstructed phase images obtained by the conventional method, the U-Net model, and the proposed cGAN model, respectively. The dark blue circles mark the region where we estimated the σ value.

7.6 Conclusions

This chapter reports a conditional generative adversarial network (cGAN) to fully reconstruct quantitative phase images from human red blood cells (RBCs). To the best of our knowledge, this is the first learning-based method to reconstruct off-axis DHM holograms of biological samples with minimum phase distortions from raw holograms without the need for robust pre- or post-numerical procedures. The raw RBCs holograms were recorded using an off-axis DHM system operating at the telecentric regime. The proposed cGAN model was trained using a L1 adversarial

loss whose convergence was dictated by two customized metrics specifically designed for tracking the imaging characteristics in DHM: (1) the number of phase discontinuities using a thresholding-and-summation metric (TSM) and (2) the noise level measured in homogenous regions of the reconstructed phase maps using the standard deviation (σ). Because we used two customized metrics (i.e., TSM and σ), the proposed cGAN model converges rapidly (i.e., only 12 epochs are needed). This learning-based method was trained using 1,512 pairs of raw holograms and their reconstructed phase images obtained by a traditional reference method [80]. Besides, the proposed cGAN model and the U-Net model are compared to evaluate the performances of both methods and validate the superior performance of the cGAN model. In summary, the proposed cGAN method surpasses the setbacks of the reference method, resulting in quantitative phase images with reduced noise and constant background level. These improvements are consequences of the model used (i.e., conditional generative adversarial networks) since these supervised models were initially designed for the specific abstraction of low-level information. Additional advantages of the cGAN model are: (1) the retrieval of inner structures of the RBCs' information and (2) its training time (approximately 2 h).

The high performance of our cGAN model paves the way for video-rate quantitative phase imaging of dynamic studies using DHM. The main disadvantages of the proposed method are the data field of view and the cell density, which are reduced to $40\ \mu\text{m} \times 40\ \mu\text{m}$ (256×256 pixels) and up to 9 cells for the field of view, respectively. In future work, we will increase the cell density and the field of view by expanding the image size fed into the model. In addition, although the cGAN model was validated using RBCs, it could be straightforwardly extended to reconstruct quantitative phase images of any dynamic biological sample. Future studies will upgrade the training dataset, including anemic RBCs, glioblastoma cells, and diatoms. The limitation of the

cGAN model is that this method only works for off-axis DHM systems operating in the telecentric regime. Table 7.2, summarize the main advantages and limitation of the proposed cGAN model.

Table 7.2. Advantages and limitations of the proposed cGAN model to fully reconstruct quantitative phase images from human red blood cells (RBCs).

Advantages	Limitations
<ul style="list-style-type: none"> ✓ Reconstructed phase images with minimum phase distortions from raw off-axis DHM holograms ✓ No need for robust pre- or post-numerical procedures. ✓ Reconstructed phase images with reduced noise and constant background level. ✓ Suitable dynamics RBCs samples. ✓ System diversity; the trained cGAN model reconstructs RBCs holograms for different off-axis DHM systems operating in the telecentric regime. 	<ul style="list-style-type: none"> ➤ Only work for off-axis DHM systems operating in telecentric regime. ➤ Only work for RBCs ➤ Reconstructed phase images with reduced field of view (e.g., approx. $40\text{ }\mu\text{m} \times 40\text{ }\mu\text{m}$, corresponding to 256×256 pixels). ➤ Reconstructed phase images with reduced cell density, up to 9 cells for the field of view.

8. SPECKLE NOISE REDUCTION IN DHM VIA HYBRID MEDIAN-MEAN FILTER

Speckle noise is inherited by all imaging techniques that utilize a coherent light as a source of illumination. The speckle is generated due to the illumination of a surface with roughness in dimensions comparable to the coherent wavelength of the light source [167]. Following Huygens' principle [168], each point of the surface acts as a spherical wave scatter emitting light with random phase distribution among them. The coherent superposition of these spherical wavefronts creates a random intensity pattern of constructive and destructive interference, dark and shiny spots, to produce the speckle pattern [167]. The speckle noise is, therefore, a random pattern of dark and shiny spots that appears on the images in any coherent (e.g., laser-based) imaging system, including laser-based photography [169], DH [170], and DHM [116]. While laser-based projectors provide a wide color gamut for vivid, super bright, and high contrast images, their major limitation is the speckle noise caused by the lasers' coherent nature. Akram and Chen [169] reviewed the current state-of-the-art solutions to reduce speckle noise. These approaches involve the decorrelation of the light through the wavelength using a source with the fast tuning of lasing wavelength or an array of sources with different wavelengths. Another decorrelation approach can involve the use of a source with reduced spatial coherence (e.g., spatial decorrelation) or the use of an array of sources with different angles at one spot on the screen (e.g., angular decorrelation). The angular decorrelation can also be achieved by changing the illumination angle at one spot or rotating a diffuser. Finally, light can be decorrelated using polarization with a source with fast changing polarization or splitting the light into two paths with sufficient path length difference and different polarizations. On the other hand, several approaches have been developed in DHM to diminish the adverse speckle effects, which ruin the image contrast and reduce the spatial

resolution. In general, these methods can be grouped into two categories: i) physical [171–176] and ii) computational [177–184] approaches. The physical techniques are commonly based on two methodologies. One method involves recording the same scene hologram Q times under different physical conditions. Because of the random behavior of the speckle noise, the speckle noise in each of the recorded holograms is uncorrelated with the others. Therefore, the average of the reconstructed images provides a numerical reconstruction with reduced speckle noise following a $1/\sqrt{Q}$ law [185]. Such holograms can be acquired by changing the angle of illumination through a rotating mirror [171], slightly rotating the object [172], and lateral shifting the object [173] or the sensor [186]. Another reported physical technique uses different wavelengths to register multiple holograms [187]. In addition, other physical methods use some optical elements to reduce the light's spatial coherence partially. Examples of these elements include rotating diffusers [174], spatial light modulators [175,176], and holography diffusers [188].

Due to the number of holograms that need to be recorded to produce significant effects, ranging from 20 to 100 images, the common disadvantage of all of these physical methods is the lengthy acquisition time, which limits the techniques to static samples. Computational techniques aim to reduce the speckle noise in dynamic applications. The main idea of these techniques is the use of filters applied in the spatial [189–191] or Fourier domain [192,193] to reduce the speckle noise. Other computational methods are based on the same idea as the physical approaches in which one averages Q partially uncorrelated speckle-distorted reconstructed images from a single hologram. These methods include the introduction of a spatial jittering in the Fresnel kernel [183], the use of a mask to generate Q sub-holograms [184], and the sequential sampling of the discrete Fourier transform of the hologram [179]. A standard limitation of these computational approaches is the

requirement of some parameters for improving the performance. For example, the WFT2F technique requires 10 input parameters [193,194]. The quality of the final denoised image depends significantly on the correct selection of those parameters. Those parameters vary from image to image. Unfortunately, the paper describing that technique does not provide information about the optimal values of those parameters. This could be a limitation for inexperienced users who may not have prior knowledge of the technique. In addition, computational methods are subject to a tradeoff between spatial resolution and speckle noise. The higher the reduction in the speckle noise is, the lower the spatial resolution in the denoised image is. This tradeoff has been avoided by implementing approaches in which physical and computational methods are integrated [179,195,196]. In particular, Bianco *et al.*, proposed a framework that combines the acquisition of multiple digital holograms with optimized joint-action computational image-denoising methods. In that work, the authors demonstrated their technique using computer-generated holograms from a single-shot recording and validated it using dual-wavelength holographic recordings [196].

With the significant advancement of deep learning (DL) techniques over the last years, DL approaches have also been applied to restore sharp images from their degraded version in the presence of speckle noise. Among the different DL approaches, speckle-free images have been achieved using a convolutional neural network [197] and conditional generative adversarial network [198], which were applied to underwater sonar images and laser-illuminated ex vivo porcine gastrointestinal tissues, respectively. Whereas traditional DL algorithms require the speckle-free image for training the model, Yin *et al.* proposed a DL method that does not require prior knowledge of speckle-free object distribution [199]. Even though DL algorithms are robust, their performance depends heavily on the number of training data and their quality.

In this Chapter, we propose a single-shot image processing method to reduce the speckle noise based on the synergetic combination of two standard denoising methods in imaging processing: the median filter and the mean approach. This single-shot image processing method aims to: (i) minimize the tradeoff between speckle noise and spatial resolution in computational denoising techniques; (ii) be a user-friendly tool with a simple understanding of the role of the parameters; and (iii) be robust for the majority of samples and speckle-distorted systems. The novelty of the presented approach, named the hybrid median-mean filter (HM2F), is the cascaded application of these techniques to the speckle-distorted images. In this work, we have focused on the implementation of the HM2F method in speckle-distorted images from different optical systems: laser-based photography, DH, and DHM. Using the HM2F, the speckle noise is reduced up to 49% for laser-based photography, 72% for DH, and 14% for DHM, which corresponds to a speckle contrast of 0.51, 0.28, and 0.86, respectively. The resolution is kept up to 97% from the original value, reducing the adding of blurring effects for all imaging modalities (e.g., laser-based photography, DH, and DHM).

This chapter follows the next structure: Section 8.1 contains a brief description about speckle noise. In section 8.2, the proposed HM2F is presented. Section 8.3 is devoted to validate the proposed method in Laser-Based RGB photography, DH and DHM. Finally, the conclusions are presented in Section 8.4. This work has been published in Optical Engineering [200], and presented in the 2021 OSA Imaging and Applied Optics Congress [201].

8.1 Speckle noise

Each time that coherent light is used as a source on illumination to form an image, speckle noise is generated. The speckle noise is generated due to the roughness of the sample has a comparable

dimension as the wavelength of the source. The whole set of roughness can be understood as emitters source of spherical waves according to the Huygens's principle. Those wavelengths emanating from each roughness mutually impinging in a particular point $p(x, y)$ with a random phase generating destructive and constructive interference. Now, consider the particular point $p(x, y)$ inside a rectangular array of dimensions $M \times N$, the interference pattern is produced on all the points inside the rectangular array, producing a random pattern of dark and bright points called speckle. The complex amplitude at a point $p(x, y)$ can be obtained add up the whole complex distribution originating by each roughness,

$$\Gamma(x, y) = \sum_{m=1}^M \sum_{n=1}^N \frac{A(m, n)}{\sqrt{M \times N}} \exp(-i\varphi(m, n)), \quad (8.1)$$

Where A and φ are the amplitude and phase distribution generated by each roughness contribution. The complex amplitude should be understood as a field with random distribution that follows the assumptions made by Goodman i) The complex field follows a uniform statistical distribution, ii) for each distribution $\Gamma(x, y)$ its amplitudes $A(m, n)$ are statistically independent, and iii) for each distribution $\Gamma(x, y)$ its phases $\varphi(m, n)$ are statistically independent and is uniformly distributed over the interval $[-\pi, \pi]$. A metric to quantify the speckle noise is the speckle contrast SC defines as

$$SC = \frac{\sigma}{\bar{I}}. \quad (8.2)$$

where σ and \bar{I} are the standard deviation and mean intensity, respectively, inside region of interest in the original noisy image.

(a)

1: **Function Hybrid Median - Mean** (g, k)

2: *Inputs*

3: $g \rightarrow$ Noise reconstructed image

4: $k \rightarrow$ Maximum kernel size

5: *Output*

6: $\hat{g} \rightarrow$ Denoise image

7: $\hat{g} \leftarrow g$

8: $i \leftarrow 2$

9: *while* $(2i - 1) \leq k$

10: $h \leftarrow \text{median}(g, [2i - 1] \times [2i - 1])$

11: $\hat{g} \leftarrow (\hat{g} + h) / 2$

13: $i \leftarrow i + 1$

14: **Return** \hat{g}

(b)

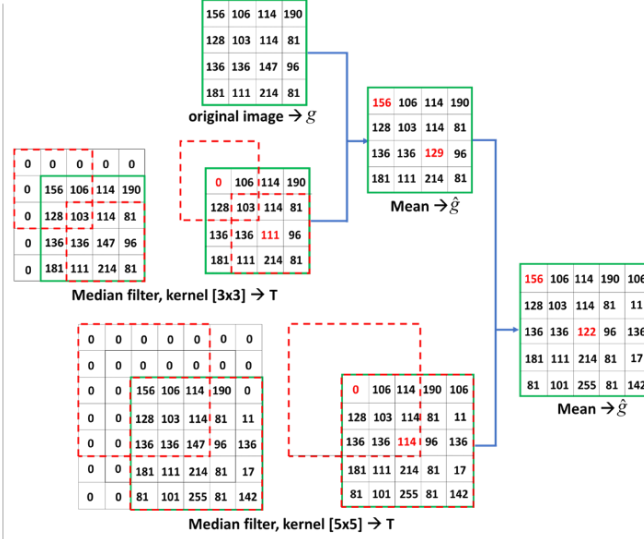


Fig. 8.1. (a) Pseudocode of the *hybrid median-mean filter* (HM2F). (b) Illustration of the hybrid median-mean filter for a maximum kernel size of $k = 5$. The input image corresponds to the noisy image. Each median filter creates a reduced speckle-noise image (e.g., denoising speckle image). The final denoised image is obtained as the average between the median filtered image and the mean result of the previous iteration.

8.2 Hybrid Median-Mean Framework

The HM2F method is an iterative method based on applying i times a median filter over the original noisy speckle-distorted image g . For each i iteration, the image after applying the median filter is saved in the variable h . The square kernel size of the median filter increases by $(2i - 1)$ for each iteration. Because the median filter with kernel size $[1 \times 1]$ provides an identical image to the noisy input image (g), the first iteration in the HM2F corresponds to $i = 2$. The novelty of the HM2F to other methods reported in the literature is the combination of several median-filtered images (h) to provide a final denoising image (\hat{g}). We propose the average between the i 'th median-filtered image (h) and the previous $(i - 1)$ 'th denoised image (\hat{g}). Therefore, in the first iteration ($i = 2$), $h = \text{median}(g, [3 \times 3])$ and $\hat{g} = (g + h) / 2$. Figure 8.1(a) shows the pseudocode of

the HM2F. The inputs of HM2F are the noisy images (g) and the maximum kernel size for the median filter (k). Figure 8.1 (b) shows the process of the HM2F for the maximum kernel size of $k = 5$ (maximum iteration, $i = 3$). For $k = 5$, the median filter is applied twice to the noisy image with kernel sizes of $[3 \times 3]$ and $[5 \times 5]$. For the first iteration, a median filter of kernel size $[3 \times 3]$ is applied to the original noise image (g) to provide the denoised h image. The average of this result and the original image results is the new image \hat{g} . For the second iteration, a new denoised h image, obtained by applying the median filter with kernel $[5 \times 5]$ to the noisy image, is averaged with the previously computed image. Figure 8.1(b) shows the operation of the median filter in two different regions, marked by the red-dashed boxes. Black values represent the original noisy data, and red values represent the new values after applying the HM2F. A zero-padding operation is required to offset border problems for each median filter. The HM2F can also be applied to RGB speckle-distorted images after splitting the color image into three-channel images, applying the HM2F to each channel image, and merging back these three-channel denoised images.

Appendix A provides a comparison between the proposed HM2F and a median filter average (MFA) approach. The difference between the MFA and HM2F denoising images is the combination between the median-filtered images.

8.3 Experimental results

The following section is devoted to showing the versatility of the proposed HM2F in laser-based photography, DH, and DHM. The HM2F was applied to the RGB noisy image of a four-color cube in laser-based photography, the reconstructed amplitude images of a dice and horse model in DH,

and the reconstructed phase images of a star target and a complex biological sample in DHM. Figure 8.2 shows the optical configuration of the three optical systems.

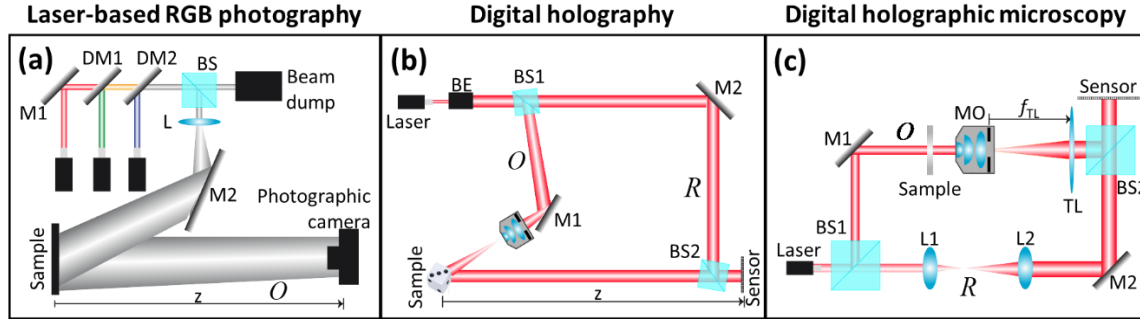


Fig. 8. 2. Illustration of the optical configurations. (a) Color laser-based photography, (b) DH, and (c) DHM systems following a Mach – Zehnder arrangement. BE, beam expander; BS, beam-splitter; DM, dichroic mirror; L, lens; M, mirror; MO, microscope objective; O, object beam; R, reference beam; SF, spatial filter; TL, tube lens.

8.3.1 Laser-Based RGB Photography Results

Figure 8.3 compares the performances of the HM2F method with the known denoising methods, including the 3D block matching (BM3D) [180], the nonlocal means (NLM) filter [178,190], the Wiener filter [181], and the conventional median filter (CMF) [40]. For this comparison, Fig. 8.2 shows the final RGB denoised image of a four-color cube utilized as a millimeter-sized object. In the laser-based RGB photographic system Fig. 8.2(a), the cube was located at 86 cm from a commercial Canon photographic camera, and directly illuminated by three lasers of wavelengths 671 nm (red), 532 nm (green), and 473 nm (blue). More details of this laser-based photographic system are provided in Ref [202]. The kernel size for both the CMF and the proposed HM2F was 11×11 . Note that for CMF we applied a median filter with a particular kernel size over the original image. To quantify and characterize the reduction in the speckle noise the speckle contrast SC was measured per channel as $SC = \sigma_i / \bar{I}_i$ [185], where σ_i and \bar{I}_i are the standard deviation and mean

intensity, respectively, inside the yellow region marked in the original noisy image in Fig. 8.3(a). The average value of the three measured speckle contrast for each denoising technique is reported in the lower right corner of Fig. 8.3. These values were normalized to those of the original noisy image. Regarding the speckle contrast reduction provided by the other approaches, the results showed better performance by the HM2F and the CMF ($SC = 0.51$ for HM2F versus 0.50 for CMF). Comparing the speckle contrast values, the reduction in the speckle contrast provided by the proposed HM2F method [Fig. 8.3(f)] is almost the same as that provided by the CMF approach [Fig. 8.3(e)]. Nonetheless, for the same kernel size, the blurring effect of the conventional median-filtered RGB image is more significant than that of the HM2F image, Figs. 8.3(e) and (f), respectively. A quantitative analysis of the blurring effects is provided by analyzing the first-order derivative of a step function (i.e., edge) for each method. The step function is defined by the mean profile along the vertical direction of the region marked by the green rectangle in Fig. 3(a). Because the first-order derivative of a step function is a Delta function [131], we have estimated the full width at half maximum (FWHM) of the first-order derivative of the step function. The step function is defined by the mean profile along the vertical direction of the region marked by the green rectangle in Fig. 8.3(a). Since our step function is noisy, we have fitted it using a smoothing spline whose parameter has been determined empirically for each method in such a way that the correlation coefficient between the noisy step function and the fitted one is higher than 0.99 . Figure 8.3(g) shows the first-order derivative of the edge for the BM3D, NLM, Wiener, CMF, and HM2F approaches. For each of these profiles, the FWHM was quantified and reported in millimeters in the top right corner of each image method inside Fig. 8.2. The FWHM is equal to 0.28 mm for the original noisy image and the denoised images obtained after applying the BM3D, NLM, Wiener, and HM2F approaches. This means that the BM3D, NLM, Wiener, and HM2F methods do not

introduce any blurring effect. By contrast, the CMF technique introduces some blurring with the FWHM being increased to 0.31 mm. Nonetheless, while the NLM and HM2F approaches are similar, the reduction of the speckle contrast is less for the BM3D (SC = 0.59 for BM3D versus 0.51 for HM2F) and the Wiener (SC = 0.58 for Wiener versus 0.51 for HM2F) methods. In conclusion, for the four-color cube, the HM2F shows the highest reduction in the speckle contrast without adding blurry effects.

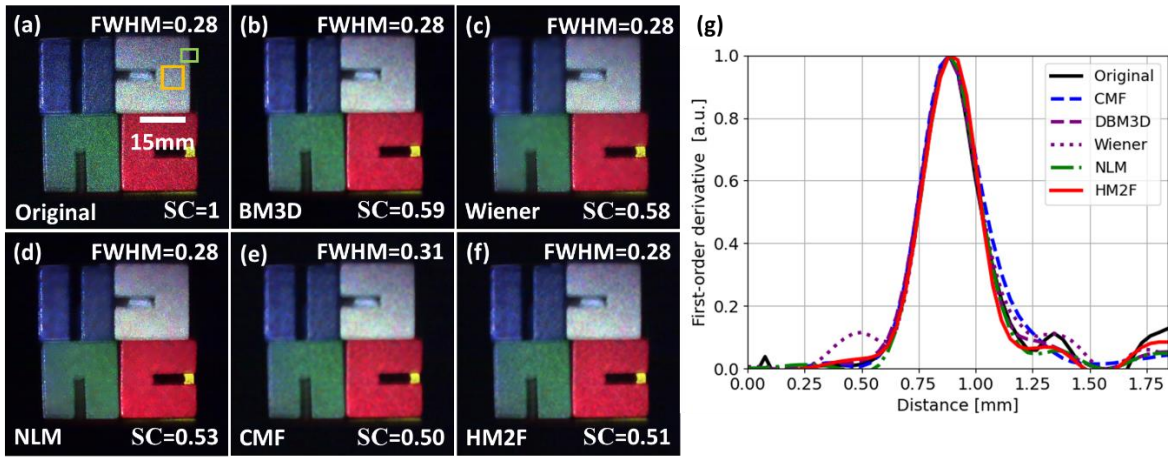


Fig. 8.3. Validation of the proposed HM2F method in laser-based photography. Denoised RGB images of the four-color cube after applying different denoising approaches. (a) Original noisy image; denoised image using (b) BM3D, (c) Wiener filter, (d) NLM filter, (e) proposed HM2F, and (f) CMF. Panel (g) compares the response of these methods to blur by plotting the first-order derivate of a step function defined by the mean profile along the vertical direction of the region marked by the green rectangle in Panel (a).

8.3.2 DH and DHM results

The holograms for two different samples (dice and horse model) were recorded in the DH system Fig. 8.2(b) operating in an off-axis Mach–Zehnder interferometer architecture [132]. The illumination source used in the DH system was a He – Ne laser of wavelength $\lambda = 632.8 \text{ nm}$. The holograms were recorded by a complementary metal-oxide-semiconductor (CMOS) camera (

$M \times N = 2592 \times 2048$ and $\Delta_{xy} = 4.8 \mu\text{m}$ square pixels). In this experiment, the camera was located at a distance $z = 70 \text{ cm}$ from the sample, producing a speckle grain with a lateral (x-y) size of $\delta_x = \lambda z / M \Delta_{xy} = 35 \mu\text{m}$ and $\delta_y = \lambda z / N \Delta_{xy} = 45 \mu\text{m}$. Figures 8.4(a)-(d) compare the reconstructed amplitude images of a dice applying different kernel sizes, which are $[9 \times 9]$ and $[17 \times 17]$, using two different approaches: (i) CMF [Figs. 8.4(a) and (c)] and (ii) the proposed HM2F [Figs. 8.4(b) and (d)]. To quantify and characterize the reduction in the speckle noise the normalized speckle contrast is plotted versus the number of iterations for each kernel size (i.e., iteration) in Fig. 8.4(e). Because the speckle contrast is highly dependent on the object information, the contrast speckle was measured in 10 different square regions to provide an experimental error. The quantitative values shown in Fig. 8.4(e) show that the speckle contrast reduces rapidly for both the CMF and HM2F. Comparing the reconstructed amplitude images from the CMF and HM2F shows that, although the CMF reduces the speckle noise faster than the HM2F, the HM2F provides final denoising images with fewer blurring effects than that provided by the CMF. These results show that the HM2F presents a better tradeoff between reducing the speckle contrast and the blurring effects. A quantitative analysis of the blurring effects is provided by estimating the FWHM of the first-order derivative of a step function defined by the profile along the transverse direction marked by the green line in Fig. 8.4(a). Figure 8.4(e) also compares the increase of the blurring effects versus the size of the kernel for the CMF and the HM2F. This panel illustrates how the speckle contrast and the response to the blurring can be controlled by selecting a different kernel size of the median filter. These curves show the tradeoff between the speckle noise and resolution in both the CMF and HM2F methods. Despite this tradeoff being present in both CMF and HM2F methods, the HM2F method shows a smaller blurring effect than the CMF method for

any kernel size of the median filter, making it a more suitable method for mitigating the tradeoff between speckle noise and blurry effects than the CMF approach.

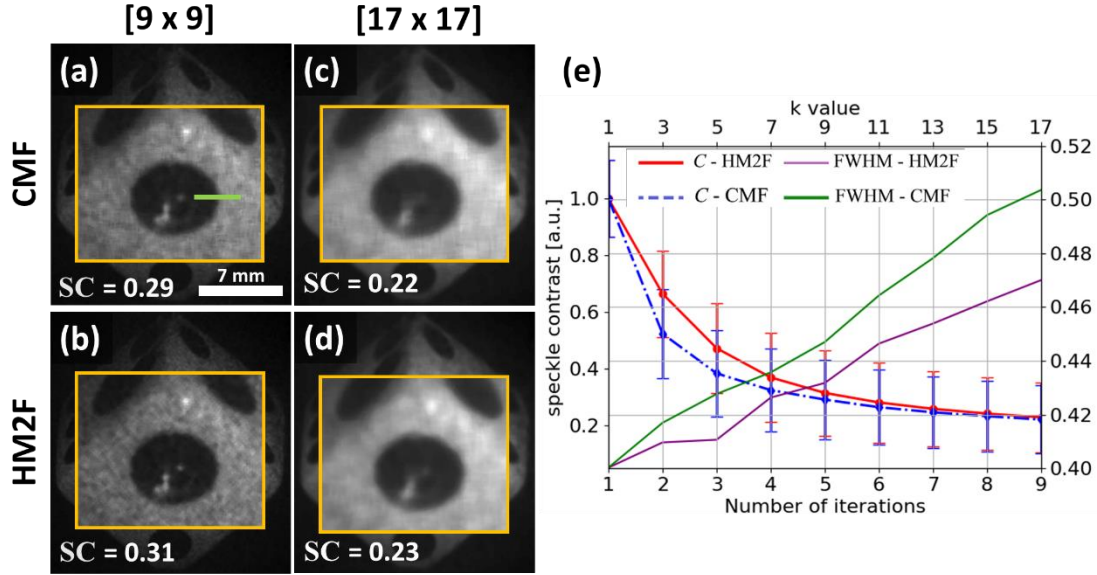


Fig. 8.4. Denoising images obtained after applying two different approaches (CMF and HM2F) and two different kernel sizes. Panels (a) – (d) correspond to the denoised amplitude images using the CMF and HM2F approaches. Panel (e) corresponds to the quantitative comparison of the speckle contrast and the FWHM value of the first-order derivate of a step function defined by the profile along the transverse direction marked by the green line in Panel (a) versus numbers of iterations (i.e., kernel size) for the CMF and HM2F methods.

To finalize the discussion for DH system, Fig. 8.5 compares the performances of the proposed method with the known denoising methods [e.g., the BM3D filter [180], the NLM filter [178,190], the Wiener filter [104], and the 2D windowed Fourier transform filter (WFT2F) [193]]. To perform this comparison, two reconstructed amplitude images are used: dice (first row) and model horse (second row). Each reconstructed amplitude image is displayed after the normalization to its own maximum and minimum values. Figure 8.5 shows that the HM2F performs equally well in high-contrast images (i.e., dice results) and low-contrast images (i.e., horse results). The speckle contrast was measured inside the green region marked in the original

images for the two samples. The speckle contrast values, which were normalized to those of the original noisy image, are reported in the lower right corner. As can be seen, the value of the speckle contrast varies from image to image. For example, for the dice image, the BM3D approach provides the denoised image with the lowest speckle contrast (i.e., $SC = 0.17$). The NLM and HM2F filters give similar values on the speckle contrast.

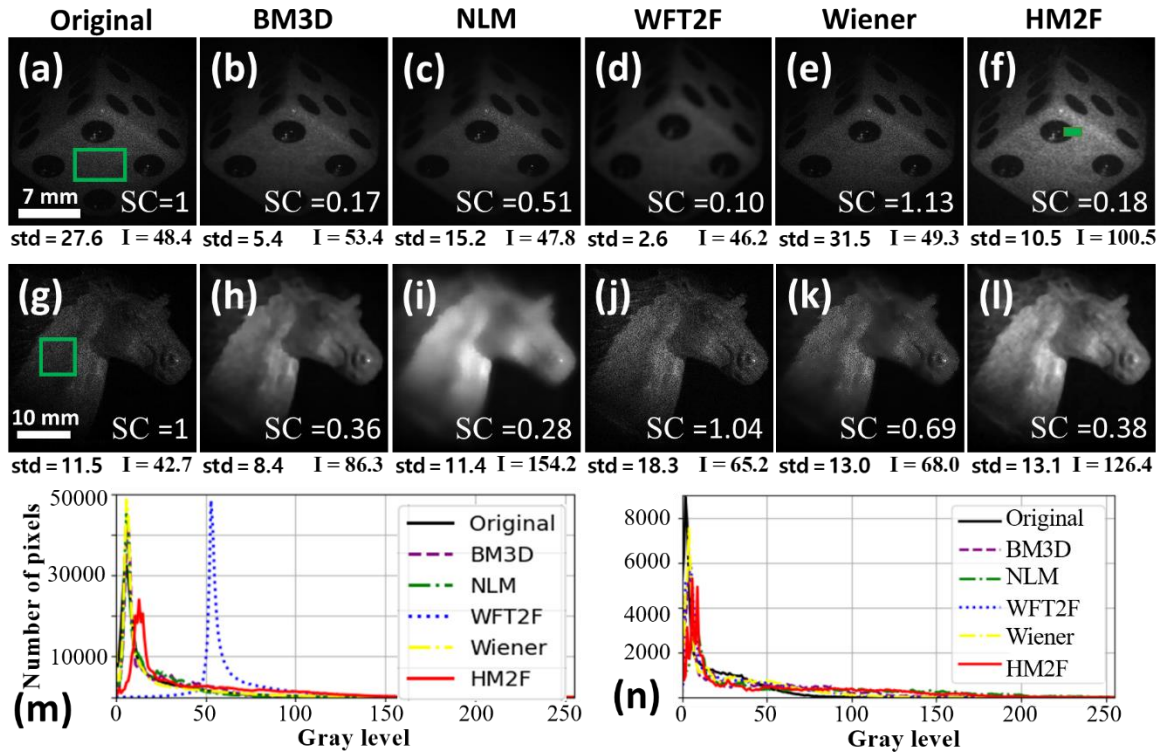


Fig. 8.5. DH results for dice (a – f), and horse (g – l). The methods used are BM3D, NLM, WFT2F, Wiener, and HM2F. Panels (m) and (n) show the histograms of the dice and horse, respectively. The average mean and standard deviation values in 10 different zones for the dice and horse model are reported below each panel.

Table 8.1 reports the FWHM values of the first derivative of the step function defined by a transverse green line, depicted in Fig. 8.5(f). Based on the FWHM values, the Wiener, BM3D, and HM2F approaches produce the denoised amplitude images with the smallest blurring effect. Nonetheless, although the Wiener filter has a lower reduction of the resolution, the speckle contrast is even higher than that of the other methods. For this sample object, the speckle contrast of the

denoised BM3D horse image is slightly lower than that of the denoised HM2F horse image ($SC = 0.36$ for the BM3D versus $SC = 0.38$ for the HM2F). Nonetheless, the HM2F method provides a final denoised amplitude image with improved contrast, as the histogram of Fig. 8.5(n) shows. Figures 8.5(m) – 8.5(n) show that the original noisy image and the denoised images for the dice and horse model present many pixels with low gray levels. The higher the amount of low gray levels is, the lower the mean value \bar{I} is and, consequently, the higher the speckle contrast is because SC is inversely proportional to \bar{I} . Nonetheless, the presence of low gray levels also affects the standard deviation value, resulting in low values of σ . For each image in Fig. 8.5, the mean and standard deviation is calculated in 10 different zones of 50×50 pixels for the dice model and 20×20 pixels for the horse model. The average value of these parameters is reported below each panel in Fig. 8.5.

Table 8.1 also reports the signal-noise ratio (SNR) of the original and denoising images for the dice and horse samples. The SNR value was estimated as $10\log_{10}(g_{\max} / std(g_b))$, where g_{\max} is the maximum value of the amplitude image over the whole field of view and $std(g_b)$ is the standard deviation of a region of the image in which there are no sample details. Because the SNR value depends on the region chosen to compute the standard deviation, 10 different areas within the dice and horse field of views were selected. Table 8.1 reports the average values of the SNR for these two DH images.

Table 8.1. Comparison for the BM3D, NLM, WFT2F, Wiener, and HM2F methods

	Original	BM3D	NLM	WFT2F	Wiener	HM2F
FMWHM						
(mm)	0.40	0.43	0.46	0.92	0.42	0.43
Dice						
SNR (dB)	9.9	18	14.2	20.3	9.3	14.3
Horse						
SNR (dB)	16.6	18.1	16.3	18.3	19.2	16.3

To evaluate the ability of the proposed method to reduce speckle contrast and mitigate the blurring effect in quantitative phase imaging recorded in the DHM system, an optical setup of the off-axis DHM system follows a Mach – Zehnder architecture has been used Fig. 8.2(c), operating in telecentric configuration and IP. The validation was performed using two samples, a star target of the commercial quantitative phase target from Benchmark Technologies and a transverse section of the head of a *Drosophila melanogaster* fly. For the star target, the illumination source was a diode laser of wavelength 532 nm, and the CMOS camera had 1920×1080 square pixels with a 2.4 μm pixel size. The DHM image system consisted of an infinity-corrected 40×/0.65 Olympus microscope objective and a TL of focal length 200 mm, resulting in an effective lateral magnification equal to 44.44×. On the other hand, the hologram of the *Drosophila melanogaster* fly was recorded using a HeNe laser of wavelength 633 nm, and a charge-coupled device camera with 1024×1024 square pixels of 6.9 μm size. The imaging system was set up using an infinity-corrected 10×/0.45 Nikon MO lens a TL of focal length 200 mm.

The star target allows measuring the experimental resolution limit (RL) by estimating the minimum resolvable star pattern and quantifying how much the resolution was reduced for each approach. The experimental RL was defined as the diameter in which the contrast of the reconstructed phase star pattern was reduced by 10% from its reference value, which is the contrast value for the diameter equal to 150 μm . The results of the star target are shown in Fig.8.6. For each method, the experimental RL is marked by a black-dashed circle original (i.e., noisy) reconstructed phase image, Figs. 8.6(b)-8.6(g) are the reconstructed phase images obtained by the different methods: CMF [Fig. 8.6(b)], BM3D [Fig. 8.6(c)], NLM [Fig. 8.6(d)], WFT2F [Fig.

8.6(e)], Wiener filter [Fig. 8.6(f)], and proposed HM2F [Fig. 8.6(g)]. For the methods that use a median approach [Figs. 8.6(b) – 8.6(g)], the kernel size applied was $[5 \times 5]$. Whereas the BM3D filter approach reduces the RL by a factor of $43\times$, the RL in the reconstructed phase image after applying the HM2F is not reduced. In addition to estimating the RL, the speckle contrast SC was measured as a metric to calculate the reduction in the speckle noise. The parameter SC was measured inside the yellow region marked in the inset of Fig. 8.6. The lower the value of SC is, the higher the reduction in the speckle noise is. The reconstructed phase image obtained by the NLM filter [Fig. 8.6(e)] is the most insensitive to the speckle noise (i.e., the smallest SC value). However, the RL was highly diminished by 12%, reducing the ability to discriminate the finer details. By contrast, the HM2F provided the second smallest SC value, resulting in the best method that minimized the tradeoff between the reduction in the RL and the speckle noise.

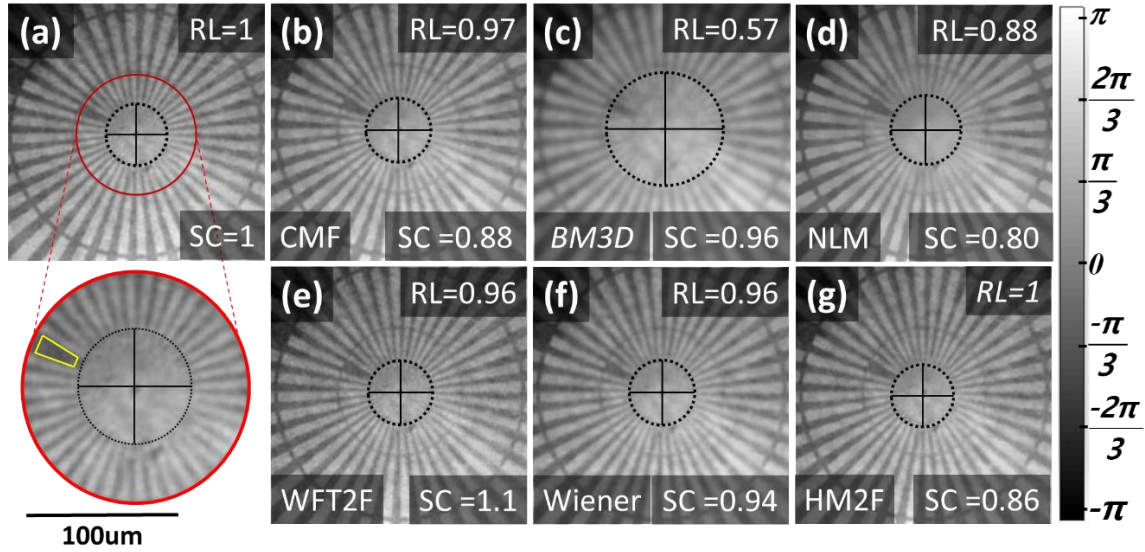


Fig. 8.6. Experimental results for the star target. The reconstructed phase image corresponds to (a) original noisy phase image, (b) denoised CMF phase image, (c) denoised BM3D phase image, (d) denoised NLM phase image, (e) denoised WFT2F phase image, (f) denoised Wiener phase image, and (g) denoised HM2F phase image. The kernel size for panels (b) and (g) is 5×5 .

Finally, Fig. 8.7 shows the reconstructed phase image provided by the BM3D, the NLM filter, the WFT2F, the Wiener filter, and the proposed HM2F for a section of the head of a *Drosophila melanogaster* fly, a biological complex sample. For comparison purposes, the noisy reconstructed phase image is shown in Fig. 8.7(a). For this sample, the BM3D and WFT2F approaches do not provide an optimal result. Nonetheless, the performance of the NLM, Wiener, and HM2F filters are similar. When an intense decorrelated noise corrupts the phase values, the reconstructed phase image has a high number of phase jumps in Fig. 8.7(g), marked by the white and black colors. We quantified the phase jumps in the original noisy image and denoised phase images inside the marked yellow region in Fig. 8.7(a). The phase jumps were reduced from 201 pixels in the original noisy image [Fig. 8.7(g)] to 195 pixels in the NLM denoised image [Fig. 8.7(h)], 176 pixels in the Wiener denoised image [Fig. 8.7(i)], and 79 pixels in the HM2F denoised image [Fig. 8.7(j)]. There is a reduction of 60% in the number of phase jumps for the HM2F, which shows that the proposed method provides a reconstructed phase image with reduced speckle noise.

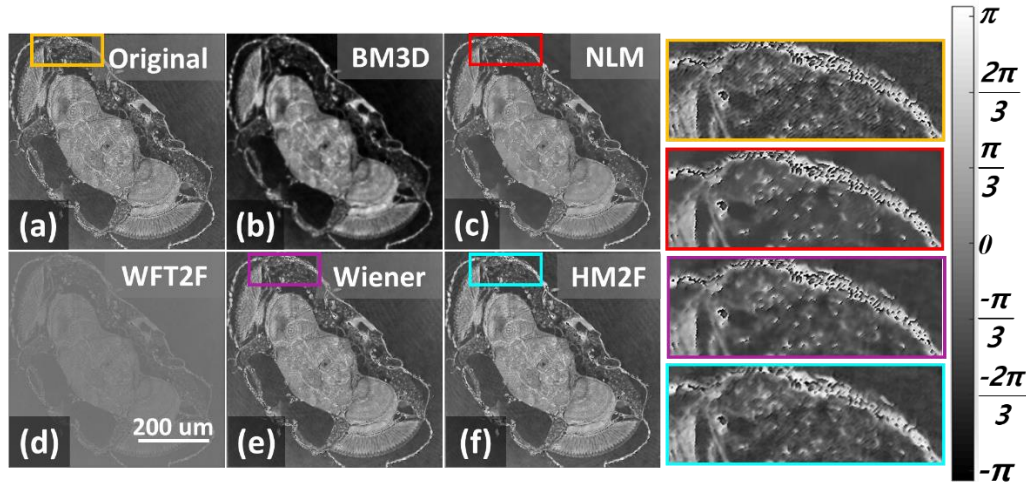


Fig. 8.7. Experimental results for a transverse section of the head of a *Drosophila melanogaster* fly.

8.4 Conclusion

In summary, the HM2F a single-shot denoising image method to reduce speckle noise, is presented in this chapter. The HM2F is based on the synergetic combination of two well-known approaches in image processing: the median and mean filters. The experimental results demonstrate that the HM2F reduces the speckle noise in color laser-based photography and both reconstructed amplitude and phase images from DH and DHM systems with a minimum addition of blurring effects. The performance of the HM2F approach was compared with that of the state-of-the-art methods in speckle denoising (e.g., BM3D, NLM, WFT2F, and Wiener). Based on our experimental results, the performance of the HM2F is more constant across the different types of images. For example, the WFT2F method does not provide satisfactory results for the dice and horse model [Figs. 8.7(d) and 8.6(e)]. By contrast, the NLM approach works for the dice image but fails for the horse model. The denoised Wiener image of the dice model presents more speckle noise (e.g., $C > 1$). Regarding the BM3D method, the denoised BM3D images for laser-based photography and DH present an adequate balance between the speckle reduction and the blurring effects. Nonetheless, this technique fails for quantitative phase imaging in DHM, reducing the RL by 43%. Another advantage of the HM2F is its simplicity in the required number of parameters and the computational processing time. While the HM2F and Wiener filter only require a single parameter (e.g., the kernel size) to provide a successful denoised image with reduced speckle noise, the WFT2F method requires the correct knowledge of the nine required parameters. Note that the maximum kernel size in the HM2F can be determined manually to obtain the best denoised HM2F image quickly and efficiently without requiring users experience or knowledge. Regarding the processing times, the average processing time for the images of the dice and horse model and the star target is 1.4 s for the HM2F, whereas the times for the Wiener filter, BM3D, NLM, and WFT2F methods are around 0.29, 9, 73, and 4390 times the processing times of the HM2F, respectively.

The processing times are reported based on a 10 Pro Windows-based AMD Ryzen 5 8192 MB RAM laptop computer. Based on these results, the simplicity of the technique, and the processing time, HM2F is proposed as an effective denoising tool for reducing the speckle noise in laser-based photography, DH, and DHM. To increase our method's use to the community, the HM2F method was implemented as a script for Python and MATLAB and is available in a public repository on GitHub — <https://oirl.github.io/Speckle-Hybrid-median-mean/>. The HM2F could be applied to any image distorted by speckle noise. Future work should further analyze the behavior of the HM2F in the Fourier Domain. Some preliminary results are shown in Appendix B. Although HM2F method reduces the speckle noise, it cannot retrieve the original sample's spectrum; some high spatial frequencies of the original image have been lost forever and some low spatial frequencies have been modified. Future work should compare the performance of HM2F with other methods in the Fourier domain.

9. CONCLUSIONS

In this Thesis, we have investigated and developed a series of novel computational methods for improving digital holographic microscopy (DHM), aiming to increase DHM systems' applicability by providing robust computational methods to reconstruct quantitative phase images with reduced processing time and user input. To sum up, we highlight the main achievements in this Thesis:

- We have implemented a fast-iterative PS-DHM method based on the demodulation of the different components of phase-shifted holograms. The proposed blind method only uses two-frame holograms with an arbitrary phase shift. The main advantage of the proposed method is the reduction in both the acquisition and computation time; the final phase image is restored using 33% fewer data since only two phase-shifted holograms are needed, as opposed to the standard three-frame PS algorithms. The only requirement of this approach is that the PS-DHM system must operate in a slightly off-axis regime without overlapping the spectrum of the $d \pm 1$ terms.
- We have implemented and developed an automatic and fast method to compensate for the tilt between the reference and object waves in off-axis DHM systems operating in telecentric configuration. This method reconstructs the quantitative phase distribution of unstained biological samples with a minimum or no phase perturbation. The input parameters in this method are minimum: an in-focus hologram, the source's wavelength, and the pixel size. Among the hallmarks of the proposed approach is the high accuracy in estimating the parameters of the digital reference wave. The interference angle is calculated precisely without compromising the computation time. The proposed method performs $40\times$ faster than a previously reported automatic approach based on nested loops and $2.3\times$ faster than the centroid-based algorithm.

- Whereas the previous implementation allows us to reconstruct phase images with minimum phase distortions at the image plane, we have upgraded such strategy for simultaneous and automatic reconstruction of phase images from out-of-focus holograms. The proposed method finds the best in-focus plane of pure phase objects by minimizing the TC sharpness function using the reconstructed amplitude images. This propagation distance is then used as an input parameter on a second minimization stage to reconstruct phase images with minimum phase aberrations. Our experimental results demonstrate the capability of the proposed method for high-quality quantitative phase imaging of biological samples. The advantages of this method are its reduced number of inputs and processing time, without penalizing the accuracy.
- To increase the applicability of DHM technology, we have created the pyDHM library for the numerical processing of digital holograms registered in DH and DHM systems. The library has PS techniques to reconstruct the phase distribution of samples in in-line and slightly off-axis DH and DHM systems. We have also implemented several automatic approaches to reconstruct phase images in single-shot off-axis DHM systems operating in telecentric and non-telecentric configurations. Finally, the library enables the numerical propagation of complex wavefields to provide in-focus amplitude and phase images.
- We have proposed a conditional generative adversarial network (cGAN) to fully reconstruct quantitative phase images from raw holograms without needing robust pre- or post-numerical procedures. Since the proposed cGAN model was trained using two customized metrics specifically selected based on DHM systems, the proposed cGAN model converges rapidly with a training time of approx. 2 h. The proposed cGAN method surpasses the conventional automatic reference method, convolutional autoencoders, and U-Nets, generating quantitative phase images with reduced noise and constant background level.

- To reduce the speckle noise with minimum penalization of the spatial resolution, we have proposed the HM2F, which combines the median and mean filters. The performance of the HM2F approach was compared with that of the state-of-the-art methods in speckle denoising (e.g., BM3D, NLM, WFT2F, and Wiener). Based on our experimental results, the performance of the HM2F is more constant across the different types of images. One advantage of the HM2F compared to the state-of-the-art methods is its simplicity in the required parameters and the computational processing time, making the HM2F an effective denoising tool for reducing the speckle noise in any image distorted by speckle noise.

9.1 List of peer-review Journal Publications

1. R. Castaneda, A. Doblas, and C. Trujillo, “pyDHM: A Python library for applications in Digital Holographic Microscopy,” PLoS ONE 17(10): e0275818 (2022).
<https://doi.org/10.1371/journal.pone.0275818>.
2. R. Castaneda, J. Garcia-Sucerquia, and A. Doblas, “Speckle noise reduction in coherent imaging systems via Hybrid Median-Mean Filter,” Opt. Engineering 60(12), 123107 (2021).
3. R. Castaneda, C. Trujillo, and A. Doblas, “Video-Rate Quantitative Phase Imaging Using a Digital Holographic Microscope and a Generative Adversarial Network,” Sensors 21(23), 8021 (2021).
4. R. Castaneda, and A. Doblas, “Fast-iterative automatic reconstruction method for quantitative phase image with reduced phase perturbations in off-axis digital holographic microscopy,” Appl. Opt. 60(32), 10214-10220 (2021).
5. R. Castaneda, C. Buitrago-Duque, J. Garcia-Sucerquia, and A. Doblas, “Fast-iterative blind phase-shifting digital holographic microscopy using two images,” Appl. Opt. 59(24) 7469-7476 (2020).

9.2 List of peer-review Conference Publications

1. R. Castaneda, C. Trujillo, and A. Doblas, “An Open-Source Python library for Digital Holographic Microscopy Imaging,” Optica Imaging and Applied Optics Congress, paper JTh2A.1 (2022).
2. R. Castaneda, A. Doblas, and C. Trujillo “Learning-based Quantitative Phase Imaging in Digital Holographic Microscopy: a comparison study between different models,” Optica Imaging and Applied Optics Congress, paper 3F3A.4 (2022).
3. R. Castaneda, C. Trujillo, and A. Doblas, “Learning-based method for full phase reconstruction of biological samples in digital holographic microscopy,” 2021 IEEE Photonics Conference (IPC) (2021).
4. R. Castaneda, and A. Doblas, “Joint Reconstruction Strategy for Telecentric-based Digital Holographic Microscopes, ” OSA Imaging and Applied Optics Congress, paper 3W5A.4 (2021).
5. R. Castaneda, J. Garcia-Sucerquia, and A. Doblas, “Synergetic combination of median filtered images to reduce speckle noise in digital holography (DH) and digital holographic microscopy (DHM),” OSA Imaging and Applied Optics Congress, paper DF4C.7 (2021).
6. R. Castaneda, C. Buitrago-Duque, J. Garcia-Sucerquia, A. Robinson, and A. Doblas, “Fast-iterative blind reconstruction algorithms for accurate quantitative phase images in phase-shifting digital holographic microscopy,” OSA Imaging and Applied Optics Congress, paper HTh5D.3, <https://doi.org/10.1364/DH.2020.HTh5D.3> (2020).
7. R. Castaneda, T. O’Connor, A. Doblas, and B. Javidi, “Reduction in data acquisition for resolution improvement in Structured Illumination Digital Holographic Microscopy,” Proc. SPIE 11402, 114020R-8 (2020).

9.3 List of international and national Conferences Presentation/Posters

1. R. Castaneda, C. Trujillo, and A. Doblas, “Concurrent execution of phase compensation and automatic focusing procedures for telecentric off-axis Digital Holographic Microscopy,” accepted to be presented on 2023 SPIE Photonics West, San Francisco (USA), 28 January – 2 February 2023.
2. R. Castaneda, C. Trujillo, and A. Doblas, “An Open-Source Python library for digital Holographic Microscopy Imaging,” Poster in Optica Imaging and Applied Optics Congress, July 2022.
3. R. Castaneda, A. Doblas, and C. Trujillo “Learning-based Quantitative Phase Imaging in Digital Holographic Microscopy: a comparison study between different models,” Oral Talk in Optica Imaging and Applied Optics Congress, July 2022.
4. R. Castaneda, C. Trujillo, and A. Doblas, “Learning-based free-of-distortion phase imaging,” Oral Talk in SPIE Meeting on Defense, Security & Sensing ’22, April 2022.
5. R. Castaneda, C. Trujillo, and A. Doblas, “Learning-based method for full phase reconstruction of biological samples in digital holographic microscopy,” Oral talk in IEEE Photonics Conference, October 2021.
6. R. Castaneda, and A. Doblas, “Joint Reconstruction Strategy for Telecentric-based Digital Holographic Microscopes,” OSA Imaging and Applied Optics Congress, July 2021.
7. R. Castaneda, J. Garcia-Sucerquia, and A. Doblas, “Synergetic combination of median filtered images to reduce speckle noise in digital holography (DH) and digital holographic microscopy (DHM),” OSA Imaging and Applied Optics Congress, July 2021.
8. R. Castaneda, C. Buitrago, J. Garcia-Sucerquia, A. Robinson, and A. Doblas, “Fast-iterative blind reconstruction algorithms for accurate quantitative phase images in phase-

shifting digital holographic microscopy,” OSA Imaging and Applied Optics Conference '20, June 2020.

9. R. Castaneda, A. Doblas, T. O'Connor, and B. Javidi, “Reduction in data acquisition for resolution improvement in Structured Illumination Digital Holographic Microscopy,” SPIE Meeting on Defense, Security & Commercial Sensing'20, Anaheim (USA), April 2020.

Appendix A: COMPARISON OF THE SPECKLE NOISE REDUCTION IN DH VIA HYBRID MEDIAN-MEAN FILTER OR CONVENTIONAL MEDIAN-FILTERED IMAGES

In Chapter 8, we have introduced the hybrid median-mean filter based on the spatial filtering of the reconstructed amplitude and/or phase images via a median filter with different kernel size around each pixel on the input image (i.e., the reconstructed noisy amplitude and/or phase image). In this HM2F approach, we have averaged two median-filtered images with two consecutive kernel sizes, resulting in a final image with reduced speckle contrast while the spatial resolution is kept up to 98% from the original value. Nonetheless, one could have averaged all the median-filtered images. In other words, one could have applied i times a median filter over the original noisy images (g), estimated the multiple median-filtered images (h), and averaged them with the same weight to provide the final denoising image (\hat{g}). Figure A.1 shows the pseudocode of this new approach, called median filter average (MFA), and the working principle for a maximum kernel size of $k = 5$. The difference between the MFA and HM2F images is the combination between the median-filtered images, h .

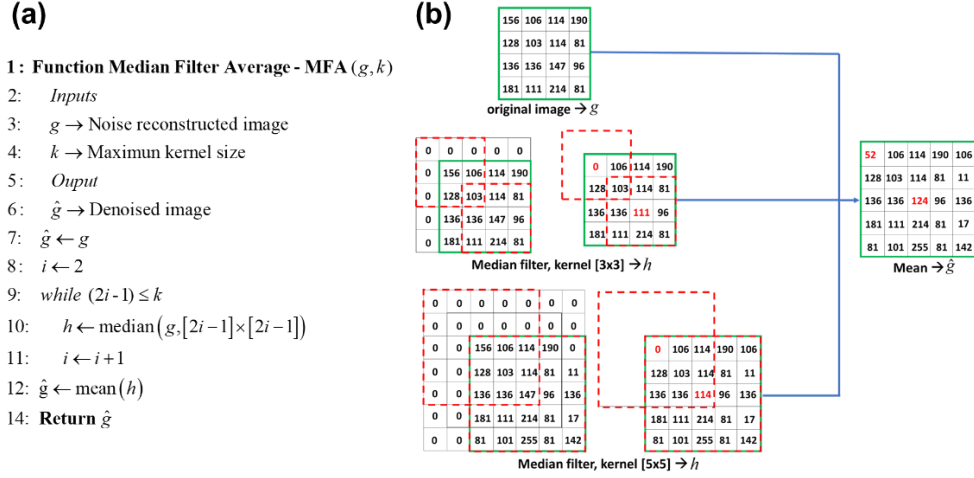


Fig. A.1. (a) Pseudocode of the median filter average (MFA) and its working principle for a maximum kernel size of $k = 5$.

To compare the performance of the MFA and the HM2F, we have used the hologram for blocks recorded in a DH system operating in off-axis architecture. All holograms were recorded using a setup operating in a Mach-Zehnder interferometer architecture. More information on the recording system is found in Chapter 8. Figure A.2 (a)-(f) compare the reconstructed amplitude images of a dice applying different kernel sizes using three different approaches: i) conventional median filter (i.e., applying a median filter with a particular value of the kernel size over the original image, Figs. A.2a&b), ii) median filter average (e.g., applying i - times a median filter with different kernel sizes over the original image and averaging all these images with the same weight, Figs. A.2c&d) and, iii) the proposed hybrid median-mean filter (Figs. A.2e&f). We have quantified and characterized the reduction in the speckle noise by plotting normalized speckle contrast versus the number of iterations for each kernel size (i.e., iteration) in Fig. A.2(g). Since the speckle contrast is highly dependent on the object information, the contrast speckle was measured in ten different square regions to provide an experimental error. From the quantitative values shown in Fig. A.2(g), one realizes that the speckle contrast reduces rapidly for the conventional median filter and HM2F compared to the one provided by the MFA. Comparing the reconstructed amplitude images from

the conventional median-filtered images and HM2F, one realizes that although the conventional median filter approach reduces the speckle noise faster than any technique, the HM2F provides final denoising images that present fewer blurring effects than the ones provided by the conventional median filter. On the other hand, for the same kernel size, the blurring effect is less significant using the MFA, compare Fig. A.2(c) vs. A.2(e) and A.2(a), and Fig. A.2(d) vs. A.2(f) and A.2(b). Nevertheless, the application of the MFA requires more iterations to achieve values of the speckle contrast equal to the values achieved for the conventional median filter and HM2F, as shown in Fig. A.2(g). In other words, the reduction in the speckle contrast provided by the MFA is not as rapid as the one obtained in the other two techniques. From these results, one can realize that the HM2F presents a tradeoff between reducing the speckle contrast and the blurring effects. A quantitative analysis of the blurring effects is provided using the reconstructed amplitude images provided by the three methods (images shown in the first column of Fig. A.2) for the kernel size of 9×9 . Because the first-order derivative of a step function (i.e., edge) is a Delta function, one can analyze the response of the methods by estimating the full width at half maximum (FWHM) of the first-order derivative of a step function. For each method, the step function is defined by the profile along the transverse direction marked by the green line in Fig. A.2(a). Figure A.2(h) shows the first-order derivative of the edge for the conventional median filter, MFA, and the HM2F. For each of these profiles, we have quantified the FWHM to be equal to 0.31 mm for the conventional median filter, and 0.29 mm for both MFA and HM2F. Because there is no difference on the measured FWHM, one can conclude that both methods (i.e., the MFA and HM2F) present the same blurring effect for a kernel size of 9×9 . Nonetheless, the HM2F filter shows a higher reduction in the speckle contrast, making it the most suitable method for mitigating the tradeoff between speckle noise and blurry effects. The increase of the kernel size in the HM2F provides a

final image with reduced speckle noise (i.e., lower value of the speckle contrast), but with worse spatial resolution, as compared Fig. A.2(d) vs. A.2(f).

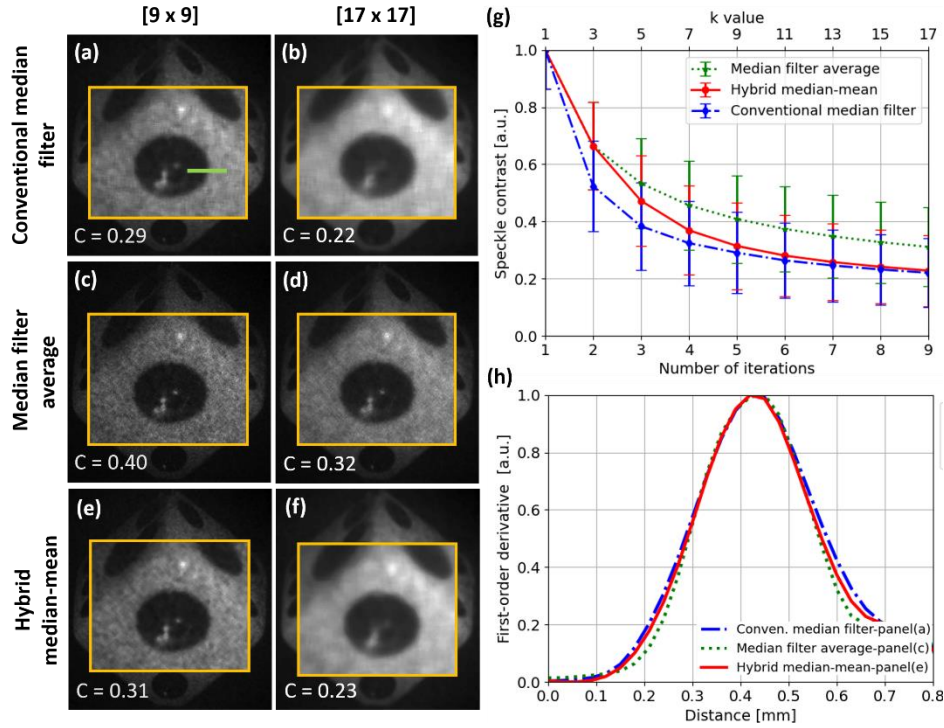


Fig. A.2. Denoising images obtained after applying three different approaches and two different kernel sizes. (a)-(b) Reconstructed images using the conventional median filter; (c)-(d) Reconstructed images using the median-filter average (MFA); (e)-(f) Reconstructed images using the HM2F. Panel (g) corresponds to the quantitative comparison of the speckle contrast versus numbers of iterations (i.e., kernel size) for the different methods. Panel (h) compares the response of the three methods by estimating the first-order derivate of a step function defined by the profile along the transverse direction marked by the green line in Fig. A2(a).

We have also compared the performance of MFA and HM2F approaches in QPI-DHM using a star target of the commercial QPI target from Benchmark Technologies. The results of the star target are shown in Fig. A.3. In each panel, the minimum resolved star pattern (i.e., experimental RL) is marked by a black dashed circles. Whereas Fig. A.3(a) shows the original (i.e., noisy) reconstructed phase image, Figs. A.3 (c-h) are the reconstructed phase images obtained by the conventional median filter [Fig. A.3c-d], MFA [Fig. A.3e-f], and HM2F [Fig. A.3g-h]. For all

methods two different kernel sizes were applied $[5 \times 5]$, and $[11 \times 11]$. Apart from estimating the resolution limit, we have also measured the dispersion parameter (D) as a metric to calculate the speckle noise reduction. The parameter D was measured inside the yellow region marked in the inset of Fig. A.3. This dispersion parameter was computed as $D = (\sigma / \bar{I}) \times 100$, where σ and \bar{I} are the standard deviation and mean intensity for each reconstructed phase image, respectively. The lower the value of D , the higher the reduction in the speckle noise. Both RL and D values are reported in Fig. A.3. The results shown in Figs. A.3(c), (e) and-(f) demonstrate that the conventional median filter and HM2F approach provide a dispersion parameter which is slightly reduced (2.09) compared to one measured in the original noisy phase image (2.18) for a kernel size $[5 \times 5]$. For this kernel size, the D values for the median filter average technique is almost identical to the one measured in the original image (2.20 vs. 2.18), indicating that the speckle noise has not been reduced when the MFA approach is applied. Note that although the conventional median and the HM2F approaches provide the same dispersion factor, $D = 2.09$, the HM2F approach is the only one that does not penalize the resolution limit. In contrast, the reconstructed phase images obtained using a kernel size $[11 \times 11]$ show tradeoff between the reduction in the speckle (i.e., reduced D values) and the penalization in the resolution limit. For example, the reconstructed phase image obtained by the conventional median filter [Fig. A.3(c)] is the most insensitive to the speckle noise (i.e., the smallest D value), however the resolution limit has been highly penalized by a factor 38%, reducing the ability to discriminate the finer details. Both the MFA and the HM2F approaches penalize the resolution limit by almost the same degree (0.80 and 0.79, respectively). Again, the HM2F approach provides the smallest D value, resulting in the best method which minimizes the tradeoff between the reduction in the resolution limit and the speckle noise. Finally, for comparison purposes, Fig. A.3(b) shows the reconstructed phase image using

the WFT2F method. We also estimated the resolution limit and the dispersion parameter to be equal to 0.79 and 2.80, respectively. Whereas the WFT2F method penalizes the resolution limit as much as the HM2F approach, the dispersion parameter is higher.

In summary, the HM2F method shows superior performance in DH and quantitative phase imaging than the MFA method, providing denoising images with reduced speckle noise whereas the resolution limit is kept constant in both approaches.

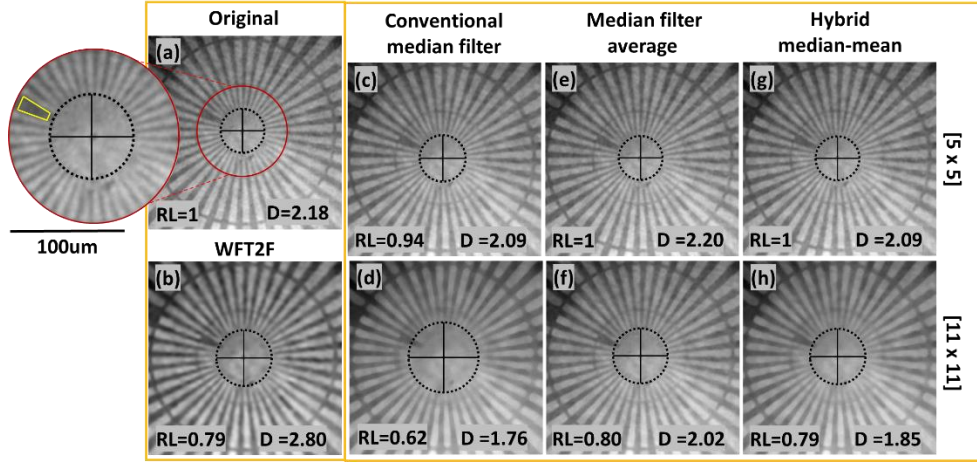


Fig. A.3. Experimental results for the star target. Panel (a) is the noisy reconstructed phase image. Panel (b) is the reconstructed phase images using the WFT2F method. Panels (c)-(d) reconstructed images using the conventional median filter; panels (e)-(f) correspond to the reconstructed images using the MFA. Finally, panels (g)-(h) are the reconstructed images using the HM2F.

Appendix B: FOURIER SPECTRUM ANALYSIS FOR THE HM2F

This Appendix aims to analyze the behavior of the HM2F in the Fourier Domain. For this reason, we have simulated a star target [Fig. B.1(a)], and added speckle noise on the simulated star target to generate four images with different speckle noise [Figs B.1(b - e)]. the speckle noise is added using the Matlab built-in function *imnoise*. This function requires an input image (the star target) to add the speckle noise and the variance. The variance of the speckle noise ranges 0.1 to 0.4. The higher the value of the variance, the higher the amount of speckle noise.

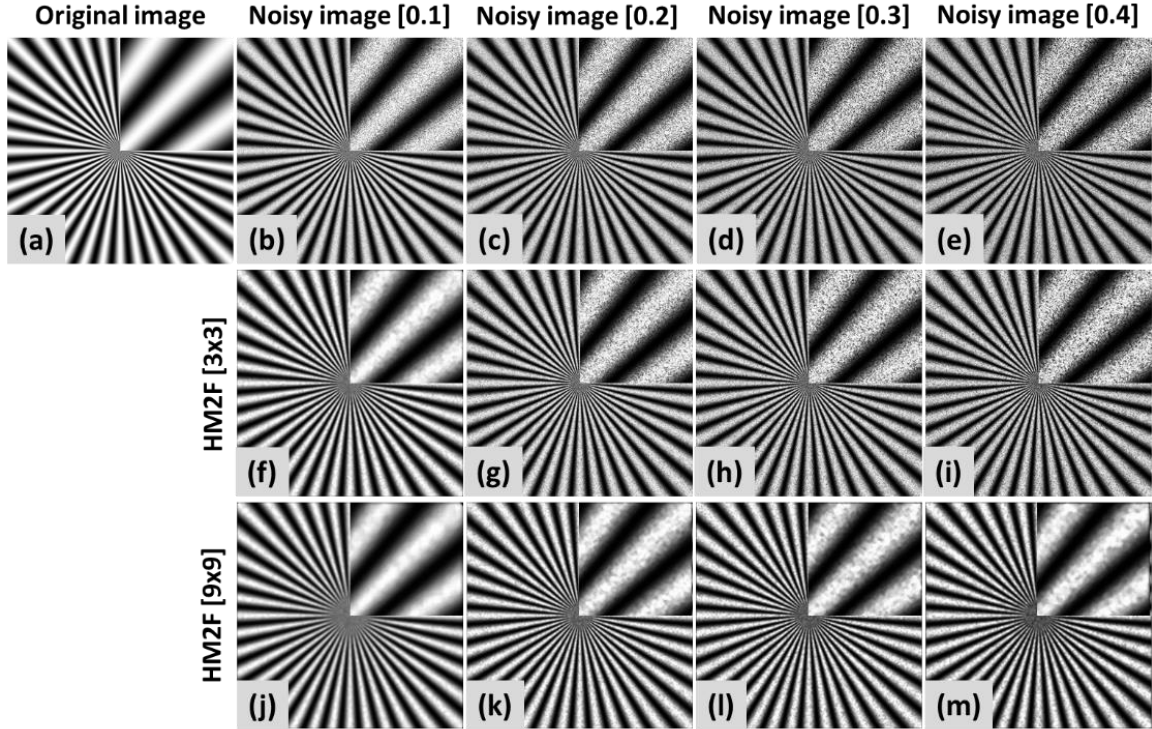


Fig. B.1. (a) Simulated star target (e.g., original/noiseless image). (b)-(e) Noisy images with speckle noise of different variance. (f)-(m) Denoising images after applying the HM2F for two different kernel size.

For each noisy image, we have applied the HM2F with different kernel values from $[3 \times 3]$ to $[11 \times 11]$. Two sets of these denoising images are shown in Figs B1(f - m). The goal of this

Appendix is to better understand how the speckle noise affects the spatial frequencies of the original star target and analyze if the application of the HM2F enables the retrieval of the original spectrum. In Fig. B2, we plotted the power spectral density for each noisy and denoising images. The power spectral density has been computed by averaging the absolute value of the Fourier transform of the image along the radial coordinate and calculated the $10\log_{10}$ of that value. Figure B2 shows the radial power spectral density for different values of speckle noise (e.g., different variance). In all the panels in Fig. B2, the black line corresponds to the noiseless/original star target. The blue curve represents the noisy profile after applying the speckle noise using the MATLAB built-in function *imnoise*. Note that, as expected, the speckle noise affects the weighting of medium and high frequencies, reducing the ability to observe the fine details of the object. In other words, speckle noise is a high-frequency noise. The higher the variance of the speckle noise, the higher the amount of frequencies affected, also distorting medium frequency content. We have applied different HM2F from kernel size equal to 3 (purple curves) to 11 (pink curves). The curves shows that although HM2F method reduces the speckle noise, it cannot retrieve the original sample's spectrum. The application of HM2F cannot generate several fine details; some high spatial frequencies of the original image have been lost forever. Also note that the HM2F has also modified the distribution of the low frequencies. Despite this unsuccessful result, there is still a need to compare the performance of other methods in the Fourier domain and/or propose a different denoising method.

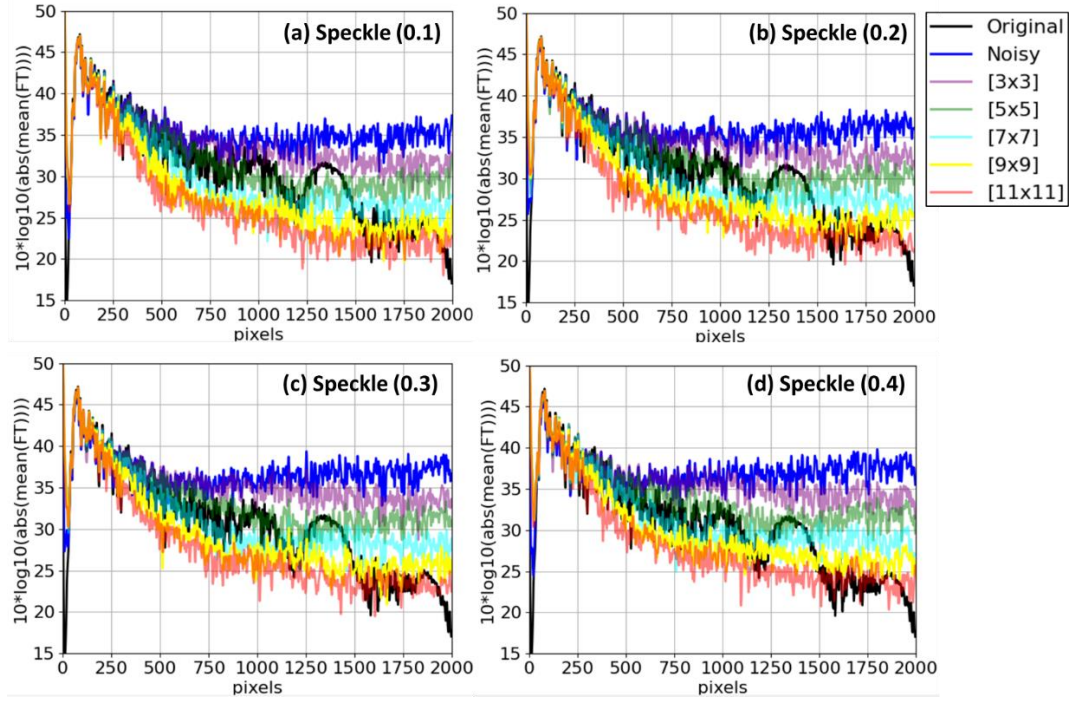


Fig. B.2. Power intensity spectrum vs the number of pixels. See the text for details.

REFERENCES

1. G. Stagaman and J. M. Forsyth, "Bright-field microscopy of semitransparent objects," *J. Opt. Soc. Am. A* **5**, 648 (1988).
2. P. F. Lott, *Handbook of Microscopy* (1985), Vol. 31.
3. D. A. Kempson, O. L. Thomas, and J. R. Baker, "A Simple Method for Phase-Contrast Microscopy," *J. Cell Sci.* **s3-89**, 351–358 (1948).
4. H. Search, C. Journals, A. Contact, M. Iopscience, and I. P. Address, "Phase-contrast Microscopy," *J. Sci. Instrum.* **19**, 71–75 (1942).
5. H. E. Rosenberger, "Differential Interference Contrast Microscopy," *Interpret. Tech. Microstruct. Anal.* 79–104 (1977).
6. C. Preza, D. L. Snyder, and J.-A. Conchello, "Theoretical development and experimental evaluation of imaging models for differential-interference-contrast microscopy," *J. Opt. Soc. Am. A* **16**, 2185 (1999).
7. R. Hoffman and L. Gross, "Modulation Contrast Microscope," *Appl. Opt.* **14**, 1169–1176 (1975).
8. Olympus, "Comparison of Phase Contrast and DIC Microscopy," <https://www.olympus-lifescience.com/en/microscope-resource/primer/techniques/dic/dicphasecomparison/>.
9. D. Shotton and N. White, "Confocal scanning microscopy: three-dimensional biological imaging," *Trends Biochem. Sci.* **14**, 435–439 (1989).
10. G. J. Brakenhoff, H. T. M. van der Voort, E. A. van Spronsen, and N. Nanninga, "Three-dimensional imaging in fluorescence by confocal scanning microscopy," *J. Microsc.* **153**, 151–159 (1989).
11. K. Svoboda and R. Yasuda, "Principles of Two-Photon Excitation Microscopy and Its Applications to Neuroscience," *Neuron* **50**, 823–839 (2006).
12. R. K. P. Benninger and D. W. Piston, "Two-photon excitation microscopy for the study of living cells and tissues," *Curr. Protoc. Cell Biol.* 1–24 (2013).
13. D. Huang, E. A. Swanson, C. P. Lin, J. S. Schuman, W. G. Stinson, W. Chang, M. R. Hee, T. Flotte, K. Gregory, and C. A. Puliafito, "Optical coherence tomography," *Science* **254**, 1178–1181 (1991).
14. W. Drexler and J. G. Fujimoto, *Optical Coherence Tomography: Technology and Applications*, Biological and Medical Physics, Biomedical Engineering (Springer Berlin Heidelberg, 2008).
15. M. K. Kim, *Digital Holographic Microscopy* (Springer, 2011).
16. G. Popescu, *Quantitative Phase Imaging of Cells and Tissues*, McGraw-Hill Biophotonics (McGraw-Hill Education, 2011).
17. B. Javidi, A. Carnicer, A. Anand, G. Barbastathis, W. Chen, P. Ferraro, J. W. Goodman, R. Horisaki, K. Khare, M. Kujawinska, R. A. Leitgeb, P. Marquet, T. Nomura, A. Ozcan, Y. Park, G. Pedrini, P. Picart, J. Rosen, G. Saavedra, N. T. Shaked, A. Stern, E. Tajahuerce, L. Tian, G. Wetzstein, and M. Yamaguchi, "Roadmap on digital holography," *Opt. Express* **29**, 35078–35118 (2021).

18. B. Bhaduri, C. Edwards, H. Pham, R. Zhou, T. H. Nguyen, L. L. Goddard, and G. Popescu, "Diffraction phase microscopy: principles and applications in materials and life sciences," *Adv. Opt. Photonics* **6**, 57 (2014).
19. Z. Wang, L. Millet, M. Mir, H. Ding, S. Unarunotai, J. Rogers, M. U. Gillette, and G. Popescu, "Spatial light interference microscopy (SLIM)," *Opt. Express* **19**, 1016–1026 (2011).
20. M. Trusiak, V. Mico, J. Garcia, and K. Paturski, "Quantitative phase imaging by single-shot Hilbert–Huang phase microscopy," *Opt. Lett.* **41**, 4344 (2016).
21. T. Cacace, V. Bianco, and P. Ferraro, "Quantitative phase imaging trends in biomedical applications," *Opt. Lasers Eng.* **135**, 106188 (2020).
22. Y. K. Park, C. Depeursinge, and G. Popescu, "Quantitative phase imaging in biomedicine," *Nat. Photonics* **12**, 578–589 (2018).
23. D. Bettenworth, P. Lenz, P. Krausewitz, M. Brückner, S. Ketelhut, D. Domagk, and B. Kemper, "Quantitative stain-free and continuous multimodal monitoring of wound healing in vitro with digital holographic microscopy," *PLoS One* **9**, (2014).
24. Z. El-Schich, A. L. Mölder, and A. G. Wingren, "Quantitative phase imaging for label-free analysis of cancer cells-focus on digital holographic microscopy," *Appl. Sci.* **8**, 1–16 (2018).
25. Z. El-Schish, A. Mölder, M. Sebesta, L. Gisselsson, K. Alm, and G. W. A, "Digital holographic microscopy – innovative and non-destructive analysis of living cells," *Microsc. Sci. Technol. Appl. Educ.* 1055–1062 (2010).
26. M. Puthia, P. Storm, A. Nadeem, S. Hsiung, and C. Svanborg, "Prevention and treatment of colon cancer by peroral administration of HAMLET (human α -lactalbumin made lethal to tumour cells)," *Gut* **63**, 131–142 (2014).
27. D. Boss, J. Kühn, P. Jourdain, C. Depeursinge, P. J. Magistretti, and P. Marquet, "Measurement of absolute cell volume, osmotic membrane water permeability, and refractive index of transmembrane water and solute flux by digital holographic microscopy," *J. Biomed. Opt.* (2013).
28. C. Mann, L. Yu, C.-M. Lo, and M. Kim, "High-resolution quantitative phase-contrast microscopy by digital holography," *Opt. Express* **13**, 8693–8698 (2005).
29. B. Kemper, P. Langehanenberg, I. Bredebusch, J. Schnekenburger, and G. von Bally, "Techniques and Applications of Digital Holographic Microscopy for Life Cell Imaging," in *Biophotonics 2007: Optics in Life Science* (Optical Society of America, 2007), p. 6633_12.
30. L. Rong, T. Latychevskaia, C. Chen, D. Wang, Z. Yu, X. Zhou, Z. Li, H. Huang, Y. Wang, and Z. Zhou, "Terahertz in-line digital holography of human hepatocellular carcinoma tissue," *Sci. Rep.* **5**, 1–6 (2015).
31. I. Moon, A. Anand, and M. Cruz, "Identification of Malaria-Infected Red Blood Cells Via Digital Shearing Interferometry and Statistical Inference Identification of Malaria-Infected Red Blood Cells Via Digital Shearing Interferometry," *IEEE Photonics J.* **5**, 6900207 (2013).
32. A. Anand, V. K. Chhaniwal, N. R. Patel, and B. Javidi, "Automatic identification of malaria-infected RBC with digital holographic microscopy using correlation algorithms," *IEEE Photonics J.* **4**, 1456–1464 (2012).
33. A. Doblas, E. Roche, F. J. Ampudia-Blasco, M. Martínez-Corral, G. Saavedra, and J. Garcia-Sucerquia, "Diabetes screening by telecentric digital holographic microscopy," *J. Microsc.* **261**,

285–290 (2016).

34. M. Mugnano, P. Memmolo, L. Miccio, F. Merola, V. Bianco, A. Bramanti, A. Gambale, R. Russo, I. Andolfo, A. Iolascon, and P. Ferraro, "Label-Free Optical Marker for Red-Blood-Cell Phenotyping of Inherited Anemias," *Anal. Chem.* **90**, 7495–7501 (2018).
35. Y. Bae, H. Song, S. B. Cho, N. H. Seong, and D. Y. Kim, "3D tracking of the brownian motion of polystyrene beads with DHM," *Digit. Hologr. Three-Dimensional Imaging*, DH 2012 3–5 (2012).
36. B. Kemper, D. Carl, J. Schnekenburger, I. Bredebusch, M. Schäfer, W. Domschke, and G. von Bally, "Investigation of living pancreas tumor cells by digital holographic microscopy," *J. Biomed. Opt.* **11**, 034005 (2006).
37. A. Mölder, M. Sebesta, M. Gustafsson, L. Gisselson, A. G. Wingren, and K. Alm, "Non-invasive, label-free cell counting and quantitative analysis of adherent cells using digital holography," *J. Microsc.* **232**, 240–247 (2008).
38. E. Sánchez-Ortiga, A. Doblas, G. Saavedra, M. Martínez-Corral, J. Garcia-Sucerquia, G. Saavedra, and J. Garcia-Sucerquia, "Off-axis digital holographic microscopy: practical design parameters for operating at diffraction limit," *Appl. Opt.* **53**, 2058–2066 (2014).
39. J. W. Goodman, *Statistical Optics*, A Wiley-Interscience Publication (Wiley, 1985).
40. R. C. Gonzalez and R. E. Woods, *Digital Image Processing* (Pearson, 2018).
41. A. Doblas, C. Buitrago-Duque, A. Robinson, and J. Garcia-Sucerquia, "Phase-shifting digital holographic microscopy with an iterative blind reconstruction algorithm," *Appl. Opt.* **58**, G311--G317 (2019).
42. "GitHub - PyDHM," <https://github.com/catrujilla/pyDHM>.
43. J. D. Gaskill, *Linear Systems, Fourier Transforms and Optics*, illustrate (Wiley, 1978).
44. E. Cuhe, P. Marquet, and C. Depeursinge, "Spatial filtering for zero-order and twin-image elimination in digital off-axis holography.," *Appl. Opt.* **39**, 4070–4075 (2000).
45. N. Verrier and M. Atlan, "Off-axis digital hologram reconstruction: some practical considerations," *Appl. Opt.* **50**, H136--H146 (2011).
46. P. Hariharan, *Optical Holography: Principles, Techniques, and Applications*, 2nd ed. (Cambridge University Press, 1996).
47. D. Malacara, M. Servin, and Z. Malacara, *Interferogram Analysis for Optical Testing*, Optical Science and Engineering (Taylor & Francis, 1998).
48. S. De Nicola, P. Ferraro, A. Finizio, and G. Pierattini, "Wave front reconstruction of Fresnel off-axis holograms with compensation of aberrations by means of phase-shifting digital holography," *Opt. Lasers Eng.* **37**, 331–340 (2002).
49. M. Kim, "Digital Holographic Microscopy," in *Digital Holographic Microscopy SE - II*, Springer Series in Optical Sciences (Springer New York, 2011), Vol. 162, pp. 149–190.
50. A. Doblas, "New advances in high-resolution optical microscopy," Doctoral dissertation, Universitat de Valencia, Spain (2015). <https://dialnet.unirioja.es/servlet/tesis?codigo=180630>
51. P. Ferraro, S. De Nicola, A. Finizio, G. Coppola, S. Grilli, C. Magro, and G. Pierattini, "Compensation of the Inherent Wave Front Curvature in Digital Holographic Coherent

- Microscopy for Quantitative Phase-Contrast Imaging," *Appl. Opt.* **42**, 1938–1946 (2003).
52. J. Min, B. Yfao, S. Ketelhut, C. Engwer, B. Greve, and B. Kemper, "Simple and fast spectral domain algorithm for quantitative phase imaging of living cells with digital holographic microscopy," *Opt. Lett.* **42**, 227–230 (2017).
 53. U. Schnars, C. Falldorf, J. Watson, and W. Jüptner, *Digital Holography and Wavefront Sensing*, 2nd ed. (Springer Berlin Heidelberg, 2015).
 54. T. Kreis, *Handbook of Holographic Interferometry: Optical and Digital Methods* (AKADEMIE VERLAG, 2005).
 55. J. F. Restrepo and J. Garcia-Sucerquia, "Magnified reconstruction of digitally recorded holograms by Fresnel-Bluestein transform.," *Appl. Opt.* **49**, 6430–6435 (2010).
 56. J.-P. Liu and T.-C. Poon, "Two-step-only quadrature phase-shifting digital holography Jung-Ping," *Opt. Lett.* **34**, 250–252 (2009).
 57. T. Tahara, R. Otani, Y. Arai, and Y. Takaki, "Multiwavelength Digital Holography and Phase-Shifting Interferometry Selectively Extracting Wavelength Information: Phase-Division Multiplexing (PDM) of Wavelengths," *Hologr. Mater. Opt. Syst.* (2017).
 58. M. Rivera, O. Dalmau, A. Gonzalez, and F. Hernandez-Lopez, "Two-step fringe pattern analysis with a Gabor filter bank," *Opt. Lasers Eng.* **85**, 29–37 (2016).
 59. J. Deng, H. Wang, F. Zhang, D. Zhang, L. Zhong, and X. Lu, "Two-step phase demodulation algorithm based on the extreme value of interference," *Opt. Lett.* **37**, 4669 (2012).
 60. V. H. Flores, A. Reyes-Figueroa, C. Carrillo-Delgado, and M. Rivera, "Two-step phase shifting algorithms: Where are we?," *Opt. Laser Technol.* **126**, 106105 (2020).
 61. J. Han, P. Gao, B. Yao, Y. Gu, and M. Huang, "Slightly off-axis interferometry for microscopy with second wavelength assistance," *Appl. Opt.* **50**, 2793–2798 (2011).
 62. P. Gao, B. Yao, J. Min, R. Guo, J. Zheng, T. Ye, I. Harder, V. Nercissian, and K. Mantel, "Parallel two-step phase-shifting point-diffraction interferometry for microscopy based on a pair of cube beamsplitters," *Opt. Express* **19**, 1930 (2011).
 63. P. Gao, B. Yao, I. Harder, J. Min, R. Guo, J. Zheng, and T. Ye, "Parallel two-step phase-shifting digital holograph microscopy based on a grating pair," *J. Opt. Soc. Am. A* **28**, 434 (2011).
 64. N. T. Shaked, Y. Zhu, M. T. Rinehart, and A. Wax, "Two-step-only phase-shifting interferometry with optimized detector bandwidth for microscopy of live cells," *Opt. Express* **17**, 15585 (2009).
 65. X. F. Meng, L. Z. Cai, Y. R. Wang, X. L. Yang, X. F. Xu, G. Y. Dong, X. X. Shen, and X. C. Cheng, "Wavefront reconstruction by two-step generalized phase-shifting interferometry," *Opt. Commun.* **281**, 5701–5705 (2008).
 66. W. T. Hsieh, M. K. Kuo, H. F. Yau, and C. C. Chang, "A simple arbitrary phase-step digital holographic reconstruction approach without blurring using two holograms," *Opt. Rev.* **16**, 466–471 (2009).
 67. C.-C. Chang, W. T. Hsieh, and M. K. Kuo, "Digital holography with arbitrary phase-step reconstruction using multiple holograms," *Hologr. Adv. Mod. Trends* **7358**, 735813 (2009).
 68. X. Yu, R. Song, X. Li, P. Jiang, K. Wang, Z. Zhang, and T. Shen, "Accurate blind extraction of arbitrary unknown phase shifts by an improved quantum-behaved particle swarm optimization in

- generalized phase-shifting interferometry," *OSA Contin.* **2**, 3404–3414 (2019).
69. C.-S. Guo, B.-Y. Wang, B. Sha, Y.-J. Lu, and M.-Y. Xu, "Phase derivative method for reconstruction of slightly off-axis digital holograms," *Opt. Express* **22**, 30553 (2014).
 70. M. Trusiak, J.-A. Picazo-Bueno, K. Patorski, P. Zdańkowski, and V. Mico, "Single-shot two-frame π -shifted spatially multiplexed interference phase microscopy," *J. Biomed. Opt.* **24**, 1–8 (2019).
 71. J. A. Picazo-Bueno, M. Trusiak, and V. Micó, "Single-shot slightly off-axis digital holographic microscopy with add-on module based on beamsplitter cube," *Opt. Express* **27**, 5655 (2019).
 72. R. Castañeda, C. Buitrago-Duque, J. Garcia-Sucerquia, and A. Doblas, "Fast-iterative blind phase-shifting digital holographic microscopy using two images," *Appl. Opt.* **59**, 7469 (2020).
 73. R. Castaneda, C. Buitrago, J. Garcia-Sucerquia, and A. Doblas, "Fast-iterative blind reconstruction algorithms for accurate quantitative phase images in phase-shifting digital holographic microscopy," in (OSA Imaging and Applied Optics Congress, paper HTh5D.3, 2020).
 74. A. Doblas, E. Sánchez-Ortiga, M. Martínez-Corral, G. Saavedra, P. Andrés, and J. Garcia-Sucerquia, "Shift-variant digital holographic microscopy: inaccuracies in quantitative phase imaging," *Opt. Lett.* **38**, 1352–4 (2013).
 75. A. Doblas, E. Sánchez-Ortiga, M. Martínez-Corral, G. Saavedra, and J. Garcia-Sucerquia, "Accurate single-shot quantitative phase imaging of biological specimens with telecentric digital holographic microscopy," *J. Biomed. Opt.* **19**, 46022 (2014).
 76. M. León-Rodríguez, J. A. Rayas, R. R. Cordero, A. Martínez-García, A. Martínez-Gonzalez, A. Téllez-Quñones, P. Yañez-Contreras, and O. Medina-Cázares, "Dual-plane slightly off-axis digital holography based on a single cube beam splitter," *Appl. Opt.* **57**, 2727 (2018).
 77. A. Lipson, S. G. Lipson, and H. Lipson, *Optical Physics* (Cambridge University Press, 2010).
 78. X. He, C. V. Nguyen, M. Pratap, Y. Zheng, Y. Wang, D. R. Nisbet, R. J. Williams, M. Rug, A. G. Maier, and W. M. Lee, "Automated Fourier space region-recognition filtering for off-axis digital holographic microscopy," *Biomed. Opt. Express* **7**, 3111 (2016).
 79. D. Carl, B. Kemper, G. Wernicke, and G. von Bally, "Parameter-optimized digital holographic microscope for high-resolution living-cell analysis," *Appl. Opt.* **43**, 6536–6544 (2004).
 80. C. Trujillo, R. Castañeda, P. Piedrahita-Quintero, and J. Garcia-Sucerquia, "Automatic full compensation of quantitative phase imaging in off-axis digital holographic microscopy," *Appl. Opt.* **55**, (2016).
 81. T. Colomb, E. Cuche, F. Charrière, J. Kühn, N. Aspert, F. Montfort, P. Marquet, and C. Depeursinge, "Automatic procedure for aberration compensation in digital holographic microscopy and applications to specimen shape compensation," *Appl. Opt.* **45**, 851–863 (2006).
 82. T. Nguyen, V. Bui, V. Lam, C. B. Raub, L.-C. Chang, and G. Nehmetallah, "Automatic phase aberration compensation for digital holographic microscopy based on deep learning background detection," *Opt. Express* **25**, 15043–15057 (2017).
 83. S. Liu, W. Xiao, and F. Pan, "Automatic compensation of phase aberrations in digital holographic microscopy for living cells investigation by using spectral energy analysis," *Opt. Laser Technol.* **57**, 169–174 (2014).
 84. R. Castaneda and A. Doblas, "Fast-iterative automatic reconstruction method for quantitative phase image with reduced phase perturbations in off-axis digital holographic microscopy," *Appl.*

- Opt. **60**, 10214–10220 (2021).
85. R. Castaneda and A. Doblas, "Joint Reconstruction Strategy for Telecentric-based Digital Holographic Microscopes," in *In 3D Image Acquisition and Display Conference OSA Technical Digest Series (Optical Society of America, 2021)* (n.d.), p. paper 3W5A.4.
 86. B. Rappaz, P. Marquet, E. Cuhe, Y. Emery, C. Depeursinge, and P. J. Magistretti, "Measurement of the integral refractive index and dynamic cell morphometry of living cells with digital holographic microscopy," *Opt. Express* (2005).
 87. C. Hayes-Rounds, B. Bogue-Jimenez, J. I. Garcia-Sucerquia, O. Skalli, and A. Doblas, "Advantages of Fresnel biprism-based digital holographic microscopy in quantitative phase imaging," *J. Biomed. Opt.* **25**, 1–11 (2020).
 88. "Optical Imaging Research Laboratory, University of Memphis, tuDHM - GitHub," <https://oirl.github.io/tuDHM/>.
 89. M. Molaei and J. Sheng, "Imaging bacterial 3D motion using digital in-line holographic microscopy and correlation-based de-noising algorithm," *Opt. Express* **22**, 32119 (2014).
 90. A. Wang, R. F. Garmann, and V. N. Manoharan, "Tracking E coli runs and tumbles with scattering solutions and digital holographic microscopy," *Opt. Express* **24**, 23719 (2016).
 91. H. Zhang, T. Stangner, K. Wiklund, A. Rodriguez, and M. Andersson, "UmUTracker: A versatile MATLAB program for automated particle tracking of 2D light microscopy or 3D digital holography data," *Comput. Phys. Commun.* **219**, 390–399 (2017).
 92. X. Yu, C. Liu, J. Hong, and M. K. Kim, "Four dimensional motility tracking of biological cells by digital holographic microscopy," *Opt. InfoBase Conf. Pap.* 4–6 (2013).
 93. J. Persson, A. Mölder, S. Pettersson, and K. Alm, "Cell motility studies using digital holographic microscopy," *Microsc. Sci. Technol. Appl. Educ.* 1063–1072 (2010).
 94. D. van Grootheest, T. Agbana, J.-C. Diehl, A. van Diepen, V. Bezzubik, and G. Vdovin, "Large volume holographic imaging for biological sample analysis.," *J. Biomed. Opt.* **26**, (2021).
 95. F. Verpillata, F. Jouda, P. Desbiollesa, and M. Grossa, "Three dimensional tracking of gold nanoparticles using digital holographic microscopy," *Opt. InfoBase Conf. Pap.* **8090**, 1–4 (2011).
 96. P. Memmolo, L. Miccio, M. Paturzo, G. Di Caprio, G. Coppola, P. A. Netti, and P. Ferraro, "Recent advances in holographic 3D particle tracking," *Adv. Opt. Photonics* **7**, 713 (2015).
 97. F. Dubois, C. Schockaert, N. Callens, and C. Yourassowsky, "Focus plane detection criteria in digital holography microscopy by amplitude analysis," *Opt. Express* **14**, 5895–5908 (2006).
 98. P. Langehanenberg, G. Bally, and B. Kemper, "Autofocusing in digital holographic microscopy," *3D Res.* **2**, 1–11 (2011).
 99. P. Langehanenberg, B. Kemper, D. Dirksen, and G. Von Bally, "Autofocusing in digital holographic phase contrast microscopy on pure phase objects for live cell imaging," *Appl. Opt.* **47**, (2008).
 100. D. G. Sirico, L. Miccio, Z. Wang, P. Memmolo, W. Xiao, L. Che, L. Xin, F. Pan, and P. Ferraro, "Compensation of aberrations in holographic microscopes: main strategies and applications," *Appl. Phys. B* **128**, 78 (2022).
 101. C. A. Trujillo and J. Garcia-Sucerquia, "Automatic method for focusing biological specimens in

- digital lensless holographic microscopy," *Opt. Lett.* **39**, 2569 (2014).
102. P. Memmolo, C. Distanto, M. Paturzo, A. Finizio, P. Ferraro, and B. Javidi, "Automatic focusing in digital holography and its application to stretched holograms," *Opt. Lett.* **36**, 1945–1947 (2011).
 103. H. A. İlhan, M. Doğan, and M. Özcan, "Digital holographic microscopy and focusing methods based on image sharpness," *J. Microsc.* **255**, 138–149 (2014).
 104. F. C. A. Groen, I. T. Young, and G. Ligthart, "A comparison of different focus functions for use in autofocus algorithms," *Cytometry* **6**, 81–91 (1985).
 105. J. L. Pech-Pacheco, G. Cristobal, J. Chamorro-Martinez, and J. Fernandez-Valdivia, "Diatom autofocus in brightfield microscopy: a comparative study," in *Proceedings 15th International Conference on Pattern Recognition. ICPR-2000* (2000), Vol. 3, pp. 314–317 vol.3.
 106. T. Pitkäaho, A. Manninen, and T. J. Naughton, "Deep convolutional neural networks and digital holographic microscopy for in-focus depth estimation of microscopic objects," 52–59 (2017).
 107. Z. Ren, Z. Xu, and E. Y. Lam, "Autofocusing in digital holography using deep learning," in *Three-Dimensional and Multidimensional Microscopy: Image Acquisition and Processing XXV*, T. G. Brown, C. J. Cogswell, and T. Wilson, eds. (SPIE, 2018), Vol. 10499, p. 104991V.
 108. J. Li and P. Picart, "Calculating Diffraction by Fast Fourier Transform," in *Digital Holography* (John Wiley & Sons, Inc., 2012), pp. 77–114.
 109. T. Kreis, *Handbook of Holographic Interferometry* (Wiley-VCH Verlag GmbH & Co. KGaA, 2004).
 110. R. Castañeda, W. Toro, and J. Garcia-Sucerquia, "Evaluation of the limits of application for numerical diffraction methods based on basic optics concepts," *Optik* **126**, 5963–5970 (2015).
 111. P. E. Gill and W. Murray, "Quasi-newton methods for unconstrained optimization," *IMA J. Appl. Math. (Institute Math. Its Appl.)* **9**, 91–108 (1972).
 112. A. Doblas, C. Hayes-Rounds, R. Isaac, and F. Perez, "Single-Shot 3D Topography of Transmissive and Reflective Samples with a Dual-Mode Telecentric-Based Digital Holographic Microscope," *Sensors* **22**, 3793 (2022).
 113. M. A. Herráez, D. R. Burton, M. J. Lalor, and M. A. Gdeisat, "Fast two-dimensional phase-unwrapping algorithm based on sorting by reliability following a noncontinuous path," *Appl. Opt.* **41**, 7437 (2002).
 114. R. Castañeda, C. Trujillo, and A. Doblas, "pyDHM: A Python library for applications in digital holographic microscopy," *PLoS One* **17**, 1–23 (2022).
 115. R. Castaneda, C. Trujillo, and A. Doblas, "An Open-Source Python library for Digital Holographic Microscopy Imaging," in *Imaging and Applied Optics Congress 2022 (3D, AOA, COSI, ISA, PcAOP)*, Technical Digest Series (Optica Publishing Group, 2022), p. JTh2A.1.
 116. M. K. Kim, *Digital Holographic Microscopy. Principles, Techniques, and Applications* (Springer, 2011).
 117. D. Malacara, "Optical shop testing," *Opt. shop Test.* Ed. by Daniel Malacara. 3rd ed. Publ. by John Wiley (2007).
 118. E. Cuche, P. Marquet, and C. Depeursinge, "Simultaneous amplitude-contrast and quantitative phase-contrast microscopy by numerical reconstruction of Fresnel off-axis holograms," *Appl. Opt.*

- 38**, 6994–7001 (1999).
119. T. Colomb, F. Montfort, J. Kühn, N. Aspert, E. Cuche, A. Marian, F. Charrière, S. Bourquin, P. Marquet, and C. Depeursinge, "Numerical parametric lens for shifting, magnification, and complete aberration compensation in digital holographic microscopy," *J. Opt. Soc. Am. A* **23**, 3177–3190 (2006).
 120. D. Mendlovic, Z. Zalevsky, and N. Konforti, "Computation considerations and fast algorithms for calculating the diffraction integral," *J. Mod. Opt.* **44**, 407–414 (1997).
 121. P. Picart and J. Leval, "General theoretical formulation of image formation in digital Fresnel holography: erratum.," *J. Opt. Soc. Am. A. Opt. Image Sci. Vis.* **26**, 244 (2009).
 122. T. Shimobaba, N. Takada, Y. Ichihashi, N. Masuda, and T. Ito, "Fast numerical wave-optics library using a graphics processing unit: GWO library, and its applications to holography," in *Biomedical Optics and 3-D Imaging* (Optica Publishing Group, 2010), p. JMA15.
 123. T. Shimobaba, J. Weng, T. Sakurai, N. Okada, T. Nishitsuji, N. Takada, A. Shiraki, N. Masuda, and T. Ito, "Computational wave optics library for C++: CWO++ library," *Comput. Phys. Commun.* **183**, 1124–1138 (2012).
 124. P. Piedrahita, R. Castañeda, and J. Garcia-Sucerquia, "Numerical Propagation plugin for ImageJ," .
 125. M. D. Abràmoff, P. J. Magalhães, and S. J. Ram, "Image processing with ImageJ," *Biophotonics Int.* **11**, 36–43 (2004).
 126. P. Piedrahita-Quintero, C. Trujillo, and J. Garcia-Sucerquia, "JDiffraction: A GPGPU-accelerated JAVA library for numerical propagation of scalar wave fields," *Comput. Phys. Commun.* (2017).
 127. C. Trujillo, P. Piedrahita-Quintero, and J. Garcia-Sucerquia, "Digital lensless holographic microscopy: numerical simulation and reconstruction with ImageJ," *Appl. Opt.* **59**, 5788 (2020).
 128. J. Hong, Y. Kim, H. Bae, and S. Hong, "OpenHolo: Open source library for hologram generation, reconstruction and signal processing," in *Imaging and Applied Optics Congress* (Optica Publishing Group, 2020), p. HF3G.1.
 129. S. Barkley, T. G. Dimiduk, J. Fung, D. M. Kaz, V. N. Manoharan, R. McGorty, R. W. Perry, and A. Wang, "Holographic Microscopy With Python and HoloPy," *Comput. Sci. Eng.* **22**, 72–82 (2020).
 130. R. Castaneda, J.-G. Garcia, and A. Doblas, "Speckle Noise Reduction in Digital Holography via a Hybrid Median-Mean Approach," *Opt. Eng.* **60**, 123107 (2021).
 131. C. Trujillo, A. Doblas, G. Saavedra, M. Martínez-Corral, and J. García-Sucerquia, "Phase-shifting by means of an electronically tunable lens: quantitative phase imaging of biological specimens with digital holographic microscopy," *Opt. Lett.* **41**, 1416 (2016).
 132. R. Castañeda, D. Hincapie, and J. Garcia-Sucerquia, "Experimental study of the effects of the ratio of intensities of the reference and object waves on the performance of off-axis digital holography," *Opt. - Int. J. Light Electron Opt.* **132**, 274–283 (2017).
 133. "pyDHM," <https://catrujilla.github.io/pyDHM/%0A>.
 134. "pyDHM library - how to install using pycharm," <https://www.youtube.com/watch?v=h76nZM6JpXo>.
 135. "how to use the blind 2-frame phase shifting function (BPS2)," <https://www.youtube.com/watch?v=Z9o0ODe1IUQ>.

136. "how to use the FRS function to reconstruct phase images with minimum phase distortions," <https://www.youtube.com/watch?v=CMHbF0uoWDk>.
137. "how to use the angular spectrum function to focus complex distributions computationally," <https://www.youtube.com/watch?v=3p6Bsh048Hw&t=254s>.
138. A. Anand, V. K. Chhaniwal, and B. Javidi, "Real-time digital holographic microscopy for phase contrast 3D imaging of dynamic phenomena," *IEEE/OSA J. Disp. Technol.* (2010).
139. R. Castaneda, C. Trujillo, and A. Doblas, "Video-rate quantitative phase imaging using a digital holographic microscope and a generative adversarial network," *Sensors* **21**, 1–16 (2021).
140. R. Castañeda, C. Trujillo, and A. Doblas, "Learning-based method for full phase reconstruction of biological samples in digital holographic microscopy," in *2021 IEEE Photonics Conference (IPC)* (2021), pp. 1–2.
141. R. Castaneda, A. Doblas, and C. Trujillo, "Learning-based Quantitative Phase Imaging in Digital Holographic Microscopy: a comparison study between different models," in *Imaging and Applied Optics Congress 2022 (3D, AOA, COSI, ISA, PcAOP)*, Technical Digest Series (Optica Publishing Group, 2022), p. 3F3A.4.
142. M. K. Kim, "Principles and techniques of digital holographic microscopy," *SPIE Rev.* **1**, 18005 (2010).
143. B. Rappaz, F. Charrière, C. Depeursinge, P. J. Magistretti, and P. Marquet, "Simultaneous cell morphometry and refractive index measurement with dual-wavelength digital holographic microscopy and dye-enhanced dispersion of perfusion medium," *Opt. Lett.* (2008).
144. T. Pitkäaho, A. Manninen, and T. J. Naughton, "Focus prediction in digital holographic microscopy using deep convolutional neural networks," *Appl. Opt.* **58**, A202--A208 (2019).
145. T. Liu, Z. Wei, Y. Rivenson, K. de Haan, Y. Zhang, Y. Wu, and A. Ozcan, "Color Holographic Microscopy Using a Deep Neural Network," in *Conference on Lasers and Electro-Optics* (Optical Society of America, 2020), p. AM11.1.
146. D. Yin, Z. Gu, Y. Zhang, F. Gu, S. Nie, J. Ma, and C. Yuan, "Digital holographic reconstruction based on deep learning framework with unpaired data," *IEEE Photonics J.* **12**, (2020).
147. Y. Rivenson, Y. Wu, and A. Ozcan, "Deep learning in holography and coherent imaging," *Light Sci. Appl.* **8**, (2019).
148. K. Wang, J. Dou, Q. Kemao, J. Di, and J. Zhao, "Y-Net: a one-to-two deep learning framework for digital holographic reconstruction," *Opt. Lett.* **44**, 4765–4768 (2019).
149. R. Vijayanagaram, "Application of Deep Learning Techniques to Digital Holographic Microscopy for Numerical Reconstruction," (2020).
150. J. Di, J. Wu, K. Wang, J. Tang, Y. Li, and J. Zhao, "Quantitative Phase Imaging Using Deep Learning-Based Holographic Microscope," **9**, 1–7 (2021).
151. I. Moon, K. Jaferzadeh, Y. Kim, and B. Javidi, "Noise-free quantitative phase imaging in Gabor holography with conditional generative adversarial network," *Opt. Express* **28**, 26284–26301 (2020).
152. S. Ma, Q. Liu, Y. Yu, Y. Luo, and S. Wang, "Quantitative phase imaging in digital holographic microscopy based on image inpainting using a two-stage generative adversarial network," *Opt. Express* **29**, 24928–24946 (2021).

153. M. A. Ionescu, *Feature Learning with Autoencoders for Automated Machine Learning* (University of Pennsylvania, 2019).
154. T. Shimobaba, Y. Endo, R. Hirayama, Y. Nagahama, T. Takahashi, T. Nishitsuji, T. Kakue, A. Shiraki, N. Takada, N. Masuda, and T. Ito, "Autoencoder-based holographic image restoration," *Appl. Opt.* **56**, F27--F30 (2017).
155. V. Bianco, P. Memmolo, M. Leo, S. Montresor, C. Distanto, M. Paturzo, P. Picart, B. Javidi, and P. Ferraro, "Strategies for reducing speckle noise in digital holography," *Light. Sci. Appl.* **7**, 48 (2018).
156. P. Isola, J.-Y. Zhu, T. Zhou, and A. A. Efros, "Image-to-image translation with conditional adversarial networks," in *ArXiv* 1611.07004 (2017).
157. D. P. Kingma and J. L. Ba, "Adam: A method for stochastic optimization," in *ArXiv* 1412.6980, 1–15 (2015).
158. O. Ronneberger, P. Fischer, and T. Brox, "U-Net: Convolutional Networks for Biomedical Image Segmentation," *Lect. Notes Comput. Sci.* **9351**, 12–20 (2015).
159. J. Brownlee, *Generative Adversarial Networks with Python: Deep Learning Generative Models for Image Synthesis and Image Translation* (Machine Learning Mastery, 2019).
160. C. Li and M. Wand, "Precomputed Real-Time Texture Synthesis with Markovian Generative Adversarial Networks," in *Computer Vision -- ECCV 2016*, B. Leibe, J. Matas, N. Sebe, and M. Welling, eds. (Springer International Publishing, 2016), pp. 702–716.
161. "cGAN QPI-DHM," <https://oirl.github.io/cGAN-Digital-Holographic-microscopy/>.
162. R. M. Goldstein and C. L. Werner, "Satellite radar interferometry Two-dimensional phase unwrapping," *Radio Sci.* **23**, 713–720 (1988).
163. J. He, A. Karlsson, J. Swartling, and S. Andersson-Engels, "Light scattering by multiple red blood cells," *J. Opt. Soc. Am. A* **21**, 1953 (2004).
164. "RBC video cGAN," <https://drive.google.com/drive/folders/1J7Us28EcrOQfaAFrUHymbKbHU-EeulLi?usp=sharing>.
165. "Apolo Supercomputing," <http://www.eafit.edu.co/apolo>.
166. C. Hayes-Rounds, B. Bogue-Jimenez, J. I. Garcia-Sucerquia, O. Skalli, and A. Doblas, "Advantages of Fresnel biprism-based digital holographic microscopy in quantitative phase imaging," *J. Biomed. Opt.* **25**, 086501 (2020).
167. J. W. Goodman, *Statistical Optics*, Wiley Series in Pure and Applied Optics (Wiley, 2015).
168. E. Hecht, *Optics*, Fourth (2016, n.d.).
169. M. N. Akram and X. Chen, "Speckle reduction methods in laser-based picture projectors," *Opt. Rev.* **23**, 108–120 (2016).
170. P. Picart and J.-C. Li, *Digital Holography* (Wiley, 2012).
171. Xin Kang, "An effective method for reducing speckle noise in digital holography," *Chinese Opt. Lett.* **6**, 100–103 (2008).
172. J. Herrera-Ramirez, D. A. Hincapié-Zuluaga, and J. Garcia-Sucerquia, "Speckle noise reduction in digital holography by slightly rotating the object," *Opt. Eng.* **55**, 121714 (2016).

173. F. Pan, W. Xiao, S. Liu, F. Wang, L. Rong, and R. Li, "Coherent noise reduction in digital holographic phase contrast microscopy by slightly shifting object," *Opt. Express* **19**, 3862 (2011).
174. F. Dubois, M.-L. Novella Requena, C. Minetti, O. Monnom, and E. Istasse, "Partial spatial coherence effects in digital holographic microscopy with a laser source," *Appl. Opt.* **43**, 1131–1139 (2004).
175. P. Memmolo, V. Bianco, M. Paturzo, B. Javidi, P. A. Netti, and P. Ferraro, "Encoding multiple holograms for speckle-noise reduction in optical display," *Opt. Express* **22**, 25768 (2014).
176. Y. Wang, P. Meng, D. Wang, L. Rong, and S. Panzai, "Speckle noise suppression in digital holography by angular diversity with phase-only spatial light modulator," *Opt. Express* **21**, 19568 (2013).
177. J. Garcia-Sucerquia, J. A. H. Ramírez, and D. V. Prieto, "Reduction of speckle noise in digital holography by using digital image processing," *Optik* **116**, 44–48 (2005).
178. A. Buades, B. Coll, and J.-M. Morel, "Non-Local Means Denoising," *Image Process. Line* **1**, 208–212 (2011).
179. J. Maycock, B. M. Hennelly, J. B. McDonald, Y. Frauel, A. Castro, B. Javidi, and T. J. Naughton, "Reduction of speckle in digital holography by discrete Fourier filtering," *J. Opt. Soc. Am. A* **24**, 1617 (2007).
180. K. Dabov, A. Foi, V. Katkovnik, and K. Egiazarian, "Image denoising with block-matching and 3D filtering," *Image Process. Algorithms Syst. Neural Networks, Mach. Learn.* **6064**, 606414 (2006).
181. X. Zhang, "Image denoising using local Wiener filter and its method noise," *Optik* **127**, 6821–6828 (2016).
182. Q. Kemao, "Windowed Fourier transform for fringe pattern analysis," *Appl. Opt.* **43**, 2695–2702 (2004).
183. M. Haouat, J. Garcia-Sucerquia, A. Kellou, and P. Picart, "Reduction of speckle noise in holographic images using spatial jittering in numerical reconstructions," *Opt. Lett.* **42**, 1047–1050 (2017).
184. D. Hincapie, J. Herrera-Ramírez, and J. Garcia-Sucerquia, "Single-shot speckle reduction in numerical reconstruction of digitally recorded holograms," *Opt. Lett.* **40**, 1623–1626 (2015).
185. J. W. Goodman, "Some fundamental properties of speckle," *J. Opt. Soc. Am.* **66**, 1145–1150 (1976).
186. T. Baumbach, E. Kolenović, V. Kebbel, and W. Jüptner, "Improvement of accuracy in digital holography by use of multiple holograms," *Appl. Opt.* **45**, 6077–6085 (2006).
187. T. Nomura, M. Okamura, E. Nitani, and T. Numata, "Image quality improvement of digital holography by superposition of reconstructed images obtained by multiple wavelengths," *Appl. Opt.* **47**, (2008).
188. Y. Park, W. Choi, Z. Yaqoob, R. Dasari, K. Badizadegan, and M. S. Feld, "Speckle-field digital holographic microscopy," *Opt. Express* **17**, 12285–12292 (2009).
189. J. Garcia-Sucerquia, J. H. Ramírez, and D. Velasquez Prieto, "Reduction of speckle noise in digital holography by using digital image processing," *Opt. J. Light Electron Opt.* **116**, 44–48 (2005).

190. A. Uzan, Y. Rivenson, and A. Stern, "Speckle denoising in digital holography by nonlocal means filtering," *Appl. Opt.* **52**, A195–A200 (2013).
191. H. A. Aebischer and S. Waldner, "Simple and effective method for filtering speckle-interferometric phase fringe patterns," *Opt. Commun.* **162**, 205–210 (1999).
192. X. Huang, Z. Jia, J. Zhou, J. Yang, and N. Kasabov, "Speckle Reduction of Reconstructions of Digital Holograms Using Gamma-Correction and Filtering," *IEEE Access* **6**, 5227–5235 (2017).
193. Q. Kemao, "Windowed Fourier transform for fringe pattern analysis: Addendum," *Appl. Opt.* **43**, 3472–3473 (2004).
194. Q. Kemao, "Two-dimensional windowed Fourier transform for fringe pattern analysis: Principles, applications and implementations," *Opt. Lasers Eng.* **45**, 304–317 (2007).
195. F. Le Clerc, M. Gross, and L. Collot, "Synthetic-aperture experiment in the visible with on-axis digital heterodyne holography," *Opt. Lett.* **26**, 1550 (2001).
196. V. Bianco, P. Memmolo, M. Paturzo, A. Finizio, B. Javidi, and P. Ferraro, "Quasi noise-free digital holography," *Light Sci. Appl.* **5**, e16142 (2016).
197. Y. Lu, R. W. Liu, F. Chen, and L. Xie, "Learning a deep convolutional network for speckle noise reduction in underwater sonar images," *ACM Int. Conf. Proceeding Ser. Part F1481*, 445–450 (2019).
198. T. L. Bobrow, F. Mahmood, M. Inserni, and N. J. Durr, "DeepLSR: a deep learning approach for laser speckle reduction," *Biomed. Opt. Express* **10**, 2869–2882 (2019).
199. D. Yin, Z. Gu, Y. Zhang, F. Gu, S. Nie, S. Feng, J. Ma, and C. Yuan, "Speckle noise reduction in coherent imaging based on deep learning without clean data," *Opt. Lasers Eng.* **133**, 106151 (2020).
200. R. Castaneda, J. Garcia-Sucerquia, and A. Doblas, "Speckle noise reduction in coherent imaging systems via hybrid median–mean filter," *Opt. Eng.* **60**, 1–12 (2021).
201. R. Castaneda, Jorge-Garcia-Sucerquia, and A. Doblas, "Synergetic combination of median filtered images to reduce speckle noise in digital holography (DH) and digital holographic microscopy (DHM)," in *OSA Imaging and Applied Optics Congress 2021 (3D, COSI, DH, ISA, PcAOP)* (Optical Society of America, 2021), p. DF4C.7.
202. D. Hincapie, D. Velasquez, and J. Garcia-Sucerquia, "Chromatic aberration compensation in numerical reconstruction of digital holograms by Fresnel–Bluestein propagation," *Opt. Lett.* **42**, 5294 (2017).